



Trapping and cooling of atomic strontium in a compact apparatus: towards a micro ring cavity QED experiment

Mathieu Bertrand

► To cite this version:

Mathieu Bertrand. Trapping and cooling of atomic strontium in a compact apparatus: towards a micro ring cavity QED experiment. Atomic Physics [physics.atom-ph]. Sorbonne Université, 2021. English. NNT : 2021SORUS073 . tel-03681706

HAL Id: tel-03681706

<https://theses.hal.science/tel-03681706>

Submitted on 30 May 2022

HAL is a multi-disciplinary open access archive for the deposit and dissemination of scientific research documents, whether they are published or not. The documents may come from teaching and research institutions in France or abroad, or from public or private research centers.

L'archive ouverte pluridisciplinaire **HAL**, est destinée au dépôt et à la diffusion de documents scientifiques de niveau recherche, publiés ou non, émanant des établissements d'enseignement et de recherche français ou étrangers, des laboratoires publics ou privés.



Département
de Physique
École normale
supérieure



THÈSE DE DOCTORAT
DE SORBONNE UNIVERSITÉ

Réalisée au
LABORATOIRE KASTLER BROSSEL
DE L'ÉCOLE NORMALE SUPÉRIEURE

Trapping and cooling of atomic strontium
in a compact apparatus

Towards a micro ring cavity QED experiment

SOUTENUE LE

22 MARS 2021

Par

MATHIEU JEAN-PAUL BERNARD BERTRAND

Composition du jury

Mme	HUGBART MATHLIDE	Université Côte d'Azur	Rapporteuse
M.	SCHRECK FLORIAN	University of Amsterdam	Rapporteur
M.	TINO GUGLIELMO	Università Degli Studi Di Firenze	Évaluateur
M.	BLATT SEBASTIAN	Ludwig-Maximilians-Universität München	Évaluateur
M.	LANDRAGIN ARNAUD	Sorbonne Université	Évaluateur
M.	REICHEL JAKOB	Sorbonne Université	Directeur de thèse

RÉSUMÉ

Notre compréhension des principes fondamentaux de la mécanique quantique a mené à la *Première Révolution Quantique*, ayant permis des inventions comme le laser et le transistor. Durant les dernières années, l'émergence de technologies quantiques basées sur l'intrication, comme le calcul quantique ou la métrologie quantique, ont défini une *Seconde Révolution Quantique*. Au cours de cette nouvelle ère enthousiasmante, les états quantiques de longue durée de vie constituent les briques élémentaires des systèmes physiques utilisés pour développer ces technologies. Parmi les différents candidats, les ensembles d'atomes de type alcalino-terreux, comme le strontium et l'ytterbium, constituent des candidats prometteurs. La présence de transitions d'*horloge* ultra fines dans leurs structures de niveaux, ainsi que la présence de larges spins nucléaires, a mené à d'impressionnantes avancées dans les domaines des horloges optiques, du magnétisme de type $SU(N)$ et de la physique des atomes de Rydberg.

Afin de produire de l'intrication dans des systèmes contenant de nombreuses particules, plusieurs plateformes physiques se sont révélées utiles. L'*ÉlectroDynamique Quantique en Cavité* (EDQC), permettant de créer des interactions effectives à longue portée entre atomes et la mesure quantique non destructive des états des qubits, en est un exemple particulièrement intéressant. Les possibilités offertes par ces systèmes ouvrent la voie à la génération d'un grand nombre d'états intriqués, qui peuvent par exemple être utilisés dans l'amélioration de la précision des horloges optiques, ainsi qu'à des simulations quantiques contenant des interactions longues distances. Dans cet esprit, nous développons une expérience combinant un ensemble d'atomes de strontium ultra froids à une cavité en anneau miniaturisée. Cette géométrie de cavité permet d'obtenir un couplage homogène entre l'ensemble atomique et la lumière du résonateur optique.

Cette thèse se concentre sur la description du montage expérimental servant à produire l'ensemble d'atomes de strontium ultra froids, tout en prenant en compte les considérations liées à l'EDQC. Sa conception compacte est basée sur une source effusive d'atomes développée par nos soins, émettant vers une cellule en verre ayant un grand accès optique. Afin de réduire la longueur et la complexité du système à vide et ainsi de bénéficier d'une faible divergence du faisceau atomique, le ralentissement et le *Piégeage Magnéto-Optique* (PMO) sont réalisés grâce à un seul et même assemblage de bobines. Les systèmes lasers utilisés pour ces opérations sur deux transitions optiques du strontium à 461 nm et à 689 nm sont détaillés dans cette thèse. De plus, les caractérisations des PMO bleu et rouge donnent les populations et températures des nuages atomiques durant ces deux phases. La cavité en anneau est actuellement prête à être ajoutée au montage expérimental, ouvrant la voie vers une plateforme stable et relativement simple pour réaliser des opérations d'EDQC sur la transition d'horloge du strontium.

ABSTRACT

Our understanding of the fundamental principles of quantum mechanics has led to a *First Quantum Revolution*, which enabled inventions such as the laser and transistor. In the past few years, the emergence of an ensemble of quantum entanglement based technologies, such as quantum computing and quantum metrology, have defined a *Second Quantum Revolution*. At the very heart of this exciting new area, long-lived quantum states constitute the building blocks of the physical systems used to develop these technologies. Among the different candidates, a promising one is given by ultra-cold ensembles of alkaline-earth-like atoms, such as strontium and ytterbium. The presence of ultranarrow clock transitions in their level structures, as well as large nuclear spins, have led to impressive advances in the domains of optical clocks, $SU(N)$ magnetism and Rydberg physics.

In order to produce entanglement in many-body quantum systems, several physical platforms have been proven useful. A particularly interesting one is *Cavity Quantum ElectroDynamics* (CQED), allowing to create long-range effective interactions between atoms and quantum non demolition measurements of the qubits states. These possibilities open the way to a wide range of multiparticle-entangled states generation, which can be used in entanglement-enhanced precision of optical atomic clocks, and quantum simulations with long-range interactions. In this spirit, we aim to develop an experiment combining ultra-cold strontium atoms and a miniaturized ring cavity. Such a cavity geometry allows for homogeneous coupling between the atomic ensemble and the resonator light.

This thesis is focused on the description of the experimental apparatus producing an ultra-cold sample of strontium atoms, taking into account the requirements of optical CQED. Its compact design is based on a home-made effusive atomic source emitting towards a glass cell with high optical access. In order to reduce the vacuum system length and its complexity, and thus benefit from a reduced divergence of the atomic beam, slowing and *Magneto-Optical Trapping* (MOT) procedures are realized with a single magnetic coil assembly. The laser systems used for these operations with two different strontium optical transitions at 461nm and 689nm are also described in this thesis. Moreover, characterizations of the obtained blue and red MOT give the clouds populations and temperatures achieved in these two phases. The ring cavity is currently ready to be added to the experimental apparatus, paving the way to a reliable and relatively simple platform for CQED operations on the strontium clock transition.

REMERCIEMENTS

Réaliser une thèse de doctorat est un grand projet, aussi bien sur le plan professionnel que personnel et il s'agit donc d'être entouré du mieux possible pour la mener à bien. Durant les trois ans et demi que j'ai passé au Département de Physique de l'ENS, j'ai eu la chance de trouver des sources de soutiens divers et variés. Je tiens d'abord à remercier Jakob Reichel de m'avoir donné l'opportunité d'évoluer dans cet environnement. J'ai pu bénéficier d'une grande confiance de sa part, me permettant de prendre part à toutes les étapes du développement de ce beau projet et ce dès mon arrivée dans le laboratoire en tant que stagiaire. Il m'a aussi donné la possibilité d'organiser une conférence scientifique au sein de l'ENS, opportunité très intéressante et formatrice. Les autres membres de l'équipe strontium ont également été des sources d'inspiration pour moi. Travailler avec Lucas Béguin a été un immense plaisir, tant pour sa joie de vivre que pour ses cours particuliers de physique (et autres) délivrés avec bienveillance autour de chacun des cafés que nous avons pu prendre ensemble. Son remarquable esprit scientifique nous a guidé dans la conception du projet et sa bonne humeur en a rendu la réalisation très agréable. Quant à Torben Pöppelau, son calme et sa détermination font de lui une force de la nature, très inspirante lorsque j'étais moi-même sujet aux doutes et à la fatigue. Son sens expérimental a été un atout majeur pour l'équipe et j'ai toujours pu bénéficier de son soutien infailible. J'ai également bénéficié de ce soutien avec les autres membres de l'équipe micropuces à atomes. Romain Long d'abord, responsable de l'expérience de rubidium *SAROCMA*, a toujours été d'une bienveillance incroyable. Les discussions passionnées de physique que nous avons eues se sont accompagnées de conseils et de réflexions extrêmement utiles, dont je suis reconnaissant. Cette bienveillance se retrouve chez tous les membres de cette équipe. Au fil des générations de doctorants, j'ai eu la chance de côtoyer Francesco Ferri, d'une gentillesse incomparable accompagnée d'un appétit scientifique florissant. Son successeur, Mohamed Baghdad, a également hérité de cette gentillesse se traduisant par un altruisme que je n'ai rencontré chez nulle autre personne jusqu'à présent. Je le remercie particulièrement pour son soutien ainsi que son art de détendre l'atmosphère, fort apprécié de tous. Aujourd'hui, c'est Pierre-Antoine Bourdel qui poursuit fièrement cette lignée de bonne humeur radiative revigorante pour le reste de l'équipe. Les anciens post-doctorants ne sont pas en rade non plus à travers Arthur La Rooij et sa légendaire joie de vivre, ayant apporté beaucoup de bonne humeur dans notre salle café. Je tiens également à remercier chaleureusement Sylvain Schwartz pour tout ce qu'il a pu m'enseigner, ses conseils, sa joie, mais aussi son soutien qui me permet à présent de poursuivre une carrière dans les technologies quantiques. Chez les membres de l'équipe *TACC* localisée au SYRTE, les discussions avec Mengzi Huang m'ont apportées autant de réponses que de curiosité nouvelle envers les phénomènes étudiés dans notre groupe. Enfin, nos membres théoriciens m'ont été d'une aide précieuse. Je remercie Alice Sinatra pour sa gentillesse et le temps accordé lors de nos différentes discussions, notamment au sujet de la théorie de la spectroscopie du jet atomique. Manuel Gessner a aussi été un très bon professeur, particulièrement au travers de ses présentations extrêmement pédagogiques. Au

laboratoire, j'ai bénéficié de la présence de mon voisin de bureau Alan Serafin à qui j'ai toujours pu confier mes questions scientifiques aussi bien que mes états d'âme.

Être en charge des opérations sur cette expérience de strontium m'a donné la chance de collaborer avec des stagiaires exceptionnels. Je tiens à remercier Jan-Philipp Bureik pour son travail sur la stabilisation des lasers repompeurs, mais surtout pour sa sympathie hautement appréciable servie sur une parfaite maîtrise de la langue de Molière. Je pense également à Vishal Sharma, ayant notamment construit un des systèmes de contrôle de fréquence de l'expérience, ainsi qu'à Enrique Morel qui a contribué au couplage du laser d'horloge sur la cavité ultra-stable. Sur les derniers mois d'expérimentation, j'ai également travaillé avec Hitheswar Prasad qui m'a été d'une grande aide sur les ultimes prises de données autant que sur l'ambiance conviviale qu'il a créée. Je leur souhaite à tous une grande réussite et beaucoup de bonheur dans leur parcours naissants.

Tous ces grands projets scientifiques ne seraient que papier et crayon sans l'aide des équipes techniques du Laboratoire Kastler-Brossel. Je tiens à remercier l'atelier mécanique qui a produit des pièces d'une grande qualité nous ayant permis de réaliser cette expérience innovante. Nous avons tous pu apprécier le travail des membres du bureau d'étude Nabil Garroum et Arnaud Leclercq ainsi que de celui de tous les mécaniciens et soudeurs dirigés par Jean-Michel Isac. Je remercie en particulier Georges Cornudet pour l'aide qu'il m'a apportée sur la construction de la cellule de spectroscopie. Ces expériences nécessitant énormément de matériel, la vie ne serait pas la même sans l'aide de Thierry Tardieu, Audrey Gohlke, Christelle Rio et les autres membres du services des commandes, anciens comme actuels. Nous n'avons pas manqué de les inonder de bons de commandes et de livraisons, sans pour autant affecter leur sympathie. Un grand merci également à Valérie Revelut et Stéphanie Dubois pour leur communication drôle et débordante de joie. Je remercie également le directeur du laboratoire Antoine Heidmann pour son travail améliorant la qualité du quotidien au laboratoire autant que sa renommée.

Sur le plan personnel, cette expérience aura été une aventure extrêmement enrichissante qui m'aura fait grandir sur bien des aspects. Traversant autant de plaines ensoleillées que de monts brumeux, j'ai toujours pu compter sur la présence de mes camarades pour traverser avec sérénité les épreuves s'offrant à moi. Mes amis de l'ESPCI, pour la plupart dans le même bateau, m'ont accompagnés et portés sur ce chemin sinueux. Mes proches compagnons d'études et d'enfance ont aussi été des bouées stables sur cet océan changeant. Bien entendu, ma famille a plus que jamais contribué à mon bien être par son soutien, surtout lorsque nous affrontions ces nouvelles périodes de confinement dont nous n'imaginions même pas l'existence quelques mois seulement auparavant. Mes parents m'ont transmis leur force et leur optimisme, et mon frère Alexandre sa sérénité. La dernière personne, et non des moindres, vers qui une majorité de mes pensées est dirigée est ma compagne Margaux. Depuis le début de cette aventure, elle a été à la fois héroïne à mes côtés et conseillère en rempart contre la solitude. Ma vie ne serait pas si belle sans sa présence et je dédie ce travail au soutien qu'elle m'apporte chaque jour.

TABLE OF CONTENTS

	Page
List of Tables	xi
List of Figures	xiii
Introduction	1
1 Exploring entanglement with alkaline-earth atoms in a ring cavity	7
1.1 Cavity QED	7
1.1.1 Optical cavity properties	8
1.1.2 Light-matter coupling in optical cavities	10
1.1.3 Fiber micro cavities	17
1.2 Physical properties of strontium atoms	18
1.2.1 Two electrons systems	19
1.2.2 Strontium energy levels	21
1.2.3 Magic trapping	26
1.3 Towards a micro ring cavity experiment with strontium atoms	27
2 Laser system	29
2.1 Blue MOT laser system	29
2.1.1 461nm master-slave architecture	30
2.1.2 Repumping lasers numerical lock	34
2.2 Red laser system	37
2.2.1 689nm master-slave architecture	37
2.2.2 Frequency stabilization on the Fabry-Pérot cavity	38
2.2.3 Absolute frequency calibration with the heat-pipe spectroscopy cell	46
3 A compact vacuum system	53
3.1 An effusive source of strontium	54
3.1.1 Capillary design	54
3.1.2 Knudsen theory of collisions	55
3.2 Vacuum system	56

TABLE OF CONTENTS

3.2.1	Strontium peculiarities motivated design	57
3.2.2	Oven section power consumption	59
3.2.3	Differential pressure stage	61
3.2.4	Science chamber	62
3.3	Atomic beam spectral properties	63
3.3.1	Effusive atomic beam flow	63
3.3.2	Laser beam absorption	67
3.4	Strontium source characterization	72
3.4.1	Oven test apparatus	73
3.4.2	Collimated beam characterization	76
4	Trapping and cooling of strontium atoms	83
4.1	A combined Zeeman slower and MOT apparatus	86
4.1.1	Magneto-optical configuration	86
4.1.2	Time sequence generation	93
4.2	Zeeman slowing of the effusive atomic beam	93
4.2.1	Constant deceleration slower theory	94
4.2.2	Quadrupole slower	96
4.3	MOT regimes and mechanisms	96
4.3.1	$ J_g = 0\rangle \rightarrow J_e = 1\rangle$ MOT description	97
4.3.2	Strontium fermionic MOT	99
4.4	Cooling on the dipole allowed blue transition at 461 nm	103
4.4.1	Absorption imaging	103
4.4.2	Experimental realization	107
4.4.3	Loading efficiency	110
4.4.4	Blue MOT characterization	114
4.5	Narrow-line cooling on the red intercombination line at 689 nm	122
4.5.1	Narrow-line cooling techniques	122
4.5.2	Red MOT time sequence	125
4.5.3	SWAP MOT characterization	127
4.5.4	CW operation	136
	Conclusion	141
	Prospectives on the ring cavity	143
	A Optical tables schemes	147
	B Laser astigmatism compensation based on ABCD matrices formalism	151

C	DDS based frequency generation setup for AOMs	155
D	Absorption on the $5s5p)^3P_2\rangle \rightarrow 5s6s)^3S_1\rangle$ line at 707 nm	157
E	Optical Bloch equations	159
	Bibliography	163

LIST OF TABLES

TABLE	Page
1.1 Strontium stable isotopes with their natural abundances, quantum statistics and nuclear spins.	21
1.2 Hyperfine splitting constants of the ^{87}Sr energy levels.	24
1.3 Isotope shifts of the energy levels used for trapping, cooling and clock operations given in MHz. The shifts are referenced to the ^{88}Sr isotope.	24
2.1 Operating parameters of the lasers involved in the blue MOT operation.	30
2.2 Operating parameters of the 689 nm lasers.	37
2.3 High-finesse Fabry-Pérot cavity characteristics.	41
2.4 FWHM laser estimation for red master and clock lasers.	46
3.1 Flow regimes criteria based on the capillary geometrical dimensions and the atomic mean free path.	56
3.2 Heat transfer toy model parameters.	61
3.3 Characteristics of the effusive atomic beam at the oven output and the collimated beam at the MOT position inside the glass cell for a source temperature of 460°C . . .	81
4.1 Coil pairs geometrical parameters. The turns are represented as a cut view perpendicular to the wire loops. The distance between the coils and the inner radii are given with respect to the closest loop.	88
4.2 Relevant set of parameters for strontium cooling on the blue and red transitions. . . .	99

LIST OF FIGURES

FIGURE	Page
1.1 Scheme of a Fabry-Pérot (left) and a triangular ring cavity (right) with their optical configurations.	8
1.2 (a) Optical cavity transmission as a function of the round-trip phase $\Phi = \omega/\omega_{FSR}$ for a mirror reflection factor $R = 0.7$. (b) Cavity finesses for symmetrical Fabry-Pérot (blue line) and triangular ring cavities (orange line) as a function of R	9
1.3 CQED scheme with an atomic ensemble placed in a ring cavity. The atomic spontaneous emission of photons into free space is characterized by a transversal decay rate $\Gamma_{\perp} = \Gamma/2$. The cavity is pumped by an incident electric field at a rate η , and losses photons by mirrors transmission at a rate κ . The coupling constant g between the intra-cavity photons and the atomic ensemble gives the strength of the dipolar interaction.	10
1.4 (a) Level scheme of a two-level atom coupled to a single cavity mode at frequency ω_c with a laser probe at frequency ω . (b) Cavity transmission as a function of the probe detuning $\Delta_c = \omega - \omega_c$ for a bare cavity in blue and a cavity on resonance with the atoms $\Delta_{ac} = \omega_0 - \omega_c = 0$ in yellow. The mean cavity mode population is supposed to be lower than one. (c) Eigenenergies of the single atom and single photon dressed states. . . .	16
1.5 (a) Multi-shot CO ₂ laser pattern on an optical fiber, resulting in a Gaussian mirror profile imaged with a profilometry technique. (b) Scanning Electron Microscope image of the fiber tip with the mirror shape in the center. (c) Mirror profiles along the fiber tip axes and residuals from a 2D spherical fit.	18
1.6 Relevant energy levels and transitions of the strontium bosonic isotopes with a nuclear spin $I = 0$	22
1.7 Relevant energy levels and transitions of the strontium fermionic isotope ⁸⁷ Sr with a nuclear spin $I = 9/2$. The frequency shifts compared to the ⁸⁸ Sr isotope are given in MHz.	25

- 1.8 (a) Principle of the strontium experiment. An home-made oven acts as an effusive source to create an atomic beam, slowed down by a laser beam associated with the decaying part of the quadrupole magnetic field used to produce a MOT in the glass cell. (b) Artistic view of the ring cavity with strontium atoms held by a standing wave dipole trap. The curved mirror of the cavity is shaped on the surface of an optical fiber, and the plane mirrors consist in glass plates. 28
- 2.1 Scheme of the laser systems at 461nm, 679nm and 707nm. Half-wave plates and exact mirror configurations have been omitted for simplicity and the slave injection simplified. The AOM diffraction orders are ± 1 depending on the orientation with respect to the RF frequency input. A realistic version of the laser system is presented in appendix A. DM - Dichroic Mirror, PD - Photodiode, MIR - Mirror, ISO - Optical Isolator, PBS - Polarising Beam Splitter, LP - Low-Pass filter, SG - Signal Generator, SP - RF Splitter, MX, RF Mixer, FC - Fiber Coupler, PM - Polarization Maintaining fiber, AOM - Acousto-Optic Modulator, EOM - Electro-Optic Modulator. 31
- 2.2 (a) Schematic view of the *Cateye Diode Laser* configuration. The diode laser emission wavelength is first selected by a bandpass filter. The beam is then focused on a mirror which position depends on a piezo electric actuator to form a tunable extended cavity with the diode laser rear facet itself. (b) Scheme of the *Littrow Diode Laser* configuration. The external cavity is created by a grating angled such that the first order reflection is superimposed to the diode laser output mode. The cavity length is also controlled by a piezo electric actuator placed on the grating. 32
- 2.3 Saturated absorption signal (left axis) and error signal (right axis) generated by a retro-reflected beam from the 461nm master laser. The beam properties are 510 μ W of optical power and a waist of 400 μ m, corresponding to a saturation parameter $s_0 = 5$. The frequency axis is referenced to the $|5s^2)^1S_0\rangle \rightarrow |(5s5p)^1P_1\rangle$ transition of ^{88}Sr . The signals exhibit Lamb dips for this transition for the different isotopes. 34
- 2.4 Frequency diagram for the laser system at 461nm. The vertical axis represents the optical frequencies referenced to the dipole allowed transition of ^{88}Sr . The AOM RF frequencies f_i are given in MHz. Transitions for the other isotopes are also given on the frequency axis. The ^{87}Sr transitions from the ground state $|5s^2)^1S_0, F_g = 9/2\rangle$ to the excited states $|5s5p)^1P_1, F_e\rangle$ are referenced by their hyperfine quantum number F_e . 35
- 2.5 (a) Scheme of the numerical PI lock of the repumping lasers. Closed loop frequency of the (b) 679nm and (c) 707nm repumpers. Data are shown in blue and an exponential fit in orange gives the $1/e$ decay time from an arbitrary frequency to the setpoint. . . 36

2.6	Scheme of the laser systems at 689nm, 698nm and the stabilization part of the dipole trap system. ICE is a software used to control the frequency of a Titanium Sapphire laser from MSquared. Half-wave plates and exact mirrors configurations have been omitted for simplicity and the slave injection simplified. The AOM diffraction orders are ± 1 depending on the orientation with respect to the RF frequency input. A realistic version of the laser system is presented in appendix A. DM - Dichroic Mirror, PD - Photodiode, MIR - Mirror, ISO - Optical Isolator, PBS - Polarising Beam Splitter, LP - Low-Pass filter, SG - Signal Generator, SP - RF Splitter, MX, RF Mixer, FC - Fiber Coupler, PM - Polarization Maintaining fiber, AOM - Acousto-Optic Modulator, EOM - Electro-Optic Modulator, f-EOM - fibred EOM.	38
2.7	Frequency diagram for the laser system at 689nm. The vertical axis represents the optical frequencies referenced to the intercombination line of ^{88}Sr . The AOM RF frequencies f_i are given in MHz. Transitions for the other isotopes are also given on the frequency axis. The ^{87}Sr transitions from the ground state $ (5s^2)^1S_0, F_g = 9/2\rangle$ to the excited states $ (5s5p)^1P_1, F_e\rangle$ are referenced by hyperfine quantum number F_e	39
2.8	(a) Picture of the notched <i>Stable Laser Systems</i> cavity with opened vacuum chamber and thermal housing. (b) Cavity ring-down in logarithmic scale with a 689nm laser beam of power $P_{in} = 60\mu\text{W}$	41
2.9	Cavity transmission and reflection for a laser beam of power $P_{in} = 160\mu\text{W}$ at 698nm as a function of the cavity detuning δ_c	43
2.10	(a) Pound-Drever-Hall error signal of the red master laser at 689nm with a $300\mu\text{W}$ beam as a function of the cavity detuning $\delta_{rc} = \nu_{rM} - N\nu_{FSR}$, with $N \in \mathbb{N}$. (b) Error signal of the clock laser at 698nm with the same optical power before the dichroic mirror as a function of cavity the detuning $\delta_c = \nu_{ck} - M\nu_{FSR}$	44
2.11	Power Spectral Density of the opened loop (blue) and closed loop (orange) error signals of the (a) red master laser at 689nm and (b) clock laser at 698nm. The β -separation lines depicted in red define the shaded areas that contributes to the laser linewidths. The black lines are flicker model fits in the $f \leq f_m$ region.	46
2.12	(a) CAD of the heat-pipe spectroscopy cell. (b) Picture of the central part of the cell with the heating wire wrapped around it. The thermocouple fixed to the strontium reservoir is also visible as a green wire.	48
2.13	(a) Saturated absorption and error signals at 689nm in the heat-pipe spectroscopy cell with a modulation frequency $f_{rm} = 6.0\text{MHz}$. The frequency axis is referenced to the ^{88}Sr resonance. (b) ^{88}Sr Lamb dip and error signal with $f_{rm} = 600\text{kHz}$. The heat-pipe is operated at 700°C	49

2.14	(a) Error signals and frequencies configurations for the laser system at 689nm. The frequency axis is referenced to the $ (5s^2)^1S_0\rangle \rightarrow (5s5p)^3P_{1,m_J=0}\rangle$ transition of ^{88}Sr at ν_{r0} such that $\delta_r = \nu_{rM} - \nu_{r0}$. The laser electric fields at frequencies ν_{rM} for the master laser, ν_{rS} for the slave, ν_{rMOT} for the red MOT and ν_c for the high-finesse cavity mode are represented as vertical dashed lines. The error signal centred on $\delta_r = f_{r2}$, in orange, corresponds to the PDH locking signal. The blue signal, centred on $\delta_r = 0$, is the saturated absorption error signal from the heat-pipe spectroscopy cell. (b) Typical data and fit for the saturated absorption error signal used as an absolute frequency reference. The data are represented in blue and the fit function from equation 2.19 in orange. (c) Cavity drift calibration for a 48 days measurement.	51
3.1	CAD of the home-made oven. The reservoir containing metallic strontium is surrounded by a heating wire and its temperature is measured with a thermocouple. A screw cap closes the reservoir from the back.	54
3.2	(a) Vapour pressures of alkali and alkaline-earth laser cooled atoms. (b) Mean free path of ^{88}Sr intra-species limited elastic collisions. Dashed lines correspond to $\tilde{\lambda} = L$ and $\tilde{\lambda} = a$ in blue and orange, respectively. This boundaries define three regimes for the atomic beam properties.	56
3.3	(a) CAD of the vacuum system apparatus. (b) Cut inside the vacuum system with selected components showing the atomic beam path and MOT position.	58
3.4	Photography of a metallic strontium sample under vacuum (bottom) and open air strontium oxide (top).	59
3.5	Photographies of the oven sustaining flange. (a) Frontside view showing the differential pressure and collimation holes. The flange also serves as a mount for one of the two right-angled mirror prisms. (b) Backside view showing the three tapped holes used to screw the oven three-legged mount.	60
3.6	Electrical power consumption used to heat the oven inside the vacuum system. A simple analytical model predicts the temperatures of the wire (orange dashed line) and the reservoir (yellow dashed line).	61
3.7	(a) Side view of the science glass cell glued on a titanium flange connected to the vacuum system. (b) Bottom view of the right-angled prism mirror glued onto the cell via three quartz plates.	63
3.8	Scheme of the atomic effusive beam at the oven output. The Cartesian and spherical coordinates considered for the mathematical flow rate description are represented at $\vec{r} = \vec{0}$, corresponding to the capillary output.	64
3.9	(a) Velocity density of probabilities for an atomic vapour in blue and an effusive atomic beam in the transparent regime in orange. (b) Angular distribution function in logarithmic scale for a cosine emitter in blue and a peaked effusive beam emitted by a $L/a = 12.5$ capillary in orange. (c) Peaking factor as a function of the oven temperature.	66

3.10	Scheme of the effusive beam transverse absorption and fluorescence spectra recording using a probe laser beam. The probe propagates along the y axis and the transmission is collected by a photodiode on this same axis. The fluorescence is recorded by an optical system composed of a collecting lens and a focusing lens converging scattered photons on a photodiode placed on the x axis.	68
3.11	Hyperfine manifold for a $^{2S+1}L_J$ quantum state.	71
3.12	(a) Picture of the vacuum test apparatus for absorption and fluorescence spectroscopy of the oven atomic output beam. The laboratory frame is defined on the top left corner. (b) Picture of the oven fixed on a custom sustaining flange.	73
3.13	(a) Transverse absorption and (b) fluorescence spectra with a 461nm probe beam located at a distance $z_0 = 1.1$ mm from the capillary output and vertical position x_0 . The oven is operated at a temperature of 463°C. The data are presented as solid lines, while the corresponding theoretical predictions from equation 3.33 are displayed as dotted lines with identical colours. (c) Absorption spectra at the large distance $z_0 = 15$ mm from the oven for different vertical positions. (d) On resonance optical depths for different probe positions along the effusive beam path with the model predictions represented as solid lines for each distance z_0	75
3.14	(a) Transmission spectra for a beam at position $x_0 = 0$ and $z_0 = 1.0$ mm from the oven output for different source temperatures. (b) Flow rate inferred from the absorption spectra in logarithmic scale. The data are represented as blue points and compared to the theoretical predictions in solid orange line, rescaled by a factor 4 in dotted yellow line.	76
3.15	(a) Scheme of the collimated beam characterization by transverse and longitudinal fluorescence. All the vacuum components have been removed except for the oven and the glass cell for clarity. (b) Fluorescence spectrum of the collimated beam for a probe laser beam counter-propagating with respect to the atomic beam. The oven temperature is equal to 467° and the saturation parameter is set below unity.	77
3.16	(a) Transverse fluorescence spectrum of the collimated atomic beam inside the glass cell with the oven operating at 460°C. The low saturation probe laser beam is scanned over the 461nm resonance referenced to the ^{88}Sr isotope. The data are represented as a solid blue line, and fit functions taking into account all the different strontium isotopes weighted by their natural abundance are shown as dashed coloured lines. The profiles sum is represented as a black dotted line. (b) Normalized theoretical profile in logarithmic scale showing the different isotopic contributions with the colour code defined in (a).	78

3.17	(a) Fluorescence spectra of the collimated beam at a distance $z_0 = 13.5\text{cm}$ from the oven, probed by a transverse beam in the vertical plane centred on y_0 . The data, shown as solid lines, are adjusted by fit functions equal to a sum of profiles from equation 3.48 taking into account the different strontium isotopes. (b) On-resonance fluorescence maxima as a function of the horizontal probe beam position y_0 . The data are shown as solid points for two different distances z_0 to the oven, adjusted by Gaussian profiles represented as solid lines.	80
4.1	Periodic table of the elements classified by families. The atomic species for which laser cooling has been demonstrated are highlighted by thick black squares.	85
4.2	(a) CAD of the coils assembly including quadrupole and bias coil pairs maintained by sustaining copper holders. The water cooling pipes entries are visible on the left part of the assembly. (b) Cut inside the vacuum system with selected components showing the MOT and slower laser beams. The quadrupole (thick square) and bias coil pairs (thinner rectangles) are represented without the holders.	87
4.3	(a) Configuration for calculating the magnetic field created by a single rectangular coil. (b) Coil pairs geometry in our assembly. The coil centres are indicated only for the positive axis values. The bias coils have similar rectangular dimensions while the quadrupole pair presents a square geometry.	88
4.4	(a) Magnetic field produced by the quadrupole coil pair along the z axis for a current $I_Q = 0.15\text{A}$. The theory with not adjustable parameter is represented as a solid blue line, and its derivative as an orange line. (b,c,d) Bias fields along the z , x and y axes produced by the corresponding bias coil pairs for currents $I_z = 1.22\text{A}$, $I_x = 0.83\text{A}$ and $I_y = 0.75\text{A}$	90
4.5	(a) Quadrupole coils current supply scheme. SSR : Solid-State Relay, PS : Power Supply, R : Resistor, D : Diode. (b) Magnetic field drop when opening the SSR on the I_b branch (blue solid line) and exponential fit (orange dotted line).	91
4.6	Scheme of the MOT, Zeeman slower and imaging optics in the horizontal plane. The fiber output couplers include lenses and half-wave plates. CCD : Charge Coupled Device camera, FOC : Fiber Output Coupler, MOT : Magneto-Optical Trap.	92
4.7	On scale geometry of the experiment for zeeman slowing and MOT operations with the quadrupole coil pair.	94
4.8	(a) Quadrupole field with $I_Q = 25\text{A}$ (blue) and constant deceleration magnetic profile with $\Delta B = 300\text{G}$ (orange) along the atomic beam axis p . The oven is located at $p_0 = -15\text{cm}$ compared to the MOT region at $p = 0$. (b) Fluorescence spectra of the atomic beam facing a Zeeman slower laser of saturation parameter $s_0 = 50$ for different fixed Zeeman detunings $\delta\nu_{ZS}$. The signal is recorded with a low saturation probe beam scanned across the resonance at detuning Δ_0 for a constant magnetic gradient $\partial_z B = 35\text{Gcm}^{-1}$	97

4.9	(a) Three-dimensional scheme of the MOT with three pairs of counter-propagating circular beams. The quadrupole coils are represented with opposite running currents generating the magnetic field linear dependency in the MOT region. (b) One dimensional scheme of a $ J_g = 0\rangle \rightarrow J_e = 1\rangle$ MOT. A pair of beams with opposite circular polarizations addresses an atomic cloud exposed to the quadrupole magnetic field gradient. The excited Zeeman states energies are represented as a function of the spatial coordinate z	98
4.10	(a) Energy levels and relative transition strengths $c_{m_F}^2 \times 165$ for the dipole allowed and the intercombination transitions of ^{87}Sr . (b) As $g_{F_g} \ll g_{F_e}$, some σ_- (σ_+) are brought on resonance in the negative (positive) $z - z_0$ region, producing anti-trapping forces. This situation is represented for an atom in the stretched $m_{F_g} = 9/2$ ($-9/2$) ground state in the left (right) part of the graphic. The dipole allowed transition is represented as a broad blue line of width Γ , while the intercombination line corresponds to the smaller red line of width Γ_r	101
4.11	(a) Energy levels of ^{87}Rb for MOT operation on the D_2 line. The different Zeeman transitions are represented by coloured lines with the corresponding relative transition strengths $c_{m_F}^2 \times 30$ from equation 3.37. (b) Zeeman detunings for the $ 5^2S_{1/2}, F_g = 2, m_{F_g}\rangle \rightarrow 5^2P_{3/2}, F_e = 3, m_{F_e}\rangle$ transitions along the z axis. The σ_+ and σ_- transitions can be separated in two distinct manifolds, all trapping the atoms toward the MOT center as shown for the stretched states.	102
4.12	(a) Absorption images of the blue MOT after different times-of-flight to illustrate the method. (b) Projection of the number of atoms on the horizontal axis of the CCD camera (blue line) and Gaussian fit (orange line). (c) Gaussian radii of the cloud (points) and associated fits (lines) according to equation 4.28 on the horizontal and vertical axes.	106
4.13	Time sequence for blue MOT operation with measured longitudinal magnetic field gradient and optical beams powers.	108
4.14	Glass cell (blue dots) and viewport (orange circles) transmissions as a function of the angle of incidence θ_i for a 461 nm horizontally polarized beam. The data are compared to a Fresnel coefficients model with a refractive index $n = 1.5$ for linear polarizations p (yellow solid line) and s (green point dotted line) as well as circular polarizations $\sigma = (s \pm ip)\sqrt{2}$ (purple point dotted line).	109
4.15	Fluorescence of the blue MOT at 689 nm. (a) Blue MOT with intensity imbalance between the laser beams probed by a single 730 μW probe on the red transition with a magnetic gradient $\partial_z B = 31 \text{ G cm}^{-1}$. (b) Blue MOT with balanced beams intensities probed by the six red MOT beams. The frequency axes are centred on the main peaks in each figure.	110

4.16	Number of atoms in the ^{88}Sr blue MOT as a function of (a) the magnetic field gradient $\partial_z B$ and the Zeeman slower beam detuning $\delta\nu_{ZS}$ and (b) the slower beam power before the glass cell. The dotted blue line is a guide to eye showing the saturation of the number of atoms. The oven is operated at 440°C	111
4.17	Fluorescence of the blue MOT when (a) loading the atoms by switching on the Zeeman slower beam and (b) switching it off for different oven temperatures. The data are represented by solid coloured lines while the black dotted lines correspond to fits according to equation 4.39.	112
4.18	(a) Steady state number of atoms in the blue MOT as a function of the oven temperature (blue points) and adjustment by a linear function (orange dotted line). (b) Loading rate of the MOT from the fits in figure 4.17(a). Two linear functions (orange and yellow dotted lines) enlight the transparent and opaque regimes, respectively, delimited by the critical temperature $T_c = 450^\circ\text{C}$. (c) Loss rate and lifetime for the MOT decay from the fits in figure 4.17(b). (d) Two-body loss rate for both MOT loading (blue points) and damping (yellow points) with linear fits. The optical powers were set to $P_{MOT} = 11.3\text{mW}$ and $P_{ZS} = 12.0\text{mW}$, with respective detunings $\delta\nu_{MOT} = -28\text{MHz}$ and $\delta\nu_{ZS} = -545\text{MHz}$	113
4.19	Bosonic blue MOT optimization as a function of the MOT beams detuning. (a) Temperature of the cloud in the horizontal h (blue points) and vertical v (orange points) directions of the CCD camera. The Doppler theory curve for $s_0 = 0.7$ (yellow dotted line) is drawn for comparison. (b) Gaussian radius of the MOT for both directions. (c) Number of trapped atoms. (d) Phase-space density derived from equation 4.40.	115
4.20	Blue MOT (a) number of atoms and (b) temperature as a function of the 461nm master laser frequency referenced to the ^{88}Sr resonance. The double resonance feature demonstrates that trapping on the all the strontium isotopes is achieved, with a bosonic ensemble centred on $\delta\nu_M = -370\text{MHz}$ and a fermionic one at $\delta\nu_M = -415\text{MHz}$	116
4.21	Fluorescence of the blue MOT at 461nm depleted by the red MOT beams scanned over the 689nm resonance. The blue curves corresponds to a fermionic blue MOT with resonances for the three different $ (5s5p)^3P_1, F_e\rangle$ manifolds, while the orange curve corresponds to an ^{88}Sr MOT with a fraction of ^{86}Sr atoms.	117
4.22	(a) Number of atoms in the bosonic (blue points) and fermionic (orange points) MOTs as a function of the blue MOT beams power per axis during the loading phase. The blue dotted line is a guide to the eye showing the number of ^{88}Sr atoms saturation. (b) Horizontal and vertical cloud temperatures (dots) with linear fits (dotted lines). (c) Phase-space density of the MOT for the two species.	118

4.23	(a) Number of atoms, (b) temperature, (c) size and (d) phase-space density of the bosonic blue MOT as a function of the longitudinal magnetic field gradient final value for a 100 ms long compression at the end of the sequence. The 3 s loading phase is operated at $\partial_z B = 32.5 \text{ G cm}^{-1}$	119
4.24	Number of atoms and temperature in the ^{88}Sr and ^{87}Sr blue MOTs as a function of the (a,b) 679 nm and (c,d) 707 nm repumpers lasers powers before the glass cell. . . .	120
4.25	(a) Picture of a typical ^{88}Sr blue MOT inside the glass cell. The right-angled mirror prism is visible on the left part of the image. The MOT fluorescence corresponds to the highly saturated blue circle at the center, while the other ones correspond to MOT and Zeeman slower beams reflections onto the surfaces of the cell. (b) Absorption image of the blue MOT taken along the horizontal h and vertical v axes of the CCD camera. . .	121
4.26	(a) One dimensional configuration for red MOT operation. Two counter-propagating beams with opposite circular polarizations are sent toward an atom with velocity \vec{v} . The Doppler shifted frequencies of the laser are indicated on the corresponding lasers. (b) BB phase scheme. The laser frequency is modulated symmetrically over time. The Doppler and Zeeman shifted energies of the excited state are represented as red lines, detuned by the recoil frequency ω_r at photonic absorption events. The stimulated emission events are presented as red arrows. (c) SWAP mechanism. The laser frequency is modulated in a saw-tooth manner, preventing stimulated emission in the beam absorbed during the upward ramp. The atoms thus have a higher probability to decay by stimulated emission, represented as a wavy arrow.	123
4.27	Time sequence for the red MOT operation. The time axis is referenced to the end of the sequence t_{end} . The blue MOT power switch off corresponds to 3.1 s after the beginning of the blue MOT loading from figure 4.13. The repumping beams are kept on with constant power during the whole sequence, while the y and z bias fields are null. Only the first imaging pulse is represented, the second one being delayed by 100 ms. . . .	126
4.28	Sweep amplitude generated by the red master-slave architecture measured with a wavelength meter. The teeth repetition rate is intentionally slowed by 2 orders of magnitude compared to SWAP operation to stay below the instrument bandwidth. . .	127
4.29	SWAP MOT pictures for different bias x field amplitudes with $N_S = 400$, $\Delta_S/2\pi = 3 \text{ MHz}$ and $v_{end} = 1.2 \text{ MHz}$	128
4.30	(a) Fluorescence signal of 5 blue MOTs in a row. The data are presented as blue points while a fit according to equation 4.39 plus an offset is given as a black line. (b) Correlation between the fluorescence loading amplitudes and the number of atoms determined by absorption imaging. The blue points corresponds to the data and the orange dotted line to a quadratic fit.	129
4.31	(a) Number of atoms and (b) Gaussian radius during a TOF experiment for a small number of sweeps $N_S = 100$ and a longer SWAP duration $N_S = 1000$	130

- 4.32 (a) Absorption image of a cloud after $N_S = 200$ sweeps and a TOF of 5.5 ms for a SWAP detuning amplitude $\Delta_S/2\pi = 8.0$ MHz and offset $\nu_{end} = 1.0$ MHz. The red beams are kept at the constant power $P_{rMOT} = 5.6$ mW per axis before the glass cell. The white circle corresponds to the fitting region which corresponds to 0.7 times the imaging beam $1/e^2$ diameter. (b) Histogram of the number of atoms on the horizontal axis of the camera. The data are presented in blue, while the orange curve represents a fit made of the sum of the three black dotted lines profiles according to equation 4.46. The central profile is gaussian while the wings are doubled-sided Gaussians from equation 4.45. The fit residuals are given by the yellow curve. 131
- 4.33 (a) Selection of *in situ* absorption images for different number of sweeps N_S . (b) Fraction of atoms in the wings profiles compared to the central gaussian. The SWAP duration t_{SWAP} is offset by 5 ms compared to $N_S T$ to account for the 5 ms part overlapped with the blue beams ramp down. (c) Temperature estimation from the standard deviation (std) of the horizontal projection of the number of atoms (orange) and from the size of the central Gaussian fit (blue). The atomic losses along the TOF experiment combined with the particular velocity distribution in the SWAP phase lead to artificial negative temperatures. The situation is improved when using the crossed profile fit function from equation 4.46. (d) Recapture fraction from the blue to the SWAP MOT, including all the atoms present on the absorption images. 132
- 4.34 (a) Recapture fraction from the blue MOT and (b) temperature estimated with the central Gaussian for varying SWAP amplitude Δ_S with a fixed offset $\nu_{end} = 1.0$ MHz. (c) Recapture and (d) temperature as a function of the final frequency offset ν_{end} with a fixed amplitude $\Delta_S = 8.0$ MHz. Both dataset are taken at the fixed red beam power of 6.2 mW per axis and for a number of sweeps $N_S = 600$ 134
- 4.35 (a) Recapture fraction from blue to SWAP MOT for a constant power P_{rMOT} during a red phase of $N_S = 600$ teeth. The detuning amplitude is $\Delta_S = 2\pi \times 8.0$ MHz and the final value is $\nu_{end} = 1.1$ MHz. (b) Temperature and (c) phase-space density of a $N_S = 900$ SWAP MOT with an initial power of 6.5 mW ramped down to a final value $P_{rMOT,f}$. The detuning parameters are $\Delta_S = 2\pi \times 6.0$ MHz and $\nu_{end} = 1.2$ MHz. The raw data estimation is presented in orange, while the blue points are inferred from the crossed fit profile. 135
- 4.36 Recapture fraction from the blue MOT to a red optical molasses after an optimized SWAP phase as a function (a) of the 689 nm laser detuning and (b) the laser power per beam in logarithmic scale. The data are represented as blue points and the orange dotted line is a fit on the lowest powers according to $\log\left(\frac{P_{CW}}{P_0}\right)^a$ with $P_0 = 7 \mu\text{W}$ and $a = 0.1$. In the first dataset, the power is kept constant to $P_{CW} = 100 \mu\text{W}$ while in the second one the detuning is fixed to $\delta_{CW} = -90$ kHz. 136

4.37	Absorption images of the CW MOT for different detunings. The maximum MOT force ellipsoids from equation 4.50 are represented as white dotted ellipses.	138
4.38	(a) Absorption image and (b) projection of the number of atoms on the two axes of the CCD camera $r \in \{h, v\}$ for $\delta_{CW} = -100\text{kHz}$. (c) Recapture fraction from the blue to the CW MOT and (d) temperature inferred from the central Gaussian as a function of the detuning for a constant power $P_{CW} = 540\mu\text{W}$	139
4.39	(a) Absorption image of the final CW MOT after optimization and (b) its projections onto the axes of the imaging camera $r \in \{h, v\}$	140
4.40	(a) Picture of the assembled high-finesse ring cavity. The fiber is held by a V-groove glued on a shearing piezoelectric actuator allowing to adjust the cavity length. The piezo, planar mirrors and coupling lenses are glued on a maintaining glass plate. (b) Picture of the cavity taken with a microscope objective. The cavity mode length is equal to $500\mu\text{m}$. (c) Scheme of the atomic transport from the red MOT to the ring cavity with two counter-propagating green laser beams at 515nm . (d) Trap depth potential along the transport axis m for a power $P_0 = 0.5\text{W}$ per beam and a waist $w_0 = 40\mu\text{m}$ located between the two planar mirrors of the cavity.	145
A.1	On scale scheme of the optical table containing the lasers at 461nm , 679nm and 707nm	148
A.2	On scale scheme of the optical breadboard containing the lasers at 689nm and 698nm , as well as the stabilization part of the 813nm laser.	149
B.1	Gaussian beam propagating along the z axis with a waist w_0 and a radius of curvature R	152
B.2	(a) Results of a z -scan performed at the 689nm ECDL output, showing a strong astigmatism between the x and y transverse directions. (b) Cylindrical telescope on the x axis computed with the ABCD matrix software to compensate for the astigmatism. (c) Resulting z -scan after compensation by the telescope. The x and y components present similar beam waists $w_{0x} \simeq w_{0y} = 520(10)\mu\text{m}$, located at the same distance $z_0 = 1.3(1)\text{m}$ from the laser.	153
C.1	(a) DDS box system including AD9959 evaluation board from Analog Devices, an Arduino Due with equipped ethernet shield and several power supplies. (b) Maximum output power of the DDS evaluation board per channel as a function of the frequency.	156
D.1	(a) Saturated absorption signal (blue line) and error signal (orange line) of the 707nm repumping laser. The frequency axis is referenced to the $ (5s5p)^3P_2\rangle \rightarrow (5s6s)^3S_1\rangle$ transition of ^{88}Sr . (b) Theoretical absorption profile for ^{88}Sr and ^{87}Sr isotopes compared to the experimental spectrum in blue. The fermionic absorption line is a sum of all the transitions from the $ (5s5p)^3P_2, F_g \in [5/2, 7/2, 9/2, 11/2, 13/2]\rangle$ to the $ (5s6s)^3S_1, F_e \in [7/2, 9/2, 11/2]\rangle$ manifolds.	158

INTRODUCTION

At the very heart of our understanding of matter and light, quantum mechanics is one of the most fundamental theories of physics. First thought as nothing more than a mathematical trick, Max Planck introduced in year 1900 the concept of energy discreteness to derive the black-body radiation law in a conference for the German Physical Society. Five years later, his eminent colleague Albert Einstein introduced the term “*quanta*” to describe the smallest quantities of light involved in the photoelectric effect, nowadays known as photons. While these milestones were setting the basics of quantum mechanics, its most intriguing properties were yet to come. Among the fathers of this theory, who modified our classical vision of the world with new physical principles during the *First Quantum Revolution*, Paul Dirac stated in the first edition of his book in 1930 that [1]

“One of the most fundamental and most drastic of these is the Principle of superposition of states.”

This entirely new property, emerging at the single particle level, was soon followed by a second astonishing principle arising from the study of multiple quanta. As first pointed out by Albert Einstein, Boris Podolsky and Nathan Rosen in their famous 1935 paper known as the *EPR Paradox* [2], bipartite quantum systems that once interacted can not be described fully by considering their constituting parts separately. While their conclusion was that quantum mechanics was not a complete theory, Erwin Schrödinger answered with the following terms [3]

“I would not call that *one* but rather *the* characteristic trait of quantum mechanics, the one that enforces its entire departure from classical lines of thought. By the interaction the two representatives (or ψ -functions) have become entangled.”

In 1964, John Bell proposed a procedure to close the debate between quantum mechanics being a complete theory or a “hidden variables” one by formulating his famous inequalities [4]. Experimental studies realized afterwards, especially by Alain Aspect in 1981 [5], concluded in favour of Schrödinger and his view of entangled systems. Nowadays, if quantum correlations between two particles are well understood, the study of many-body entanglement is still an active research area. On the theoretical side, its negative definition based on the impossibility of separating a N -body quantum state into a product of N independent substates makes the

establishment of quantitative criteria for entanglement a complicated problem [6]. Nonetheless, these marvellous non-classical correlations between quantum systems, initially simply envisioned as an academic debate, have lead to a variety of applications referred to as the *Second Quantum Revolution*. This area of entanglement-based technologies can be divided into the following categories :

QUANTUM COMPUTING : Using two quantum states labelled $|0\rangle$ and $|1\rangle$ as a "qubit" (the quantum counter-part of a classical bit in electronics), the superposition principle and entanglement allow implementing quantum algorithms which address some *Nondeterministic Polynomial time* (NP) problems in a polynomial time on quantum computers. For instance, Shor's algorithm established in 1996 reduces the computation time for factoring integers to a sub-exponential dependency [7]. The physical implementation of quantum computers currently gives rise to a technological competition between international companies as well as emerging spin-offs, covering a large spectrum of hardware platforms such as photons, superconducting circuits, quantum dots, NV centres, trapped ions and neutral atoms [8].

QUANTUM SIMULATIONS : As pointed out by Richard Feynman in 1981 [9], simulating the probabilities of the different configurations of a quantum system scales exponentially with the number of particles in this system. This scaling emerges from the necessity of considering quantum correlations between all of these components. Exploring interesting many-body systems on classical computers in reasonable times is thus quickly limited by available memory and processing power. On the other hand, well-controlled quantum systems such as neutral atom lattices can be used to simulate completely different ones, for instance electrons in solids, by implementing similar types of Hamiltonians and study their steady state solutions, while having access to the model parameters [10].

QUANTUM COMMUNICATIONS : Exchanging confidential messages between two parties relies on encoding using a secret key. Taking qubits as a basis for cryptography allows to detect the presence of an eavesdropper along the transmission channel, due to the no-cloning theorem of unknown quantum states [11]. This statement led Charles Bennett & Gilles Brassard in 1984 [12] to develop a quantum public key distribution protocol. In 1991, Arthur Ekert added entanglement to the process [13], allowing to detect eavesdropping with Bell tests. Both have now been further improved in order to prevent from different types of attacks, and commercial implementations are today available. One of the main goals of quantum communications is to develop a worldwide quantum network, with a most realistic solution provided by pairs of entangled photons. Due to attenuation limitations in fiber-based telecommunications, technical implementations of this dream will probably require quantum repeaters and memories [14]. Another approach is to transfer informations

through the atmosphere, using optical links between ground stations and satellites [15], thus strongly reducing attenuation issues.

QUANTUM METROLOGY : In order to measure physical properties such as electromagnetic fields, gravity, accelerations, distances or time, quantum sensors rely on fundamental entities such as photons and matter particles to obtain the highest accuracies available to date. Moreover, quantum effects and especially entanglement can enhance the measurements precisions beyond the classical limitations [16]. The advents in quantum metrology, and atomic clocks in particular¹, for instance led to the redefinition of the *International System* (SI) of units by means of seven fundamental constants of physics in 2019. The time accuracy of these devices is also involved in distances measurements with *Global Positioning Systems* (GPS). Examples of quantum devices applications in the industry are as well found in the domains of accelerometry and gyroscopy for inertial navigation of aircraft and spacecraft, gravimetry applied to geophysical exploration or even magnetometry used in ship and vehicle detection [18].

Entanglement has thus become a key resource in a variety of applications. Among the physical platforms used to create and study many-body entanglement, ultra-cold atomic ensembles provide the most controllable environments at the single particle level, associated with high coherence times of particular energy states. This area of physics has been pioneered by Theodor Hänsch & Arthur Schawlow [19] and David Wineland & Hans Dehmelt [20], simultaneously proposing cooling of neutral atoms and ions with laser beams in 1975. In 1985, Jean Dalibard & Claude Cohen-Tannoudji applied the dressed atom formalism to cold atoms [21, 22], which later allowed them to explain sub-Doppler cooling mechanisms such as the so-called Sisyphus effect [23]. Jean Dalibard also proposed an ingenious combination of laser cooling and spatially varying magnetic fields known as the *Magneto-Optical Trap* (MOT), realized for the first time with sodium atoms in 1987 [24]. These trapped samples of ultra-cold atoms are nowadays the foundations of many ground-breaking experiments, with for instance the first atomic *Bose-Einstein Condensate* (BEC) realized in 1995 [25, 26] by applying magnetic [27] and optical dipole trapping [28] to a MOT.

Using ultra-cold atoms as the experimental basis, several tools are available for creating many-body entanglement in such atomic samples. First, atomic collisions can be used as a resource for entanglement and have been deeply studied in the context of BECs, including those produced on atom chips [29, 30]. A recent demonstration of spontaneous creation of entangled states in this context has been demonstrated on the *Trapped-Atom Clock on a Chip* (TACC) experiment with rubidium atoms, in a collaboration between our group and the *SYstème de*

¹The second, defined by the SI as “the duration of 9 192 631 770 periods of the radiation corresponding to the transition between the two hyperfine levels of the ground state of the ¹³³Cs atom”, is now measured with a fractional uncertainty at the 10⁻¹⁶ level after a few hours of integration [17].

Référence Temps-Espace (SYRTE) [31]. Entanglement can also be produced by dipole-dipole interactions, especially relevant in Rydberg physics, to for instance create quantum computing gates [32]. One can as well induce light-matter interactions with lasers in cold atomic clouds to generate quantum correlations [33]. A particularly promising platform is created by coupling atomic ensembles to optical cavities, opening the way to a variety of interesting schemes in the framework of *Cavity Quantum Electrodynamics* (CQED) [34–40]. In the past few years, our group has specialized in strong coupling between rubidium ensembles and high-finesse miniaturized cavity laser modes [41], for instance demonstrating the generation of W-states with more than 40 atoms [42] and quantum Zeno dynamics based on non-destructive measurement with the cavity [43]. Similar studies are currently led on the *Single Atom Register in an Optical Cavity* (SAROC-EMA) experiment, where a high numerical aperture lens is placed above a fiber cavity in order to study single-particle dynamics. CQED schemes are also extremely interesting as a resource for producing entangled states relevant for quantum enhanced precision metrology. Indeed, some classes of atomic states such as *Spin Squeezed States* (SSS) introduced by Masahiro Kitagawa & Masahito Ueda in 1993 [44], reduce the measurement uncertainty of an ensemble of spins compared to an uncorrelated *Coherent Spin State* (CSS) limited to the *Standard Quantum Limit* (SQL) [16]. To date, several implementations of spin squeezing have already been demonstrated in CQED [45, 46], revealing the great potential of these techniques.

So far, physics in the Atom Chips group has been realized with rubidium atoms which are part of the alkali metals family. However, an increasing interest has been given over the past few years to alkaline-earth-like atoms, which possess a richer energy level structure compared to well known alkalis, thus bringing new perspectives in the fields of quantum gases, quantum metrology and quantum information. The presence of ultranarrow optical transitions in particular constitutes an amazing opportunity for metrological applications and extremely long-lived qubits. In atomic clocks for instance, optical transitions with linewidths in the mHz range offered by atoms such as strontium and ytterbium improved the relative frequency precision compared to hyperfine alkali clock transitions, reaching the impressive 10^{-18} level after a few hours of integration [47, 48]. Accessing these unprecedented long coherence time transitions is made possible by the presence of less drastically forbidden narrow optical transitions which opened access to recoil limited cooling mechanisms. These novel mechanisms allowed to reach MOT temperatures below the μK level [49, 50]. Moreover, the diverse energy schemes provided by alkaline-earth-like atoms allows for operating so-called *magical* optical traps, which cancel differential AC Stark shifts between the states of interest [51]. This method applied to narrow-line cooling transitions is used to perform sideband and Sisyphus cooling in optical tweezers [52, 53], while magic trapping on the clock transitions allows for trap depth insensitive optical clocks [54–56]. This levels richness is also an asset for implementing innovative CQED protocols [57, 58], where the possibility of distinguishing the qubit states even in the far detuned regime is another advantage compared to

alkali atoms. Alkaline-earth-like atoms with high nuclear spins is as well useful for accessing paradigmatic models of $SU(N)$ magnetism [59]. Moreover, the presence of two electrons on their outer shell allows for trapping of Rydberg states in optical tweezers [60].

In this spirit of quantum enhanced metrology with alkaline-earth species in the context of CQED, we developed a new apparatus aiming to place strontium atoms inside a micro high-finesse ring cavity. The two aspects of the project were realized in parallel, with the implementation of the cavity described by Torben Pöpplau in his PhD thesis [61], and the development of the apparatus producing an ultra-cold strontium sample detailed in this thesis. Due to the complexity of the targeted physical schemes, we particularly focused our efforts on the simplification of the experimental apparatus, including only diode lasers and combining atomic slowing with MOT operations in a very compact vacuum system.

Scope of this thesis

My work in the Atomchips group has been focused on the design and building of the new strontium experiment. The main goal was to produce and characterize an ultra-cold cloud of strontium atoms inside a vacuum chamber, starting from a home-made effusive source.

Chapter 1 is dedicated to an introduction on CQED with alkaline-earth atoms. The particular case of neutral strontium atoms is then studied by reviewing their physical and spectral properties.

In chapter 2, I describe the laser system used for slowing and trapping of strontium atoms on two different transitions at 461 nm and 689 nm.

The vacuum system containing the atomic source is detailed in chapter 3. This setup was meant to be particularly compact and constitutes the smallest cold strontium experiment to date. A characterization of the atomic beam properties is also derived and compared to experimental data.

Finally, the slowing procedures from the effusive source to the cold sample region is characterized in chapter 4. Moreover, the experimental configurations used to produce MOTs on the blue and red cooling transitions as well as characterizations of the obtained atomic samples are detailed.

EXPLORING ENTANGLEMENT WITH ALKALINE-EARTH ATOMS IN A RING CAVITY

The study of entanglement in modern physics has been performed on several platforms such as photons, trapped ions, cold neutral atoms and superconducting circuits. Among them, the field of *Cavity Quantum ElectroDynamics* (CQED), which consists in coupling atomic qubits to the modes of an optical cavity, is a promising one. This chapter is an introduction to the generation of strong interactions between neutral atoms and cavity light fields. Starting from the optical cavity properties, we derive the Hamiltonian describing the dynamics of such systems. In a second part, we present the new features offered by alkaline-earth-like atoms compared to the widely studied alkalis, before focusing on the strontium physical properties. We introduce the level diagrams of the different strontium isotopes, necessary to understand the slowing and cooling mechanisms implemented in this project.

1.1 Cavity QED

In a majority of CQED experiments, the cavity is composed of two mirrors in a linear configuration. These Fabry-Pérot cavities have been deeply studied in our group. Combined with rubidium atoms, large number of qubit entanglement has been demonstrated [42]. In order to obtain maximum light-matter coupling, the wavelength of the optical lattice maintaining the atoms in the cavity was carefully adjusted to overlap the probe light anti-nodes [62]. As the alkalis clock transitions are provided by hyperfine ground states, the trapping light do not drastically modify the clock transition frequency. In contrast, state-of-the-art optical clocks realized with alkaline-earth-like atoms suffer from lattice induced differential AC Stark shifts [47, 48, 55, 56]. Fortunately, there exists so-called *magic wavelength* dipole traps which let the clock frequency

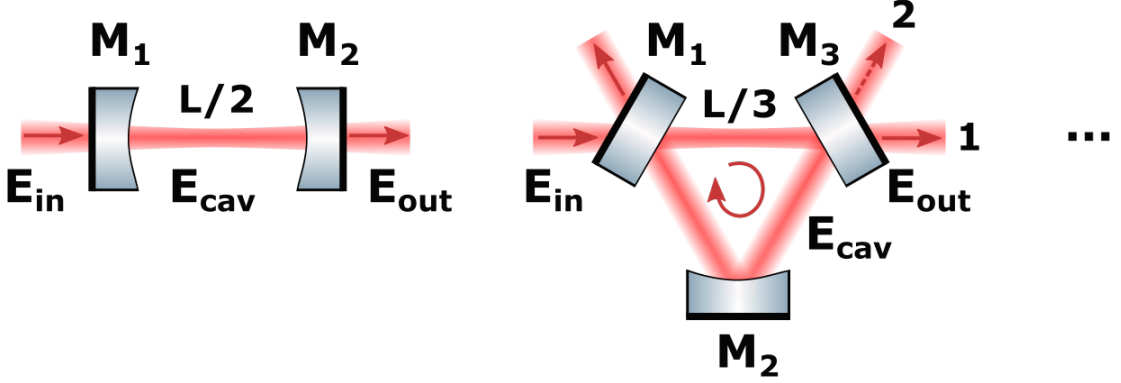


Figure 1.1: Scheme of a Fabry-Pérot (left) and a triangular ring cavity (right) with their optical configurations.

unchanged while varying the trapping light intensity [51], as will be detailed in 1.2.3. As such wavelengths have no *a priori* reason to be commensurate with the clock transition wavelength, both magic trapping and maximum overlap with the probe can not be achieved at the same time with Fabry-Pérot cavities. On the other hand, ring cavities of three or more mirrors offer the choice between standing and running waves for both trapping and probing lights, thus ruling out the overlap problem.

1.1.1 Optical cavity properties

The optical cavities are made of a number of M mirrors distributed along a spatial path of length L . In figure 1.1, a linear Fabry-Pérot and a three-mirror ring cavity are represented. Each mirror, labelled by an index $j \in [1, M]$, is characterized by a reflectivity r_j and a transmission t_j to electromagnetic fields amplitudes. For an incoming time varying electric field E_{in} at frequency ω , one can compute the intra-cavity field E_{cav} and the output one E_{out} using the following stationary conditions

$$(1.1) \quad \begin{cases} E_{cav} = t_1 e^{i\varphi_1} E_{in} + \prod_{j=1}^M r_j e^{i\Phi} E_{cav} \\ E_{out} = t_M e^{i\varphi_M} E_{cav}, \end{cases}$$

where, by convention, the first mirror is chosen as the input and the last $j = M$ mirror as the output. In equation 1.1, the φ phase factors are induced by the mirrors, while $\Phi = n\omega L/c$ corresponds to the round-trip phase acquired by the light field after a complete loop in the cavity with refractive index n . The total intensity transmission \mathcal{T} is thus given by

$$(1.2) \quad \mathcal{T}(\omega) \equiv \left\| \frac{E_{out}}{E_{in}} \right\|^2 = \frac{\mathcal{T}_0}{1 + m \sin^2 \frac{\Phi}{2}},$$

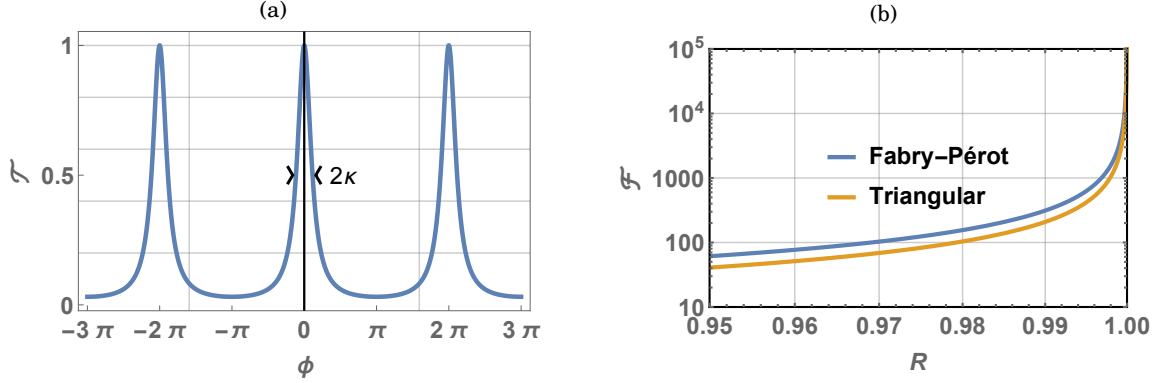


Figure 1.2: (a) Optical cavity transmission as a function of the round-trip phase $\Phi = \omega/\omega_{FSR}$ for a mirror reflection factor $R = 0.7$. (b) Cavity finesse for symmetrical Fabry-Pérot (blue line) and triangular ring cavities (orange line) as a function of R .

with $R_T = |\prod_j r_j|^2$ the product of the reflection coefficients, $T_j = |t_j|^2$ the intensity transmission coefficients, $\mathcal{T}_0 = T_1 T_M / (1 - \sqrt{R_T})^2$ the resonant transmission and m a parameter expressed as

$$(1.3) \quad m = \frac{4\sqrt{R_T}}{(1 - \sqrt{R_T})^2}.$$

Equation 1.2 shows that incoming light can only be efficiently coupled to the cavity when Φ is a multiple of 2π , as shown in figure 1.2(a). Cavities thus act as optical resonators, presenting transmission peaks at harmonic frequencies of the *Free Spectral Range* (FSR) defined as¹

$$(1.4) \quad \omega_{FSR} = 2\pi \times \frac{c}{nL}.$$

The width of the transmission peaks is defined by the cavity finesse $\mathcal{F} = \omega_{FSR}/(2\kappa)$, where κ is the photon decay rate at the output port of the cavity. This definition is linked to the cavity transmission as κ corresponds to the peaks *Half-Width at Half Maximum* (HWHM). Using equation 1.2, it gives

$$(1.5) \quad \mathcal{F} = \frac{\pi}{2 \arcsin(\frac{1}{\sqrt{m}})} \underset{m \gg 1}{\simeq} \frac{\pi}{2} \sqrt{m}.$$

A simple physical interpretation of the finesse is given by the number of round-trips performed by a photon before exiting the cavity, equal to \mathcal{F}/π . In order to compare linear to ring cavities, we can compute the finesse for these two types of cavities. For simplicity, we consider mirrors with equal reflection coefficients R .

FABRY-PÉROT : With two mirrors, $R_T = R^2$. We recover the well-known expression $\mathcal{F} = \pi\sqrt{R}/(1 - R)$.

¹For Fabry-Pérot cavities, the cavity length is generally defined as the distance $L' = L/2$ between the two mirrors rather than the round-trip length. The FSR then writes $\omega_{FSR} = 2\pi c/(2nL')$.

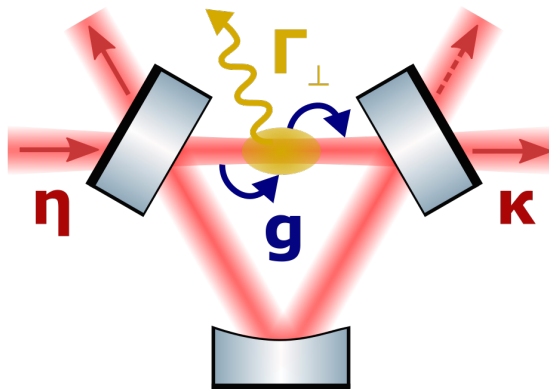


Figure 1.3: CQED scheme with an atomic ensemble placed in a ring cavity. The atomic spontaneous emission of photons into free space is characterized by a transversal decay rate $\Gamma_{\perp} = \Gamma/2$. The cavity is pumped by an incident electric field at a rate η , and losses photons by mirrors transmission at a rate κ . The coupling constant g between the intra-cavity photons and the atomic ensemble gives the strength of the dipolar interaction.

RING CAVITY : A triangular cavity with three mirrors gives $R_T = R^3$. The finesse is then given by $\mathcal{F} = \pi R^{3/4} / (1 - R^{3/2})$.

Considering high-finesse cavities, the ring cavity finesse is approximately 2/3 smaller than a Fabry-Pérot with same quality mirrors, as shown in figure 1.2(b).

1.1.2 Light-matter coupling in optical cavities

Placing an atomic ensemble into an optical cavity, as represented in figure 1.3, leads to an exchange of energy driven by the atomic absorption and re-emission of photons into the cavity modes. The Hamiltonian \hat{H} of the atoms-cavity system can be separated into three contributions

$$(1.6) \quad \hat{H} = \hat{H}_{at} + \hat{H}_{cav} + \hat{H}_{int},$$

where \hat{H}_{at} corresponds to the atomic energy, \hat{H}_{cav} to the cavity and \hat{H}_{int} to the dipolar light-matter interaction. The different Hamiltonians describing this system can be derived as follows.

Atomic contribution : The energy of a single atom of mass m can be divided into one kinetic term, depending on its momentum p , and one internal energy term. This second term depends on the energy $\hbar\omega_0$ between the ground state $|g\rangle$ and the excited state $|e\rangle$, leading to the following expression

$$(1.7) \quad \hat{H}_0 = \frac{\hat{p}^2}{2m} + \frac{\hbar\omega_0}{2} \hat{\sigma}_z,$$

expressed by means of the z Pauli matrix $\hat{\sigma}_z = |e\rangle\langle e| - |g\rangle\langle g|$. For an ensemble of N identical atoms, the internal energy can be generalized by considering a pseudo-spin $\hat{\mathbf{J}}$ given by the sum of

all the spin-1/2 contributions coming from each j atom

$$(1.8) \quad \hat{\mathbf{J}} = \sum_{j=1}^N \hat{\mathbf{J}}^{(j)}.$$

This operator has a norm given by

$$(1.9) \quad \hat{J}^2 = \hat{J}_x^2 + \hat{J}_y^2 + \hat{J}_z^2,$$

where the x , y and z components satisfy the angular momentum commutation relations $[J_i, J_j] = i\hbar \epsilon_{ijk} J_k$ with ϵ_{ijk} the Levi-Civita symbol. The raising, lowering and $\mu \in \{x, y, z\}$ components of the pseudo-spin are given by

$$(1.10) \quad \hat{J}_{\pm} = \sum_{j=1}^N \hat{\sigma}_{\pm}^{(j)} \quad \text{and} \quad \hat{J}_{\mu} = \frac{1}{2} \sum_{j=1}^N \hat{\sigma}_{\mu}^{(j)},$$

with $\sigma_+ = |e\rangle\langle g|$ and $\sigma_- = |g\rangle\langle e|$. In a similar way, the total kinetic energy is given by the sum of each atomic contribution. The Hamiltonian of the atomic ensemble thus simply writes

$$(1.11) \quad \hat{H}_{at} = \frac{\hat{P}^2}{2m} + \hbar\omega_0 \hat{J}_z,$$

with $\hat{P}^2 = \sum_{j=1}^N \hat{p}_j^2$.

In 1954, Robert H. Dicke described a basis of eigenstates solving the internal Hamiltonian [63]. The Dicke basis $\{|J, J_z\rangle\}$ is characterized by the total spin value $J \in [0, N/2]$, associated with its projection onto the z axis $J_z \in [-J, J]$. A subspace of particular interest in the context of CQED is called the symmetrical subspace given by $J = N/2$. Transferring excitations from one atom to another in this particular manifold leaves the state unchanged. This particle indistinguishably serves useful in entanglement generation. An example has been made by the group in 2014 with the generation of a $|W\rangle = |J = N/2, J_z = -N/2 + 1\rangle$ state with more than 40 rubidium atoms in a Fabry-Pérot cavity [42].

Another convenient basis used in the contexts of quantum metrology and quantum computing is composed of the *Coherent Spin States* (CSS). These states are represented by a vector on the Bloch sphere with a polar angle θ , an azimuthal angle Φ and a length $N/2$ for a coherent ensemble of N particles. Their expression are simply given by a rotation of the $|0_N\rangle$ state where all the atoms are in the ground-state [64] :

$$(1.12) \quad |\theta, \Phi\rangle = \hat{R}(\theta, \Phi) |0_N\rangle = \left[\sin\left(\frac{\theta}{2}\right) e^{i\frac{\Phi}{2}} |0\rangle + \cos\left(\frac{\theta}{2}\right) e^{-i\frac{\Phi}{2}} |1\rangle \right]^{\otimes N}.$$

The Heisenberg principle defines an isotropic variance of the CSS along the directions perpendicular to the pseudo-spin direction. This limit is well known in quantum metrology as the *Standard*

Quantum Limit (SQL). In atomic clock Ramsey spectroscopy, the phase variance obtained with a CSS is given by [44]

$$(1.13) \quad \Delta\Phi_{CSS} = \frac{1}{\sqrt{N}},$$

which can be compared to the photonic shot-noise in optics. The field of research called quantum enhanced metrology, which includes our group, is focused on the use of entanglement to generate quantum states with a reduced variance beyond the SQL on one axis of the Bloch sphere². Exploiting quantum correlations thus lead to a reduced noise measurement compared to an independent set of particles. The theoretical minimal achievable variance is known as the Heisenberg limit defined as [16]

$$(1.14) \quad \Delta\Phi_H = \frac{1}{N}.$$

Cavity contribution : In order to derive the cavity Hamiltonian, we consider a cavity with modes l at frequency ω_l pumped at a rate η by a laser through the first mirror. The electric field at position \mathbf{r} in the cavity can be written as

$$(1.15) \quad \mathbf{E}(\mathbf{r}) = \sum_l \mathcal{E}_l \mathbf{u}_l(\mathbf{r}) \hat{a}_l + h.c.,$$

where the \mathbf{u}_l vectors include the field polarization and spatial dependencies, the operators \hat{a}_l annihilate one photon in the l -th mode and $h.c.$ stands for hermitian conjugate. The field amplitudes \mathcal{E}_l are linked to the cavity modes volumes V_l by

$$(1.16) \quad \mathcal{E}_l = \sqrt{\frac{\hbar\omega_l}{2\epsilon_0 V_l}}.$$

The input laser field is supposed to have a narrow linewidth compared to the cavity FSR. In the Fabry-Pérot cavity case, it thus only excites one longitudinal mode at frequency ω_c . Removing the vacuum state energy, the cavity Hamiltonian for a single mode then writes

$$(1.17) \quad \hat{H}_{FP} = \hbar\omega_c \hat{a}^\dagger \hat{a},$$

which is proportional to the mode energy multiplied by the photon number $\hat{n} = \hat{a}^\dagger \hat{a}$. For ring cavities, each clockwise propagating longitudinal mode presents a nearly degenerate counter-clockwise equivalent. Two modes thus have to be considered for the cavity Hamiltonian, referred to as the propagating mode labelled $l = 1$ and the counter-propagating one labelled $l = 2$. The ring cavity operator is thus given by

$$(1.18) \quad \hat{H}_{cav} = \sum_{l=1}^2 \hbar\omega_l \hat{a}_l^\dagger \hat{a}_l,$$

²Of course, if the noise reduction is performed on an axis i perpendicular to the mean pseudo-spin axis k , the Heisenberg principle $(\Delta J_i)^2 (\Delta J_j)^2 \geq |\langle J_k \rangle|^2 / 4$ induces an enhanced variance in the perpendicular direction j .

Electric dipole interaction : The dipolar Hamiltonian between an atomic spin-1/2 ensemble and an electromagnetic field is given by the following expression

$$(1.19) \quad \hat{H}_{int} = -\hat{\mathbf{d}} \cdot \mathbf{E}(\mathbf{r}),$$

with $\hat{\mathbf{d}} = \mathbf{d}(\hat{J}_- + \hat{J}_+)$ the pseudo-spin dipole operator. The general formulation of the dipolar Hamiltonian includes the coupling strengths g_{jl} between the j -th atom and the l -th cavity mode [65]

$$(1.20) \quad \hat{H}_{int} = \sum_{j,l} \hbar \left(g_{jl}(\mathbf{r}) \hat{a}_l + g_{jl}^*(\mathbf{r}) \hat{a}_l^\dagger \right) \left(\hat{\sigma}_-^{(j)} + \hat{\sigma}_+^{(j)} \right).$$

These coupling strengths depend on the atomic positions inside the cavity. Taking the z axis as the light propagating axis, their expression can be deduced from the single particle coupling with the l -th mode g_l as follows

$$(1.21) \quad g_{jl}(\mathbf{r}) = g_l(\mathbf{r}) \sqrt{N} e^{ikz_j},$$

with

$$(1.22) \quad g_l(\mathbf{r}) = -\frac{\mathbf{d} \cdot \mathcal{E}_l \mathbf{u}_l(\mathbf{r})}{\hbar}.$$

The maximum coupling g for a mode at frequency ω_c is achieved for atoms sitting at the anti-nodes of the probe light field, *i.e.* for z_j being a multiple of $\lambda/2$, leading to

$$(1.23) \quad g = \sqrt{\frac{d^2 \omega_c}{2 \hbar \epsilon_0 V_c}}.$$

When this condition is not fulfilled, the light-matter interaction is ruled by a reduced effective coupling which takes into account the cavity mode overlap with the atomic wavepackets [66, 67].

1.1.2.1 Dynamics of the open system

The unitary evolution described by the Hamiltonian approach is not sufficient to model real quantum systems. Indeed, the energy losses are not encountered in the previous descriptions. For a CQED experiment, photonic losses are observed for either spontaneous emission by the atoms outside the cavity volume, either by mirror transmission at a rate κ . The evolution of the density operator $\hat{\rho} = |\psi\rangle\langle\psi|$ for this open system is described by the master equation

$$(1.24) \quad \frac{\partial \hat{\rho}}{\partial t} = \frac{1}{i\hbar} [\hat{H}, \hat{\rho}] + \hat{\mathcal{L}}(\hat{\rho}).$$

As for the Hamiltonian description, the Liouvillian operator $\hat{\mathcal{L}}$ can be separated into one atomic and one photonic parts as follows [68]

$$(1.25) \quad \hat{\mathcal{L}}(\hat{\rho}) = \hat{\mathcal{L}}_{at}(\hat{\rho}) + \hat{\mathcal{L}}_{cav}(\hat{\rho}),$$

with

$$(1.26) \quad \hat{\mathcal{L}}_{at}(\hat{\rho}) = \Gamma (2\hat{J}_- \hat{\rho} \hat{J}_+ - \hat{J}_+ \hat{J}_- \hat{\rho} - \hat{\rho} \hat{J}_+ \hat{J}_-),$$

and

$$(1.27) \quad \hat{\mathcal{L}}_{cav}(\hat{\rho}) = \kappa \sum_{l=1}^2 \left(2\hat{a}_l \hat{\rho} \hat{a}_l^\dagger - \hat{a}_l^\dagger \hat{a}_l \hat{\rho} - \hat{\rho} \hat{a}_l^\dagger \hat{a}_l \right).$$

In order to compensate for photonic losses, an effective imaginary Hamiltonian \hat{H}_P needs to be added to equation 1.24. Considering a laser probe pumping the propagating $l = 1$ mode at a rate η , as represented in figure 1.3, this contribution writes

$$(1.28) \quad \hat{H}_P = -i\hbar(\hat{a}_1 - \hat{a}_1^\dagger).$$

1.1.2.2 CQED applications in the weak and strong coupling regimes

In 1946, Edward M. Purcell stated that the spontaneous emission of an atom into a linear optical cavity mode was enhanced by a factor P given by

$$(1.29) \quad P = \frac{3Q\lambda^3}{4\pi V^2},$$

where Q is the cavity quality factor [69]. This Purcell factor has been generalized by Bonifacio and Lugiato in 1977 [70], who introduced the concept of cooperativity in CQED which compares the coupling strength of the light-matter interaction to the decay mechanisms characterized by κ and Γ . The collective cooperativity C_N for an ensemble of N atoms is defined as [34]

$$(1.30) \quad C_N = \frac{g^2}{\kappa\Gamma} \times N,$$

where g is the single atom maximum coupling strength defined in equation 1.22. The single atom cooperativity is thus linked to the Purcell factor by $P = 2C_1$. The collective cooperativity serves useful in CQED to distinguish from the weak to the strong coupling regime, separated by the condition $C_N = 1$. These two regimes can be described as follows.

Strong coupling regime ($C_N \gg 1$) : Strong light-matter interactions in the context of CQED led to the discovery of numerous interesting phenomena. In addition to the cooperativity, a second important criterion to describe the different physical effects is the comparison between the atomic natural linewidth Γ and the cavity linewidth κ .

GOOD-CAVITY LIMIT ($\kappa \ll \Gamma$) : In the context of ring cavities, strong coupling of an atomic ensemble to a cavity with a linewidth narrower than the atomic one results in a *Collective Atomic Recoil Laser* (CARL), predicted by Bonifacio *et al.* in 1994 [71]. In this regime,

the system is described by the total Hamiltonian from equation 1.6, accounting for the particles motion as well as the light-matter interaction driven by a laser field entering the propagating mode. The first atomic absorption event with a re-emission into the counter-propagating mode starts a build-up in this originally unpopulated mode. The two ring cavity modes thus interfere to create a standing wave, which modulates the atomic cloud density. This effect results in further Bragg scattering of the pumping photons into the counter-propagating mode, transferring a momentum $p = 2\hbar k$ for each absorption-emission cycle. This positive feedback thus reinforces the CARL effect while pushing the atoms along the propagating direction [65, 72, 73]. Using a BEC as the atomic medium rather than a thermal cloud allows the creation of a supersolid [74], simultaneously presenting global phase coherence and density modulation as recently demonstrated experimentally with rubidium atoms [75].

BAD-CAVITY LIMIT ($\kappa \gg \Gamma$) : In the bad-cavity limit, atomic recoil events lead to a negligible Doppler shift compared to the cavity linewidth. The atomic motion can thus be neglected in this regime, leading to the two-modes Dicke Hamiltonian \hat{H}_D expressed as

$$(1.31) \quad \hat{H}_D = \hbar\omega_0 \hat{J}_z + \sum_{l=1}^2 \hbar\omega_l \hat{a}_l^\dagger \hat{a}_l + \sum_{l=1}^2 \hbar g_N (\hat{a}_l + \hat{a}_l^\dagger) (\hat{J}_- + \hat{J}_+),$$

where we supposed identical coupling to the two modes leading to $g_N = g\sqrt{N}$. In the *Rotating-Wave Approximation* (RWA), the fast oscillating terms $\hat{a}_l \hat{J}_-$ and $\hat{a}_l^\dagger \hat{J}_+$, rotating at twice the laser frequency 2ω , are neglected. The remaining term $\hat{a}_l \hat{J}_+$, corresponding to the absorption of a cavity photon by the atomic ensemble which promotes one atom to the excited state, and its hermitian conjugate $\hat{a}_l^\dagger \hat{J}_-$ leads to the Tavis-Cummings Hamiltonian \hat{H}_{TC} . In the frame rotating at the laser frequency, the two-modes Tavis-Cummings operator writes [76]

$$(1.32) \quad \hat{H}_{TC} = -\hbar\Delta_a \hat{J}_z - \sum_{l=1}^2 \hbar\Delta_l \hat{a}_l^\dagger \hat{a}_l + \sum_{l=1}^2 \hbar g_N (\hat{a}_l \hat{J}_+ + \hat{a}_l^\dagger \hat{J}_-),$$

with $\Delta_a = \omega - \omega_0$ the atomic detuning and $\Delta_l = \omega - \omega_l$ the cavity detuning. In 1985, Jean Dalibard and Claude-Cohen Tannoudji introduced the *Dressed-atom* approach [22] to solve the single atom and single cavity mode Hamiltonian known as the Jaynes-Cummings model [77]. The dressed states eigenbasis is composed of manifolds of atom-photon hybrid states $\{|g, n\rangle, |e, n-1\rangle\}$ containing either the atom at rest and n photons in the cavity, or the atom excited by a photonic absorption which only leaves $n-1$ photons in the cavity. The following linear combinations of these states diagonalize the Jaynes-Cummings Hamiltonian

$$(1.33) \quad \begin{cases} |+, n\rangle = \cos\theta_n |e, n-1\rangle + \sin\theta_n |g, n\rangle \\ |-, n\rangle = -\sin\theta_n |e, n-1\rangle + \cos\theta_n |g, n\rangle, \end{cases}$$

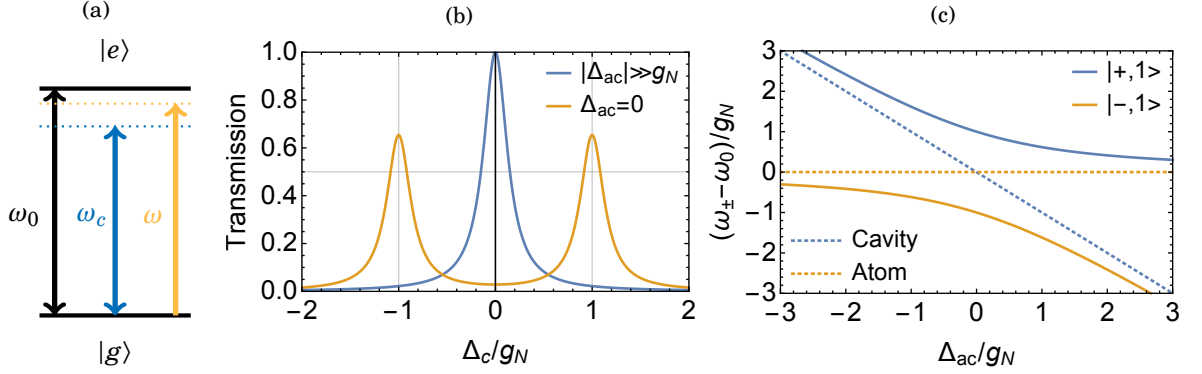


Figure 1.4: (a) Level scheme of a two-level atom coupled to a single cavity mode at frequency ω_c with a laser probe at frequency ω . (b) Cavity transmission as a function of the probe detuning $\Delta_c = \omega - \omega_c$ for a bare cavity in blue and a cavity on resonance with the atoms $\Delta_{ac} = \omega_0 - \omega_c = 0$ in yellow. The mean cavity mode population is supposed to be lower than one. (c) Eigenenergies of the single atom and single photon dressed states.

with an angle defined by $\tan(2\theta_n) = 2g\sqrt{n}/\Delta_{ac}$ and $\Delta_{ac} = \omega_0 - \omega_c$. The eigenenergies of the dressed states generalized to N atoms are given by

$$(1.34) \quad \frac{E_{\pm,n}}{\hbar} = \omega_{\pm,n} = n\omega_c + \frac{1}{2} \left(\Delta_{ac} \pm \sqrt{\Delta_{ac}^2 + 4ng_N^2} \right).$$

For a laser probe on resonance with the cavity, the dressed states energies are separated by an amount $2g_N\sqrt{n}$ compared to the bare cavity, as represented in figure 1.4. This so-called Rabi splitting is used to implement *Quantum Non-Demolition* (QND) schemes. This non-deterministic class of processes performs projective measurements of the pseudo-spin, thus reducing the noise of the measured component. This scheme is implemented in CQED with probe lights close to the atomic and cavity resonances [37, 78]. Repeated measurements by the cavity leads to Quantum Zeno Dynamics, explored by the group in 2015 [43].

Deterministic schemes are also available to reduce the variance. The *One-Axis Twisting* process, proposed by Kitagawa and Ueda in 1995 [44], acts as a shearing mechanisms for the atomic spin ensemble governed by the following Hamiltonian

$$(1.35) \quad \hat{H}_{OAT} = \hbar\chi\hat{J}_+\hat{J}_- = \hbar\chi(\hat{J}_z^2 - \hat{J}_z),$$

where χ corresponds to the shearing strength. The \hat{J}_z^2 factor in equation 1.35 is responsible for the shearing effect by rotating the spins around the Bloch sphere poles faster than the ones placed along the equator. Experimental realizations of this Hamiltonian have been performed with cavities on resonance with the atoms and detuned laser probes, leading to $\chi = 4g^2\Delta_c/(4\Delta_c^2 + \kappa^2)$ [79, 80]. Detuning the cavity to the middle of two hyperfines levels, such as the two hyperfine ground states of rubidium, leads to the cavity-feedback protocol

which combines QND and OAT [80, 81]. A CSS evolving under the OAT dynamics leads to a *Spin Squeezed State* (SSS), characterized by an azimuthal angular variance

$$(1.36) \quad \Delta\Phi_{SSS} = \frac{\xi}{\sqrt{N}},$$

where ξ is the squeezing parameter [16]. The condition $\xi < 1$ ensures a variance reduction, which induces entanglement of the atomic spins [82]. While optimal OAT squeezing leads to $\Delta\Phi \propto N^{-2/3}$, further quantum enhancement can be obtained with *Two-Axis Twisting* (TAT) which in theory saturates the Heisenberg limit [83]. In a ring cavity, such scheme can be implemented using the two counter-propagating resonant modes [84, 85].

A very promising scheme allowing to generate arbitrary superpositions of the Dicke states in the symmetrical subspace has been introduced in 2015 in the group of Vladan Vuletić [86]. This *Carving* method relies on a three-level scheme, such as the two hyperfine ground states $\{|\uparrow\rangle, |\downarrow\rangle\}$ and the excited state $|e\rangle$ of the rubidium D_2 line, with a cavity red-detuned by an amount Δ_c compared to the $|\uparrow\rangle \rightarrow |e\rangle$ transition. This scheme leads to an effective Rabi coupling $\Omega = g^2/\Delta_c$. Pumping the cavity modes by an electric field presenting a superposition of frequencies separated by integers values of Ω thus leads to populate the corresponding superposition of Dicke states. Recording a transmitted photon then projects the atomic ensemble onto this particular state, allowing to generate entangled states with a metrological gain such as SSS or *Greenberger-Horne-Zeilinger* (GHZ) states [87].

Finally, the strong coupling and bad-cavity regime has been used to explore the Dicke phase transition [88]. This model predicts a superradiant phase for strong light-matter couplings, resulting in an enhanced coherent emission of light into the cavity modes at a rate ΓC_N [89, 90].

Weak coupling regime ($C_N \ll 1$) : In the weak coupling regime, the loss mechanisms resulting from spontaneous emission and cavity transmission are faster than the photon exchange dynamics between the atoms and the cavity modes. This regime is used to generate single-photon sources [91], as well as quantum controlled-NOT gates [92].

1.1.3 Fiber micro cavities

As detailed in 1.1.1, the spectral properties of optical cavities are characterized by their lengths and finesses. Moreover, the spatial shapes of the cavity field eigenmodes, given by the Hermite-Gauss *Transverse Electromagnetic Modes* (TEM_{mn}) as detailed in appendix B, are determined by the mirrors radii of curvature. In particular, these parameters sets the $1/e^2$ radius (or beam waist) w_0 of the fundamental transverse Gaussian mode TEM_{00} . Interestingly, the cooperativity

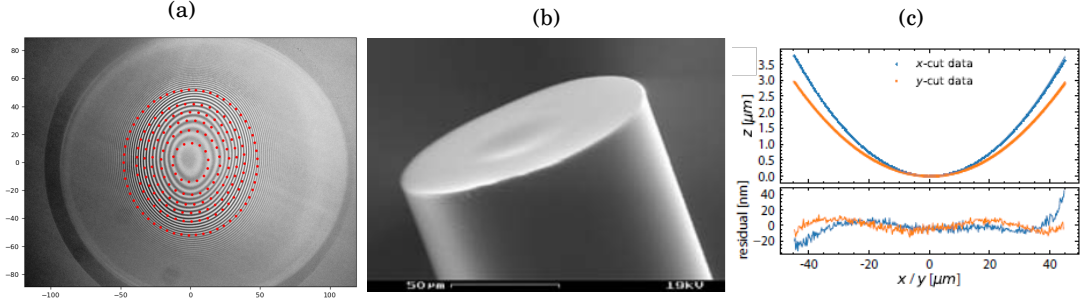


Figure 1.5: (a) Multi-shot CO₂ laser pattern on an optical fiber, resulting in a Gaussian mirror profile imaged with a profilometry technique. (b) Scanning Electron Microscope image of the fiber tip with the mirror shape in the center. (c) Mirror profiles along the fiber tip axes and residuals from a 2D spherical fit.

factor of CQED written in equation 1.30 can be expressed by means of the cavity finesse and the beam waist of the mode of interest. For a travelling wave configuration, the single atom cooperativity writes³

$$(1.37) \quad C_1 = \frac{6}{k^2 w_0^2} \times \frac{\mathcal{F}}{\pi}.$$

Building high-finesse cavities with a small beam waist thus tremendously increase the cooperativity. For this reason, the group has implemented a CO₂ laser machining technique in order to shape small glass substrates, such as optical fibers [61, 62, 93]. Using multi-shot patterns, this technique allows to produce micro mirrors with radii of curvature in the 10 – 500 μm range, with a surface roughness as low as 1 nm which leads to cavity finesse in the 10⁴ range. Moreover, the deviations of the resulting profiles compared to ideal Gaussian shapes reach the impressively low value of 5 nm [61]. An example of such CO₂ machined fiber from ref. [61] is given in figure 1.5.

1.2 Physical properties of strontium atoms

Due to their relatively simple level structures, alkali metals have been deeply studied in the cold atoms community, starting with the first MOT realized with sodium atoms in 1987 [24]. Their low vapour pressures, combined with broad cooling transitions lying in the MHz range, have been proven useful for implementing simple trapping and cooling apparatuses. During the last 20 years, the second column of the periodic table filled with alkaline-earth atoms and some lanthanides with similar structures have received increasing interest. The richer level structure of this atomic family contains ultra-narrow optical transitions, which find applications in optical atomic clocks and long-lived qubits. In atomic clocks, the Allan deviation $\sigma_y(\tau)$ characterizing the variance of the frequency ratio $y = \delta\nu/\nu$ after an integration time τ is expressed for a Ramsey

³For a standing wave, the mode volume is divided by 2, leading to an increased cooperativity by a factor of 2.

sequence as

$$(1.38) \quad \sigma_y(\tau) = \frac{1}{Q\sqrt{N}} \sqrt{\frac{T_c}{\tau}},$$

with Q the transition quality factor, N the number of atoms and T_c the interrogation time. Using the narrow transitions in the optical domain provided by alkaline-earth-like atoms thus brings a factor 10^4 improvement compared to microwave alkali clocks. The latest results in optical lattice and optical cavity clocks with strontium and ytterbium exhibit outstanding frequency instabilities in the 10^{-19} range after a few hours of integration [94, 95], outperforming the best fountain microwave cesium clocks [17, 96, 97]. Motivated by these results, the new apparatus developed in this thesis is based on strontium atoms. Due to more accessible clock and cooling lasers wavelengths, as well as the possibility to reduce its temperature below the μK level, this species has been preferred to ytterbium and mercury also used in optical clocks.

In this section, we first derive the properties of two electrons systems such as alkaline-earth atoms. In a second part, we expose the energy level structure of strontium atoms, revealing how it can be used to perform cooling and clock operations. Finally, we discuss the so-called magic wavelength mechanism used to trap alkaline-earth atoms in optical clocks without perturbing the clock transition.

1.2.1 Two electrons systems

Alkali atoms present an hydrogen-like structure, with one electron on their outer electronic shell. For alkaline-earth species, two electrons have to be considered in order to understand their helium-like energy levels structure. Strontium, for instance, possesses the electronic structure $[\text{Kr}]5s^2$. The two electrons on the outer shell can repel each other via Coulomb interaction, leading to a more complex Hamiltonian than for the previous class of atoms. In the nucleus frame, the *Two-Active-Electron* (TAE) Hamiltonian is given by

$$(1.39) \quad \hat{H}_{2e} = \frac{\hat{p}_1^2}{2m_e} + \frac{\hat{p}_2^2}{2m_e} + \hat{V}_{l_1}(\hat{r}_1) + \hat{V}_{l_2}(\hat{r}_2) + \frac{e^2}{4\pi\epsilon_0} \frac{1}{|\hat{r}_2 - \hat{r}_1|},$$

with \hat{r}_i the position operator of the i -th electron and $\hat{V}_{l_i}(\hat{r}_i)$ an angular-momentum dependent semi-empirical potential representing the Sr^{2+} ion [98]. The first two terms of the Hamiltonian correspond to the kinetic energies of the electrons. Associated with the third and fourth terms, which describe central attraction of the nucleus, it consists in the hydrogen-like Hamiltonian. The last term corresponds to Coulomb repulsion between the electrons. As it breaks the central symmetry of the problem, the analytical resolution becomes more complicated than for alkali atoms. The spin situation also contributes to the complexity of this system, and the resolution of the model requires perturbation or variational techniques [99]. In Rydberg physics, the two electrons configuration of alkaline-earth atoms opens the perspective of trapping Rydberg states in optical tweezers [60]. The basic idea is to trap the ion core comprising one of the two electrons

in a tightly focused beam, while the extension of the wavepacket of the second electron placed in a high- n Rydberg state is larger than the beam waist.

Despite the system complexity, an intuitive insight of the two electrons Hamiltonian eigenstates can still be given by considering the symmetries of the system. In first approximation, we can neglect the repulsive Coulomb term and the system reduces to two hydrogen-like parts. Within this simplification, we can express the wavefunction as a tensor product of a spatial part $|\phi_{nL}(r_i)\rangle$ which depends on the principal quantum number n and the angular momentum L , and a spin part with projections $|\uparrow\rangle$ or $|\downarrow\rangle$ for each electron. According to Pauli's principle, the wavefunction of the electrons must be antisymmetric. The spatial and orbital parts must then present reversed symmetries, leading to different families of spin states. The symmetric spin states with a degeneracy $2S + 1 = 1$ are called the singlet states, while the antisymmetric ones with a degeneracy $2S + 1 = 3$ correspond to the triplet states.

In the strontium case, the ground state finds the two electrons in their 5s shells, leading to the following spatially symmetric and spin anti-symmetric singlet state

$$(1.40) \quad |(5s^2)^1S_0\rangle = |\phi_{5s}(r_1)\phi_{5s}(r_2)\rangle \otimes \frac{1}{\sqrt{2}}(|\uparrow\downarrow\rangle - |\downarrow\uparrow\rangle).$$

The lowest singlet excited state accessible with a laser presents the same kind of symmetries, with one atom promoted to the 5p shell. It is given by

$$(1.41) \quad |(5s5p)^1P_1\rangle = \frac{1}{\sqrt{2}} [|\phi_{5s}(r_1)\phi_{5p}(r_2)\rangle + |\phi_{5s}(r_2)\phi_{5p}(r_1)\rangle] \otimes \frac{1}{\sqrt{2}}(|\uparrow\downarrow\rangle - |\downarrow\uparrow\rangle),$$

For the triplet states, the spatial part is anti-symmetric while the spin part is symmetric. The lowest triplet excited states consist in the 3P_J manifold expressed as

$$(1.42) \quad |(5s5p)^3P_J\rangle = \frac{1}{\sqrt{2}} [|\phi_{5s}(r_1)\phi_{5p}(r_2)\rangle - |\phi_{5s}(r_2)\phi_{5p}(r_1)\rangle] \otimes \begin{cases} |\uparrow\uparrow\rangle & (J = 2) \\ \frac{1}{\sqrt{2}}(|\uparrow\downarrow\rangle + |\downarrow\uparrow\rangle) & (J = 1) \\ |\downarrow\downarrow\rangle & (J = 0) \end{cases}$$

The success of alkaline-earth atoms is due to the fact that, as a consequence of the spin-orbit selection rules, electric dipole transitions from the singlet to the triplet manifolds are forbidden. Moreover, transitions from a total angular momentum $J = L + S = 0$ to another $J = 0$ state are also not allowed. This doubly forbidden condition leads to extremely narrow $|^1S_0\rangle \rightarrow |^3P_0\rangle$ clock transitions, with a decay rate lying in the mHz range for fermionic species [99].

In the $|^1S_0\rangle \rightarrow |^3P_1\rangle$ transitions, known as the *intercombination lines*, the spin-orbit coupling allows a stronger decay rate in the kHz range. These lines are used to perform narrow-line cooling mechanisms, reaching temperatures at the μ K level.

Finally, the singlet-singlet transitions $|^1S_0\rangle \rightarrow |^1P_1\rangle$ are called the *dipole allowed* transitions, with high decay rates in the MHz range. These transitions are used to perform slowing techniques, as well as first step cooling leading to mK cold samples.

Z	Abundance	Statistics	Nuclear Spin
84	0.56%	Boson	0
86	9.86%	Boson	0
87	7.00%	Fermion	9/2
88	82.58%	Boson	0

Table 1.1: Strontium stable isotopes with their natural abundances, quantum statistics and nuclear spins.

1.2.2 Strontium energy levels

Named after the Strontian city in Scotland where it was discovered for the first time in a lead mine in 1790 [100], strontium is an alkaline-earth element of atomic number 38. It has four stable isotopes, summarized in table 1.1, which have all been brought to the quantum-degenerate level using magneto-optical traps and optical dipole traps [101]. In the following paragraphs, we present the energy level diagrams of the bosonic and fermionic isotopes separately. The different MOT repumping schemes are also discussed.

1.2.2.1 Bosonic isotopes

The two valence electrons of strontium give rise to the energy level diagram presented in figure 1.6, where the transition linewidths are taken from [102]. The bosonic isotopes of strontium have a nuclear spin $I = 0$. These species thus do not present an hyperfine level structure, and the diagram is simply given by the fine structure which depends on the total spin $J = L + S$. The relevant energy levels for trapping, cooling and CQED schemes are presented in spectroscopic notation $^{2S+1}L_J$.

On the singlet side of the diagram, the wide $\Gamma = 2\pi \times 32\text{MHz}$ ⁴ transition at 460.862nm is called the *blue* or *dipole allowed* transition. This fast cycling transition is used for slowing high-speed strontium atoms, as presented in section 4.2 of chapter 4. Moreover, it allows to implement a first step cooling mechanism known as the blue MOT, described in details in section 4.4 of the same chapter. The transition from the ground state to the $|(5s5p)^3P_1\rangle$ at 689.449nm is called the *red* transition or *intercombination line*. A second step narrow-line cooling mechanism on this transition is described in section 4.5. The so-called clock transition corresponds to the $|(5s^2)^1S_0\rangle \rightarrow |(5s5p)^3P_0\rangle$ line at 698.446nm. For the bosonic isotopes, the linewidth of the clock transition is extremely small, lying in the 10^{-12}Hz range. Consequently, it can not be addressed by a laser, unless mixing the $|(5s5p)^3P_0\rangle$ state with the $|(5s5p)^3P_1\rangle$ by applying a magnetic field on the order of $10^1 - 10^2\text{G}$ [103]. With this technique, a laser tuned on the clock frequency induces

⁴A consensus on this value does not seem to have been reached in the community. Depending on the references, values of $\gamma = 32\text{MHz}$, 30.5MHz or 30.2MHz are reported.

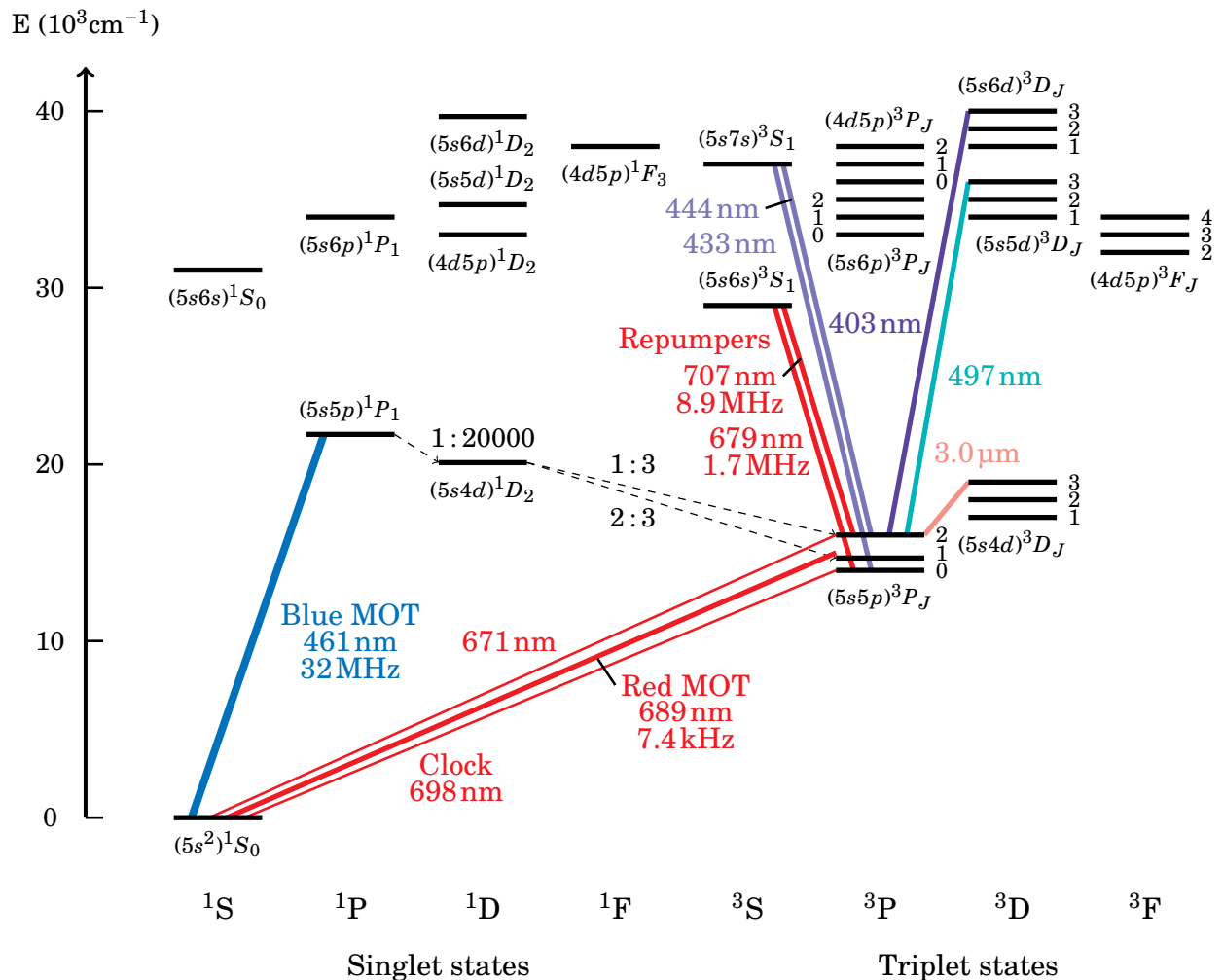


Figure 1.6: Relevant energy levels and transitions of the strontium bosonic isotopes with a nuclear spin $I = 0$.

a coupling between the ground and the clock states with a Rabi frequency given by

$$(1.43) \quad \Omega_{clock} = \frac{\Omega_L \Omega_B}{\Delta_{10}},$$

where $\Omega_L = \langle (5s5p)^3P_1 | \hat{\mathbf{d}} \cdot \mathbf{E} | (5s^2)^1S_0 \rangle / \hbar$ depends on the intercombination line dipole matrix element, $\Omega_B = \langle (5s5p)^3P_1 | \hat{\mu} \cdot \mathbf{B} | (5s5p)^3P_0 \rangle / \hbar$ corresponds to the magnetic-dipole coupling between the two excited states and Δ_{10} is the frequency difference between the $|(5s5p)^3P_1\rangle$ and the $|(5s5p)^3P_0\rangle$ states.

1.2.2.2 Repumping schemes

During a MOT operation, electrons are expected to be promoted from the ground state to an excited one by absorbing a photon, and then decay back to the first state. This quantum trajectory

is referred to as a cycling transition. Nevertheless, electrons can also decay from the excited state to all the others states with non zero branching ratios. Repumping lasers are thus used to optically pump electrons to any state decaying exclusively to the ground state. Brought back to the cycling transition, atoms can keep absorbing photons in order to be slowed down. Considering the level scheme shown in figure 1.6, one can observe that during the blue MOT operation, the electrons are cycling from the ground $|5s^2\ ^1S_0\rangle$ state to the singlet excited state $|5s5p\ ^1P_1\rangle$. It can then decay back to the former, or explore the $|5s4d\ ^1D_2\rangle$ state with a branching ratio of 1 : 20000, according to recent experimental studies [53]. From there, two transitions to the lower excited triplet states $|5s5p\ ^3P_1\rangle$ and $|5s5p\ ^3P_2\rangle$ are possible, with branching ratios of 2 : 3 and 1 : 3, respectively [102]. Electrons from the $|5s5p\ ^3P_1\rangle$ state decay back to the ground-state with a $1/e$ lifetime $\tau = 21.5\ \mu\text{s}$, sufficiently short to keep the atoms in the MOT region. For the $|5s5p\ ^3P_2\rangle$ state, the lifetime for the same decay has been measured to $\tau = 500\text{s}$ [104]. This time is basically infinite compared to the timescales involved in the experiment which typically lay in the microsecond to second range. The number of atoms in the blue MOT can thus be increased using one or several repumping lasers able to pump the atoms back to the cycling transition at 461 nm.

Several repumping schemes have been used by different groups in order to maximize the number of atoms in the blue MOT. The different strategies can be grouped in two classes. The first one consists in repumping to the $|5snd\ ^3D_2\rangle$ states, with $n = 4, 5$ or 6. These transitions occur at wavelengths of $3\ \mu\text{m}$, 497 nm and 403 nm, respectively. One advantage of these schemes is to only require one repumping laser to efficiently increase the MOT population. However, indirect dipole-allowed decay channels from the $|5snd\ ^3D_2\rangle$ states to the clock states $|5s5p\ ^3P_0\rangle$ still exist [105]. This state lifetime theoretically being equal to 1000 s for the fermion and even longer lived for the boson, atoms falling in this state are quickly lost from the trap. Furthermore, even if convenient Blu-ray laser diodes are available at 403 nm, using the transitions at $3\ \mu\text{m}$ and 497 nm is more involved technically as it needs to develop *Optical Parametric Oscillators* (OPOs) for the former and doubling diode laser schemes for the latter [106].

The second scheme is based on a two lasers repumping scheme from the $|5s5p\ ^3P_0\rangle$ and $|5s5p\ ^3P_2\rangle$ states to the $|5sns\ ^3S_1\rangle$ states, with $n = 6$ or 7. For the $n = 6$ level, the transitions respectively occur at 679.289 nm and 707.202 nm. For $n = 7$, the wavelengths are 432.6 nm and 443.8 nm. Using two lasers instead of one could seem less convenient than in the previous schemes, but it actually brings a lot of advantages. First of all, the implied wavelengths used to address the $|5s6s\ ^3S_1\rangle$ state are easily found as diode lasers outputting several tenths of milliwatts. More importantly, it allows repumping from the untrapped clock state back to the cycling transition, preventing any loss mechanisms from the $|5s5p\ ^3P_J\rangle$ manifold. Finally, this scheme allows for state selective imaging in many different contexts such as atomic clocks, optical

State	A (MHz)	B (MHz)
1S_0	0	0
1P_1	-3.4(4) [110]	39(4) [110]
3P_0	0	0
3P_1	-260.085(2) [111]	-35.667(21) [111]
3P_2	-212.765(1) [112]	67.340(15) [112]
3S_1	-542.0(1) [102]	-0.1(5) [102]

Table 1.2: Hyperfine splitting constants of the ^{87}Sr energy levels.

Z	1P_1	3P_0	3P_1	3P_2	3S_1
87	-46.5 [100]	-62.9 [102]	-62.15 [102]	-61.8 [113]	-54.9 [102]
86	-124.8 [100]		-163.81 [100]		
84	-270.8 [100]		-351.49 [100]		

Table 1.3: Isotope shifts of the energy levels used for trapping, cooling and clock operations given in MHz. The shifts are referenced to the ^{88}Sr isotope.

tweezers and Rydberg physics [53, 107, 108]. One can also transfer the atoms in the $|(5s5p)^3P_2\rangle$ state for magnetic trapping and bring them back to the ground-state for further operations [109].

With these considerations in mind, we chose to use the $|(5s6s)^3S_1\rangle$ repumping scheme with two diode lasers at 679 nm and 707 nm, further described in 2.1.2.

1.2.2.3 Fermionic isotope

The level structure of the strontium stable fermionic isotope ^{87}Sr is modified compared to the bosonic diagram in figure 1.6 by the presence of an hyperfine structure due to a non-zero nuclear spin $I = 9/2$. This large spin allows to study $SU(N)$ quantum magnetism with strontium atoms, which finds applications in topological matter, quantum information and superfluidity [59]. Due to the presence of this non-zero nuclear spin, the energy levels are splitted into manifolds of total spin $F = I + J$ containing $2F + 1$ Zeeman sublevels, with $|I - J| \leq F \leq I + J$. The hyperfine energy splittings of these manifolds are given by the following formula

$$(1.44) \quad \frac{\Delta E_{hf}}{h} = \frac{A}{2}K + \frac{B}{4} \frac{3K(K+1) - 4I(I+1)J(J+1)}{2I(2I-1)J(2J-1)},$$

with

$$(1.45) \quad K = F(F+1) - J(J+1) - I(I+1).$$

The A and B coefficients in equation 1.44 correspond to the electric-dipole and magnetic-quadrupole shifts, respectively. These coefficients for the transitions of interest are given in

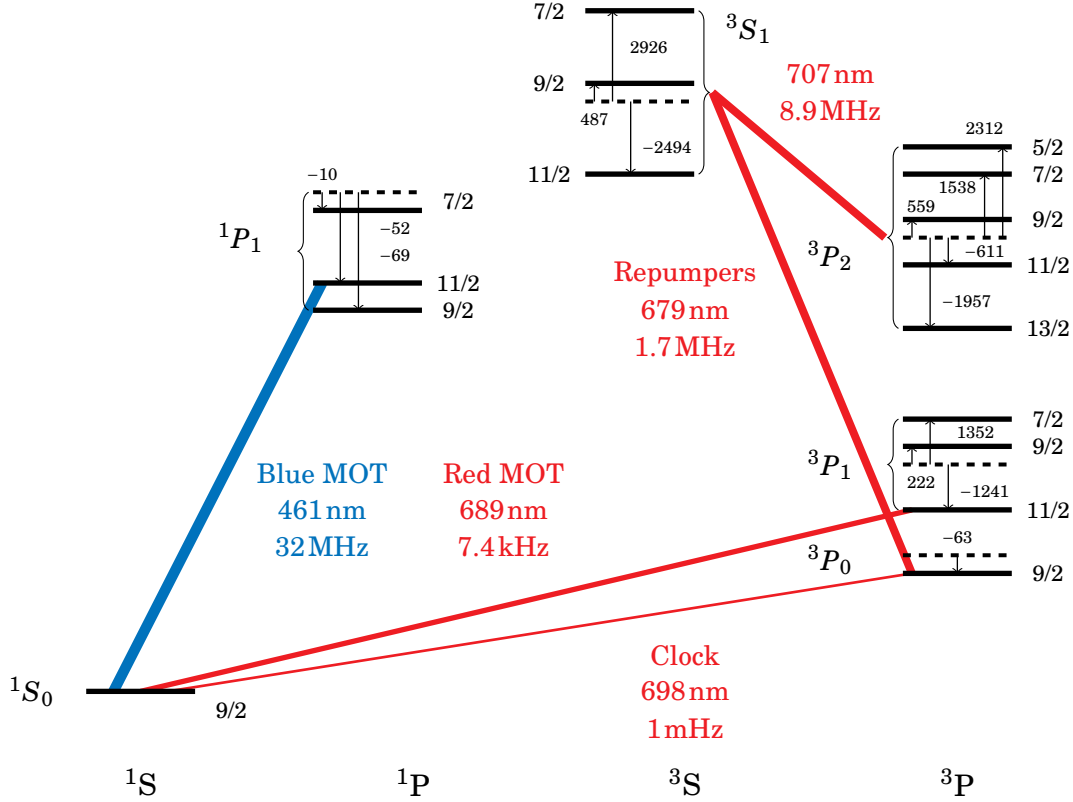


Figure 1.7: Relevant energy levels and transitions of the strontium fermionic isotope ^{87}Sr with a nuclear spin $I = 9/2$. The frequency shifts compared to the ^{88}Sr isotope are given in MHz.

table 1.2. Moreover, each strontium species experience isotope shifts of the energy levels compared to the most abundant ^{88}Sr used as a reference. These shifts are given in table 1.3, and the resulting level diagram for the fermionic isotope is presented in figure 1.7.

The MOT operations for the fermionic isotope are modified compared to the bosonic ones. In order to obtain closed transitions, the blue and red excited manifolds used for cooling are the $F = 11/2$. In the blue MOT case, the natural linewidth is on the same order of magnitude as the hyperfine splittings. The different hyperfine transitions are thus not fully resolved, which results in populating the $F = 7/2$ and $F = 9/2$ manifolds. However, the small lifetime of the transition insures a rapid decay to either the ground state, either the repumped $|(5s5p)^3P_0, F = 9/2\rangle$ and $\{|(5s5p)^3P_2, F\rangle\}$ manifolds. As can be seen in figure 1.7, this last set of states covers a frequency range of 4.27 GHz. Moreover, the repumping excited state $|(5s6s)^3S_1\rangle$ get splitted into three manifolds covering a range of 5.42 GHz. The main difference between the bosonic and fermionic MOTs thus lies in the repumping lasers, which have to be scanned over 5.42 GHz in order to cover all the possible repumping transitions. In the red MOT case, the hyperfine splittings are 10^3 times larger than the natural linewidth, limiting this depumping effect.

1.2.3 Magic trapping

As described in 1.1.2, the light-matter interaction between an atom and a laser is governed by the dipolar interaction expressed in equation 1.19. In the far detuned limit, where all the detunings from the laser frequency to the atomic transitions are larger than the natural linewidths, this interaction creates an energy shift known as the AC Stark shift. Within the framework of the second-order perturbation theory, the energy shift of a Zeeman state $|v\rangle$ of spin J_v and spin projection m_J induced by an electric field of amplitude \mathcal{E}_0 at frequency ω , is given by [114]

$$(1.46) \quad \Delta E_v = -\frac{1}{2}\alpha_0^{(v)}(\omega)\mathcal{E}_0^2 - \frac{1}{2}\alpha_2^{(v)}(\omega)\frac{3m_J^2 - J_v(J_v + 1)}{J_v(2J_v - 1)}\mathcal{E}_0^2 + \mathcal{O}(\mathcal{E}_0^4),$$

where α_0 (α_2) corresponds to the scalar (tensor) polarizability. These parameters, expressing the sensitivity of a state to applied electric fields, can be expressed as a sum over all the $|k\rangle$ states of the multi-level atom such that

$$(1.47) \quad \alpha_i^{(v)}(\omega) = \sum_k c_i(J_v, J_k) |\langle k | \hat{d} | v \rangle|^2 \frac{E_k - E_v}{(E_k - E_v)^2 - (\hbar\omega)^2},$$

with $i \in \{0, 2\}$, $c_i(J_v, J_k)$ a constant factor depending on the spins of each state and $\langle k | \hat{d} | v \rangle$ the electric-dipole matrix element of the $|k\rangle \rightarrow |v\rangle$ transition.

This effect is extremely useful in cold atoms experiments, as it can be implemented in atomic cloud transportation, trapping or condensation via evaporative cooling. However, this energy shift is also one of the main limitations in state-of-the-art optical clocks, as it modifies the clock transition energy when varying the dipole trap intensity $I_0 \propto \mathcal{E}_0^2$. For a two-level atom, the ground state energy shift is exactly opposite to the excited one. The energy difference between these two levels derived from equation 1.46 can thus not be cancelled. In multi-level atoms such as alkaline-earth species, a situation where the polarizability of the two clock states are equal can be found. The laser frequencies fulfilling this condition for a given transition occur at so-called *magic wavelengths*, introduced by Katori *et al.* in 1999 [115]. In strontium, a magic crossing for the clock transition appends at 813.4 nm [116]. For the red MOT transition, the $|5s^2)^1S_0\rangle$ and $|(5s5p)^3P_1, m_J = 0\rangle$ polarizabilities cross at 501 nm, while the crossing with the $|(5s5p)^3P_1, m_J = \pm 1\rangle$ Zeeman levels occurs at 520 nm [53]. These magic wavelengths can be tuned either by controlling the angle between the linear polarization of the dipole trap and a magnetic field [52], either by modifying its ellipticity [53]. These methods have been applied to implement arrays of optical clocks in tweezers, where the magic trapping of the red MOT transition is used to perform sideband cooling and the magic tapping of the clock transition leads to an intensity-variation free clock [54, 55, 117].

1.3 Towards a micro ring cavity experiment with strontium atoms

Inspired by both CQED schemes for exploring entanglement and the new perspectives brought by alkaline-earth atoms, the new experiment that we are setting up aims to place a cold sample of strontium atoms into a micro ring cavity. As a first step towards a combined atom-cavity setup, we developed a compact experiment allowing to prepare an ultra-cold strontium sample, pictured in figure 1.8(a). This apparatus includes a low-consumption home-made effusive source placed in an unusually short vacuum system. In order to reduce transverse spreading of the atomic beam, we combined the Zeeman slowing and MOT magnetic configurations into a single coils setup. The cold sample is obtained in a glass cell, ensuring maximum optical access. In the next chapter of this thesis, the development of the laser setup used to perform slowing and cooling on both the blue and red strontium transitions is presented. A complete description of the vacuum system and the atomic beam properties are then provided in the third chapter. Finally, a full characterization of the obtained atomic sample is given in the last chapter.

As a next step, the high-finesse micro triangular cavity developed in parallel with the strontium apparatus will be added to the vacuum system. The produced ultra-cold strontium sample will then be transported to the cavity in order to perform CQED, as represented in figure 1.8(b). The advantage of this design lies in the possibility of trapping the atoms in a standing wave magic lattice, thus limiting collisional frequency shifts in clock-like operations, while probing them with a running wave to ensure an homogeneous coupling over the cloud. With a $500\mu\text{m}$ long cavity of finesse $\mathcal{F} \simeq 4 \times 10^4$ and waist $w_0 = 3.5\mu\text{m}$, we expect to achieve a single atom cooperativity $C_1 = 80$ on the clock transition. Despite impressive recent achievements in the field [58, 118], the milestone of direct squeezing on the clock transition with alkaline-earth-like atoms yet remains to be achieved.

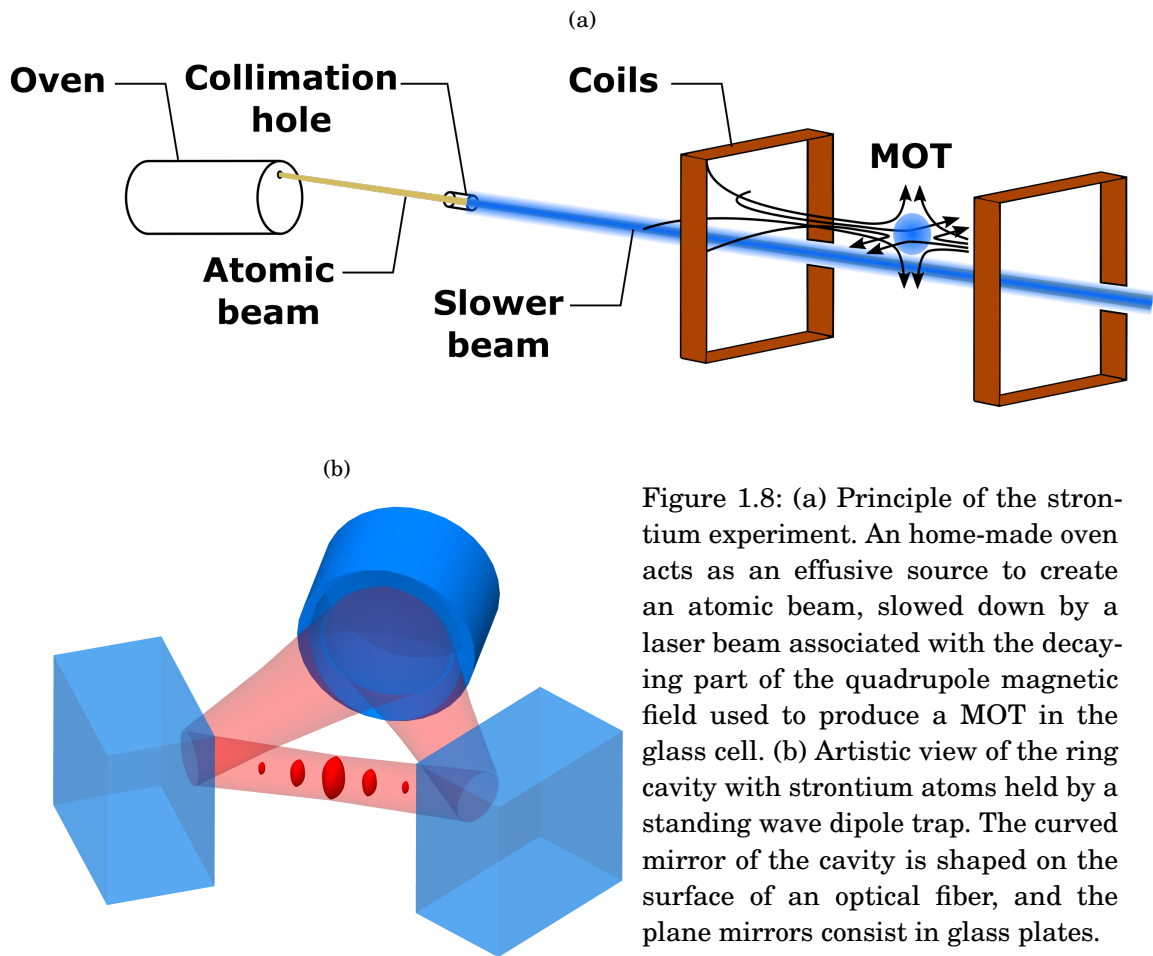


Figure 1.8: (a) Principle of the strontium experiment. An home-made oven acts as an effusive source to create an atomic beam, slowed down by a laser beam associated with the decaying part of the quadrupole magnetic field used to produce a MOT in the glass cell. (b) Artistic view of the ring cavity with strontium atoms held by a standing wave dipole trap. The curved mirror of the cavity is shaped on the surface of an optical fiber, and the plane mirrors consist in glass plates.

LASER SYSTEM

In atomic physics, lasers are a powerful tool for probing atomic transitions. Their impressive phase coherence properties allow to address spectroscopic lines, perform atomic trapping and cooling, CQED schemes and many other features. In the laboratory though, solid-state diode lasers can be subject to the environment instabilities, such as temperature variations or laser intensity drifts. It is thus mandatory to stabilize their frequency on well known etalons. Moreover, real lasers have finite spectral linewidths, which needs to be narrower than the natural linewidths of the addressed transitions.

This chapter is dedicated to the different laser systems and frequency stabilization schemes implemented in the experiment. In a first part, we describe the laser system used in trapping and cooling of strontium atoms on the wide dipole-allowed transition $|(5s^2)^1S_0\rangle \rightarrow |(5s5p)^1P_1\rangle$ at 461nm. The repumping lasers at 679nm and 707nm, necessary for efficient MOT operation, are also presented with their numerical frequency stabilization scheme. In the second part, we describe the red laser system containing the lasers addressing the intercombination line $|(5s^2)^1S_0\rangle \rightarrow |(5s5p)^3P_1\rangle$ at 689nm and the clock transition $|(5s^2)^1S_0\rangle \rightarrow |(5s5p)^3P_0\rangle$ at 698nm. The common frequency stabilization procedure for these two lasers on an ultra-stable cavity is presented, and an absolute frequency reference based on a strontium spectroscopic cell is detailed.

2.1 Blue MOT laser system

The interesting physical properties of alkaline-earth elements are mainly due to the presence of narrow forbidden transitions. However, addressing such transitions can only be realized on cold atomic sample. In order to produce such cold clouds, several tasks as Zeeman slowing from a fast

Laser	Power (mW)	Waist (μm)	Temperature ($^{\circ}\text{C}$)	Current (mA)
Master 461 nm	12	350	27	110
MOT slave	153	330	13.7	143
Zeeman slower slave	125	330	17.6	139
Repumper 679 nm	19.2	250	17.0	120.2
Repumper 707 nm	35.0	250	26.4	96.0

Table 2.1: Operating parameters of the lasers involved in the blue MOT operation.

atomic beam, cooling from a hot sample and imaging processes necessitate transitions with a fast scattering rate. In strontium, this condition is provided by the large $|(5s^2)^1S_0\rangle \rightarrow |(5s5p)^1P_1\rangle$ transition at 461 nm, with a natural linewidth $\Gamma = 2\pi \times 32\text{MHz}$. In this section, we present a master-slave diode laser architecture on this transition, stabilized on a discharge strontium cell. The repumping lasers stabilization procedure using a wavemeter is also presented hereafter. The operating parameters of the blue MOT laser system are given in table 2.1, and a scheme of the optical setup is presented in figure 2.1.

2.1.1 461 nm master-slave architecture

In strontium experiments, producing blue light is mainly achieved with two possible schemes. The first one consists in a frequency doubling system, with a pump provided by an *External Cavity Diode Laser* (ECDL) at 922 nm such as a Ti:Sapphire [119] or a Toptica DLpro [100, 120]. The second possibility is to use an ECDL directly emitting at 461 nm [121, 122]. As this method presents the advantages of reducing the costs and simplifying the system compared to the first one, we chose to implement a blue diode laser scheme. However, using a single ECDL do not produce enough power to create the different beams needed for trapping, cooling and imaging. We tackle this problem by implementing a master-slave architecture, where a first frequency stabilized ECDL laser is injected into high-power laser diodes emitting at 461 nm.

2.1.1.1 Blue diode lasers

The laser system at 461 nm is based on a master-slave architecture with two slave lasers referred to as Zeeman slower and MOT. The first one is used to both slow down the atoms coming out of the home-made oven, further described in 3.1, and image the cold atomic cloud as detailed in 4.4.1. The second one provides the beams for the first stage blue MOT detailed in section 4.4. The master laser is a commercial *Littrow Diode Laser* (LDL) from Moglabs¹ with a single-mode AR coated diode from Nichia². Initially, we have been using a *Cateye Diode Laser* (CEL) but after approximately one year of daily operation, the power started to continuously drop down.

¹See <http://www.moglabs.com>.

²Diode NDBA116T. See <https://www.nichia.co.jp>.

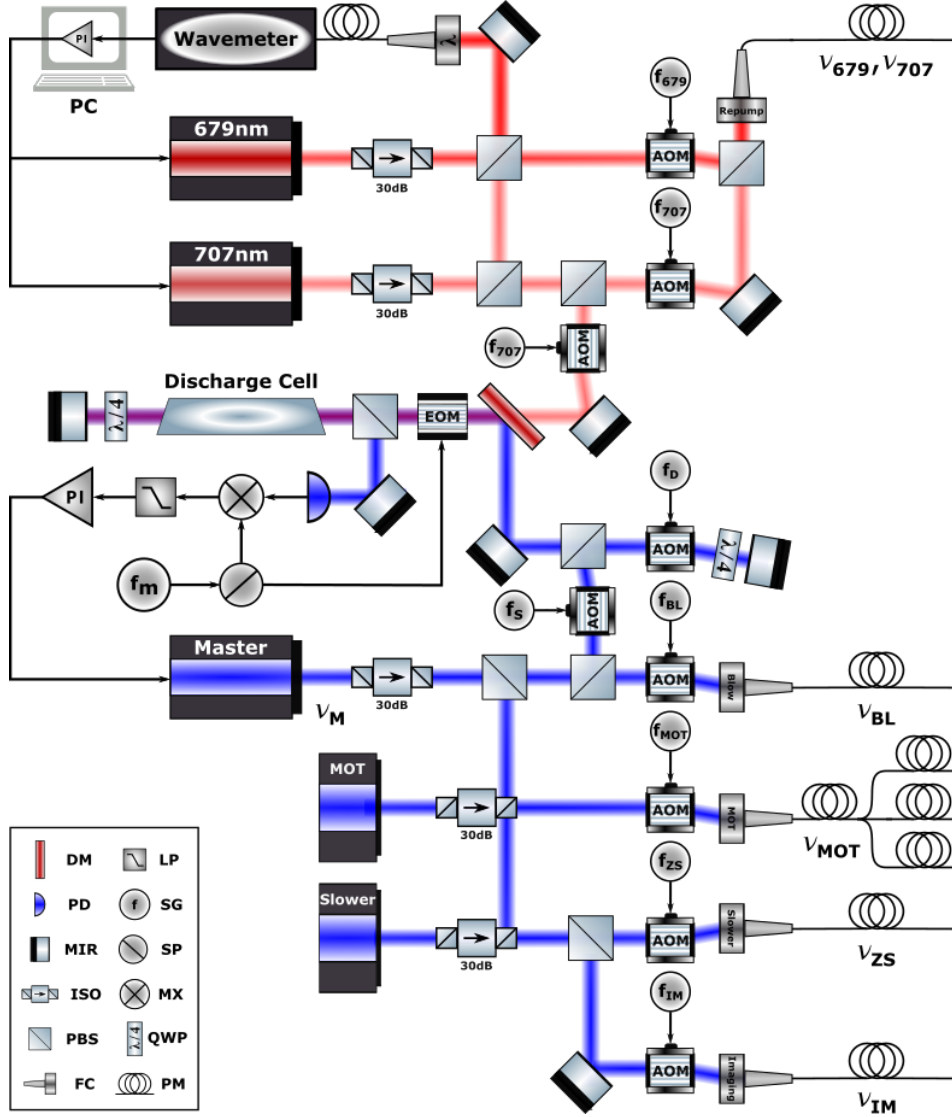


Figure 2.1: Scheme of the laser systems at 461nm, 679nm and 707 nm. Half-wave plates and exact mirror configurations have been omitted for simplicity and the slave injection simplified. The AOM diffraction orders are ± 1 depending on the orientation with respect to the RF frequency input. A realistic version of the laser system is presented in appendix A. DM - Dichroic Mirror, PD - Photodiode, MIR - Mirror, ISO - Optical Isolator, PBS - Polarising Beam Splitter, LP - Low-Pass filter, SG - Signal Generator, SP - RF Splitter, MX, RF Mixer, FC - Fiber Coupler, PM - Polarization Maintaining fiber, AOM - Acousto-Optic Modulator, EOM - Electro-Optic Modulator.

It is well known that focused high-energy beams in the UV and near-UV range can induce photo-activated chemistry reactions [123]. In the Littrow configuration, this effect is minimized as the beam is collimated on a grating instead of being focused on the Cateye mirror. These two ECDL configurations are represented in figure 2.2 for comparison. Both laser architectures induce laser beam astigmatism, which are compensated for all our lasers following the procedure

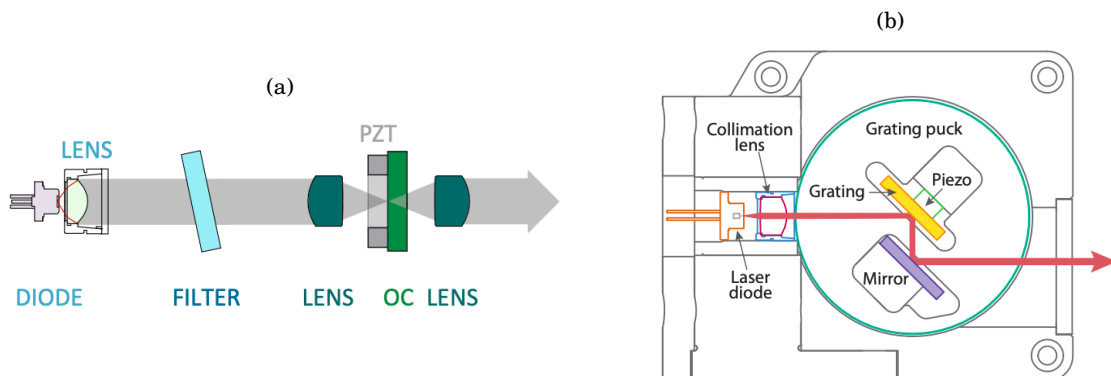


Figure 2.2: (a) Schematic view of the *Cateye Diode Laser* configuration. The diode laser emission wavelength is first selected by a bandpass filter. The beam is then focused on a mirror which position depends on a piezo electric actuator to form a tunable extended cavity with the diode laser rear facet itself. (b) Scheme of the *Littrow Diode Laser* configuration. The external cavity is created by a grating angled such that the first order reflection is superimposed to the diode laser output mode. The cavity length is also controlled by a piezo electric actuator placed on the grating.

described in appendix B.

The frequency of the master laser is stabilized by a saturated absorption scheme, described in 2.1.1.2. In order to amplify the available blue light and control the different beam frequencies, it injects two slave lasers made of multimode laser diodes in temperature-controlled mounts³. The injection is performed by overlapping the slave laser beams with one arm of the master light on optical isolators, as shown in figure 2.1. The master frequency presents a mode hop free range of 15 GHz and the injection follows on 5 GHz for both slaves, with an injecting optical power of 2.5 mW. Good injection conditions are identified by a reduction of the slave lasers intensity noises in the injection frequency range, recorded with monitoring photodiodes placed on the leaking ports of one polarizing beam splitter on each slave laser path. In order to increase the injection stability over temperature drifts from several tenths of minutes to several hours, we implement two identical empirical locking schemes by modulating the slave lasers intensities and demodulating the monitoring photodiode signals at the same frequency to produce error signals. The intensity noises reductions are thus traduced by jumps on the error signals, which can be used to lock the slave intensities in the injection range.

2.1.1.2 Master laser saturated absorption stabilization

In cold atoms experiments, several operations such as cooling, slowing and imaging require laser frequency stabilities smaller than the natural linewidth of the considered transition. In

³Diodes NDB4216 from Nichia. Temperature-controlled mount LDM90/M from Thorlabs.

the $|5s^2)^1S_0\rangle \rightarrow |5s5p)^1P_1\rangle$ transition case, this linewidth equals $\Gamma = 2\pi \times 32$ MHz. Therefore, the master diode laser frequency is stabilized via a saturated absorption locking scheme, compensating for both fast and slow drifts induced by intensity noise and temperature drifts, respectively. As represented in figure 2.1, one part of the master laser beam is phase modulated by an *Electro-Optic Modulator* (EOM)⁴ with a *Radio Frequency* (RF) signal at $f_m = 16$ MHz. The beam is then sent into a strontium hollow cathode discharge cell⁵ in a retro-reflected configuration, providing a pump-probe scheme. The retro-reflection is collected on a photodiode and its signal is mixed with the RF signal at f_m . A low-pass filter is added to generate an error signal, shown in figure 2.3. The error signal is then fed into a *Proportional and Integral* (PI) regulator which separates the fast proportional part, added to the current of the master laser, to the slow integral part added to the piezo high-voltage signal. The retroaction on the current is limited to 1 MHz by the master laser circuit board and the piezo typically reacts to frequencies lower than a few kHz. A gaussian fit on the absorption signal reveals a Doppler broadening of $\sigma_v = 620$ MHz, corresponding to an effective temperature of 580 °C inside the cell. An estimation of the in-loop laser linewidth can be done by measuring the error signal *Root Mean Square* (rms). Indeed, frequency fluctuations are linked to voltage noises through the on resonance slope \mathcal{D} of the error signal ϵ through

$$(2.1) \quad \mathcal{D} = \left\| \frac{d\epsilon}{d\nu} \right\|.$$

Assuming a gaussian white intensity noise, the laser frequency noise ν_{rms} can be estimated using the relation [124]

$$(2.2) \quad \nu_{rms} = 2\sqrt{2\ln 2} \frac{\epsilon_{rms}}{\mathcal{D}}.$$

We experimentally measure $\nu_{rms} = 470$ kHz, which is 65 times smaller than the natural linewidth and sufficient for any operations on the dipole allowed transition.

2.1.1.3 Slave lasers frequency generation

With the master laser frequency being locked on the discharge cell absorption signal and the slave lasers injected at the master frequency ν_M , a set of *Acousto-Optic Modulators* (AOM) is used to generate the different frequencies necessary for atomic slowing, cooling, imaging and blowing out of the cavity. Moreover, these AOMs allow to switch on and off the diffracted laser beams coupled to the optical fibers which connect the lasers optical table to the main experiment. The RF signals feeding the AOMs are generated by a *Direct Digital Synthesis* (DDS) setup detailed in appendix C. The optical and RF frequencies are represented in figure 2.4 in an energy-like diagram. All optical transitions are referenced to the $|5s^2)^1S_0\rangle \rightarrow |5s5p)^1P_1\rangle$ transition of ^{88}Sr at ν_0 . In order to obtain an agile frequency system capable of addressing the blue transition of both the bosonic ^{88}Sr and the fermionic ^{87}Sr isotopes, the frequency of the master laser arm used

⁴Model PM7-VIS F16 from QUBIG. See <https://www.qubig.com/>.

⁵Cell L233-38NB from Hamamatsu. See <https://www.hamamatsu.com/>.

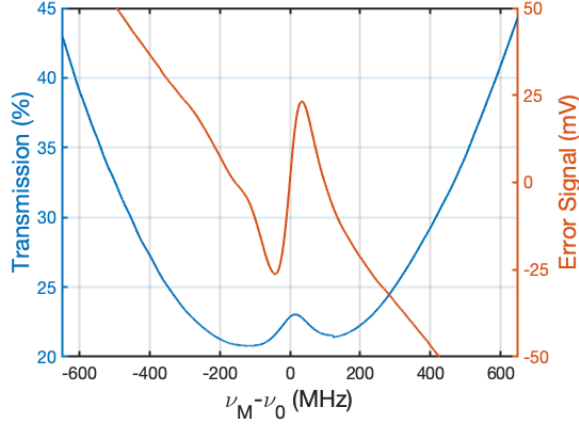


Figure 2.3: Saturated absorption signal (left axis) and error signal (right axis) generated by a retro-reflected beam from the 461 nm master laser. The beam properties are 510 μ W of optical power and a waist of 400 μ m, corresponding to a saturation parameter $s_0 = 5$. The frequency axis is referenced to the $|5s^2)^1S_0\rangle \rightarrow |(5s5p)^1P_1\rangle$ transition of ^{88}Sr . The signals exhibit Lamb dips for this transition for the different isotopes.

for saturated absorption stabilization is detuned from its central frequency ν_M by a set of two AOMs. The first one is used in a single passage configuration with an RF frequency f_S , and the second is a double passage AOM at frequency f_D . Switching from one isotope to the other is thus done by modifying the double passage frequency f_D from 355 MHz for the boson to 378.5 MHz for the fermion, while keeping the single passage one at a fixed value $f_S = -340$ MHz.

The blue MOT beams are generated by detuning the MOT slave laser frequency from the master by an amount $f_{MOT} = -342$ MHz, and coupling the obtained light into a fiber splitter 1×3 at 461 nm⁶, as shown in figure 2.1. The atomic slower and imaging beams are derived from the Zeeman slower slave laser, splitted by a PBS. An AOM driven by an RF signal at frequency $f_{ZS} = -175$ MHz produces the Zeeman slower beam. The imaging beam is nearly resonant with the blue transition, due to a frequency shift $f_{IM} = 380$ MHz from the master. Finally, the future blowing beam used to expel the atoms from the ring cavity is derived from the master laser detuned by $f_{BL} = 370$ MHz.

2.1.2 Repumping lasers numerical lock

Following the arguments developed in 1.2.2.2, we implemented a two-laser repumping system at 679 nm⁷ and 707 nm⁸. Both lasers are ECDLs from Moglabs. The setting points for stable operation are given in table 2.1. The repumping laser at 707 nm is superimposed to the 461 nm

⁶ 1×3 coupler array with Corning PM48-U25D fibers from Evanescent Optics Inc. See <http://www.evanescentoptics.com/>.

⁷ Laser diode EYP-RWE-0690 from Eagleyard photonics. See <https://www.toptica-eagleyard.com/>.

⁸ Laser diode HL7001MG from Opnext.

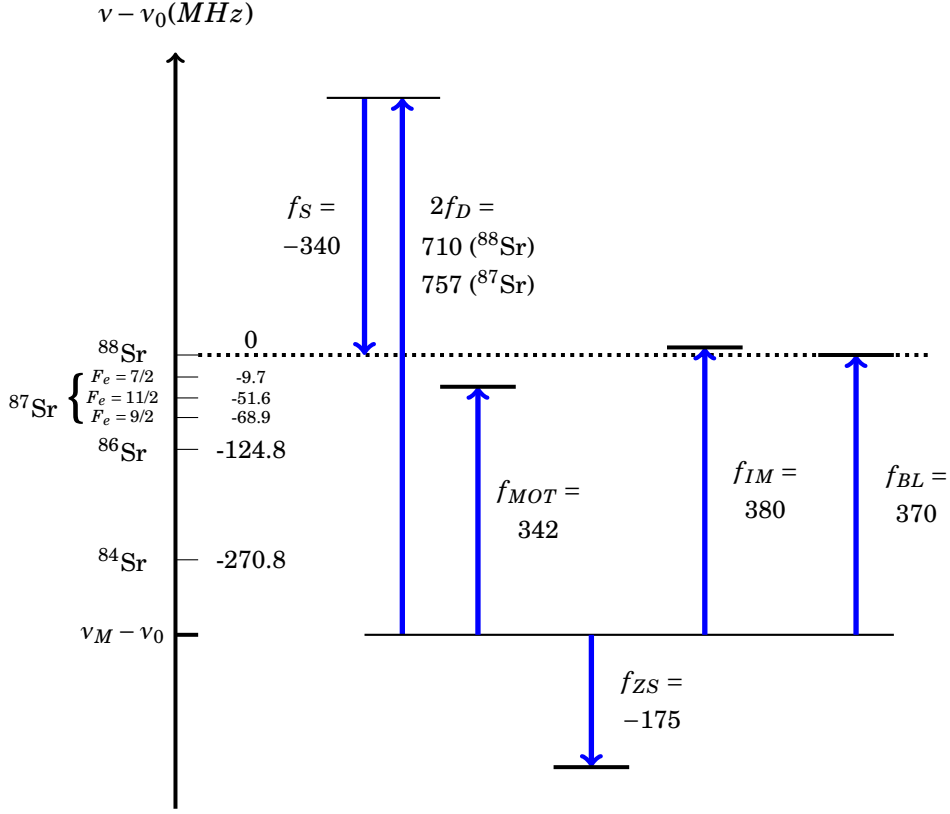


Figure 2.4: Frequency diagram for the laser system at 461 nm. The vertical axis represents the optical frequencies referenced to the dipole allowed transition of ^{88}Sr . The AOM RF frequencies f_i are given in MHz. Transitions for the other isotopes are also given on the frequency axis. The ^{87}Sr transitions from the ground state $| (5s^2)^1S_0, F_g = 9/2 \rangle$ to the excited states $| (5s5p)^1P_1, F_e \rangle$ are referenced by their hyperfine quantum number F_e .

saturated absorption beam via a dichroic mirror through the hollow cathode discharge cell. This scheme, represented in figure 2.1, allows to implement a saturated absorption scheme at 707 nm. The resulting absorption and error signal are detailed in appendix D. However, due to the large hyperfine splittings of the fermionic isotope ^{87}Sr , as well as a reported 50 smaller signal at 679 nm using the same type of cell [125], we have decided to implement a numerical lock and scan the repumping lasers frequencies at a rate of 900 Hz, even for the bosonic isotope ^{88}Sr . For the 707 nm laser, this scan covers a range of 250 MHz for the boson, and 6 GHz for the fermion. The 679 nm laser is scanned over 150 MHz for the boson, and is technically limited to 2 GHz for the fermion. In order to implement the numerical lock, the two repumpers are measured simultaneously on a wavelength meter⁹, as represented in figure 2.5(a). A Python interface interacting with the device extract the frequency ν_{WM} at time t with an absolute accuracy of 60 MHz and a resolution of 2 MHz. This value is compared to a setpoint ν_i , where the index i stands either for 707 or for

⁹Model WS7-60 from High-Finesse. See <https://www.highfinesse.com/en/wavelengthmeter>.

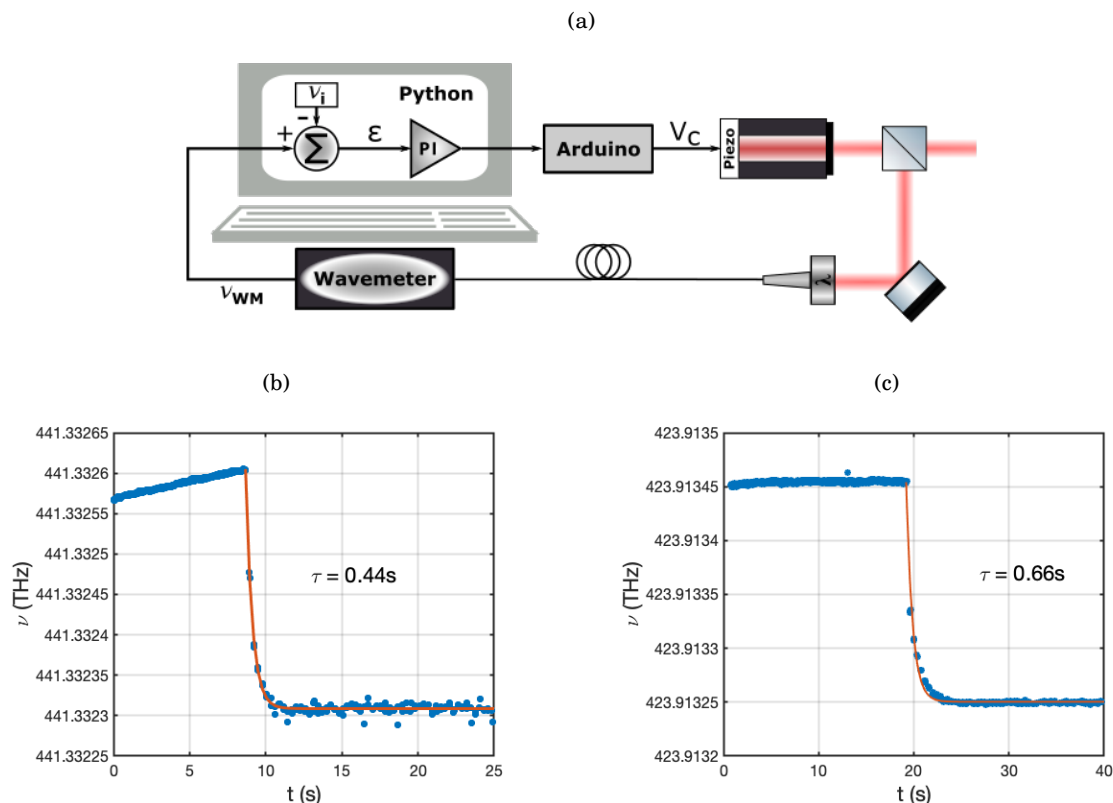


Figure 2.5: (a) Scheme of the numerical PI lock of the repumping lasers. Closed loop frequency of the (b) 679nm and (c) 707nm repumpers. Data are shown in blue and an exponential fit in orange gives the $1/e$ decay time from an arbitrary frequency to the setpoint.

679. Both setpoints are experimentally found by maximising the number of atoms in the targeted isotope blue MOT. Finally, a correction V_c is applied to the lasers piezos by an arduino-based lock box. The correction at time $t = m\Delta t$ after an integer number $m > 1$ of steps of length Δt is computed as follows

$$(2.3) \quad V_c(t) = K_p \left[\epsilon(t) + \sum_{j=1}^{m-1} \epsilon(j\Delta t) \frac{\Delta t}{T_I} \right],$$

with $\epsilon(t) = \nu_{WM}(t) - \nu_i$ the frequency error signal, K_p the proportional gain equal to $5.6 \times 10^{-7} \text{ VHz}^{-1}$ for the 707nm laser and $7.7 \times 10^{-8} \text{ VHz}^{-1}$ for the 679nm, and $T_I = 50 \text{ ms}$ the integrator time constant. Figure 2.5 shows the locking signals with an exponential fit giving a response time of the PI of approximately half a second for both loops. In order to perform blue MOT operations, the two repumping lasers are combined in a single fiber with PBSs, as shown in figure 2.1.

Laser	Power (mW)	Waist (μm)	Temperature ($^{\circ}\text{C}$)	Current (mA)
Master 689nm	23.3	340	22.1	141.03
Red MOT Slave	55	400	22.1	124.0

Table 2.2: Operating parameters of the 689nm lasers.

2.2 Red laser system

The red laser system refers to the lasers at 689nm and 698nm, addressing the red MOT and clock transitions, respectively. The natural linewidths of these transitions being much narrower than for the blue laser system, a more involved frequency stabilization scheme needs to be implemented. In our experiment, this scheme is realized by comparing the lasers frequencies to a standard consisting in an ultra-stable high-finesse Fabry-Pérot cavity. This cavity will also be used as a standard for the magic trap at 813nm, which will be superimposed to the red and clock lasers with dichroic mirrors, as represented on the red laser system scheme in figure 2.6. This sections begins with a description of the master-slave architecture at 689nm, with a master locked on the cavity and a slave used to enhance the available optical power. The frequency stabilization protocol on the cavity is then described for both the red and clock lasers, to end with a description of the absolute frequency calibration of the 689nm master laser on an home-made spectroscopy cell.

2.2.1 689nm master-slave architecture

The laser system at 689nm is made of a Cateye ECDL from Moglabs used as a master laser and an injected diode¹⁰ as a slave. Table 2.2 resumes the operating parameters for these two lasers. Similarly to the blue laser system, the master laser is used as a frequency reference and the slave provides sufficient optical power for strontium cooling on the intercombination line. The frequency stabilization procedure of the master laser relies on a lock on the ultra-stable cavity, described in 2.2.2, combined with an absolute frequency calibration on a spectroscopy cell described in 2.2.3. The slave laser is injected by a fraction of the master light via an optical isolator, as pictured in figure 2.6. An AOM driven by an RF signal at a fixed frequency $f_{r,S} = 220\text{MHz}$ acts as a switch before a fiber splitter at 689nm¹¹ used to produce the three red MOT retro-reflected beams. The frequency accordability of these beams is ensured by a double-pass AOM on the injection path, which detunes the master from the slave by an amount of $2f_{r,M}$, as represented in figure 2.7.

¹⁰Diode HL673MG from Thorlabs.

¹¹ 1×3 coupler array with Corning PM63-U40D fibers from Evanescence Optics Inc.

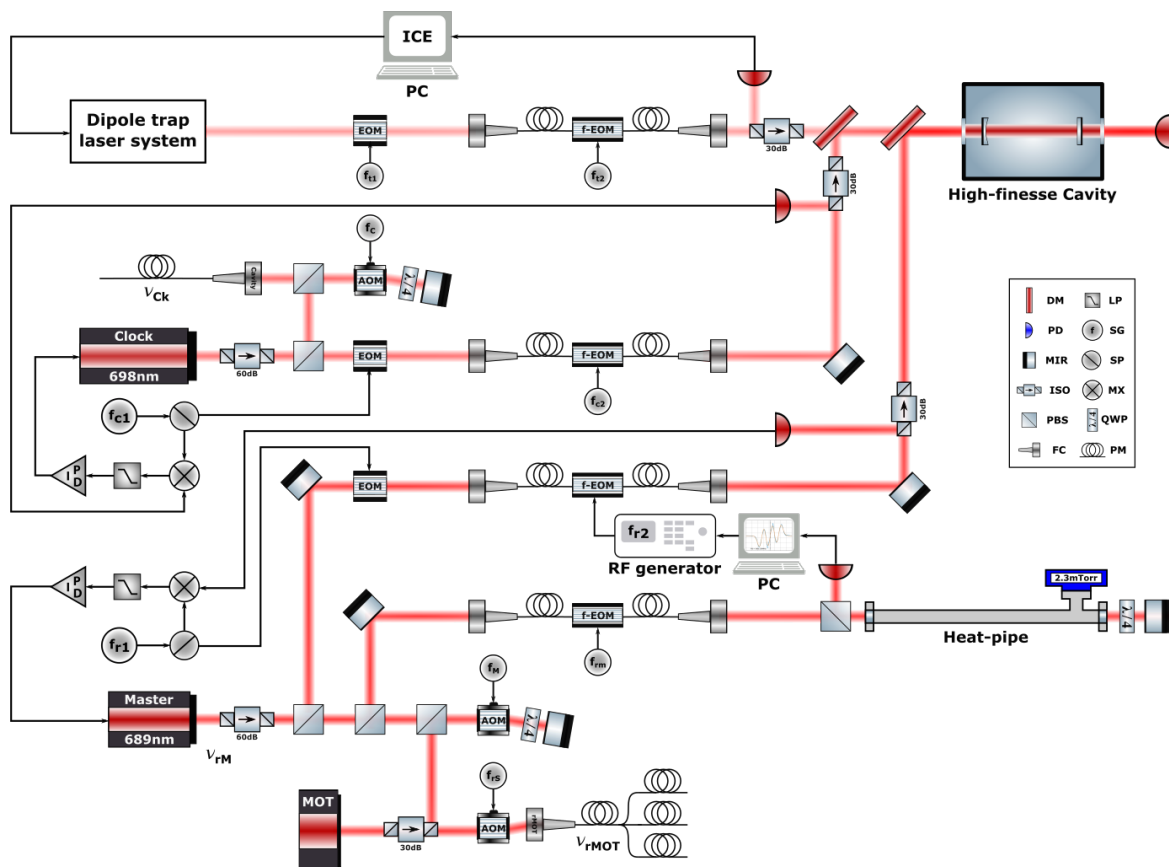


Figure 2.6: Scheme of the laser systems at 689nm, 698nm and the stabilization part of the dipole trap system. ICE is a software used to control the frequency of a Titanium Sapphire laser from MSquared. Half-wave plates and exact mirrors configurations have been omitted for simplicity and the slave injection simplified. The AOM diffraction orders are ± 1 depending on the orientation with respect to the RF frequency input. A realistic version of the laser system is presented in appendix A. DM - Dichroic Mirror, PD - Photodiode, MIR - Mirror, ISO - Optical Isolator, PBS - Polarising Beam Splitter, LP - Low-Pass filter, SG - Signal Generator, SP - RF Splitter, MX, RF Mixer, FC - Fiber Coupler, PM - Polarization Maintaining fiber, AOM - Acousto-Optic Modulator, EOM - Electro-Optic Modulator, f-EOM - fibred EOM.

2.2.2 Frequency stabilization on the Fabry-Pérot cavity

The natural linewidth of the intercombination line at 689nm is $\Gamma_r = 2\pi \times 7.4$ kHz. To operate a MOT at this wavelength, it is thus mandatory to use a laser with absolute accuracy, linewidth and stability much smaller than this value. Our approach is to stabilize the master laser on a high-finesse ultra-stable cavity for both frequency narrowing and short term stability. The accuracy is then provided by a calibration on a home-made heat-pipe spectroscopy cell filled with strontium. The requirements on the clock transition at 698nm are even more drastic, as the theoretical linewidth of the fermionic transition equals 1 mHz. Even if this limit is beyond the

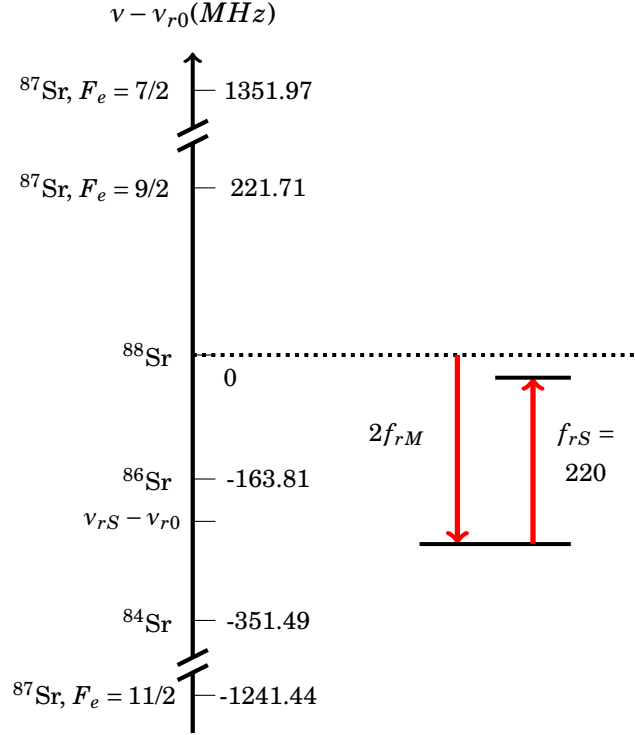


Figure 2.7: Frequency diagram for the laser system at 689 nm. The vertical axis represents the optical frequencies referenced to the intercombination line of ^{88}Sr . The AOM RF frequencies f_i are given in MHz. Transitions for the other isotopes are also given on the frequency axis. The ^{87}Sr transitions from the ground state $|(5s^2)^1S_0, F_g = 9/2\rangle$ to the excited states $|(5s5p)^1P_1, F_e\rangle$ are referenced by hyperfine quantum number F_e .

reach of our current setup, we measure the clock laser linewidth, which gives an estimation of the expected Fourier limited resolution in future clock experiments.

2.2.2.1 High-finesse ultra-stable cavity

Cavity design : The reference cavity is a commercial Fabry-Pérot from Stable Laser Systems¹² shown in figure 2.8(a). It provides a frequency etalon with equally spaced TEM_{00} modes separated by a *Free Spectral Range* (FSR) $\nu_{FSR} = c/(2L) = 1.50 \text{ GHz}$. Any variations of the cavity length L is thus imprinted on the frequency stability of this etalon. In order to minimize these fluctuations, the design of the ultra-stable cavity is based on mirrors optically contacted onto an *Ultra Low Expansion Glass* (ULE) support. The ULE piece is shaped in a so called *notched* manner, combining Airy points which minimize the bending of the edges and Bessel points which ensure a maximum length of the cavity. Its has a hollow core geometry between the mirrors. The material also possesses an expansion coefficient $\alpha(T)$ which depends on the temperature. Relative cavity length variations thus follow the equation

¹²<http://www.stablelasers.com/>

$$(2.4) \quad \frac{\delta L}{L} = \alpha(T)\delta T + \frac{1}{2}\alpha'(T)\delta T^2 + O(\delta T^3).$$

In the vicinity of the critical temperature, given by $T_c = 30(1)^\circ\text{C}$ for this particular cavity, the first order coefficient of the expansion vanishes. Quadratic deviations are still present at a typical level of $\alpha'(T_c) = 1.7 \times 10^{-9} \text{K}^{-2}$ [126]. Thermoelectric Peltier modules inside the housing, driven by an external temperature controller allows, for stabilization at the 10^{-1} – 10^{-2}K level which corresponds to frequency drifts in the 10^{-1} – 10^{-3}Hz range, well below the required stability. Another layer of stability is ensured by a vacuum chamber surrounding the cavity. An 8Ls^{-1} ion pump connected to the CF16 flange of the housing allows us to reach a pressure below 10^{-6}mbar . These design choices allow a passive reduction of the frequency standard drifts. However, we still measure long term drifts measured with the atomic spectroscopy cell reference, as presented in 2.2.3.

Cavity finesse measurement : The Fabry-Pérot cavity is made of one planar mirror and a curved one with a radius of curvature R_m . The relevant parameters of the high-finesse cavity are summarized in table 2.3. The finesse has been measured with a ring-down method. This technique consists in coupling an optical beam to a TEM_{00} mode of the cavity and suddenly switching off the input intensity [127]. We model the mirrors as having equal intensity reflection R , transmission T and loss \mathcal{L} coefficients holding the conservation rule $R + T + \mathcal{L} = 1$. Assuming that the intracavity power P_c is reduced by a factor R^2 after each cavity round trip, this quantity satisfies the following differential equation

$$(2.5) \quad \frac{dP_c}{dt} + \gamma_c P_c(t) = 0,$$

where $\gamma_c = (1 - R^2)\nu_{FSR}$ corresponds to the exponential damping rate of the intracavity power. A measurement of that parameter performed with a 689nm optical beam from the master laser and recorded on a photodiode is presented in figure 2.8(b), with the associated exponential fit. The cavity mirrors reflectivity and finesse, deduced from γ_c , are summarized in table 2.3.

2.2.2.2 Pound-Drever-Hall stabilization

The frequency stabilization of the red master laser at 689nm, the clock laser at 698nm and the future dipole trap at 813nm are realized by implementing the *Pound-Drever-Hall* (PDH) locking scheme with the ultra-stable cavity [128]. This procedure is used to both stabilize the lasers frequencies and reduce their linewidths. Unfortunately, the cavity frequency is not completely stable but subject to drifts which need to be compensated for. Moreover, the maximum frequency separation between one longitudinal mode of the cavity and an eventual atomic transition is equal to $\nu_{FSR}/2 = 750\text{MHz}$, beyond the reach of usual AOMs. In order to deal with these two

Parameter	Expression	Value
Cavity length	L	100 mm
Mirror radius of curvature	R_m	50 cm
Mirror reflectivity	$1 - R$	95 ppm
Cavity finesse	$\mathcal{F} = \pi\sqrt{R}/(1 - R)$	33000
FSR	$\nu_{FSR} = c/(2L)$	1.50 GHz
FWHM	$\delta\nu_c = \nu_{FSR}/\mathcal{F}$	45.6 kHz

Table 2.3: High-finesse Fabry-Pérot cavity characteristics.

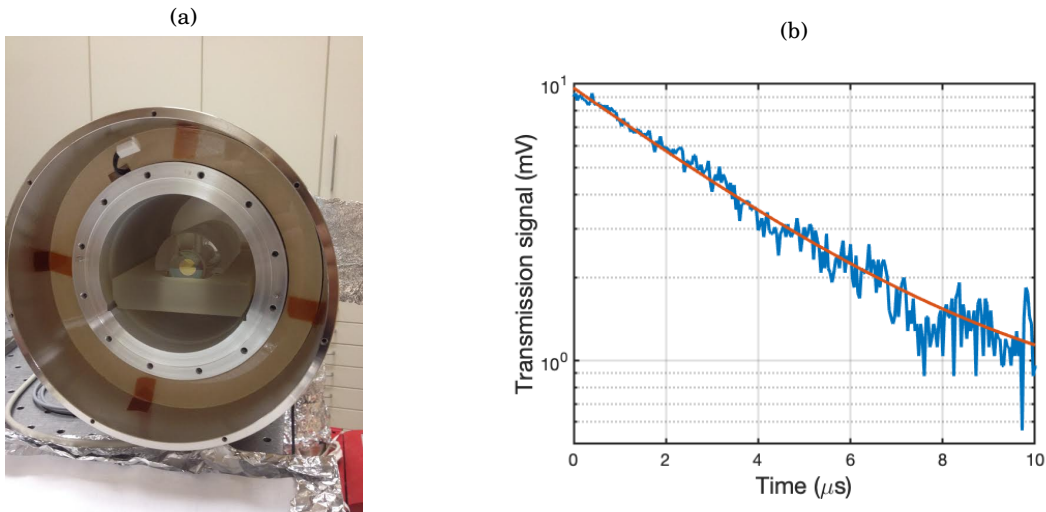


Figure 2.8: (a) Picture of the notched *Stable Laser Systems* cavity with opened vacuum chamber and thermal housing. (b) Cavity ring-down in logarithmic scale with a 689 nm laser beam of power $P_{in} = 60 \mu\text{W}$.

issues, one part of each laser is successively sent through a free space resonant EOM¹³ driven by a signal at frequency f_1 , and a fibred EOM¹⁴ at frequency f_2 , as pictured in figure 2.6. While f_1 is kept constant to implement the PDH scheme for each laser, frequency tuning of f_2 allows to tune the laser frequency and compensate for the cavity drifts, measured by means of the absolute frequency reference described in 2.2.3. In the following paragraphs, we detail this double frequency PDH scheme.

EOM principle : The EOM working principle is based on the linear electro-optic (or Pockels) effect in noncentrosymmetric crystals [129]. Applying an alternating electric field $V = V_m \sin \omega_m t$ to such crystal induces a modulation of its refractive index with different intensities along the principal axes. An optical beam polarized along one of these axes experience a phase shift at the

¹³Model PM7-VIS from QUBIG. See <https://www.qubig.com/>.

¹⁴Model PM635 from Jenoptik. See <https://www.jenoptik.com/>.

same frequency with a modulation depth $\Delta\Phi$ given by

$$(2.6) \quad \Delta\Phi = \pi \frac{V_m}{V_\pi},$$

where V_π is a characteristic property of the crystal defined as the electric field needed to induce a phase shift of π . The complex optical electric field of a laser at central frequency ω after the two EOMs and incoming on the cavity can thus be written

$$(2.7) \quad \mathbf{E}_{in}(t) = \mathbf{E}_0 e^{i\omega t} e^{i\Delta\Phi_1 \sin \omega_1 t} e^{i\Delta\Phi_2 \sin \omega_2 t}.$$

The beam is then reflected onto the cavity, which is characterized by the optical transfer function $F(\omega)$ expressed as [130]

$$(2.8) \quad F(\omega) = -\sqrt{R} + \frac{\sqrt{R} T e^{2i\pi \frac{\omega}{\omega_{FSR}}}}{1 - R e^{2i\pi \frac{\omega}{\omega_{FSR}}}}.$$

Making use of the Jacobi-Anger expansion, we can express the electric field reflected by the cavity as

$$(2.9) \quad \mathbf{E}_r(t) = \mathbf{E}_0 \sum_{n,m=-\infty}^{\infty} i^{n+m} J_n(\Delta\Phi_1) J_m(\Delta\Phi_2) F(\Omega_{n,m}) e^{i\Omega_{n,m} t},$$

with J_n the Bessel function of order n and $\Omega_{n,m} = \omega + n\omega_1 + m\omega_2$. In order to pick up the reflected beam of the cavity on a photodiode, a 30dB optical isolator is placed at its input port, as shown in figure 2.6. The resulting electronic signal is then proportional to reflected beam intensity $I_r(t) = \epsilon_0 c |\mathbf{E}_r(t)|^2/2$. In our setup, we drive the free space EOMs at a fixed resonant frequency $f_{r1} = 20.2\text{MHz}$ for the red master laser, $f_{c1} = 18.3\text{MHz}$ for the clock laser and the trap laser will be driven at $f_{t1} = 22.4\text{MHz}$. These three frequencies are intentionally separated to avoid cross talks between the different error signals. The signals in figure 2.9 shows the ultra-stable cavity transmission and reflection of the clock laser with a modulation at f_{c1} .

At this stage of the experiment, only the red master fibred EOM is used as no clock experiment or atom trapping has been realized yet. This EOM is driven by an analog signal generator¹⁵ at a frequency $f_{r2} \simeq 860\text{MHz}$, generating sidebands at $\omega_{rM} \pm m\omega_{r2}$, where ω_{rM} corresponds to the red master frequency. We then bring the $m = 1$ sideband on resonance with one peak of the cavity. This scheme is used as a frequency tuner for the master laser to the ν_{0r} atomic resonance $|(5s^2)^1P_0\rangle \rightarrow |(5s5p)^3P_1\rangle$ of ^{88}Sr with a procedure detailed in section 2.2.3. The modulation depth for this EOM is tuned at the zeroth order Bessel function first zero corresponding to $\Delta\Phi_{r2} = 2.40$, also close to the first order Bessel function maximum at 1.84. Similar schemes will be used for the clock and trap lasers in order to stabilize their frequencies while keeping tunability with fibred EOMs at the same time.

¹⁵Model E8257D from Keysight. See <https://www.keysight.com/>.

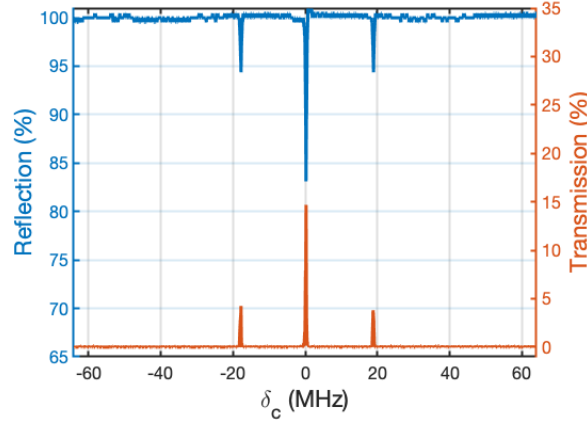


Figure 2.9: Cavity transmission and reflection for a laser beam of power $P_{in} = 160 \mu\text{W}$ at 698 nm as a function of the cavity detuning δ_c .

PDH error signal : In order to produce the PDH error signal ϵ_{PDH} , the photodiode signal is mixed with a *Local Oscillator* (LO) at frequency f_1 and phase ϕ . The product is then low-pass filtered with a cutting frequency $f_c \ll f_1$. In the expansion of $|\mathbf{E}_r(t)|^2$, only the terms oscillating at $\pm\omega_1 t$ are thus non zero. Up to a constant factor including photodiode and other electronic gains that we encapsulate in a term G , the error signal writes down

$$(2.10) \quad \epsilon_{PDH} = G \times \frac{1}{2} \epsilon_0 c |\mathbf{E}_0|^2 \sum_{n,m=-\infty}^{\infty} J_n(\Delta\Phi_1) J_{n-1}(\Delta\Phi_1) J_m^2(\Delta\Phi_2) \times \\ \left[\sin \Phi \left(\Re \{F(\Omega_{n,m})\} \Re \{\bar{F}(\Omega_{n-1,m})\} - \Im \{F(\Omega_{n,m})\} \Im \{\bar{F}(\Omega_{n-1,m})\} \right) \right. \\ \left. - \cos \Phi \left(\Re \{F(\Omega_{n,m})\} \Im \{\bar{F}(\Omega_{n-1,m})\} + \Im \{F(\Omega_{n,m})\} \Re \{\bar{F}(\Omega_{n-1,m})\} \right) \right],$$

with \Re (\Im) standing for real (imaginary) part and \bar{F} corresponding to the complex conjugate of F .

The error signals of the red master laser at 689 nm and the clock laser at 698 nm as well as fits according to equation 2.10 are presented in figure 2.10(a) and 2.10(b). These signals are linear in the cavity resonance region, and can thus be used to compensate for frequency shifts in a locking scheme. Even if the two curves were recorded with the same incident powers towards the cavity, the dichroic mirror combining the two laser beams only transmits 50% of the 698 nm light. After being transmitted twice through the mirror, we end up with a factor of 4 between the two signals amplitudes. These error signals are fed into PID regulators¹⁶ for laser stabilization. The fast part of the retroactions are applied to the laser currents and the slow one to the extended cavities piezo electric actuators.

¹⁶Model D2-125 Laser Servo from Vescent. See <https://www.vescent.com/>.

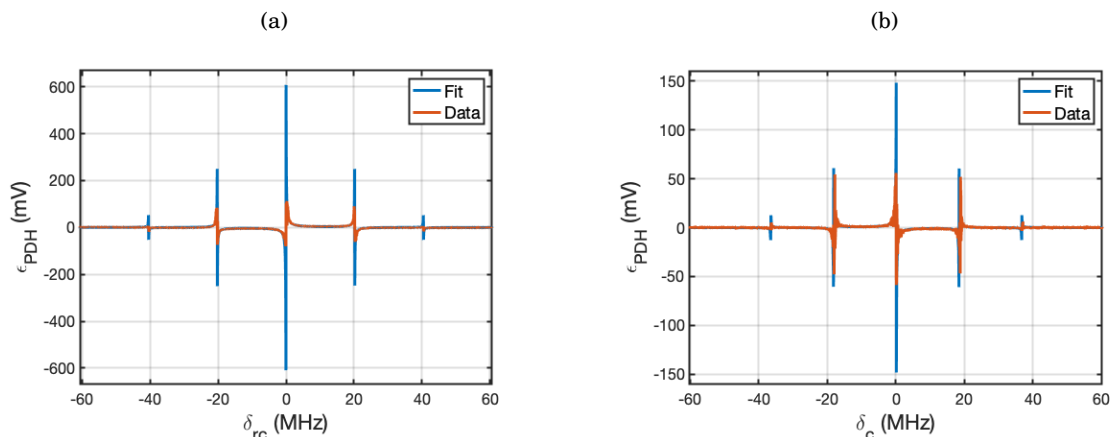


Figure 2.10: (a) Pound-Drever-Hall error signal of the red master laser at 689nm with a 300μW beam as a function of the cavity detuning $\delta_{rc} = \nu_{rM} - N\nu_{FSR}$, with $N \in \mathbb{N}$. (b) Error signal of the clock laser at 698nm with the same optical power before the dichroic mirror as a function of cavity the detuning $\delta_c = \nu_{ck} - M\nu_{FSR}$.

2.2.2.3 Laser linewidth estimation

As previously described in paragraph 2.1.1.2, a first estimation of the linewidth of a laser can be done by dividing the PDH error signal voltage rms by its slope at cavity resonance. The result is described by equation 2.2. However, it is possible to obtain more information by computing the *Power Spectral Density* (PSD) of the error signal. According to the Wiener-Khintchine theorem, a temporal signal ϵ has a PSD defined by the Fourier transform of its autocorrelation function Γ_ϵ , relating the signal value at time t to the one at time $t + \tau$ through

$$(2.11) \quad \Gamma_\epsilon(\tau) = \langle \epsilon(t + \tau) \epsilon(t) \rangle.$$

The PSD S_V at Fourier frequency f is thus defined as

$$(2.12) \quad S_V(f) = \int_{-\infty}^{\infty} \Gamma_\epsilon(\tau) e^{-2i\pi f \tau} d\tau.$$

This function is giving information on the amount of electronical noise contained in the error signal at a given frequency, expressed in V^2/Hz . In order to define a criterion on the laser linewidth, S_V has to be converted into frequency noise. This operation is realized by dividing the electronical PSD by the slope \mathcal{D} in $V\text{Hz}^{-1}$ of the PDH signal at the cavity resonance. One obtains

$$(2.13) \quad S_\nu(f) = \frac{S_V(f)}{\mathcal{D}^2}$$

in Hz^2/Hz . The PDH error signal peaks being very narrow, a direct measurement of the slope at the central resonance is perturbed by short term laser frequency fluctuations. The signals in figures 2.10(a) and 2.10(b) are thus partially averaged and exhibit reduced peak heights. To overcome this issue, they are adjusted by the theoretical function from equation 2.10 in a region

excluding the peaks. The slope is then deduced from these adjustments.

An approach described by Di Domenico *et al.* [131] allows for *Full Width at Half Maximum* (FWHM) laser linewidth estimation by integrating the frequency PSD area lying above the so-called β -separation line defined as

$$(2.14) \quad \beta(f) = \frac{8\ln(2)}{\pi^2} f.$$

This line is interpreted as a separation between a region $S_v(f) > \beta(f)$ where the noise is contributing to the line shape of the laser, and a region $S_v(f) < \beta(f)$ where it only contributes to the wings of the profile. A first geometrical approximation of the linewidth is given by computing the PSD area A above the β -separation line defined as

$$(2.15) \quad A = \int_{1/T_0}^{\infty} H[S_v(f) - \beta(f)] S_v(f) df,$$

where T_0 is the measurement time and $H(x)$ the Heaviside step function. One can estimate the FWHM of the laser using the following formula

$$(2.16) \quad FWHM_A = \sqrt{8\ln(2)A}.$$

A more complex evaluation is also proposed in the paper, to encounter for flicker noise in the laser PSD [132]. This type of noise writes as a power law of the Fourier frequency $S_v(f) = af^{-\alpha}$, with $1 \leq \alpha \leq 2$. For $\alpha > 1$, the FWHM is estimated by the following formula

$$(2.17) \quad FWHM = f_m \frac{8\ln(2)}{\pi} \sqrt{\frac{(f_m T_0)^{\alpha-1} - 1}{\alpha - 1}},$$

where f_m corresponds to the frequency where the PSD crosses the β line. The PSD for both the red master and the clock lasers are measured with the error signals taken at the PID modules inputs. Two spectrum analysers¹⁷ are used for low and high Fourier frequency ranges. The results, associated with the β lines and flicker fits are presented in figures 2.11(a) and 2.11(b).

The FWHM measured for the different methods are listed in table 2.4. The results indicate a sufficiently narrow linewidth for red MOT operations as it is small compared to the natural linewidth $\Gamma_r = 2\pi \times 7.4$ kHz. Concerning clock operations, a linewidth of 200 Hz limits the coherence time for Rabi or Ramsey oscillations to 5 ms. We observe a noise reduction of 4 orders of magnitude at frequencies in the 10^2 Hz range for the closed loop signals, inducing a linewidth reduction by a factor of 25 for the clock laser and 50 for the red master laser compared to free running operations. The removed noise is rejected at higher frequencies, with a noise peak around 1.2 MHz. As this rejection is appearing at comparable frequencies for the two different systems,

¹⁷Model EXA N90110A from Keysight Technologies for frequencies higher than 20 kHz and SRS760 FFT from Stanford Research Systems for lower frequencies. See <https://www.keysight.com/> and <https://www.thinksrs.com/>.

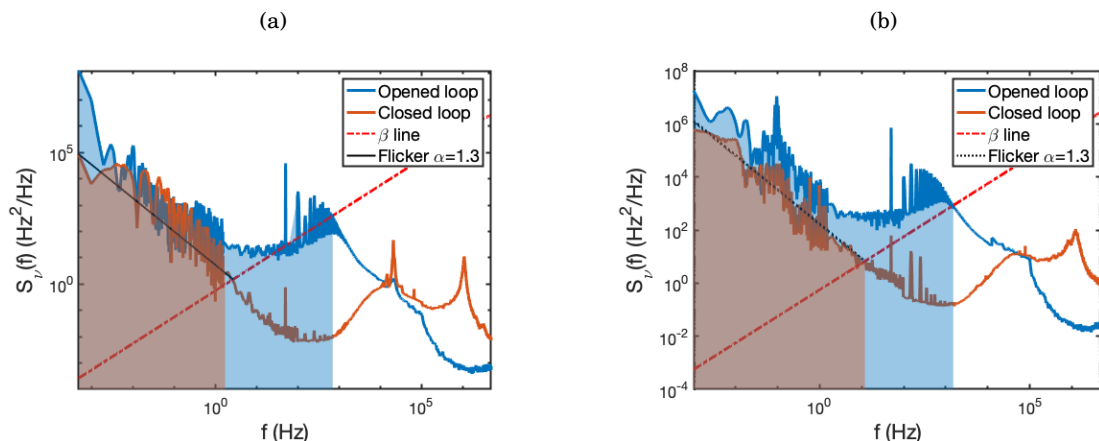


Figure 2.11: Power Spectral Density of the opened loop (blue) and closed loop (orange) error signals of the (a) red master laser at 689nm and (b) clock laser at 698nm. The β -separation lines depicted in red define the shaded areas that contributes to the laser linewidths. The black lines are flicker model fits in the $f \leq f_m$ region.

Laser	Opened loop area	Closed loop area	Closed loop flicker
Master 689nm	1.48 kHz	63.8 Hz	27.5 Hz
Clock 698nm	4.63 kHz	209 Hz	167 Hz

Table 2.4: FWHM laser estimation for red master and clock lasers.

the lock is most likely limited by the common PID laser servo rather than the laser electronic circuits coming from two different companies. The very low frequency part of the PSD contains the laser central peak optical power.

2.2.3 Absolute frequency calibration with the heat-pipe spectroscopy cell

Fabry-Pérot cavities are a powerful tool for laser frequency stabilization. As shown in the previous paragraph, the high-finesse cavity allows for linewidth reduction of the red master laser to approximately 30Hz, as well as short-term frequency stabilization. However, in the long-term range, such cavities present frequency drifts due to ongoing crystallization of the mirrors glass phases [133]. In order to measure and compensate for these drifts, we implemented a saturated absorption scheme based on a home-made spectroscopy cell. This setup also serves as an absolute frequency reference for the strontium red transition.

2.2.3.1 Home-made heat-pipe spectroscopy cell

According to Beer-Lambert's law, a probe beam on resonance with a two-level atomic medium of density n , along a path L , is exponentially damped by a factor called the *Optical Depth* (OD). This parameter is expressed as

$$(2.18) \quad OD = n(T)\sigma_0 L,$$

where σ_0 corresponds to the atomic cross-section and T to the medium temperature. The design of our home-made spectroscopy cell is thus based on a heat-pipe configuration, as shown in figure 2.12. This elongated geometry allows to obtain an 80cm long interaction region between the probe laser and a vapour of strontium. This vapour is created by heating a metallic strontium sample located in the reservoir part of a cross-shaped CF16 tube visible on the *Computer-Aided Design* (CAD) in figure 2.12(a). A flange facing the reservoir allows to fill the cell with about 2g at maximum. As metallic strontium reacts with air to form strontium oxide, this procedure has to be realized in a tent filled with argon. The pipe is terminated on each side by CF16 viewports soldered with an angle in order to avoid etalon effects inside the cell. Two other flanges near the extremities of the pipe allow for pressure monitoring with a gauge¹⁸ and connection to a pumping system. The cell is surrounded by a heating wire on its external part of the pipe, rising the temperature up to 900°C. A 10cm thick layer of SuperWool isolating ceramic fiber covers the heating wire for thermal isolation to the environment.

A well-known issue with strontium vapours is that it coats optical surfaces, reducing drastically the cell transmission [134]. To avoid this problem, we apply two strategies. First, we enrol the heating wire mainly around the central part of the tube, as shown in figure 2.12(b). This induces a temperature gradient along the pipe axis with cold parts near the viewports. Atomic re-emission from the inner surface is thus drastically reduced on the pipe edges, reducing the adsorption on the windows. The second strategy consists in filling the pipe with a buffer gas. Its role is to induce collisions with strontium atoms, thus reducing their mean free path. The drawback of this technique lies in the fact that buffer gases induce transition pressure-broadening and line-shifting. It has been measured for several gases in the case of strontium on the $|(5s^2)^1S_0\rangle \rightarrow |(5s5p)^3P_1\rangle$ transition [135]. When considering line modifications as well as buffer gas price and availability, argon appears to be a reasonable choice. It induces the lowest pressure-broadening among the considered gases in the study (helium, neon, krypton and xenon) with a value of $3.68(5)\text{MHzmbar}^{-1}$. Line-shifting is also fairly small with a shift of $-1.09(3)\text{MHzmbar}^{-1}$.

The argon filling procedure started with a clean-up and a bake-out of the pipe at 200°C in its center and 40°C at the edges due to the viewports limitations. It was then filled with strontium through the flange, under an argon atmosphere to avoid strontium oxide formation. An amount

¹⁸Model 275i from Kurt J. Lesker. See <https://www.lesker.com/>.

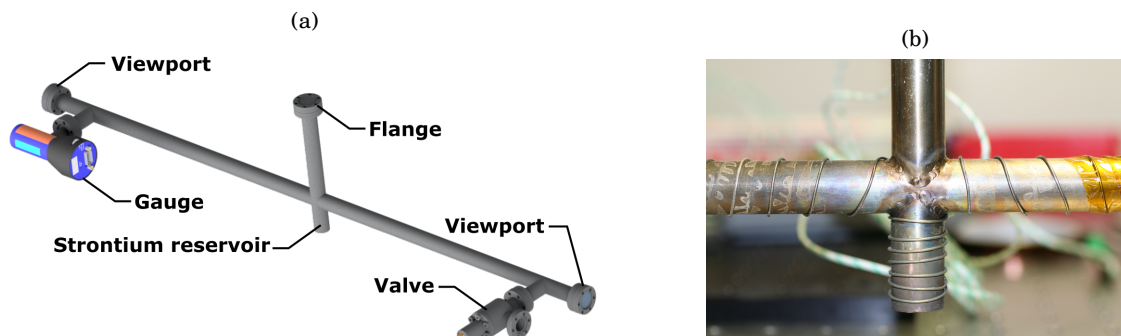


Figure 2.12: (a) CAD of the heat-pipe spectroscopy cell. (b) Picture of the central part of the cell with the heating wire wrapped around it. The thermocouple fixed to the strontium reservoir is also visible as a green wire.

of 2.7×10^{-3} mbar of argon was then introduced into the pipe, leading to a 689 nm line-shift of -2.94 kHz and a broadening of 9.94 kHz. At that time, the valve was closed to seal the cell and remove the turbo pump. When increasing the temperature for the first time to 400°C , the pressure rose to 256×10^{-3} mbar, probably due to outgassing. Surprisingly, after going back to room temperature and increasing a second time the temperature to 470°C , the pressure reached the low level of 3.1×10^{-3} mbar. This same value is now reached in day-to-day operations. This experience can be explained by the fact that strontium acts as an efficient getter, as reported in [136].

2.2.3.2 Absolute frequency calibration at 689 nm

The heat-pipe spectroscopy cell described in the previous paragraph is used to perform saturated absorption spectroscopy in order to measure the ^{88}Sr resonance at 689 nm. We typically operate the pipe at $T = 755^\circ\text{C}$ to obtain a significant signal. An optical beam coming from the 689 nm laser and phase modulated by a fibred EOM at $f_{rm} = 600$ kHz is sent through the pipe, retro-reflected and collected on a photodiode to act as a pump-probe system for saturated absorption. This beam has a waist $w_0 = 4.4$ mm and an optical power $P_0 = 950$ μW for sufficient signal on the photodiode, leading to a saturation parameter $s_0 = 1040$. The linewidth of the transition is thus power broadened to $\Gamma_r \sqrt{1 + s_0} = 2\pi \times 240$ kHz, larger than the pressure-broadening due to argon. To obtain an error signal, the photodiode signal is demodulated at f_{rm} and low-pass filtered. The resulting absorption spectrum and error signals are presented in figures 2.2.3.2 and 2.13(b), respectively.

The two visible resonances on the error signal in figure 2.2.3.2 correspond to the ^{88}Sr and ^{86}Sr transitions. In order to measure precisely the ^{88}Sr resonance position, this signal is displayed on an oscilloscope which data can be retrieved on the main experiment controlling computer with a Python software. The absolute frequency correction procedure is then implemented by locking the

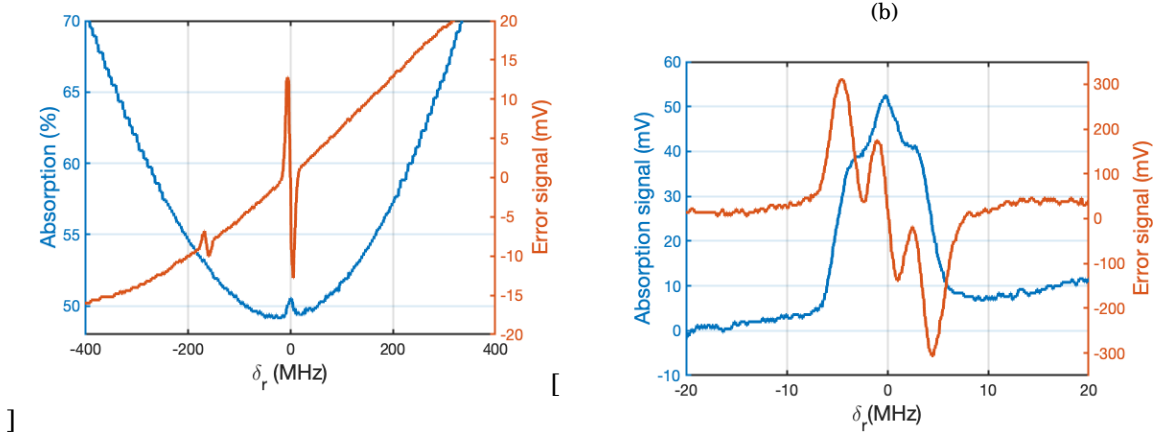


Figure 2.13: (a) Saturated absorption and error signals at 689nm in the heat-pipe spectroscopy cell with a modulation frequency $f_{rm} = 6.0\text{MHz}$. The frequency axis is referenced to the ^{88}Sr resonance. (b) ^{88}Sr Lamb dip and error signal with $f_{rm} = 600\text{kHz}$. The heat-pipe is operated at 700°C .

master laser on the cavity with the PDH scheme described previously. The modulation frequency f_{r2} produced by an ethernet controlled RF generator is then scanned between 850 and 870 MHz with the same Python code, as pictured in figure 2.14(a). In this frequency range, the master laser frequency is brought on resonance with the three transitions between the ground state $|5s^2)^1S_0\rangle$ and the excited Zeeman states $|5s5p)^3P_{1,m_J} \in [-1, 0, 1]\rangle$ of ^{88}Sr . The three excited states are resolved due to the presence of a constant magnetic field produced by the heating wire itself, as shown in figure 2.13(b). Indeed, this single pass wire is wrapped in a helicoidal way around the central part of the cell, thus creating an horizontal magnetic field in that region. The wire also covers the strontium reservoir, ending up with a vertical field in the central part. The pump and probe beams are polarized horizontally and vertically, respectively. Pumping is thus realized on the σ_+ and σ_- transitions with equal weights, while the probe is addressing an equal superposition of σ_+ and σ_- in the horizontal B field region and the π transition in the reservoir region.

In order to precisely determine the frequency f_{r2} which brings the red master laser on resonance with the $m_J = 0$ transition, the error signal is adjusted by the derivative $\frac{df(\delta)}{d\delta}$ of the theoretical atomic absorption profile of the three Zeeman transitions f given by

$$(2.19) \quad f(\delta_r) = \sum_{m_J=0,\pm 1} A_{m_J} \text{Voigt} \left(\delta_r + m_J \Delta_Z, \frac{\Gamma_r}{2\pi} \sqrt{1+s_0}, u \right),$$

which includes Voigt profiles of relative amplitudes A . These profiles are defined as the normalized convolution of a Lorentzian atomic lineshape of width Γ_r and a Gaussian velocity distribution profile of width $u = \sqrt{k_B T/m}$. A detailed derivation of this expression is given in appendix E. The amplitudes are set as $A_{+1} = A_{-1}$ and we measure $A_{\pm 1} = 0.77 A_0$. The detuning $\delta_r = \nu_{rM} - \nu_{r0}$ is

referenced to the π resonance and the Zeeman splitting δ_Z for the σ_+ transitions writes

$$(2.20) \quad \delta_Z = m_J g_J \frac{\mu_B}{h} B_{eff},$$

with $g_J = 3/2$ the Landé factor for this transition and B_e the effective magnetic field norm. We measure a splitting between the central and first peaks $\delta_Z = 3.64 \text{ MHz}$ corresponding to $B_e = 1.73 \text{ G}$. The transition broadening is $\sigma_D = 2.7 \text{ MHz}$, much larger than the power broadening probably due to second order Doppler effect and strontium-strontium collisions.

In figure 2.14(c), a measurement over 48 days of the fibred EOM frequency f_{r2} which brings the master laser locked onto the Fabry-Pérot cavity on resonance with the red transition is presented. This dataset acts as a direct measurement of the cavity drift, equal to $5.94(3) \text{ kHz day}^{-1}$. As this value remains smaller than the natural linewidth of the 689 nm transition, one calibration of the atom-cavity detuning per day is sufficient to operate the red MOT without loss of capture efficiency.

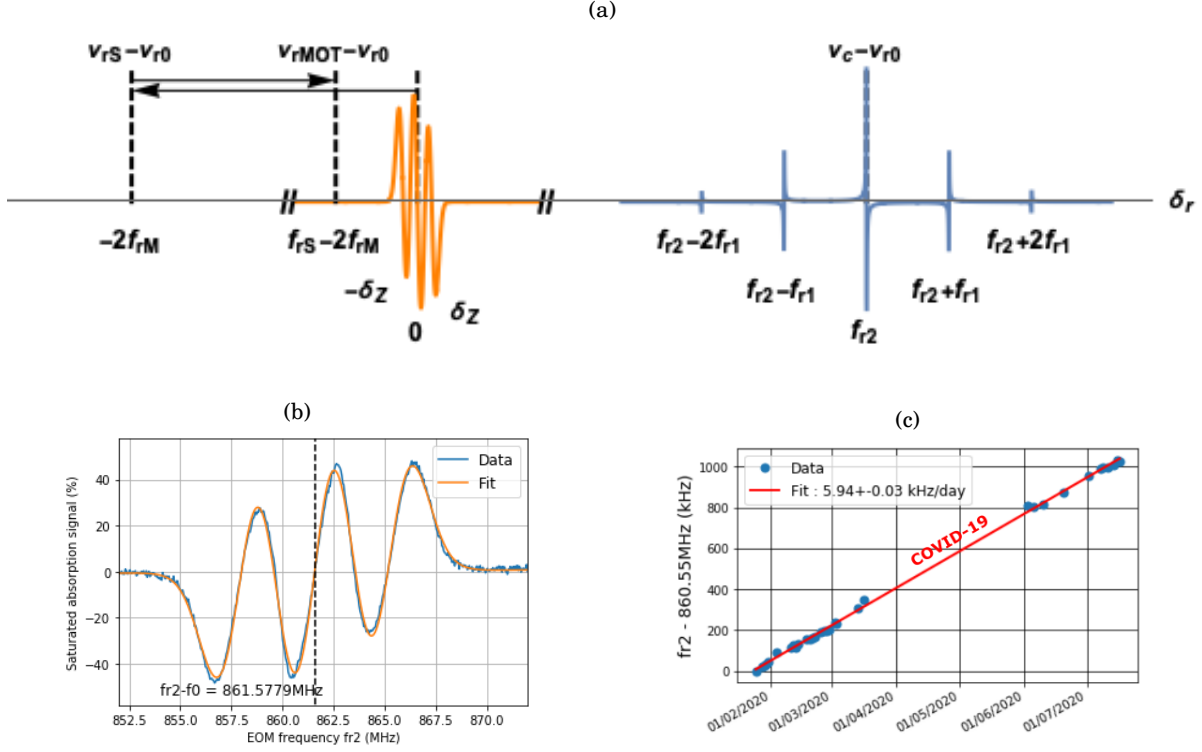


Figure 2.14: (a) Error signals and frequencies configurations for the laser system at 689nm. The frequency axis is referenced to the $|(5s^2)^1S_0\rangle \rightarrow |(5s5p)^3P_1, m_J = 0\rangle$ transition of ^{88}Sr at ν_{r0} such that $\delta_r = \nu_{rM} - \nu_{r0}$. The laser electric fields at frequencies ν_{rM} for the master laser, ν_{rS} for the slave, ν_{rMOT} for the red MOT and ν_c for the high-finesse cavity mode are represented as vertical dashed lines. The error signal centred on $\delta_r = f_{r2}$, in orange, corresponds to the PDH locking signal. The blue signal, centred on $\delta_r = 0$, is the saturated absorption error signal from the heat-pipe spectroscopy cell. (b) Typical data and fit for the saturated absorption error signal used as an absolute frequency reference. The data are represented in blue and the fit function from equation 2.19 in orange. (c) Cavity drift calibration for a 48 days measurement.

A COMPACT VACUUM SYSTEM

The preparation of cold atomic samples require reliable atomic sources. In the case of alkalis, relatively low melting points lying in the 30–180°C (for decreasing atomic mass from cesium to lithium) only requires the need for dispensers in order to load magneto-optical traps. For alkaline-earth atoms such as strontium, higher melting points within the 650–850°C range¹ complicate the use of such atomic sources. Common alkaline-earth sources are thus provided by effusive atomic beams. Inspired by a design developed in a collaboration between two teams at LENS in Italy and PTB in Germany [137], we developed a home-made strontium oven. Motivated by the simplification of the original design consisting in an array of micro capillaries, we developed an easy to manufacture single capillary oven. Moreover, concerned by the mechanical stability of the vacuum system, affected by undesired heating of its components, we aimed to reduce its electrical power consumption. The first section of this chapter is dedicated to this effusive source of strontium, associated with a description of the atomic collisional processes undergone in its reservoir. In the second section, our vacuum system built in the spirit of a collimated atomic beam for cold sample loading is described. Its compact design is motivated by the combination of the atomic slowing from the effusive beam and the MOT capture. A set of technical solutions implemented in the system in order to tackle the strontium peculiarities is also described. Finally, in a third and last section, the atomic beam properties are extracted from a series of two experiments. In the first one, the oven was placed in a simplified vacuum chamber and transverse spectroscopy on the blue transition was performed on the effusive source output. The second experiment consisted in both longitudinal and transverse spectroscopy on the same transition, performed on the collimated effusive beam of strontium in the main vacuum system.

¹Except for beryllium with a very high melting point at 1290°C.

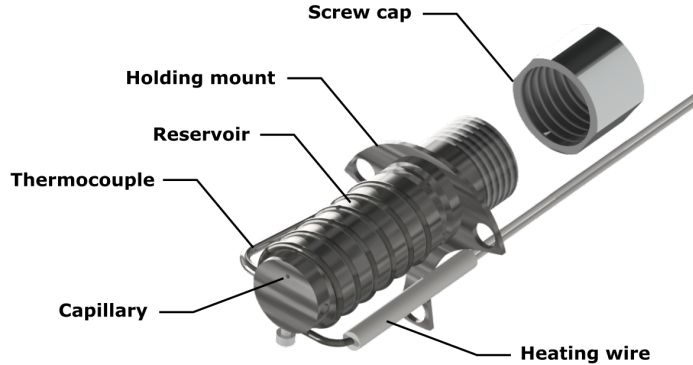


Figure 3.1: CAD of the home-made oven. The reservoir containing metallic strontium is surrounded by a heating wire and its temperature is measured with a thermocouple. A screw cap closes the reservoir from the back.

3.1 An effusive source of strontium

The first step in any cold atom experiment is the choice of an atomic source. In the majority of existing strontium experiments, this source is made of a reservoir drilled with one or several elongated holes referred to as micro capillaries [100, 119, 120, 138–145]. In this world of ovens, we can notice some exceptions as the one developed in the group of Kai Bongs in Birmingham that uses a strontium dispenser pierced by a slit and directed onto a 45° angled foil that deflects the atoms toward the main chamber [146]. In this section, we describe the design of a home-made oven with a single capillary manufactured by the mechanical workshop at LKB. Relying on the Knudsen theory of gas collisions, we present the different effusive beam regimes produced by such atomic sources.

3.1.1 Capillary design

In molecular effusive beams theory, it is a well known effect that an elongated hole in a gas reservoir collimates the output beam near the propagation axis. With this effect in mind, we designed a simple and efficient strontium oven inspired by the capillary architecture of the LENS-PTB collaboration [137]. Taking into consideration the fact that the diameter of the capillary should not be too small to avoid strontium blocking the exit, we built our oven as a stainless steel reservoir drilled on its edge with a $L = 5$ mm long hole of diameter $d = 0.8$ mm. A *Computer-Aided Design* (CAD) of the oven assembly is presented in figure 3.1. Its temperature raising is ensured by a heating wire from ThermoExpert², fitted around the capsule in a spiral manner via a drilled slot. The inner double passage configuration of the wire avoids magnetic fields creation in the reservoir. The oven can be filled by the back with up to 2.5 g of metallic strontium and closed by a screw cap. To avoid clogging the capillary, the hotter part of the wire is placed on the drilled

²See <http://thermoexpert.com/mineral-insulated-heating-cables-single-core>.

surface side. A thermocouple sitting just below the capillary, inside the stainless steel, monitors the oven temperature. The reservoir is embraced by a three legged mount used to screw the oven to a custom CF40 sustaining flange described in 3.2.2.

3.1.2 Knudsen theory of collisions

This chapter being dedicated to the description of an effusive source of atomic strontium, it is important to derive the basic principles of atomic collisions in an effusive beam. For this purpose, we refer to the kinetic gas theory developed by Knudsen in 1935 [147]. The main parameter of this theory is the mean free path $\tilde{\lambda}$ corresponding to the distance an atom can travel without colliding with other particles. It is defined for a temperature T as

$$(3.1) \quad \tilde{\lambda}(T) = \frac{1}{\sqrt{2} \tilde{\sigma} n(T)},$$

where n is the gas density and $\tilde{\sigma}$ the molecular collisional cross-section. In the cases of ^{88}Sr and ^{86}Sr , intra-species elastic cross-sections of $\tilde{\sigma}_{88-88} = 3(1) \times 10^{-13} \text{cm}^2$ and $\tilde{\sigma}_{86-86} = 1.3(0.5) \times 10^{-10} \text{cm}^2$ have been measured by Sorrentino *et al.* [50]. The factor $\sqrt{2}$ in equation 3.1 originates from particles motion assuming a Maxwell-Boltzmann density of probability. We assume here that the density is following the ideal gas relation $n(T) = P(T)/k_B T$, where the vapour pressure of strontium P is given by Antoine's equation [148]

$$(3.2) \quad \log_{10} \left(\frac{P(T)}{\text{Pa}} \right) = 14.232 - \frac{8572}{T} - 1.1926 \log_{10}(T).$$

The vapour pressures of the alkali and alkaline-earth species as a function of the temperature are given in figure 3.2(a). The strontium mean free path calculated from its pressure is given in figure 3.2(b). Comparing this parameter to the diameter of the aperture $d = 2a$ defines the Knudsen number Kn expressed as

$$(3.3) \quad \text{Kn} = \frac{\tilde{\lambda}}{d}.$$

Depending on this ratio, three different regimes are defined. A non-exhaustive set of criteria for distinguishing these regimes are resumed in table 3.1. The physical properties for the different situations are defined as follows.

TRANSPARENT MODE : The regime corresponding to the smallest values of $\tilde{\lambda}$ is referred to as *molecular flow* or *transparent mode*. Atoms or molecules in this regime only experience wall collisions.

OPAQUE MODE : For intermediate values of the mean free path, a *transitional regime* or *opaque mode* corresponds to non-negligible contributions of both wall and atomic collisions.

Beijerinck & Vertser [149]		Livesey [150]	
Regime	Criterion	Regime	Criterion
<i>Transparent mode</i>	$\tilde{\lambda} > L$	<i>Molecular flow</i>	$Kn > 0.5$
<i>Opaque mode</i>	$a < \tilde{\lambda} < L$	<i>Transitional flow</i>	$0.01 < Kn < 0.5$
<i>Continuum flow</i>	$\tilde{\lambda} < a$	<i>Continuum flow</i>	$Kn < 0.01$

Table 3.1: Flow regimes criteria based on the capillary geometrical dimensions and the atomic mean free path.

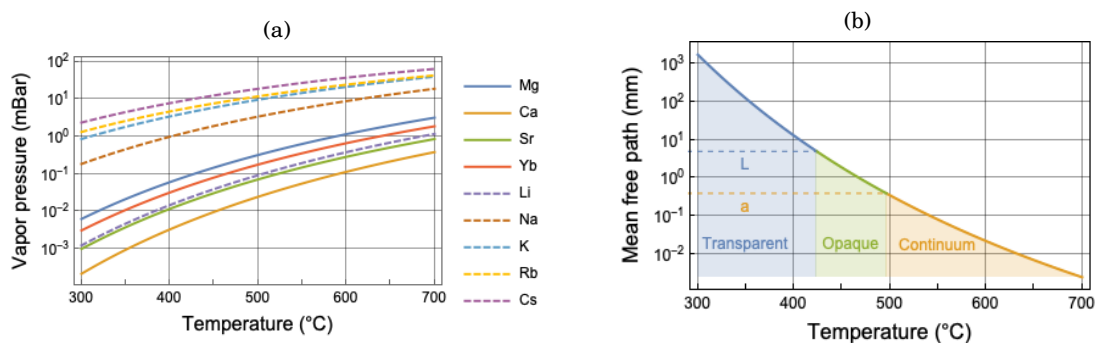


Figure 3.2: (a) Vapour pressures of alkali and alkaline-earth laser cooled atoms. (b) Mean free path of ⁸⁸Sr intra-species limited elastic collisions. Dashed lines correspond to $\tilde{\lambda} = L$ and $\tilde{\lambda} = a$ in blue and orange, respectively. These boundaries define three regimes for the atomic beam properties.

CONTINUUM FLOW : For the highest values of $\tilde{\lambda}$, inter particles collisions are dominant in a regime called *continuum flow*.

In the majority of experiments presented in this thesis, we operate the oven at 450°C, corresponding to a mean free path of 2.5mm which lies at the frontier between the transparent and opaque modes.

3.2 Vacuum system

Under ambient pressure and temperature conditions, the mean free path of air molecules is on the order of a few tens of nanometres. Dividing this path by the particles mean velocity, on the order of a few hundreds of meters per second, we simply estimate the average time between two-body collisions with the background gas to the nanosecond scale. It is thus clear that high vacuum conditions are required in order to obtain a few seconds lived cold atomic sample. In this section, we describe our vacuum apparatus used to reach the needed low pressure conditions. In addition, the system needs to tackle several technical difficulties associated with the strontium physico-chemical properties, described in the first paragraph. In the second paragraph, an analysis of the

electrical power consumption used to heat the oven in its dedicated part of the vacuum system is presented. As our system aims to produce a MOT inside a glass cell using the particles emitted by the oven, a differential pressure stage is necessary to isolate the oven section from the science cell section. This stage, also used as a collimator for the atomic beam, is described in the third paragraph. Finally, the science chamber including the glass cell is presented at the end of this section.

3.2.1 Strontium peculiarities motivated design

One of the main issues concerning strontium atoms lies in the fact that it can be adsorbed onto optical surfaces, thus reducing light transmission in the corresponding areas [134]. Several strategies have been implemented by different groups and companies to avoid strontium coating of surfaces. A first idea consists in deflecting the atomic beam to avoid direct impinging on optical surfaces. This strategy is implemented by the company *AOSense*³ which sells a complete cold atomic beam system based on an effusive source deflected by a 461 nm laser beam towards the main vacuum chamber. Several experimental groups use the same technique [113, 119].

In a set of experiments where the atomic beam is directly facing the science chamber, a chopping valve is used to parse the beam into packets used to load the MOT [100, 120, 138, 139, 141]. Sometimes used in combination with this idea, it is also possible to limit strontium pressure inside the science chamber by adding a differential pressure stage. Nevertheless, in such strategies, a slowing optical beam has to face the atomic beam in order to slow it down. To prevent coating at the crossing point between the optical surface, the laser and the atomic beam, it is possible to use heated sapphire windows to enhance strontium evaporation [143]. Another approach, detailed by Hukans *et al.* [134], consists in placing a SiO₂ coated mirror under vacuum facing the atomic beam. The team showed that strontium layers less than 1.5 µm thick onto such optical surfaces preserve the original mirror reflectance.

Regarding the different strategies, we based our design on a glass cell as a science chamber, directly facing the atomic beam coming from the oven. An overview of the vacuum system is presented in figure 3.3(a), and a cut in figure 3.3(b) shows the atomic beam trajectory. In order to ensure an ultra-high vacuum level at the MOT position, the oven chamber and the science cell are separated by a differential pressure stage tube of length $L_1 = 13$ mm and diameter $d_1 = 1.5$ mm. The role of this aperture is twofold as it also collimates the atomic beam towards the glass cell. The axis of this hole makes an angle $\theta_0 = 7^\circ$ with the horizontal plane of the experiment, as can be seen in figure 3.3(b). This geometry allows to collimate the atoms onto the bottom of an under vacuum dielectric coated mirror prism. This mirror is glued⁴ onto the underside face of the cell

³See <https://aosense.com/product/cold-atomic-beam-system/>.

⁴Glue form Epoxy Technology, model EPO-TEK H77T. See <https://www.epotek.com/site/>.

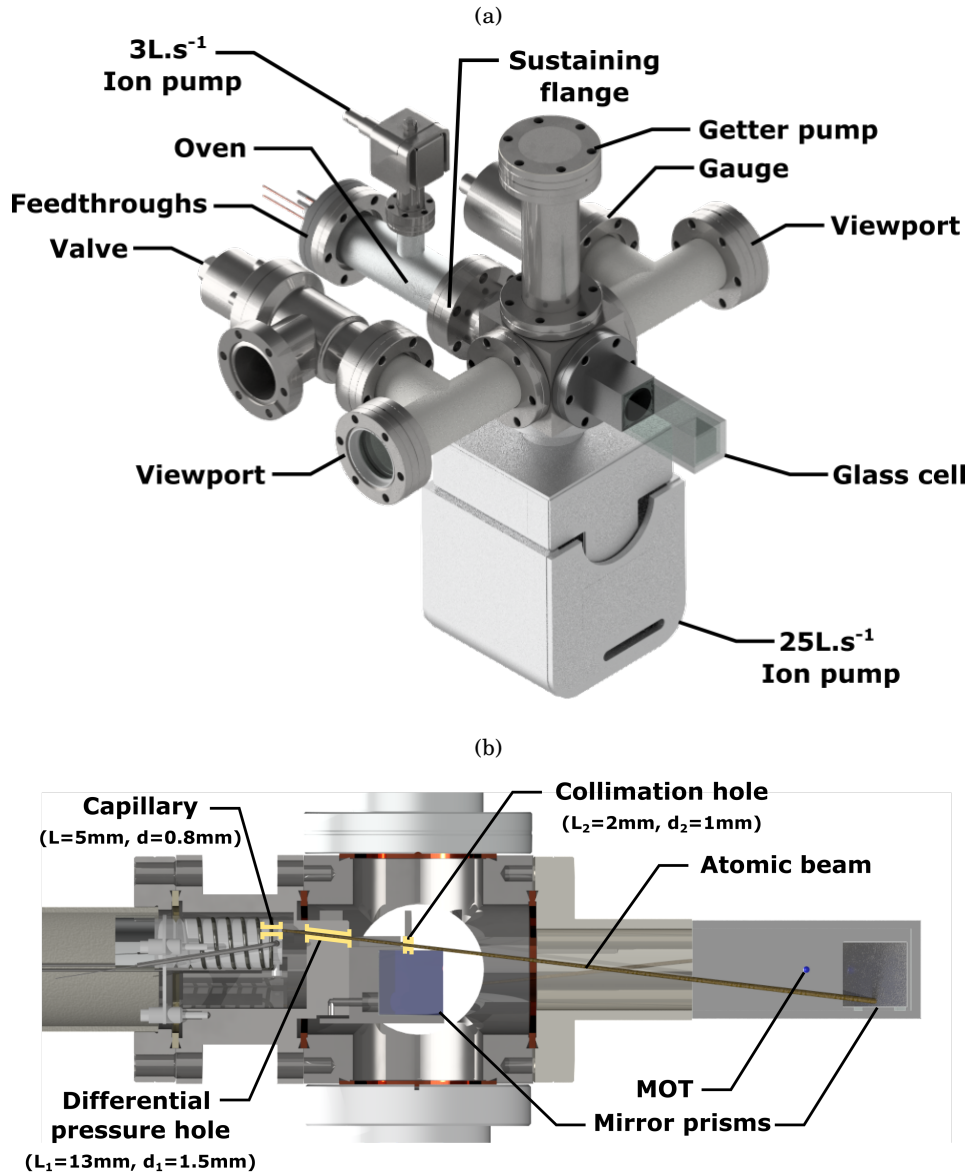


Figure 3.3: (a) CAD of the vacuum system apparatus. (b) Cut inside the vacuum system with selected components showing the atomic beam path and MOT position.

via three quartz glass plates⁵ of dimensions $2.5 \text{ mm} \times 2.5 \text{ mm} \times 1 \text{ mm}$. The other advantage of the atomic beam angle is to place it under the MOT region, avoiding direct hitting of fast atoms into the cold sample. This spatial selection is enhanced by a second aperture of length $L_2 = 2 \text{ mm}$ and diameter $d_2 = 1 \text{ mm}$ called the collimation hole. For manufacturing issues, this second tube is not tilted at the angle θ_0 but horizontal.

⁵Model FQP-25 from UGQ optics. See <https://www.uqgoptics.com/>.



Figure 3.4: Photography of a metallic strontium sample under vacuum (bottom) and open air strontium oxide (top).

The last but not the least of the strontium peculiarities, actually common to alkali and alkaline-earth elements, is to react with air to form strontium oxides. A photography of strontium protected by a glass tube under vacuum compared to oxidized strontium taken in our laboratory is shown in figure 3.4. The reaction leading the sample from a shiny metallic appearance to a white powder typically occurs within several tens of minutes when exposed to air. For this reason, oven filling and vacuum system assembling operations have to be realized under an argon atmosphere inside a dedicated plastic tent.

3.2.2 Oven section power consumption

Along with compacity, our design aims to minimize the oven heating electrical power consumption in order to increase the passive mechanical stability of the system. Power waists can appear through undesired vacuum component heating as well as thermal radiations by the oven itself. To tackle the first problem, a three-legged mount with minimal matter allows to fix the oven to a CF40 sustaining flange shown in figure 3.5. The junction is ensured by slotted screws and insulating ceramic spacers in order to minimize thermal contact with the flange and thus unwanted heating of the surrounding parts. For the radiation problem, one can reduce the stainless steel emissivity by polishing it. Also, the sustaining flange maintaining the oven partially emit one part of the black-body radiation back to the capsule.

A measurement of the oven temperature using the thermocouple for a given electrical power input is shown in figure 3.6. A complete heat numerical simulation of the system has been realized by Torben Pöpplau in his PhD thesis [61]. It includes thermal contributions from the

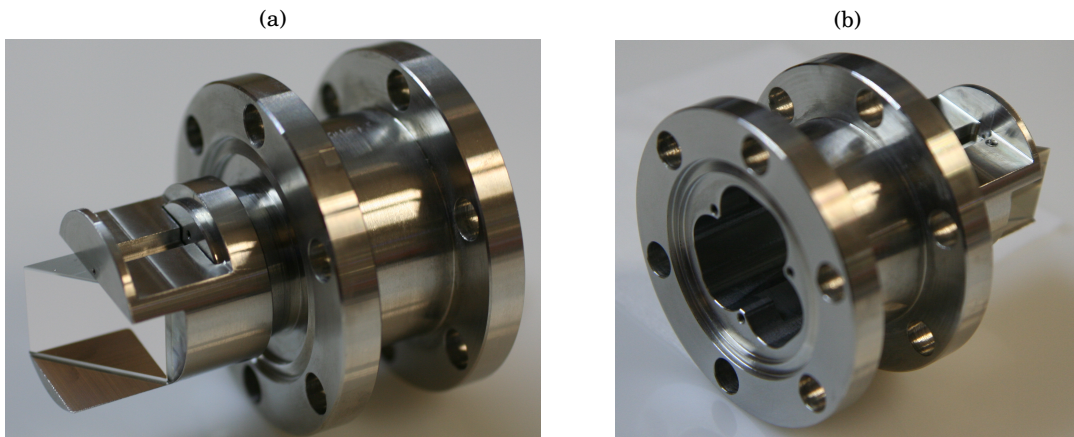


Figure 3.5: Photographies of the oven sustaining flange. (a) Frontside view showing the differential pressure and collimation holes. The flange also serves as a mount for one of the two right-angled mirror prisms. (b) Backside view showing the three tapped holes used to screw the oven three-legged mount.

oven capsule, heating wire, thermocouple, ceramic spacers and surrounding flange. I hereafter propose a simplified model based on a two step calculation predicting the oven temperature. In a first step, heating wire temperature elevation due to Joule's effect with an input electrical power $P = UI$ is considered. This elevation is mitigated by the heat conduction of the inner metallic roads inside the heating wire as well as thermal radiation according to Stefan's law. At equilibrium, the temperature T_w of the wire follows

$$(3.4) \quad P = \frac{1}{R}(T_w - T_0) + A\epsilon_w\sigma(T_w^4 - T_0^4),$$

where $R = \frac{L}{\pi r^2 k}$ is the thermal resistance of a wire of length L , radius r and thermal conductivity k in $\text{W m}^{-1} \text{K}^{-1}$. The first part of equation 3.4 corresponds to direct heating of the wire, while the second part corresponds to the radiation term with an external wire area A , the Stefan's constant $\sigma = 5.67 \times 10^{-8} \text{W/m}^2/\text{K}^4$, the wire emissivity ϵ_w and the ambient temperature $T_0 = 22^\circ\text{C}$.

In a second step, I consider that one third of the heating wire is in contact with the reservoir, thus heating the oven via thermal contacting. The contact resistance $R_c = \frac{3L}{Ak_c}$ depends on the effective thermal conductivity k_c at the interface which writes down [151]

$$(3.5) \quad k_c = \frac{2kk_s}{k + k_s},$$

with k_s being the stainless steel thermal conductivity. Considering thermal radiations as in equation 3.4, the oven temperature T_{ov} can be written as

$$(3.6) \quad \frac{1}{R_c}(T_{ov} - T_w) = A_{ov}\epsilon_{ov}\sigma(T_{ov}^4 - T_0^4).$$

The result of this simple model is presented in figure 3.6, with the parameters summarized in table 3.2. Despite omitting several effects such as thermal exchanges between the parts, losses

Component	A (mm ²)	L (mm)	r (mm)	k (Wm ⁻¹ K ⁻¹)	ϵ
Heating wire	1000	200	0.5	391.1	0.6
Oven	3000	-	-	16-20 (50-480 °C)	0.08

Table 3.2: Heat transfer toy model parameters.

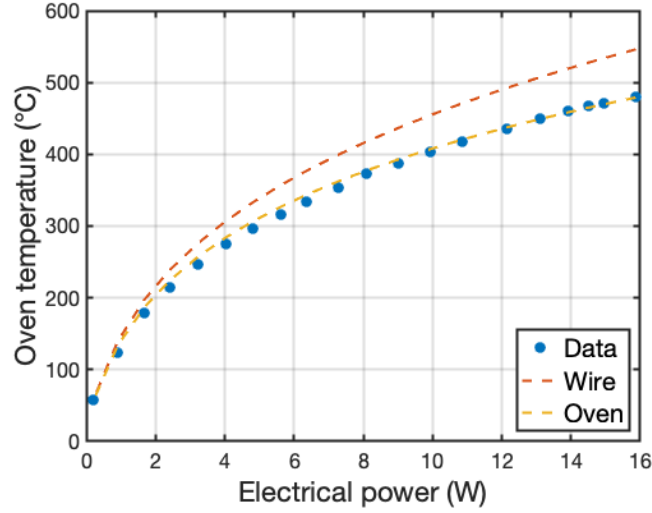


Figure 3.6: Electrical power consumption used to heat the oven inside the vacuum system. A simple analytical model predicts the temperatures of the wire (orange dashed line) and the reservoir (yellow dashed line).

through the ceramic holders and maintaining screws as well as re-emission from the flange, this toy model reproduces the experimental data with the effective emissivities of the two parts as the only adjustable parameters.

3.2.3 Differential pressure stage

As the oven emits strontium atoms in the first part of the vacuum system, visible in figure 3.3(a), the pressure rises when the reservoir is heated. The pressure being a limiting factor for the cold atomic sample lifetime, a differential pressure stage between the oven section and the glass cell allows to isolate the two parts. In the first section, a 3 Ls⁻¹ ion pump⁶ is used as a first pumping stage. In the science chamber, a bigger 25 Ls⁻¹ pump⁷ ensures a low pressure level and sustains the experiment at the same time. A differential pressure ΔP between the two parts is ensured by the $L_1 = 13$ mm long and $d_1 = 2a_1 = 1.5$ mm large tube. At room temperature, the main vacuum limiting gases such as H₂, CO₂ and air are in the molecular flow regime. The gas throughput Q

⁶Model Titan 3S from Gamma Vacuum. See <https://www.gammavacuum.com/>.

⁷Model Titan 25S from Gamma Vacuum.

can then be written as [150]

$$(3.7) \quad Q = c_1 \Delta P,$$

with c_1 the conductance of the differential pressure hole. This parameter writes down

$$(3.8) \quad c_1 = \frac{1}{4} \pi a_1^2 \bar{v} W_1$$

where $\bar{v} = \sqrt{8k_B T / \pi m}$ is the mean velocity of the Maxwell-Boltzmann distribution. The transmission probability for reaching the aperture output W_1 is given by Santeler's formula expressed as [152]

$$(3.9) \quad W_1 = \frac{8a_1/3L_1}{1 + 8a_1/3L_1}.$$

At room temperature, the conductances of H_2 , CO_2 and air equal 0.096, 0.020 and 0.025 L s^{-1} respectively.

The pressure in the two sections can be estimated knowing the outgassing rates of the different materials constituting the vacuum system and their respective surfaces. In the oven section, all the part are made of 316L austenitic stainless steel, which has a typical outgassing rate of $2 \times 10^{-12} \text{ mbar L cm}^{-2} \text{ s}^{-1}$ after one day of bakeout at 250°C . This section represents a total surface of 210 cm^2 . This part of the system being pumped by a 3 L s^{-1} ion pump, the theoretical pressure in this region lies in the 10^{-10} mbar range. After a bakeout of 48h at 150°C for the component containing glue such as the cell, and 250°C for the components less sensitive to the temperature, we experimentally measure a pressure $P_1 = 1 \times 10^{-7} \text{ mbar}$ at room temperature. This value rises up to $2 \times 10^{-7} \text{ mbar}$ with the oven operating at 450°C . These values are thus not limited by stainless steel components but rather by the oven reservoir itself and the thermocouple feedthroughs, surrounded by a polymer protecting layer presenting higher outgassing rates.

3.2.4 Science chamber

In the science section, the stainless steel parts cover an area of 770 cm^2 . The glass cell⁸ is a parallelepiped with outer dimensions $30 \text{ mm} \times 30 \text{ mm} \times 70 \text{ mm}$ and a thickness of 2.5 mm , as shown in figure 3.7. The cell material possesses an outgassing rate of $5 \times 10^{-12} \text{ mbar L cm}^{-2} \text{ s}^{-1}$. It is glued to a custom titanium flange⁹ with an inner surface of 38 cm^2 and an outgassing rate of $7 \times 10^{-12} \text{ mbar L cm}^{-2} \text{ s}^{-1}$. This metal has been chosen to match the glass cell coefficient of thermal expansion. The glue contains particles of size $50 \mu\text{m}$ in order to avoid leaks in the contact

⁸Uncoated SCHOTTTM type UK 5 glass cell from Hellma. See <https://www.hellma.com/en/laboratory-supplies/>.

⁹Titanium Grade 5, 6Al-4V.

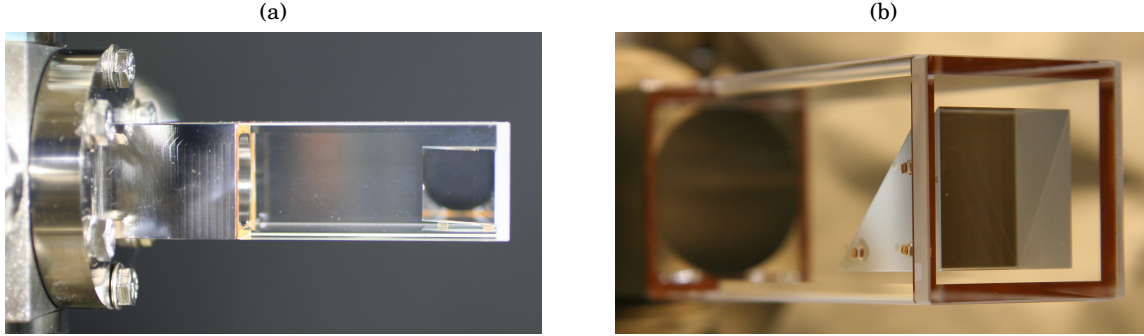


Figure 3.7: (a) Side view of the science glass cell glued on a titanium flange connected to the vacuum system. (b) Bottom view of the right-angled prism mirror glued onto the cell via three quartz plates.

area between the cell and the flange. An estimate of the pressure P_2 in the science section can be made by dividing the outgassing contributions from the different surfaces and the leak from the oven section through the differential pressure stage by the $S_{25} = 25 \text{ L s}^{-1}$ pumping speed of the main ion pump, resulting in

$$(3.10) \quad P_2 = \frac{cP_1 + Q_{\text{outgassing}}}{S_{25}} \simeq 2 \times 10^{-10} \text{ mbar}.$$

This estimation is consistent with the initial pressure in the science chamber of 1.3×10^{-10} mbar at room temperature and 5×10^{-10} mbar with the strontium oven switched on. After one year and half of oven operation, this level rose to 3×10^{-10} mbar at room temperature.

3.3 Atomic beam spectral properties

The capillary design of our home-made oven serves as a peaked effusive source of strontium atoms. In this section, we present the theoretical background predicting the effusive beam properties consisting in the angular atomic distribution, the velocity density of probability and the source flow rate. In a second time, we show how laser spectroscopy can probe these different properties and derive explicit formulas to predict both absorption and fluorescence spectra. This study will be compared to a set of experimental data taken for both the oven output distribution and the collimated beam in the vacuum chamber in section 3.4.

3.3.1 Effusive atomic beam flow

Starting in the 1920's, molecular beams were intensely studied in several contexts among masers, mass spectrometers, transverse spectroscopy and many others including fundamental studies such as magnetic moment determination [153, 154]. In 1960, Giordmaine & Wang derived a theory of effusive beam source properties [155]. In their model, they considered the beam angular

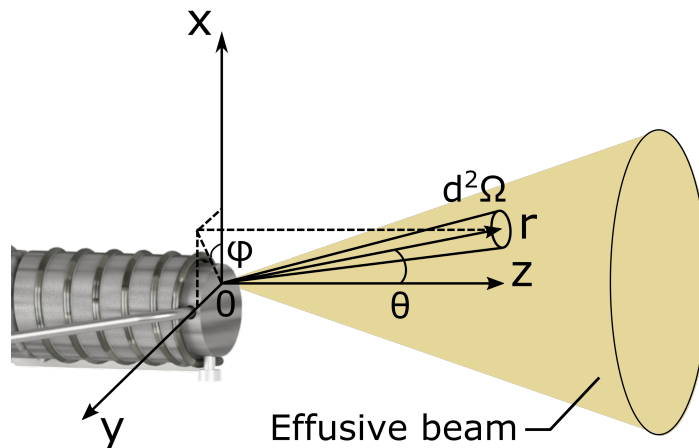


Figure 3.8: Scheme of the atomic effusive beam at the oven output. The Cartesian and spherical coordinates considered for the mathematical flow rate description are represented at $\vec{r} = \vec{0}$, corresponding to the capillary output.

and velocity distributions in different regimes, defined by the Knudsen number from equation 3.3. Depending on the flow types given in table 3.1, strontium atoms leaving the oven by the capillary would undergo different types of collisions. Depending on the temperature, our experiment lies either in the transparent mode, where atoms only undergo collisions with the walls of the capillary, or in the opaque mode where Sr-Sr collisions have to be taken into account. The physics at the very end of the tube is of particular relevance for the source properties. Indeed, collisions in this spatial section modify drastically the particles propagation at the oven output. In several studies during the 1970's, the beam angular properties in particular have been corrected by studying the scattering properties in this region. In this thesis, we will rely mostly on the work of Beijerinck & Vertser published in 1975 [149].

The effusive beam properties are characterized by the atomic flow rate, namely the number of atoms per second exiting the oven. A scheme of the effusive beam, associated with the laboratory frame of reference is represented in figure 3.8. By a simple symmetry argument, the atomic distribution should be isotropic with respect to the capillary axis. Moreover, one should find more atoms near this central axis than in peripheral regions. The mathematical description is then simplified by considering a spherical coordinate system with a polar angle θ between the propagation axis z and the observed region, as well as an azimuthal angle φ given by the position vector projection in the $\{x, y\}$ plane. The Cartesian and spherical coordinates are linked by the following equations

$$(3.11) \quad \begin{cases} x = r \sin \theta \cos \varphi \\ y = r \sin \theta \sin \varphi \\ z = r \cos \theta. \end{cases}$$

The number of atoms per unit of time in a solid angle $d^2\Omega$ centred on a direction θ with a velocity modulus $v \pm dv$ can be described by the following equation

$$(3.12) \quad \frac{d^4N}{dt} = J(\theta)F_\theta(v)d^2\Omega dv,$$

where $J(\theta)$ corresponds to the flow intensity in $\text{atoms s}^{-1} \text{sr}^{-1}$ and $F_\theta(v)$ to the normalized velocity distribution. According to [149], the angular dependency of the velocity distribution is small in the relevant parameter set concerning our experiment. We thus neglect it in the following description, labelling the velocity distribution as $F(v)$. The normalization conditions write as follows

$$(3.13) \quad \int_0^{+\infty} F(v)dv = 1$$

and

$$(3.14) \quad \iint_{2\pi} J(\theta)d^2\Omega = \dot{N},$$

where \dot{N} is the total flow rate of the source.

To understand the angular and velocity distribution shapes, let us recall the velocity distribution of an atomic vapour, given by the Maxwell-Boltzmann distribution M defined as [156]

$$(3.15) \quad M(v) = \frac{4}{\sqrt{\pi}\alpha^3}v^2 e^{-(\frac{v}{\alpha})^2},$$

with $\alpha = \sqrt{2k_B T/m}$ for a gas of molecular mass m at a temperature T . Placing such a gas into a reservoir which aperture length is considered infinitely small compared to its radius a and the atomic mean free path leads to a differential output flow rate given by [157]

$$(3.16) \quad \frac{d^4N}{dt} \Big|_{L \ll a \ll \bar{\lambda}} = \pi a^2 n v \cos\theta M(v) d^2\Omega dv,$$

with n the number density inside the reservoir. This simple case of a thin aperture, or diaphragm, allows to define the normalized velocity distribution F as

$$(3.17) \quad F(v) = \frac{2}{\alpha^4}v^3 e^{-(\frac{v}{\alpha})^2}.$$

One can also derive from equation 3.16 the angular distribution function of the diaphragm as a cosine. Taking into account the finite length L of the hole leads to a modification of this angular distribution, while the velocity density probability remains basically unaffected. In order to compare the diaphragm to a tube with a geometrical ratio L/a , the atomic intensity J is expressed by means of the angular distribution function f as follows

$$(3.18) \quad J(\theta) = \frac{\dot{N}}{\pi} \kappa^* f(\theta),$$

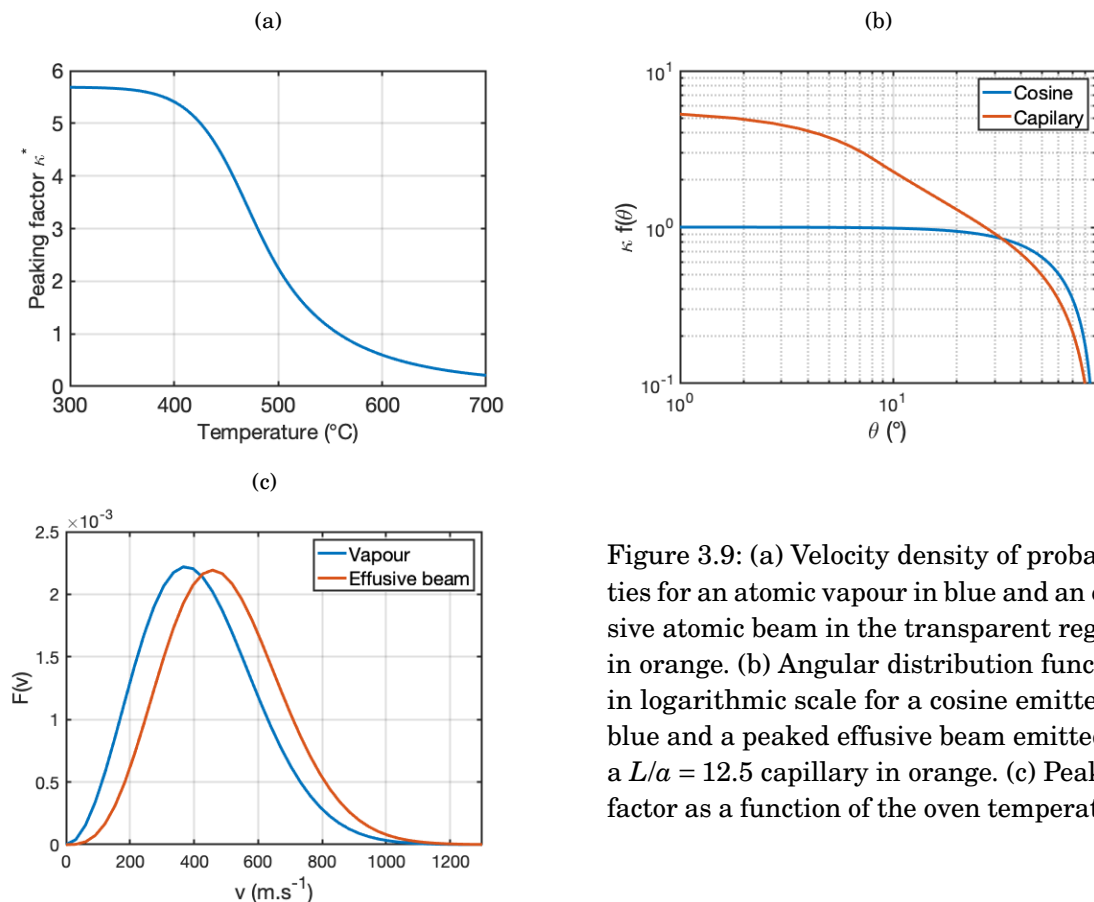


Figure 3.9: (a) Velocity density of probabilities for an atomic vapour in blue and an effusive atomic beam in the transparent regime in orange. (b) Angular distribution function in logarithmic scale for a cosine emitter in blue and a peaked effusive beam emitted by a $L/a = 12.5$ capillary in orange. (c) Peaking factor as a function of the oven temperature.

where κ^* is called the peaking factor. This parameter gives the central intensity of the atomic beam. It is thus equal to 1 for a cosine emitter in the transparent mode, and given by

$$(3.19) \quad \kappa^* = \frac{A(n^*)}{W},$$

for a tube having a probability W for an atom to escape the reservoir, given by Santeler's formula from equation 3.9. The function A expressed as

$$(3.20) \quad A(n^*) = \sqrt{\frac{\pi}{2n^*}} \operatorname{erf}\left(\sqrt{\frac{n^*}{2}}\right)$$

is a correction depending on the reduced density $n^* = L/\tilde{\lambda}$, which compares the capillary length to the atomic mean free path determined by the temperature in the reservoir as shown in figure 3.9(a). Our oven geometry is such that $L/a = 12.5$, giving $\kappa = 5.7$ at low temperatures and $\kappa^* = 3.9$ at 460 $^{\circ}\text{C}$.

The angular distribution is a piecewise function defined for two sets of polar angles and normalized by the condition $f(0) = 1$. Below the critical angle $\theta_c = \arctan(2a/L)$ given by the tube geometry, the atoms escape the oven reservoir without colliding the aperture walls. Above this value, the situation is modified by a more complex path through the hole. Studying the collision

rate along the propagation inside the aperture, Beijerinck & Verster computed the angular distribution in the transparent regime, corresponding to $A(n^*) = 1$, given by [149]

$$(3.21) \quad \kappa f(\theta) = \begin{cases} \frac{2 \cos \theta}{\pi W} \left\{ \left(1 - \frac{1}{2} W\right) R(p) + \frac{2}{3} (1 - W) \frac{1 - (1 - p^2)^{3/2}}{p} \right\} + \frac{\cos \theta}{2} & , \text{ if } 0 < \theta \leq \theta_c \\ \frac{1}{\pi} \frac{\cos^2 \theta}{\sin \theta} \frac{8a/3L}{W} (1 - W) + \frac{\cos \theta}{2} & , \text{ if } \theta > \theta_c \end{cases}$$

where $p = \tan \theta / \tan \theta_c$ and $R(p) = \arccos(p) - p \sqrt{1 - p^2}$. This distribution is represented in figure 3.9(b). The theoretical flow rate \dot{N} is thus proportional to the exit probability W and can be expressed as

$$(3.22) \quad \dot{N} = \frac{1}{4} \pi \alpha^2 W n \bar{v},$$

where \bar{v} is the mean velocity in the source defined as

$$(3.23) \quad \bar{v} = \int_0^{+\infty} v M(v) dv = \frac{2\alpha}{\sqrt{\pi}}.$$

This theory provides a full calculation of the source flow rate, angular and velocity distributions. Experimentally, these expressions can be tested by probing the atomic beam with a laser and record either fluorescence or absorption spectra. In the following paragraphs, we derive the theoretical predictions for these spectra shapes.

3.3.2 Laser beam absorption

Transverse (longitudinal) absorption spectroscopy is performed by sending a probe laser beam towards a direction perpendicular (parallel) to the oven axis and record the transmitted power with a photodiode. Fluorescence spectra recorded with a photodiode on a direction perpendicular to the laser beam also gives informations on the atomic probability distributions. In the following paragraphs, we make use of the effusive atomic beam properties derived in 3.3.1 to predict the absorption and fluorescence spectra for a two-level atom. In the last paragraph, we consider the modifications induced by the presence of an hyperfine structure in the probed atom such as the fermionic ^{87}Sr isotope.

3.3.2.1 Transverse beam spectroscopy

In order to derive the absorption theoretical properties, we consider a collimated Gaussian laser beam propagating along the y axis, centred on a vertical position x_0 and a distance z_0 from the end of the oven capillary as represented in figure 3.10. The incident laser intensity before propagating inside the atomic beam can thus be written as

$$(3.24) \quad I_i(x, z) = I_0 e^{-2 \left[\left(\frac{x - x_0}{w_0} \right)^2 + \left(\frac{z - z_0}{w_0} \right)^2 \right]},$$

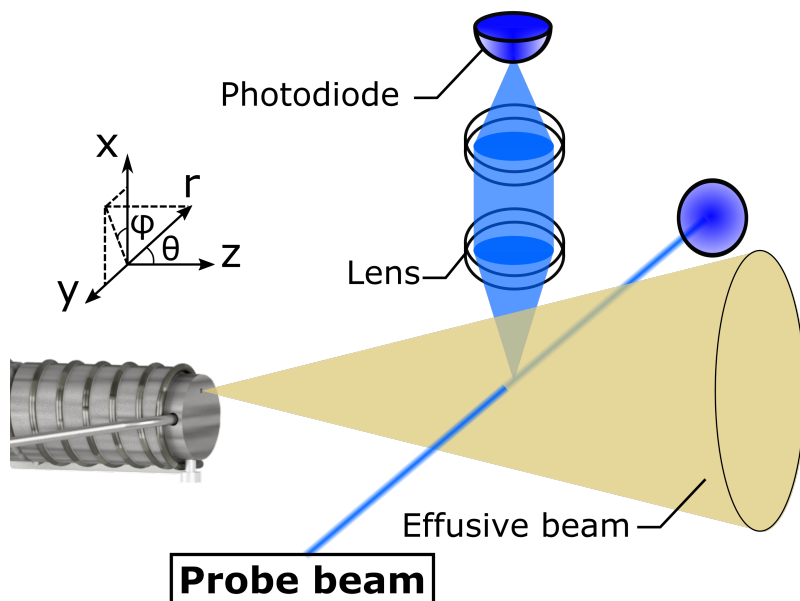


Figure 3.10: Scheme of the effusive beam transverse absorption and fluorescence spectra recording using a probe laser beam. The probe propagates along the y axis and the transmission is collected by a photodiode on this same axis. The fluorescence is recorded by an optical system composed of a collecting lens and a focusing lens converging scattered photons on a photodiode placed on the x axis.

with w_0 the beam waist and I_0 the peak intensity. According to the Beer-Lambert law, the intensity variation dI for a laser propagating through a medium of number density n over a distance dy at position \vec{r} is given by

$$(3.25) \quad \frac{dI}{dy} = -n(\vec{r})\sigma(\Delta_0, \vec{v})I(\vec{r}).$$

In this equation, σ corresponds to the atomic cross-section. In the absence of magnetic field, the cross-section of a two-level atom propagating at a velocity \vec{v} with a resonance at ω_0 , probed by a laser at frequency ω and wave vector \vec{k} can be written as

$$(3.26) \quad \sigma(\Delta_0, \vec{v}) = \frac{\sigma_0}{1 + s_0 + \frac{4(\Delta_0 - \vec{k} \cdot \vec{v})^2}{\Gamma^2}},$$

where $\Delta_0 = \omega - \omega_0$ is the laser field detuning, s_0 the saturation parameter and $\sigma_0 = 3\lambda^2/(2\pi)$ the on resonance cross-section. In this description, we assume a low saturation parameter $s_0 \leq 1$ in order to neglect cross-section intensity dependency. The analytical solution of equation 3.25 in this regime gives the transmitted intensity I_t after propagation through the atomic beam

$$(3.27) \quad I_t(\Delta_0, x, z) = I_i(x, z)e^{-\int dy n(\vec{r})\sigma(\Delta_0, \vec{v})}.$$

The absorption part in the exponential is called the optical depth, defined as $OD(\Delta_0, x, z) = \int dy n(\vec{r}) \sigma(\Delta_0, \vec{v})$. In this expression, the velocity dependency is included in the integration over the y axis, as the atomic speeds and positions are directly correlated.

In the experimental setup considered here, the detection is realized by recording the transmitted power with a photodiode. Equation 3.27 thus has to be integrated over the x and z remaining spatial coordinates in order to obtain the optical power. At this stage, we make a second assumption consisting in $OD \ll 1$ for all probe positions and frequencies. This approximation allows to expand the exponential in equation 3.27. At first order, it results in a transmitted power P_t expressed as

$$(3.28) \quad P_t(\Delta_0, x_0, z_0) \simeq \iint dx dz I_i(x, z) \left(1 - \int dy n(\vec{r}) \sigma(\Delta_0, \vec{v}) \right).$$

Dividing this expression by the incident optical power $P_0 = \iint dx dz I_i(x, z) = \frac{1}{2} \pi w_0^2 I_0$, we obtain the transmission T defined as

$$(3.29) \quad T(\Delta_0, x_0, z_0) \equiv \frac{P_t(\Delta_0, x_0, z_0)}{P_0} = 1 - \iiint d^3V n(\vec{r}) \sigma(\Delta_0, \vec{v}) g(x) g(z),$$

where d^3V is the volume integration element and $g(x)$ is the following normalized Gaussian function

$$(3.30) \quad g(x) = \sqrt{\frac{2}{\pi w_0^2}} e^{-2 \left(\frac{x-x_0}{w_0} \right)^2}.$$

Expressing equation 3.29 in terms of the volume integration element allows to relate the atomic density at position \vec{r} to the source effusive properties derived in 3.3.1. Indeed, inserting d^3V expressed in spherical coordinates inside the flow rate equation 3.12 leads to

$$(3.31) \quad \frac{d^4N}{d^3V} \times \frac{d^3V}{dt} = dn \times v r^2 d^2\Omega,$$

where we identified $v = \frac{dr}{dt}$. As the atomic angular and velocity distributions have been established previously, equation 3.31 gives an explicit formula for the density :

$$(3.32) \quad n(\vec{r}) = \frac{1}{r^2} J(\theta) \int_0^{+\infty} \frac{F(v)}{v} dv = \frac{1}{\bar{v} r^2} J(\theta).$$

Physically, this expression highlights the density decay in $1/r^2$ expected from a simple flow conservation argument. However, the divergence of the density at small distances from the capillary indicates that edge effects are neglected in this theory. A more complex expression for $r \ll a$, beyond the reach of this analysis, should be considered in order to describe the density in this regime. Nonetheless, the experimental spectra presented in section 3.4 are in agreement with this theory even for distances as small as $r \simeq 3a$.

Another physical phenomenon revealed by equation 3.32 is that the velocity distribution probed by the laser beam is reduced compared to the flow density of probability by a factor $1/v$. This

behaviour can be understood by realizing that atoms which travel at a velocity v interact with the laser beam during a time proportional to w_0/v . The slow atoms thus contribute more to the signal than faster ones. Combining equations 3.29 and 3.32 provides a complete model to understand absorption spectra. The explicit formula for the absorption of a beam centred on positions x_0 and z_0 at a detuning Δ_0 is given by

$$(3.33) \quad T(\Delta_0, x_0, z_0) = 1 - \int_0^{+\infty} dr \iint_{2\pi} d^2\Omega \int_0^{+\infty} dv J(\theta) g(r \sin \theta \cos \varphi) g(r \cos \theta) \frac{F(v)}{v} \frac{\sigma_0}{1 + s_0 + \frac{4(\Delta_0 + kv \sin \theta \sin \varphi)^2}{\Gamma^2}}.$$

This equation can be compared to experimental spectra by performing numerical integrations on the velocity, determined by the oven temperature, and the solid angle. The only remaining adjustable parameters thus are the total flow rate \dot{N} and the laser beam position (x_0, z_0) . Also, longitudinal absorption properties can easily be deduced from equation 3.33 by exchanging the role of the different spatial coordinates in the Gaussian functions g and the atomic cross-section σ .

3.3.2.2 Fluorescence spectra

With the determination of the transmission spectrum of a laser beam propagating in a transverse direction compared to the atomic beam, one can develop a simple model for predicting fluorescence emission spectra. In first approximation, all the photons absorbed by the atoms are spontaneously emitted after an average time equal to the excited state lifetime. Assuming for simplicity that the probe beam polarization is linear, for instance in the $\{y, z\}$ plane, the dipolar atom-light interaction presents an emission pattern that covers a solid angle Ω_{tot} given by [137]

$$(3.34) \quad \Omega_{tot} = \iint_{4\pi} d^2\Omega \sin^2 \theta = \frac{8\pi}{3}.$$

The atomic fluorescence can be collected with a lens of focal f and radius r_L combined with a photodiode, as represented in figure 3.10. Assuming that the lens is placed on an axis perpendicular to the laser polarization plane, such as x , at a distance f from the atom-laser interaction region, the collected number of photons per second \dot{N}_{ph} is given by

$$(3.35) \quad \dot{N}_{ph}(\Delta_0, x_0, z_0) = \frac{\Omega_{ph}}{\Omega_{tot}} \frac{P_0}{\hbar\omega} \left[1 - T(\Delta_0, x_0, z_0) \Big|_{V_{int}} \right],$$

where $\Omega_{ph} = 2\pi(1 - \cos \theta_f)$ is the collection solid angle defined by the lens aperture angle $\tan \theta_f = r_L/f$. The transmission calculation in equation 3.35 is performed over the interaction volume V_{int} seen by the photodiode. In practice, using the fluorescence to determine the flow rate is thus more challenging than using absorption spectra as the collection angle and photodiode gain have to be carefully characterized in order to obtain quantitative agreements between the data and the model. Moreover, several effects such as the optics transmissions can also deviate measured values from the predictions.

3.3.2.3 Hyperfine structure considerations

The previous spectral properties derivation was performed considering a two-level atom, which can be generalized to any atom without hyperfine structure such as the bosonic isotopes of strontium. For atomic species presenting a non zero nuclear spin I like ^{87}Sr , the fine structure of the energy levels given by the quantity $J = L + S$ is enriched by a hyperfine non-degeneracy, characterized by the total spin $F = I + J$. In this paragraph, we consider a transition from a manifold of total spin number F_g to an excited manifold F_e . Such manifolds encapsulate a number $2F + 1$ of Zeeman levels with projection numbers $-F \leq m_F \leq F$, as shown in figure 3.11.

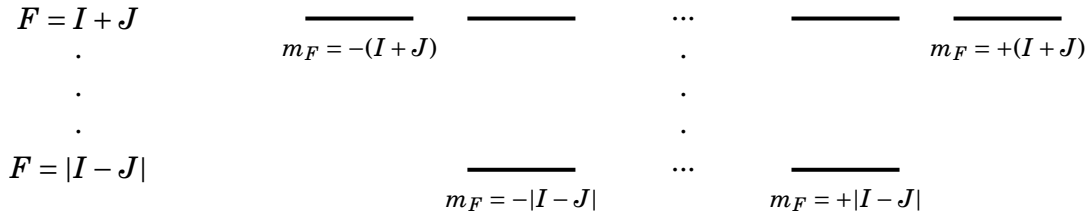


Figure 3.11: Hyperfine manifold for a $^{2S+1}L_J$ quantum state.

The spectral properties derived in paragraph 3.3.2.1 can take into account the hyperfine structure by generalizing the cross-section expression to σ_F . Computing the absorption on the transition from the F_g manifold to the F_e one results in summing the contributions of all the $|F_g, m_{F_g}\rangle \rightarrow |F_e, m_{F_e}\rangle$ transitions. The dipole operator overlap between the ground and excited states is defined by the reduced dipole matrix element d written as [158]

$$(3.36) \quad \langle F_g, m_{F_g} | D | F_e, m_{F_e} \rangle = c_{m_F} \langle L_g | D | L_e \rangle = c_{m_F} d,$$

where the Zeeman coefficient c_{m_F} is expressed as a product of Wigner 3-j and 6-j symbols via

$$(3.37) \quad c_{m_F} = (-1)^{2F_e + I + J_g + J_e + L_g + S + m_{F_g} + 1} \sqrt{(2F_g + 1)(2F_e + 1)(2J_g + 1)(2J_e + 1)(2L_g + 1)} \\ \times \begin{pmatrix} F_e & 1 & F_g \\ m_{F_e} & -q & -m_{F_g} \end{pmatrix} \begin{Bmatrix} J_g & J_e & 1 \\ F_e & F_g & I \end{Bmatrix} \begin{Bmatrix} L_g & L_e & 1 \\ J_e & J_g & S \end{Bmatrix}.$$

The q parameter in equation 3.37 corresponds to the probe laser polarization being equal to 0, -1 or 1 for π , σ_- or σ_+ polarizations respectively. The selection rules impose that the c_{m_F} coefficients are non zero if and only if $m_{F_e} = m_{F_g} + q$. The reduced matrix dipole element is linked to the total decay rate Γ of the excited state through the following equations

$$(3.38) \quad \Gamma = \frac{\omega_0^3}{3\pi\epsilon_0\hbar c^3} \frac{2J_g + 1}{2J_e + 1} |\langle J_g | D | J_e \rangle|^2$$

and

$$(3.39) \quad \langle J_g | D | J_e \rangle = (-1)^{J_e + L_g + S + 1} \sqrt{(2J_e + 1)(2L_g + 1)} \begin{Bmatrix} L_g & L_e & 1 \\ J_e & J_g & S \end{Bmatrix} \times d.$$

The total transition strength C_F^2 for the F_g to F_e manifolds transition can be expressed as a sum of the Zeeman transitions strengths as

$$(3.40) \quad C_F^2 = \sum_{m_F} c_{m_F}^2.$$

Under a final assumption which consists in considering that the atomic populations are equally distributed between the m_{F_g} sublevels, the hyperfine cross-section σ_F is proportional to the transition strength C_F^2 divided by the degeneracy of the ground state. As each F_g manifold counts a number $2F_g + 1$ Zeeman sublevels, the total number of states in the ground state manifolds writes down

$$(3.41) \quad \sum_{F_g=|I-J_g|}^{I+J_g} (2F_g + 1) = (2I + 1)(2J_g + 1).$$

We thus obtain the cross-section expression given by

$$(3.42) \quad \sigma_F(\Delta_0, \vec{v}) = \frac{2k}{\hbar\epsilon_0\Gamma} \frac{C_F^2 d^2}{(2I + 1)(2J_g + 1)} \frac{1}{1 + s_0 + \frac{4(\Delta_0 - \vec{k} \cdot \vec{v})^2}{\Gamma^2}},$$

where Δ_0 accounts for both the isotope and hyperfine shifts. One can verify that in the two-level case, given by $I = 0$ associated with a unique manifold in the ground and excited states, we recover the cross-section expression from equation 3.26. For instance, considering a $|J_g = 0\rangle \rightarrow |J_e = 1\rangle$ such as the bosonic dipole allowed transition gives $\sigma_0 = 2k/(\hbar\epsilon_0\Gamma) \times C_F^2 d^2$.

The theoretical background derived in this section provides the tools for comparing effusive beam calculations with experimental data. The next section is dedicated to such comparison, using two sets of data characterizing the oven output properties, as well as the collimated beam inside the vacuum system.

3.4 Strontium source characterization

During the experiment development, we realized a series of studies aiming to probe the effusive beam properties described in the previous section. A first experiment was realized using the home-made oven placed in a simple test apparatus. The setup was consisting of a vacuum chamber surrounded by three viewports used to probe the atomic beam by transverse spectroscopy and collect both the transmitted and scattered light. This experiment, presented in the first part of this section, allowed to measure the source flow rate. In a second experiment led in the main vacuum system described in section 3.2, we realized both transverse and longitudinal spectroscopy of the effusive beam in order to define the flux after the cold apertures, as well as the velocity distributions in these directions.

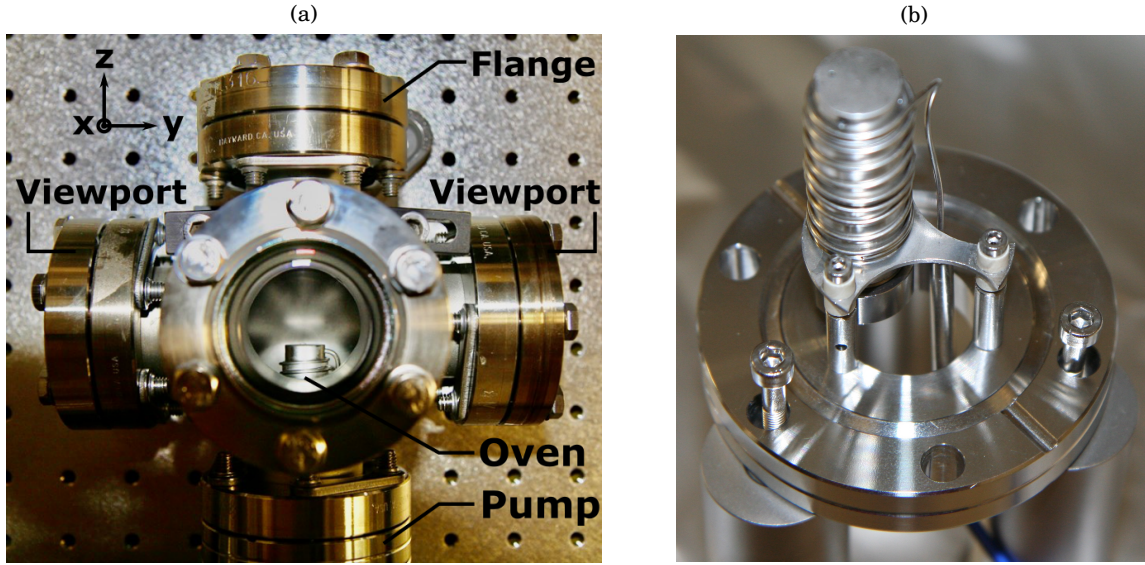


Figure 3.12: (a) Picture of the vacuum test apparatus for absorption and fluorescence spectroscopy of the oven atomic output beam. The laboratory frame is defined on the top left corner. (b) Picture of the oven fixed on a custom sustaining flange.

3.4.1 Oven test apparatus

The first experiment realized on the effusive oven is described hereafter. In a first paragraph, the test setup containing a vacuum chamber and an optical set for transverse spectroscopy is introduced. The measurements results using this system as well as a comparison with the theory are described in a second paragraph.

3.4.1.1 Vacuum test apparatus design

In order to characterize the strontium effusive source, we developed a simple test apparatus exposed in figure 3.12(a). This apparatus was containing the oven fixed to a custom flange, shown in figure 3.12(b). This sustaining mechanical piece was connected to a five-way CF40 cross on one side, and to a tee on the other side allowing to connect the heating wire and thermocouple feedthroughs as well as a turbo pump to place the system under vacuum. The cross port facing the oven was sealed with a plain flange, and three viewports were located on top and on the sides of the oven. This setup allows for transverse beam absorption spectroscopy along the y axis as well as fluorescence collection on the vertical axis x , realizing the scheme from figure 3.10. The axis of the atomic beam is defined as z , with the origin of this frame being located at the output of the oven capillary.

The effusive beam was probed by a laser beam generated with the blue master laser scanned in frequency over the 461nm resonance. This pump was horizontally polarized in the lab frame

and sent through the right viewport in figure 3.12(a), in order to maximize the fluorescence emission on the vertical axis. To record the emitted photons, a collecting lens of focal $f = 100\text{ mm}$ associated with a focusing lens and a photodiode were placed on a breadboard located on the top of the apparatus. The transmission was recorded with a photodiode at the output port, on the left of the picture. The beam waist $w_0 = 270\mu\text{m}$ was chosen to be smaller than the capillary radius $a = 0.4\text{ mm}$ to be able to probe a selective cylinder inside the atomic effusive pattern. Accordingly, the optical power was set to $P_0 = 55\mu\text{W}$ in order to collect a sufficient number of fluorescence photons while keeping a saturation parameter on the order of 1. The probe spatial region selection was performed by sending the laser towards a mirror mounted on two translation stages on the x and z axes before the vacuum chamber, setting the central beam position x_0 and z_0 in equation 3.33.

3.4.1.2 Transverse absorption beam probing

Using the test apparatus and varying the beam spatial degrees of freedom, we recorded a set of absorption and fluorescence spectra presented in figure 3.13. The absorption spectra at a small distance from the oven $z_0 = 1.1\text{ mm}$ in figure 3.13(a) and at a large distance $z_0 = 15\text{ mm}$ in figure 3.13(c) show a good agreement with the predictions from equation 3.33, with the flow rate \dot{N} and the positions x_0 and z_0 as the only adjustable parameters. These predictions are established by considering the absorption of the two most abundant bosonic isotopes ^{88}Sr and ^{86}Sr . The fermionic contribution is neglected to avoid numerical complications arising from the hyperfine structure calculations, but this effect should not modify the presented results by more than a few percent due to the spectral spreading of the different lines and the low natural abundance of this isotope. The fluorescence spectra in figure 3.13(b) also demonstrate the validity of equation 3.35. For a measured voltage U , with a photodiode of gain G in VW^{-1} and quantum efficiency η , the number of photon per second is computed with the following formula

$$(3.43) \quad \dot{N}_{ph} = \frac{U}{\eta G \hbar \omega}.$$

In order to fully describe the effusive beam angular distribution, we present in figure 3.13(d) the optical depth for a probe beam on resonance with ^{88}Sr atoms at ν_0 . This measurement is thus related to the transmission minimum as, according to the approximations established in 3.3, the optical depth writes

$$(3.44) \quad OD(\Delta_0, x_0, z_0) \simeq 1 - T(\Delta_0, x_0, z_0).$$

Up to experimental imperfections, the predicted absorption behaviour corresponds to the measured spatial dependencies. However, the measured total flow rate $\dot{N} = 3.9(2) \times 10^{13} \text{ atoms s}^{-1}$ is 3.5 times smaller than the predicted value from equation 3.22 at $T_{oven} = 463^\circ\text{C}$, which corresponds to a reduced density $n^* = 3.1$.

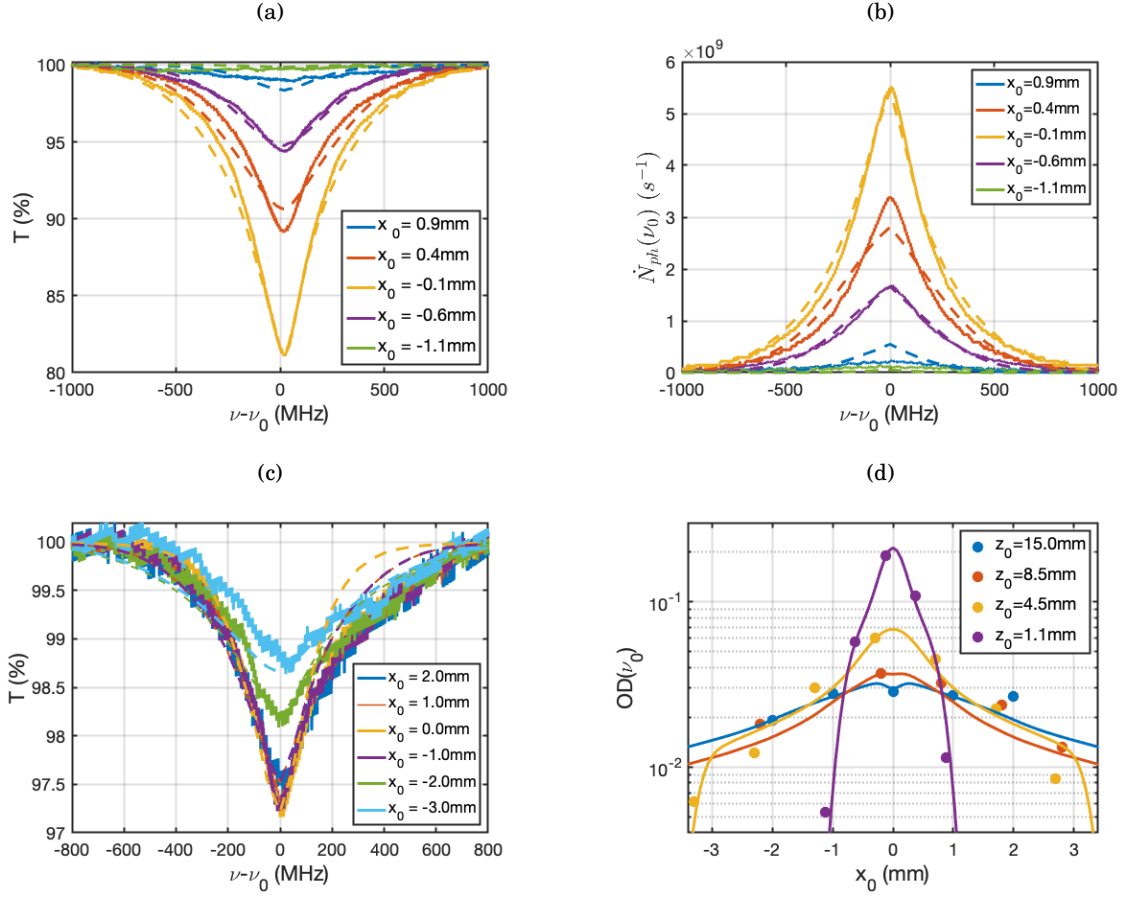


Figure 3.13: (a) Transverse absorption and (b) fluorescence spectra with a 461 nm probe beam located at a distance $z_0 = 1.1$ mm from the capillary output and vertical position x_0 . The oven is operated at a temperature of 463 °C. The data are presented as solid lines, while the corresponding theoretical predictions from equation 3.33 are displayed as dotted lines with identical colours. (c) Absorption spectra at the large distance $z_0 = 15$ mm from the oven for different vertical positions. (d) On resonance optical depths for different probe positions along the effusive beam path with the model predictions represented as solid lines for each distance z_0 .

In order to study the temperature dependency of the atomic flow rate and confirm the constant factor disagreement between the predicted and measured values, we present a series of spectra taken at the center of the beam $x_0 = 0$ and a short distance $z_0 = 1.0$ mm from the oven output in figure 3.14. The source density was modified by increasing the heating wire temperature, measured with the thermocouple. The absorption spectra in figure 3.14(a) match the theoretical predictions up to a constant correction factor of 4.0(5). This observation is confirmed by the comparison between the expected flow rate from equation 3.22 and the measured values in figure 3.14(b). We thus find a good agreement between experiment and theory after renormalization in the studied temperature regime. The Florence group reported a correction factor of 3.4 [137], measured by fluorescence with a calibrated photodiode. As the temperature dependency is

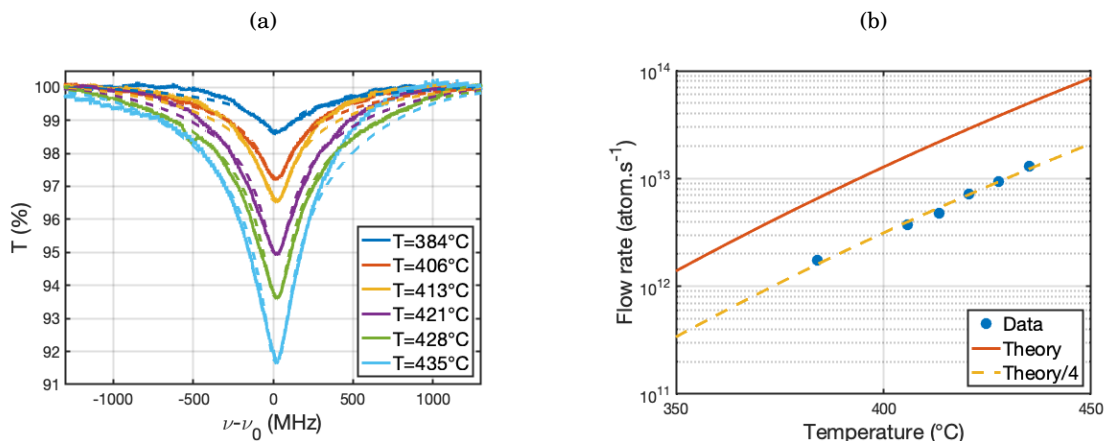


Figure 3.14: (a) Transmission spectra for a beam at position $x_0 = 0$ and $z_0 = 1.0$ mm from the oven output for different source temperatures. (b) Flow rate inferred from the absorption spectra in logarithmic scale. The data are represented as blue points and compared to the theoretical predictions in solid orange line, rescaled by a factor 4 in dotted yellow line.

perfectly predicted in both experiments, the total flow rate disagreements could either come from experimental calibration errors, or from an overestimated capillary output probability which calculation results from approximations in the wall collisions.

3.4.2 Collimated beam characterization

After the validation of the effusive beam theory and the flow rate determination using the oven test apparatus, we placed the atomic source inside the main vacuum chamber presented in section 3.2. The presence of the differential pressure and collimation holes along the atomic beam acts as a spatial filter selecting only a fraction of the effusive beam. In the following paragraphs, we describe a spectral analysis realized on this collimated beam. Both transverse and longitudinal fluorescence spectra were recorded by probing the atoms with laser beams in the glass cell region. A complete description of these data provides a determination of the atomic flux, as well as longitudinal and transverse beam velocity distributions.

3.4.2.1 Longitudinal velocity distribution

Inside the vacuum chamber, the atomic beam is first transmitted through the differential pressure hole before going through the collimation hole of length $L_2 = 2$ mm and diameter $d_2 = 1$ mm. This second aperture is placed at a distance $z_2 = 3$ cm of the oven output, as shown in figure 3.3. Its vertical position is such that the collimated atomic beam makes an angle $\theta_0 = 7^\circ$ with the z axis. This configuration thus acts as a spatial filter selecting atoms from the effusive beam propagating

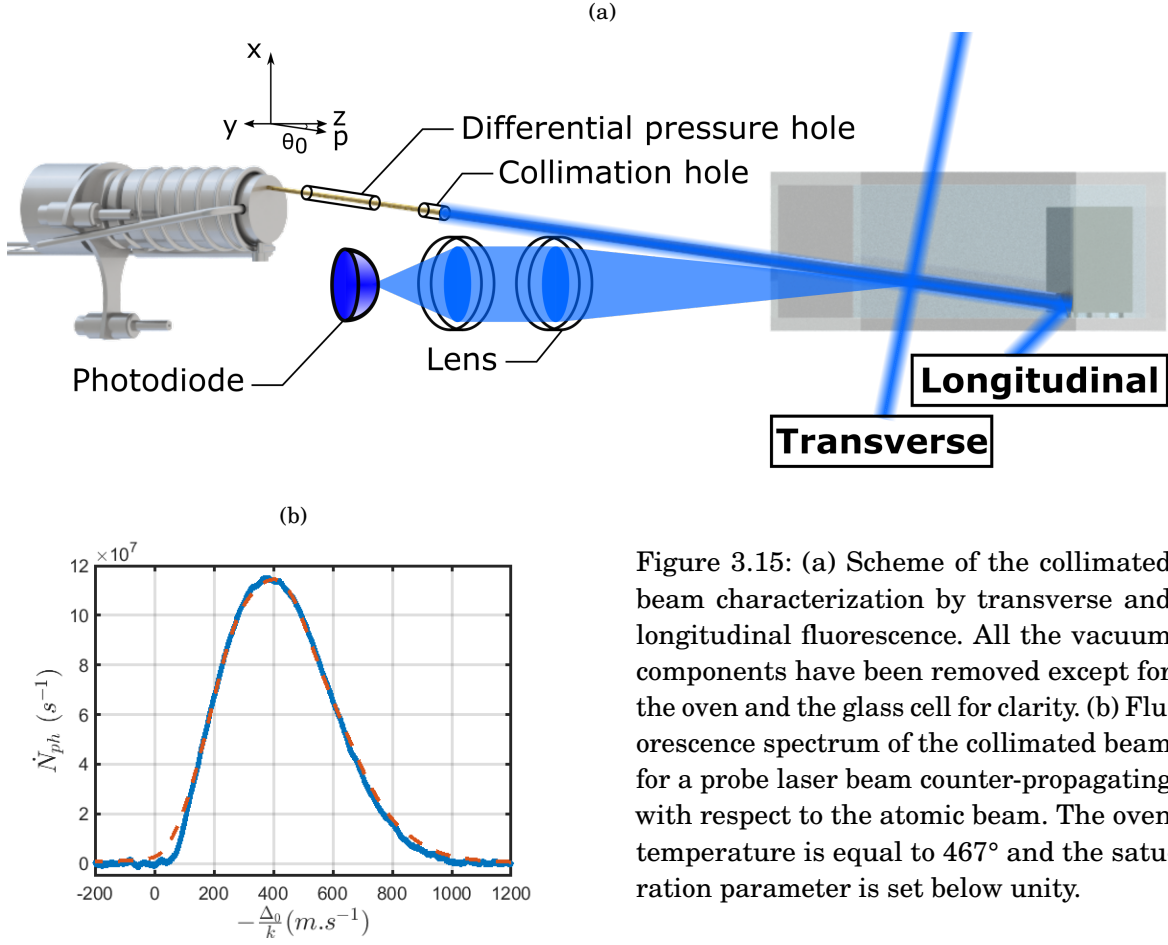


Figure 3.15: (a) Scheme of the collimated beam characterization by transverse and longitudinal fluorescence. All the vacuum components have been removed except for the oven and the glass cell for clarity. (b) Fluorescence spectrum of the collimated beam for a probe laser beam counter-propagating with respect to the atomic beam. The oven temperature is equal to 467° and the saturation parameter is set below unity.

in the solid angle Ω_c characterized by

$$(3.45) \quad \Omega_c = \int_{\pi-\delta\varphi}^{\pi+\delta\varphi} \int_{\theta_0-\delta\theta}^{\theta_0+\delta\theta} d^2\Omega = 2\delta\varphi [\cos(\theta_0 - \delta\theta) - \cos(\theta_0 + \delta\theta)],$$

with $\delta\theta \simeq \delta\varphi \simeq 1^\circ$ estimated from the hole radius and position, giving $\Omega_c \simeq 2 \times 10^{-4} \text{sr}$.

In order to probe the resulting angular and velocity distributions of the collimated atomic beam, we realized a first experiment with a counter-propagating laser beam scanned over the 461 nm resonance. The direction of propagation $p = \cos\theta_0 z + \sin\theta_0 x$ being common to the atoms and the light, the Doppler effect was sensitive to the longitudinal component of the collimated beam velocity distribution. With a photodiode placed on the y axis, as pictured in figure 3.15(a), we recorded the fluorescence spectrum presented in figure 3.15(b). According to equation 3.26, the atomic cross-section is maximum when the probe laser frequency and the atomic velocity fulfil the condition $\Delta_0 + kv_p = 0$. Rescaling the probe laser detuning by $-1/k$ thus gives access to the longitudinal velocity density of probability, broaden by the strontium response function. The data are adjusted by the fluorescence theoretical expressions from equations 3.33 and 3.35

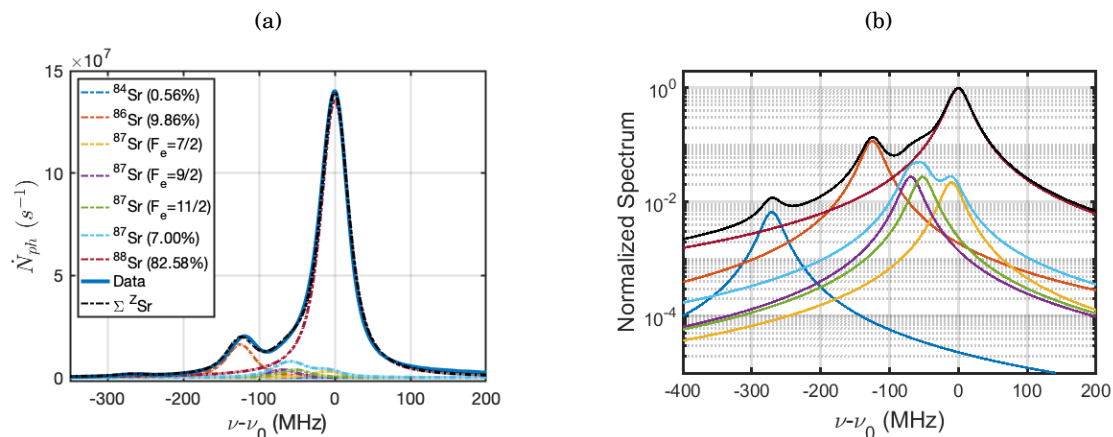


Figure 3.16: (a) Transverse fluorescence spectrum of the collimated atomic beam inside the glass cell with the oven operating at 460°C. The low saturation probe laser beam is scanned over the 461nm resonance referenced to the ^{88}Sr isotope. The data are represented as a solid blue line, and fit functions taking into account all the different strontium isotopes weighted by their natural abundance are shown as dashed coloured lines. The profiles sum is represented as a black dotted line. (b) Normalized theoretical profile in logarithmic scale showing the different isotopic contributions with the colour code defined in (a).

for a laser beam propagating along p . The integration is performed within the collimated beam solid angle Ω_c . With the amplitude as the unique fitting parameter, we find excellent agreement between the theoretical prediction and the measured fluorescence profile.

3.4.2.2 Isotope resolved fluorescence spectra

The collimation hole not only acts as a spatial filter, but also as a transverse velocity one. Indeed, as only the central part of the v_y distribution gets transmitted towards the glass cell, the transverse velocity distribution is drastically reduced compared to the oven output beam. Probing such distribution with a laser thus gives much narrower fluorescence spectra than the one explored in the oven test section, and the different strontium isotopic contributions must be taken into account. To illustrate this feature, we show in figure 3.16(a) an experimental dataset taken with a laser beam propagating along a transversal axis with respect to the collimated atomic beam and recorded by a lens and a photodiode assembly on the y axis, as shown in figure 3.15(a). The spectrum is adjusted by a sum of the isotopic absorption profiles, weighted by their natural abundances and taking into account the hyperfine structure of the fermionic isotope as derived in 3.3.2.3. The normalized theoretical profile is also shown in logarithmic scale in figure 3.16(b) in order to distinguish the low abundance isotopes such as ^{84}Sr .

3.4.2.3 Collimated atomic flux

In the same spirit as the oven effusive beam characterization using the test apparatus described in 3.4.1, we characterized the collimated beam properties by transverse fluorescence inside the glass cell of the main vacuum system. A small probe beam of waist $w_0 = 140\mu\text{m}$ and optical power $P_0 = 55\mu\text{W}$, resulting in a saturation parameter $s_0 = 4.3$, was sent along an axis perpendicular to p in the vertical plane, with translation stages on the y and z directions in order to set the central probe position as represented in figure 3.15(a). The fluorescence spectra taken at different positions are presented in figure 3.17(a).

In order to simplify the fluorescence description derived in 3.3.2.2, we consider that the spatial distribution is reduced to its central value around θ_0 . With this simplification, the beam velocity distribution can be expressed in Cartesian coordinates as a product of one dimensional Maxwell-Boltzmann distributions defined by

$$(3.46) \quad v^2 dv d^2\Omega \frac{F(v)}{v^3} = \frac{\pi^{3/2}}{\alpha} \prod_{i \in \{x,y,z\}} dv_i m(v_i)$$

with

$$(3.47) \quad m(v_i) = \frac{1}{\sqrt{\pi}\alpha} e^{-\left(\frac{v_i}{\alpha}\right)^2}.$$

Making use of equation 3.47, we can approximate the on-resonance fluorescence amplitude for each isotope by the following formula

$$(3.48) \quad \dot{N}_{ph}(\Delta_0, y_0, z_0) \simeq \frac{\Omega_{ph}}{\Omega_{tot}} \frac{P_0}{\hbar\omega_0} \times n_0 L_e(y_0, z_0) \int_{-\infty}^{+\infty} dv_x m(v_x) \sigma_F(\Delta_0, v_x),$$

where we define the effective length L_e , corresponding to the width of the laser interrogation region, and the collimated beam average number density n_0 . At the fluorescence maximum, this length is given by the diameter of the collimation hole d_2 . The spectra in figure 3.17(a) are adjusted by a sum of the strontium isotopes contributions following equation 3.48, with the density and the transverse velocity as free parameters. We find a small transverse velocity $\alpha_t = 7(2)\text{ms}^{-1}$, resulting from the collimation hole filtering in the x and y dimensions. Indeed, the mean velocity of the Gaussian transverse distribution from equation 3.47 multiplied by the ratio of the hole radius over its distance from the oven gives a simple estimation of $\alpha \times r_2/z_2 = 6\text{ms}^{-1}$.

Experimentally, the effective length is well approximated by a Gaussian profile, as shown in figure 3.17(b) representing the on-resonance fluorescence level for the different positions. These results give an estimation of the collimated beam divergence by measuring the profile spreading between the two z_0 values. We determine a half width at half maximum angle $\delta\theta = 1.2(1)^\circ$, in agreement with the vacuum system mechanical considerations. From this parameter, we can compute the flow rate of the collimated beam inside the glass cell \dot{N}_b given by

$$(3.49) \quad \dot{N}_b = J(\theta_0)\Omega_c,$$

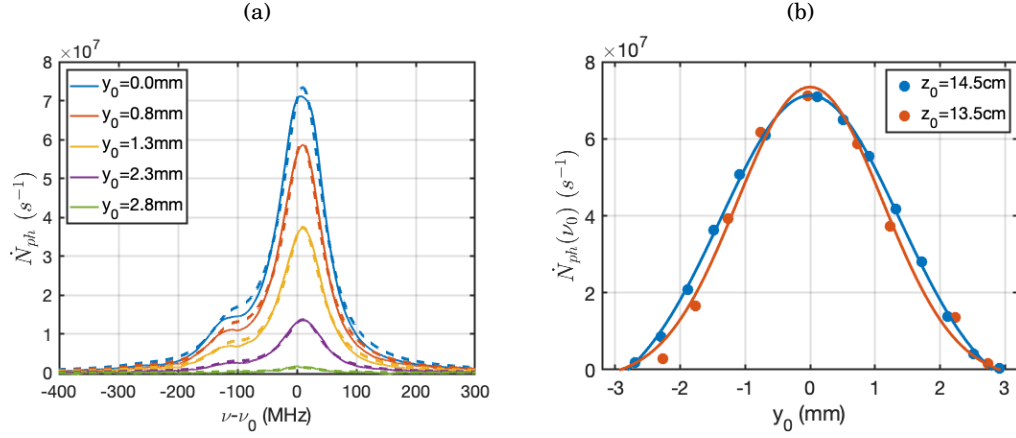


Figure 3.17: (a) Fluorescence spectra of the collimated beam at a distance $z_0 = 13.5$ cm from the oven, probed by a transverse beam in the vertical plane centred on y_0 . The data, shown as solid lines, are adjusted by fit functions equal to a sum of profiles from equation 3.48 taking into account the different strontium isotopes. (b) On-resonance fluorescence maxima as a function of the horizontal probe beam position y_0 . The data are shown as solid points for two different distances z_0 to the oven, adjusted by Gaussian profiles represented as solid lines.

which gives $\dot{N}_b = 3.0(2) \times 10^{10} \text{ atoms s}^{-1}$ at 460°C . This expression gives access to the density inside the atomic beam using equation 3.32. At the MOT position, located at a distance $p_0 = 15$ cm from the oven, we obtain $n_0 = 1.5(1) \times 10^{13} \text{ atom/m}^3$. Finally, we obtain the atomic flux inside the cell calculated with the following expression

$$(3.50) \quad \mathfrak{F} = \frac{\dot{N}_b}{\pi r_2^2 \cos \theta_0},$$

giving $\mathfrak{F} = 3.8(2) \times 10^{12} \text{ atom/s/cm}^2$ at 460°C .

Conclusion on the atomic beam characterization

To conclude on the different analyses performed on both the effusive atomic beam at the oven output and the collimated beam inside the main vacuum system, we summarize the measured properties in table 3.3. We find a flow rate 3 times smaller than in the LENS-PTB collaboration [137], in agreement with the product of the ratio between the total output surface of their 120 capillaries design over the surface of our single capillary, multiplied by the inverse ratio of the measured peaking factors. A similar ratio is observed for the collimated atomic flux inside the glass cell, but we measure a twice smaller transverse velocity due to the collimation hole. The presence of this aperture collimates the atomic beam in a direction making an angle $\theta_0 = 7^\circ$ compared to the horizontal plane, thus reducing direct collisions with the cold strontium sample in the MOT region¹⁰. The presence of the differential pressure hole ensures an ultra-high vacuum level of 1.3×10^{-10} mbar in the science chamber and reduces strontium coating onto the right-angled mirror prism. This system thus provides a simple and efficient collimated source of strontium atoms in a reduced vacuum system of size $40 \text{ cm} \times 40 \text{ cm} \times 40 \text{ cm}$.

	Effusive Beam	Collimated Beam
Peaking factor	$\kappa^* = 3.9$	
Flow rate	$\dot{N} = 3.9(2) \times 10^{13} \text{ atom s}^{-1}$	$\dot{N}_b = 3.0(2) \times 10^{10} \text{ atom s}^{-1}$
Longitudinal velocity	$\bar{v} = 420 \text{ m s}^{-1}$	$\bar{v} = 420 \text{ m s}^{-1}$
Transverse velocity	$\alpha = 370 \text{ m s}^{-1}$	$\alpha_t = 7(2) \text{ m s}^{-1}$
Flux		$\mathfrak{F} = 3.8(2) \times 10^{12} \text{ atom/s/cm}^2$
Density		$n_0 = 1.5(1) \times 10^{13} \text{ atom/m}^3$
Divergence		$\delta\theta = 1.2(1)^\circ$

Table 3.3: Characteristics of the effusive atomic beam at the oven output and the collimated beam at the MOT position inside the glass cell for a source temperature of 460°C .

¹⁰Due to manufacturing limitations, the capillary could not be drilled at the angle θ_0 , which would have increased the flow rate by a factor $f(0)/f(\theta_0) \simeq 5/3$.

TRAPPING AND COOLING OF STRONTIUM ATOMS

The 20th century has hosted a rich and fast history of atomic slowing and trapping. Starting in 1917 with Einstein’s predictions on photon recoil modifying the momenta of atoms [159], several ground-breaking discoveries very soon followed, as enlightened by the impressive number of Nobel Prizes related to this field of physics. In 1975, Theodor Hänsch & Arthur Schawlow at Stanford University [19] in parallel with David Wineland & Hans Dehmelt at the University of Washington [20] came up with the idea that absorbers can be cooled when illuminated with “quasi-monochromatic light confined to the lower-frequency half of a resonance line’s Doppler width” [19]. Schawlow received the prize in 1981 with Bloembergen & Siegbahn “for their contribution to the development of laser spectroscopy”, followed by Hall & Hänsch in association with Glauber in 2005 “for their contributions to the development of laser-based precision spectroscopy, including the optical frequency comb technique”.

These pioneering contributions were also directed by Wolfgang Paul, who first achieved magnetic trapping for charged and neutral particles. This achievement led him to the Nobel Prize in 1989 with Dehmelt & Ramsey “for the development of the ion trap technique” [160]. Magnetic trapping methods were then combined to optical cooling, developed among others by William Phillips at National Bureau of Standards, Steven Chu at Bell Laboratories and Claude Cohen-Tannoudji here at École Normale Supérieure. These contributions have earned them the prize in 1997 “for development of methods to cool and trap atoms with laser light”. At that time, Jean Dalibard was working at former Laboratoire Kastler-Brossel (Laboratoire de Spectroscopie Hertzienne) in the team of Claude Cohen-Tannoudji. A series of papers in 1985 [21, 22, 161] with different collaborators among eminent names cited earlier in this paragraph initiated the idea of combining laser cooling with a quadrupole magnetic field, leading to the so-called *Magneto-Optical Trap* (MOT). First realized with sodium atoms in Steven Chu & David Pritchard’s laboratory in 1987 [24], the

technique was further improved and applied to several elements of the periodic table, as shown in figure 4.1. The most common MOTs are nowadays realized with alkali atoms, especially rubidium which benefits from easily accessible and low price lasers built for telecommunications and CD players. Nonetheless, even if these first column alkali metals have all been domesticated by photons, the second column, filled with alkaline-earth elements, have nothing to be ashamed of as magnesium, calcium, strontium and barium have been brought to temperatures in the μK range or lower. The collection is completed by all the noble gases except for radon, seven elements from the transition metals and other metals group and five from the lanthanides [162, 163]. This last category of heavy atoms interestingly presents atomic structures resembling the alkaline-earths ones. Both benefiting from the existence of forbidden transitions, so-called narrow-line cooling can be applied to these two families of elements, allowing to achieve colder temperatures than for well known alkalis.

In this chapter, we start from a description of our MOT apparatus for strontium atoms, focusing on magnetic field generation and optical beam access in the previously described vacuum system. In a second part, we demonstrate atomic slowing of atoms from the effusive beam, using the decaying part of the quadrupole magnetic field between the oven and the MOT region. We then characterize trapping and cooling on the wide dipole allowed transition at 461 nm, referred to as the blue MOT. This first stage cooling operates in the so-called Doppler regime, similarly to the alkali MOTs. Finally, we focus on cooling schemes on the inter-combination line at 689 nm, exploring the recently proposed *Saw-Tooth Wave Adiabatic Passage* (SWAP) scheme [164] and *Continuous Wave* (CW) MOT. In addition, the production of red optical molasses on this same transition is also demonstrated. The combination of SWAP and CW constitutes the red MOT. Relying on recoil dynamics, at the very heart of quantum mechanics, this narrow-line MOT is able to achieve colder temperatures than in the so-called Doppler regime.

1 H																	2 He
3 Li	4 Be											5 B	6 C	7 N	8 O	9 F	10 Ne
11 Na	12 Mg											13 Al	14 Si	15 P	16 S	17 Cl	18 Ar
19 K	20 Ca	21 Sc	22 Ti	23 V	24 Cr	25 Mn	26 Fe	27 Co	28 Ni	29 Cu	30 Zn	31 Ga	32 Ge	33 As	34 Se	35 Br	36 Kr
37 Rb	38 Sr	39 Y	40 Zr	41 Nb	42 Mo	43 Tc	44 Ru	45 Rh	46 Pd	47 Ag	48 Cd	49 In	50 Sn	51 Sb	52 Te	53 I	54 Xe
55 Cs	56 Ba	57-71	72 Hf	73 Ta	74 W	75 Re	76 Os	77 Ir	78 Pt	79 Au	80 Hg	81 Tl	82 Pb	83 Bi	84 Po	85 At	86 Rn
87 Fr	88 Ra	89-103	104 Rf	105 Db	106 Sg	107 Bh	108 Hs	109 Mt	110 Ds	111 Rg	112 Cp	113 Uut	114 Fl	115 Uup	116 Lv	117 Uus	118 Uuo

57 La	58 Ce	59 Pr	60 Nd	61 Pm	62 Sm	63 Eu	64 Gd	65 Tb	66 Dy	67 Ho	68 Er	69 Tm	70 Yb	71 Lu
89 Ac	90 Th	91 Pa	92 U	93 Np	94 Pu	95 Am	96 Cm	97 Bk	98 Cf	99 Es	100 Fm	101 Md	102 No	103 Lr

Alkali Metals
 Alkali Earth Metals
 Transition Metals
 Other Metals
 Metalloids
 Non Metals
 Halogens
 Noble Gases
 Lanthanides
 Actinides

Figure 4.1: Periodic table of the elements classified by families. The atomic species for which laser cooling has been demonstrated are highlighted by thick black squares.

4.1 A combined Zeeman slower and MOT apparatus

In order to be able to capture fast atoms from an effusive source to a MOT, it is mandatory to drastically reduce their velocity. The conventional way of stopping atoms from a high speed source is to use a Zeeman slower. The basic principle of such devices is to use the radiative force of a laser beam counter-propagating with respect to the atomic beam to slow the atoms down. This procedure necessitates a particular magnetic field, which relies on a series of coils or permanent magnets typically 15 cm to 50 cm long in the case of strontium [165, 166]. As only the projection of the velocity along the longitudinal axis of the beam can be decreased, a main problem with these devices is the transverse velocity spreading across the propagation towards the MOT region. In this part of the experiment, a quadrupole magnetic field is necessary to operate the magnetic trap. Our design idea is thus to make use of the decaying magnetic field outside the MOT region as a slower. This section presents our magnetic coils assembly design and optical access for the cooling and trapping beams inside our vacuum system.

4.1.1 Magneto-optical configuration

In MOT experiments, magnetic fields are a key ingredient in several tasks. First, MOT operation requires a quadrupole field in order to trap and slow the atoms, as will be further described in 4.3. Such fields present a zero in their geometrical center. Any stray field at that particular position, for instance due to the earth permanent field or other contributions such as the stray fields produced by the ion pumps or any electrical device, would then displace the magnetic zero. The MOT center could then lie away from the laser beams crossing point and the capture being drastically reduced. This permanent fields have thus to be compensated for with a set of bias coils pair in Helmholtz-like configurations along the three dimensional axes. Another important aspect is that the quantum description of atomic levels and thus laser polarization is well defined for atoms with a given quantization axis. This axis can be physically defined by a constant magnetic field produced by the bias coils. In our experiment, this point will be relevant when placing the atoms inside the ring cavity to implement CQED schemes with a well defined qubit axis.

4.1.1.1 Coils assembly

Our design aim to combine slowing and trapping with the same pair of magnetic coils in near anti-Helmholtz configuration. To do so, it is mandatory to bring the coils close enough to the output of the oven and use the decaying part of the magnetic field to slow down the atoms. Our coils assembly is thus build in a rectangular architecture that can fit around the glass cell, as shown in figure 4.2(a). The first quadrupole coil is placed around the titanium flange of the glass cell, as close as possible to the main chamber. The second one is placed at the other

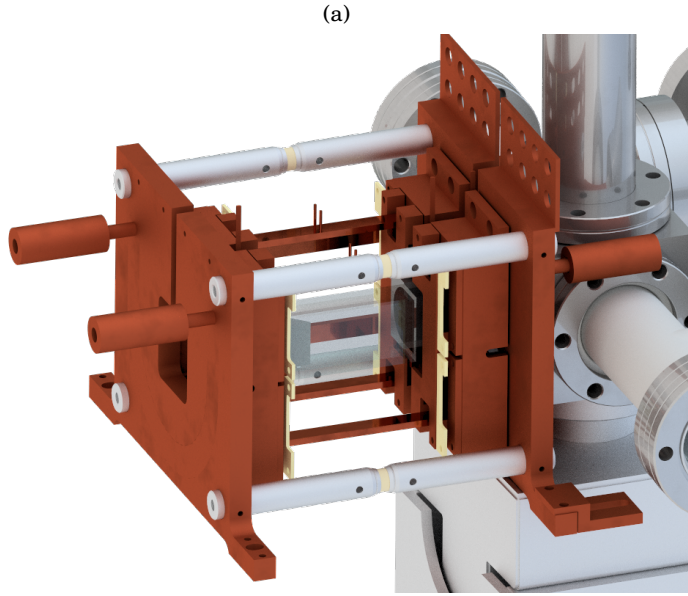
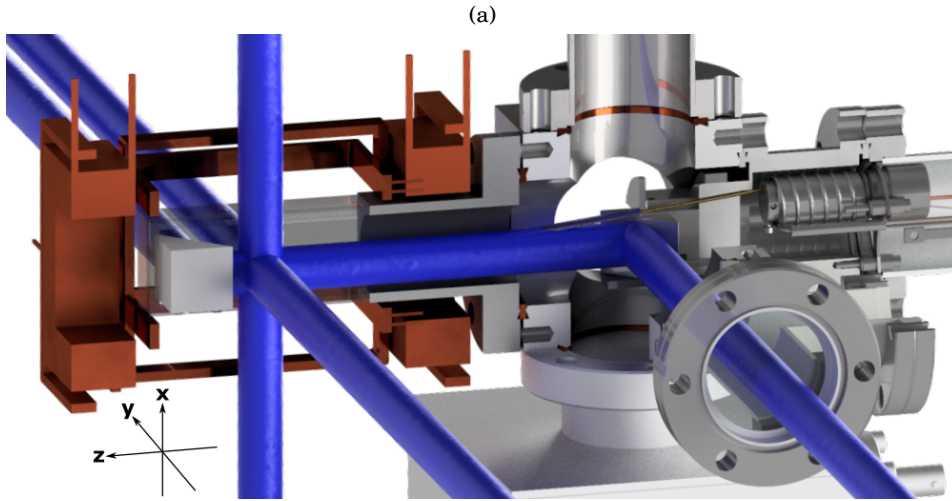


Figure 4.2: (a) CAD of the coils assembly including quadrupole and bias coil pairs maintained by sustaining copper holders. The water cooling pipes entries are visible on the left part of the assembly. (b) Cut inside the vacuum system with selected components showing the MOT and slower laser beams. The quadrupole (thick square) and bias coil pairs (thinner rectangles) are represented without the holders.



extremity of the cell such that the MOT region is defined at a position slightly closer to the under vacuum right-angled mirror prism than the titanium flange. This configuration allows to leave space for the ring cavity on the flange side. The bias z coils are placed around the quadrupole coils themselves. The other two bias pairs are directed along the vertical x and the transverse horizontal y axes compared to the atomic beam, as shown in figure 4.3(a).

As coils crossed by a current produce heat due to Joule's effect, a cooling system is needed. In our setup, it is provided by water at 15°C coming out of a chiller which flows into the coils maintaining pieces. These holders consist in copper plates drilled in a U shape and covered by soldered copper caps with the same shape. Two input and output ports on each holder allow to accommodate water pipes. In normal operation, the coils temperature is typically brought from 50°C to the ambient value. The assembly is held on the same breadboard as MOT and slower

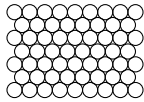
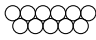
Coils pair	Distance (cm)	Turns	Wire diameter (mm)	Inner radii (cm)
Quadrupole	$L_Q = 8.6$		$d_{Qw} = 2.25$	$R_Q = 2.0$
Bias x	$L_x = 3.46$		$d_w = 1.18$	$R_s = 3.55, R_b = 3.9$
Bias y	$L_y = 3.46$			
Bias z	$L_z = 11.1$			

Table 4.1: Coil pairs geometrical parameters. The turns are represented as a cut view perpendicular to the wire loops. The distance between the coils and the inner radii are given with respect to the closest loop.

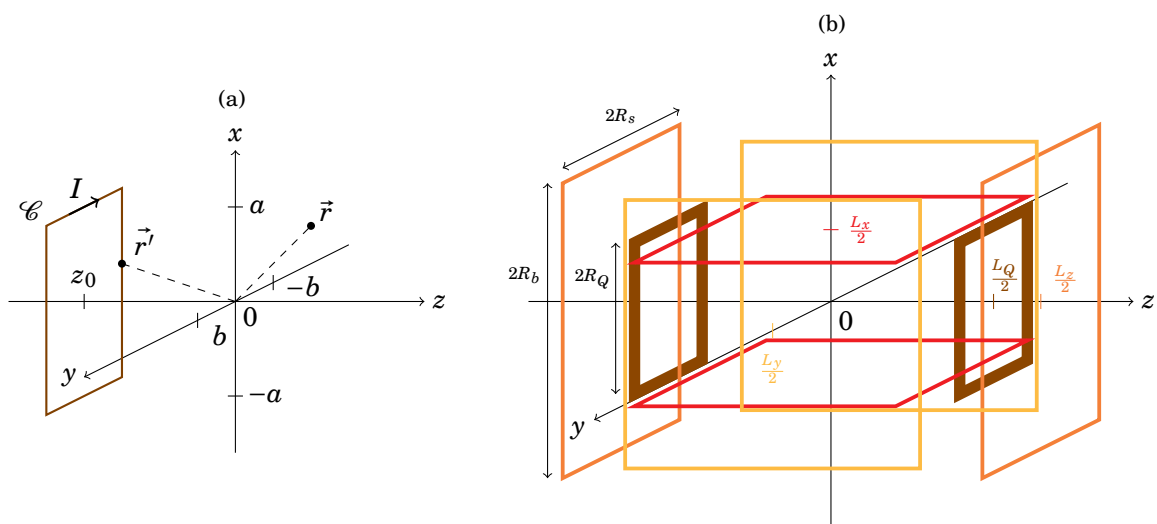


Figure 4.3: (a) Configuration for calculating the magnetic field created by a single rectangular coil. (b) Coil pairs geometry in our assembly. The coil centres are indicated only for the positive axis values. The bias coils have similar rectangular dimensions while the quadrupole pair presents a square geometry.

optics, further described in 4.1.1.2. The coils pairs have a rectangular shape with several turns. Table 4.1 summarizes the different coil geometries and separation distances.

The magnetic field produced by a single rectangular wire crossed by a current of intensity I can be calculated using the Biot-Savart law. For the geometry represented in figure 4.3(a), the field at position \vec{r} created by a coil centred on the position z_0 is given by

$$(4.1) \quad \vec{B}(\vec{r}) = \frac{\mu_0 I}{4\pi} \oint_{\mathcal{C}} d\vec{r}' \wedge \frac{\vec{r} - \vec{r}'}{|\vec{r} - \vec{r}'|^3},$$

where the integration is taken over the closed wire loop \mathcal{C} and \vec{r}' corresponds to the position vector located on \mathcal{C} . According to Herceg *et al.* [167], the three components of \vec{B} can be computed

using the following formulas

$$(4.2a) \quad B_x(\vec{r}) = \frac{\mu_0 I}{4\pi} \sum_{k=1}^4 \frac{(-1)^{k+1}(z - z_0)}{r_k(r_k + d_k)},$$

$$(4.2b) \quad B_y(\vec{r}) = \frac{\mu_0 I}{4\pi} \sum_{k=1}^4 \frac{(-1)^{k+1}(z - z_0)}{r_k(r_k + c_k)},$$

$$(4.2c) \quad B_z(\vec{r}) = \frac{\mu_0 I}{4\pi} \sum_{k=1}^4 (-1)^k \left[\frac{c_k}{r_k(r_k + d_k)} + \frac{d_k}{r_k(r_k + c_k)} \right],$$

with

$$(4.3) \quad \begin{cases} c_1 = c_4 = x + a \\ c_2 = c_3 = x - a \end{cases}, \quad \begin{cases} d_1 = d_2 = y + b \\ d_3 = d_4 = y - b \end{cases}$$

and

$$(4.4) \quad r_k = \sqrt{c_k^2 + d_k^2 + (z - z_0)^2}.$$

Making use of the magnetic field superposition principle, we can compute the actual field for our geometry by summing all the contributions from the wires displayed in table 4.1. The resulting profiles are compared to experimental data in figure 4.4. The fields were measured with a three axis magnetometer placed on translation stages inside the coils assembly, before the assembling on the vacuum system.

In the central region where the MOT is located, the quadrupole field components can be approximated by linear functions. For the bias fields case, one can observe that the x and y coil pairs are near Helmholtz configuration, and produce a constant field in this region. For the z axis, the geometrical constraints force the bias coil pair to be centred around the quadrupole pair in order to let optical access to the cell free. The coils are then separated by a greater distance than their radii. Nevertheless, we can also approximate the bias z field by a constant field near the $\vec{r} = \vec{0}$ position. The total magnetic field produced by the coils assembly can thus be written as

$$(4.5) \quad \vec{B}(\vec{r}) \underset{r \ll \frac{L_Q}{2}}{\simeq} \begin{pmatrix} B_{0x} \\ B_{0y} \\ B_{0z} \end{pmatrix} + \partial_z B \begin{pmatrix} -\frac{x}{2} \\ -\frac{y}{2} \\ z \end{pmatrix},$$

where $\partial_z B$ is the magnetic gradient along the z axis. As we experimentally vary the currents flowing through the coil pairs to tune the different parameters in equation 4.5, it is convenient to express them as $\partial_z B = \partial B'_Q I_Q$ for the quadrupole and $B_{0j} = B'_{0j} I_j$ with $j \in \{x, y, z\}$ for the biases. According to the results presented in figure 4.4, we experimentally find values of $\partial B'_Q = 1.307(2) \text{ G cm}^{-1} \text{ A}^{-1}$, $B'_{0x} = B'_{0y} = 2.341(2) \text{ GA}^{-1}$ and $B'_{0z} = 0.652(2) \text{ GA}^{-1}$.

During the MOT sequence, we need to rapidly switch the gradient from a high value for the blue MOT to a small one for the red MOT, typically going from $\partial_z B \simeq 50 \text{ G cm}^{-1}$ to 1 G cm^{-1} .

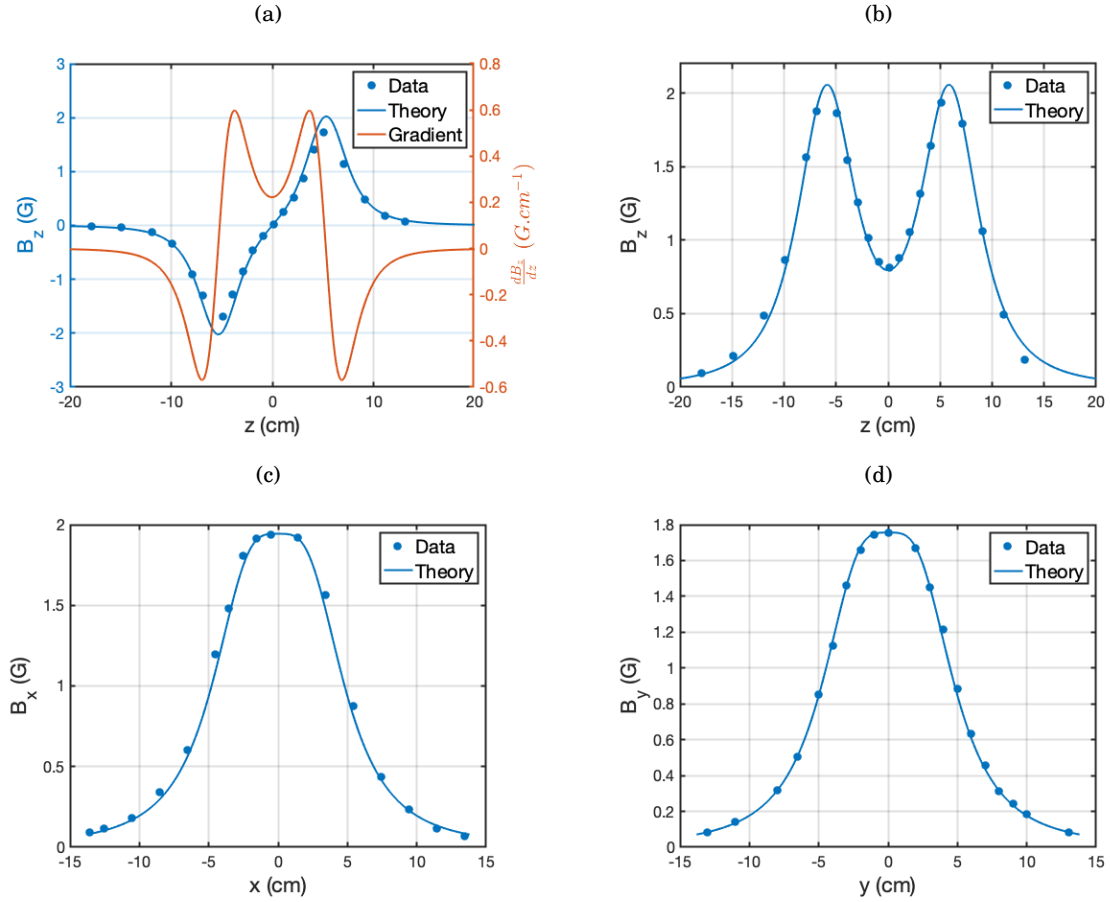


Figure 4.4: (a) Magnetic field produced by the quadrupole coil pair along the z axis for a current $I_Q = 0.15$ A. The theory with not adjustable parameter is represented as a solid blue line, and its derivative as an orange line. (b,c,d) Bias fields along the z , x and y axes produced by the corresponding bias coil pairs for currents $I_z = 1.22$ A, $I_x = 0.83$ A and $I_y = 0.75$ A.

Moreover, when performing absorption images to measure the cloud density, the magnetic fields have to be entirely switched off. To do so, we use the electrical scheme described in figure 4.5(a). Two solid-state relays¹ allow us to switch between the small current I_r , the greater I_b or the sum I_Q inside the quadrupole coils². The sets of resistors and diodes are used as power dissipaters to compensate for the voltage overshoot when opening the relays. A dataset of the magnetic field drop when switching from $I_Q = 23$ A to $I_Q = 1$ A is presented in figure 4.5(b). An exponential fit gives a $1/e$ time constant $\tau = 160 \mu s$.

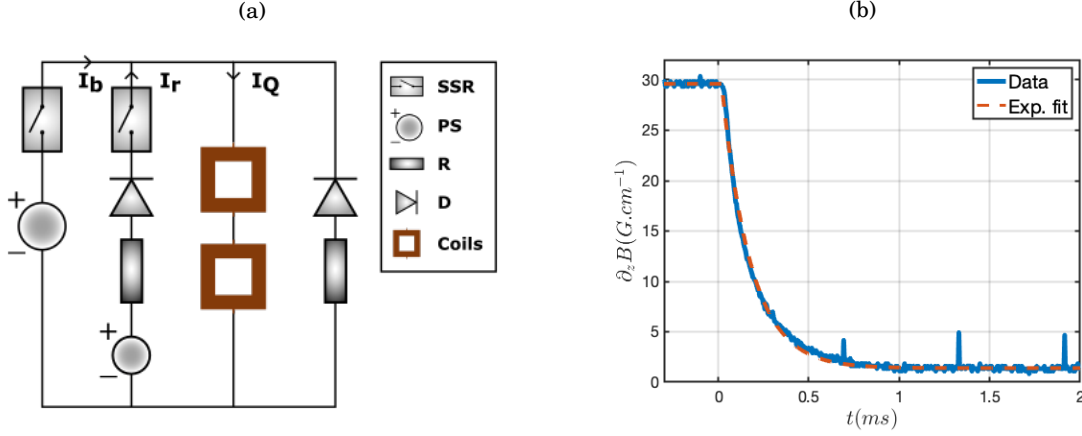


Figure 4.5: (a) Quadrupole coils current supply scheme. SSR : Solid-State Relay, PS : Power Supply, R : Resistor, D : Diode. (b) Magnetic field drop when opening the SSR on the I_b branch (blue solid line) and exponential fit (orange dotted line).

4.1.1.2 Laser beams configuration

In our experiment, the blue and red MOTs are performed along the same spatial axes with laser beams generated by the system described in chapter 2. A CAD in figure 4.3(a) allows for optical access visualization inside the vacuum chamber, and a scheme of the optical configuration in the (y, z) plane is presented in figure 4.6. The blue MOT beams are created with the outputs of the 461nm fiber splitter and $f = 75$ mm lenses, giving a $1/e^2$ radius of 4.9mm. They cross at the MOT position located at the center of symmetry of the quadrupole coils. The vertical and horizontal beams, directed along the \vec{u}_x and $-\vec{u}_y$ vectors, respectively, are transmitted through the glass cell and retro-reflected. The third beam, propagating along the $-\vec{u}_z$ direction, which corresponds to the quadrupole coils central axis, is reflected by both right-angled mirror prisms before going out of the vacuum chamber by the viewport visible in figures 4.3(a) and 4.6. This beam is also retro-reflected after the viewport, fulfilling the six beam configuration necessary for MOT operation. The red beams are similarly produced with a second splitter at 689nm and $f = 25$ mm lenses, giving a smaller radius equal to 2.4mm. We superimpose the two sets of laser beams with dichroic mirrors having a sharp cut-off frequency in the green range³.

On the laser system side, the two repumpers are combined into the same fiber as described in chapter 2, and overlapped with the blue and red MOT beams along the z axis. The output coupler has a focal length of 60mm, defining beam waists of approximately 6.5mm at 679nm

¹Model D1D40 from Crydom. See <http://www.crydom.com/>.

²The current I_b is generated by a power supply SM15-100 from delta elektronika. The second one I_r is produced by a model ES030-5 from the same company. See <https://www.delta-elektronika.nl/>.

³Dichroic beamsplitter FF510-Di02-25x36 from Semrock. See <https://www.semrock.com/>. Warning : the beam-splitter being very thin (1.1mm), tightening too much this optic induce strong aberrations on the MOT beams which become elliptical.

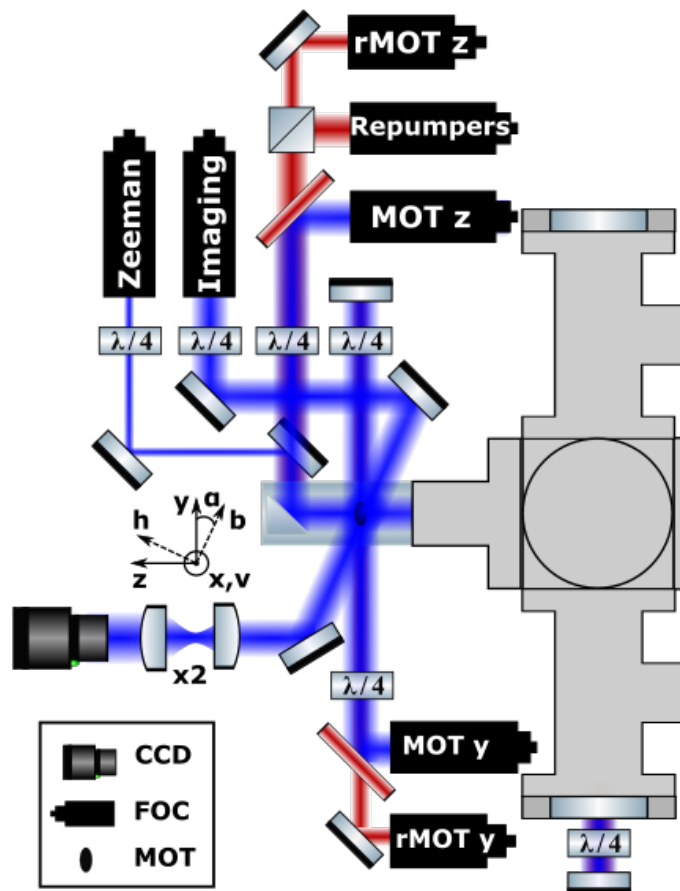


Figure 4.6: Scheme of the MOT, Zeeman slower and imaging optics in the horizontal plane. The fiber output couplers include lenses and half-wave plates. CCD : Charge Coupled Device camera, FOC : Fiber Output Coupler, MOT : Magneto-Optical Trap.

and 6.8 mm at 707 nm. As these lasers have perpendicular polarizations at the fiber input on the laser optical table, we necessarily lose half of the total repumping power when combining them on the polarizing beam splitter in figure 4.6. Nonetheless, the remaining power is sufficient to ensure efficient repumping. The MOT and repumpers beams are circularly polarized when propagating towards the glass cell by a first set of bichromatic quarter-wave plates operating both at 461 nm and 689 nm⁴. At the outputs of the vacuum system, the beams are retro-reflected by dielectric mirrors and a second set of similar waveplates is used to invert their polarizations. The vertical axis x , not represented in figure 4.6, possesses the same configuration as the y axis. The beams are coming from below the breadboard sustaining all the horizontal plane optics and is retroreflected on top of the vacuum system by a mirror held on a circular breadboard with a hole in its center.

⁴Custom quarter-wave plates from Altechna. See <https://www.altechna.com/>.

The Zeeman slower beam is located under the MOT z beam. It reflects onto the right-angled mirror prism under vacuum to counter-propagate with respect to the atomic beam. It is generated by a $f = 4.0\text{mm}$ output coupler and a $\times 2$ telescope, ending with a waist of $600\mu\text{m}$ before the cell. The first lens is placed at a distance slightly higher than its focal length from the fiber output so that the beam is converging inside the vacuum system to match the atomic beam divergence. A zeroth order quarter-wave plate gives the slower a σ_+ polarization inside the cell, accounting for the polarization switches when reflecting onto 45° angled mirrors. A last beam is used to take pictures of the MOT by absorption imaging, collected onto a CCD camera⁵ after a $\times 2$ magnifying telescope. It is also circularly polarized and created by a $f = 100\text{mm}$ lens producing a 7.3mm waist. For optical access reasons, it makes an angle $\alpha = 15^\circ$ with respect to the y axis.

4.1.2 Time sequence generation

In cold atoms experiments, several tasks require a time control setup. In our case, a precise timing is for instance necessary to switch on or off the laser beam powers and magnetic field gradients in order to load the atoms into the blue MOT and transfer them into the red MOT, to create short imaging pulses in order to perform absorption imaging, etc. These timings are determined by a C++ code run onto the experiment control computer. A digital card⁶ generates trigger pulses for the DDS box systems described in appendix C which controls laser powers and frequencies, for the magnetic field solid-state relays status and for a pulse generator⁷ controlling the imaging pulses durations. Two analog cards⁸ output control voltages for the quadrupole and bias coils currents⁹. This configuration allows for a $5\mu\text{s}$ time precision in the trigger pulses generation. The main limitation in the actual physical signals timings is introduced by the SPCI communications from the Arduino to the DDS card inside the DDS boxes described in appendix C. However, the delays introduced during this communication can be measured for each operation and compensated for. They are typically equal to $30\mu\text{s}$, and we separate the critical timing channels on different boxes to avoid issues as much as possible.

4.2 Zeeman slowing of the effusive atomic beam

As a first step towards the production of an ultra-cold atomic sample in the MOT, the effusive atomic beam emitted by the oven needs to be slowed down from a mean velocity of several hundreds of meters per second to a near-zero value. In 1981, Phillips & Metcalf proposed a

⁵Blackfly GigE camera, model BFLY-PGE-23S6M-C by FLIR. See <https://www.flir.com/products/blackfly-gige/?model=BFLY-PGE-23S6M-C>.

⁶Card PCI-DIO-32HS from National Instruments.

⁷Model DS345 from Stanford Research Systems. See <https://www.thinksrs.com/>.

⁸Card PCI6733 from National Instruments.

⁹Current control on delta eltronika power supplies with ISO AMP modules.

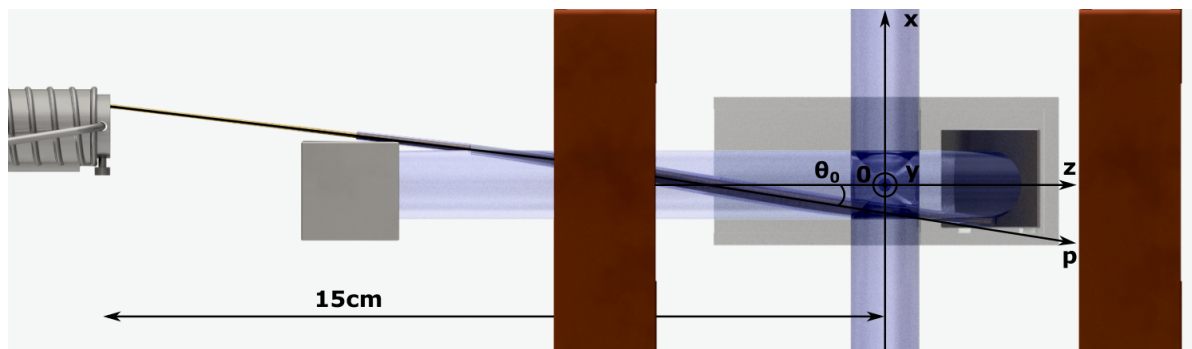


Figure 4.7: On scale geometry of the experiment for Zeeman slowing and MOT operations with the quadrupole coil pair.

method to decelerate sodium atoms using a spatially varying magnetic field [168]. Indeed, atomic slowing is done by sending a laser beam towards the particles in order to obtain a mean force due to photonic recoils directed along the light propagation axis. The arising problem is that atoms with changing velocities will see a different Doppler shift along their propagation. The idea of the procedure, known as Zeeman slowing and implemented in numerous experiments, is to compensate for the Doppler shift seen by the counter-propagating particles with the Zeeman effect.

4.2.1 Constant deceleration slower theory

The originally proposed Zeeman slowing procedure is based on the constant deceleration of atoms by the laser beam. In order to derive the equations corresponding to this physical situation, we consider an atomic beam propagating along an axis p as pictured in figure 4.7. The laser addresses an hyperfine transition $|F_g, m_{F_g}\rangle \rightarrow |F_e, m_{F_e}\rangle$, with a resonance frequency ω_0 . The scattering force induced by the laser field with a wave vector \vec{k} and a detuning $\Delta_0 = \omega - \omega_0$ is given by

$$(4.6) \quad \vec{F} = \hbar \vec{k} \frac{\Gamma}{2} \eta,$$

where η corresponds to the scattering rate written as

$$(4.7) \quad \eta = \frac{s_0}{1 + s_0 + \left(\frac{2\Delta}{\Gamma}\right)^2}.$$

In this equation, the ratio between the laser and saturation intensities $s_0 = I_0/I_{sat}$ is the saturation parameter [169]. The detuning Δ seen by an atom at velocity v in a magnetic field of amplitude B is shifted both by the Doppler and Zeeman effects such that

$$(4.8) \quad \Delta = \Delta_0 - \vec{k} \cdot \vec{v} - (m_{F_e} \gamma_{F_e} - m_{F_g} \gamma_{F_g}) B,$$

with $\gamma_F = g_F \mu_B / \hbar$ the gyromagnetic ratio of a state with a Landé factor g_F .

A constant atomic deceleration $a_0 = -|\vec{F}|/m$ can be obtained if the scattering force is also kept constant. According to equations 4.6 and 4.7, this statement is fulfilled if the detuning also remains constant over the propagation. The energy conservation from the output of the oven located at position p_0 to a location p is given by

$$(4.9) \quad \frac{1}{2}mv^2(p_0) = \frac{1}{2}mv^2(p) - \int \vec{F} \cdot \vec{u}_p dp.$$

Combining equations 4.6, 4.8 and 4.9 gives the theoretical magnetic profile for constant deceleration

$$(4.10) \quad B(p) = B(p_0) + \Delta B \left(1 - \sqrt{1 - \left(\frac{p - p_0}{L} \right)^2} \right).$$

Considering, for simplicity, a fine structure $|J_g = 0, m_{J_g} = 0\rangle \rightarrow |J_e = 1, m_{J_e} = m_J\rangle$ transition such as the blue and red transitions of the strontium bosonic isotopes, the field at the oven output can be expressed as

$$(4.11) \quad B(p_0) = \frac{\Delta_0 - \Delta + kv(p_0)}{m_J \gamma_J},$$

the field amplitude as

$$(4.12) \quad \Delta B = -\frac{kv(p_0)}{m_J \gamma_J},$$

and the slower length as

$$(4.13) \quad L = \frac{mv^2(p_0)}{\eta \hbar k \Gamma}.$$

The magnetic profile from equation 4.10 is represented in figure 4.8(a). One can notice that two configurations are possible for the laser beam polarisation. Indeed, either a σ_+ beam with a negative magnetic field or a σ_- polarisation with a positive field provides efficient slowing. In order to be consistent with the following MOT descriptions and the field presented in 4.4(a), we choose the $m_J = +1$ and $\Delta B < 0$ configuration.

A convenient experimental choice for the Zeeman slower consists in taking $B(p_0) \simeq 0$ and $\Delta = 0$ in equation 4.10, which leads to $\Delta_0 = -kv(p_0)$. For our oven heated to 450°C, the mean velocity of the atomic beam is $\bar{v} = 500 \text{ ms}^{-1}$. Capturing atoms with velocities $v < \bar{v}$ would lead in this context to a Zeeman shift $\Delta_0/2\pi = -1.1 \text{ GHz}$, a magnetic field amplitude $\Delta B = -530 \text{ G}$ and a length $L = 27 \text{ cm}$ for a saturation parameter $s_0 = 1$.

4.2.2 Quadrupole slower

The beauty of Zeeman slowing lies in the fact that all the velocity classes below the capture velocity $v(p_0)$ can be slowed and potentially trapped by the MOT beams. Moreover, even if the spatial magnetic profile differs from the one in equation 4.10, the atoms can still non-constantly decelerate, at the cost of presenting a higher probability of being lost from the slowing procedure. For instance, we can use the decaying part of the quadrupole field between the oven and the first coil as an effective slower. A key point in this configuration is that the effective length of the slower is fixed by the position of the first quadrupole coil to $L = 10$ cm. The distance between the oven and the MOT being equal to 15 cm, the atoms have to travel for 5 cm inside the cell before being captured by the MOT beams. The velocity at the end of the slower should therefore not be strictly null. Figure 4.8 compares the constant deceleration profile derived in equation 4.10 to the quadrupole magnetic field expressed in equation 4.2c.

Experimentally, the slower beam is produced by the blue Zeeman slave laser as described in chapter 2. It typically has a power of 10 to 12 mW and a waist of 200 μ m, slightly converging to match the atomic beam transverse expansion. In order to characterise the slowing effect, we recorded fluorescence spectra inside the vacuum system with the Zeeman slower beam fixed at a detuning δv_{ZS} and a probe beam scanned across the 461 nm resonance. The two lasers were combined on a beam splitter and circularly polarized by a quarter wave-plate. Similarly to the effusive beam characterization scheme presented in figure 3.15(a) in chapter 3, a photodiode and a collection lens were placed perpendicularly to the glass cell on the MOT optics breadboard in order to record the fluorescence of the atomic beam. The results are presented in figure 4.8(b).

As described in 3.4.2.1, the probe laser gets on resonance with a longitudinal velocity class v_p at the detuning $\Delta_0 + kv_p = 0$. Rescaling the probe laser detuning by $-1/k$ thus give access to the density of probability of the longitudinal velocity, broaden by the strontium response function. We observe a strong modification of the probability distribution in the low velocity region compared to the atomic beam in the absence of slower beam, shown in figure 3.15(b). The presence of an absorption peak in this region proves the efficiency of the quadrupole slowing procedure, which splits the distribution into a slowed ensemble and a fast fraction, not captured by the MOT beams. The slow fraction peak amplitude is increased for higher absolute values of the Zeeman slower detuning in the explored range of $\delta v_{ZS} \in [-750 \text{ MHz}, -350 \text{ MHz}]$. However, we will show in 4.4.3 that the optimum value for the combined slowing and blue MOT operation lies in between these maximum values.

4.3 MOT regimes and mechanisms

The textbook description of a MOT originally described by Jean Dalibard and collaborators is defined for a $|J_g = 0\rangle \rightarrow |J_e = 1\rangle$ transition. In this section, we derive the MOT equations in

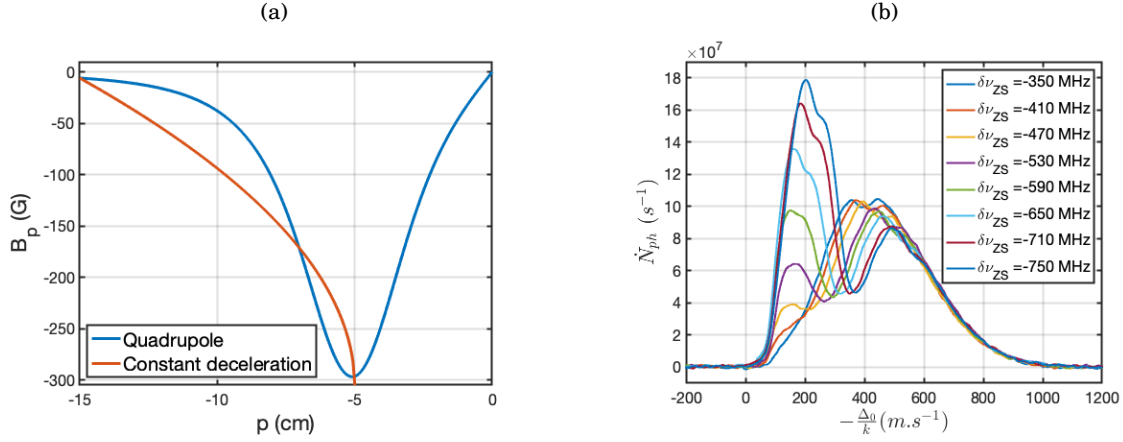


Figure 4.8: (a) Quadrupole field with $I_Q = 25$ A (blue) and constant deceleration magnetic profile with $\Delta B = 300$ G (orange) along the atomic beam axis p . The oven is located at $p_0 = -15$ cm compared to the MOT region at $p = 0$. (b) Fluorescence spectra of the atomic beam facing a Zeeman slower laser of saturation parameter $s_0 = 50$ for different fixed Zeeman detunings $\delta\nu_{ZS}$. The signal is recorded with a low saturation probe beam scanned across the resonance at detuning Δ_0 for a constant magnetic gradient $\partial_z B = 35$ G cm⁻¹.

this framework, allowing to define different cooling regimes based on the comparison between scattering and recoil effects. In a second part, a more complicated description of the MOT mechanisms, including hyperfine structure effects, is described. This description is involved in the fermionic strontium MOT operations, as the ⁸⁷Sr isotope presents a nuclear spin $I = 9/2$.

4.3.1 $|J_g = 0\rangle \rightarrow |J_e = 1\rangle$ MOT description

As opposed to the majority of alkaline MOTs presenting an hyperfine structure, some alkaline-earth isotopes possess the basic structure for simple MOT operation between a $|J_g = 0\rangle$ ground state and a $|J_e = 1\rangle$ excited state. It is for instance the case for the bosonic strontium isotopes, operating on the $|(5s^2)^1S_0\rangle \rightarrow |(5s5p)^1P_1\rangle$ or $|(5s^2)^1S_0\rangle \rightarrow |(5s5p)^3P_1\rangle$ transitions. The MOT ingredients are a set of three pairs of counter-propagating laser beams with circular and opposite polarizations on each Cartesian axis, in combination with a quadrupole magnetic field as represented in figure 4.9(a). A simple derivation of the MOT equations can be done in one dimension, with the scheme represented in figure 4.9(b).

Considering for instance the z axis, a σ_- beam is sent towards the negative axis region while a σ_+ one propagates towards the positive region. According to equation 4.6, the sum of the two scattering forces projected on the z axis writes down

$$(4.14) \quad F_z = \hbar k \frac{\Gamma}{2} \left[\frac{s_{0+}}{1 + s_{0+} + \left(\frac{2\Delta_+}{\Gamma}\right)^2} - \frac{s_{0-}}{1 + s_{0-} + \left(\frac{2\Delta_-}{\Gamma}\right)^2} \right],$$

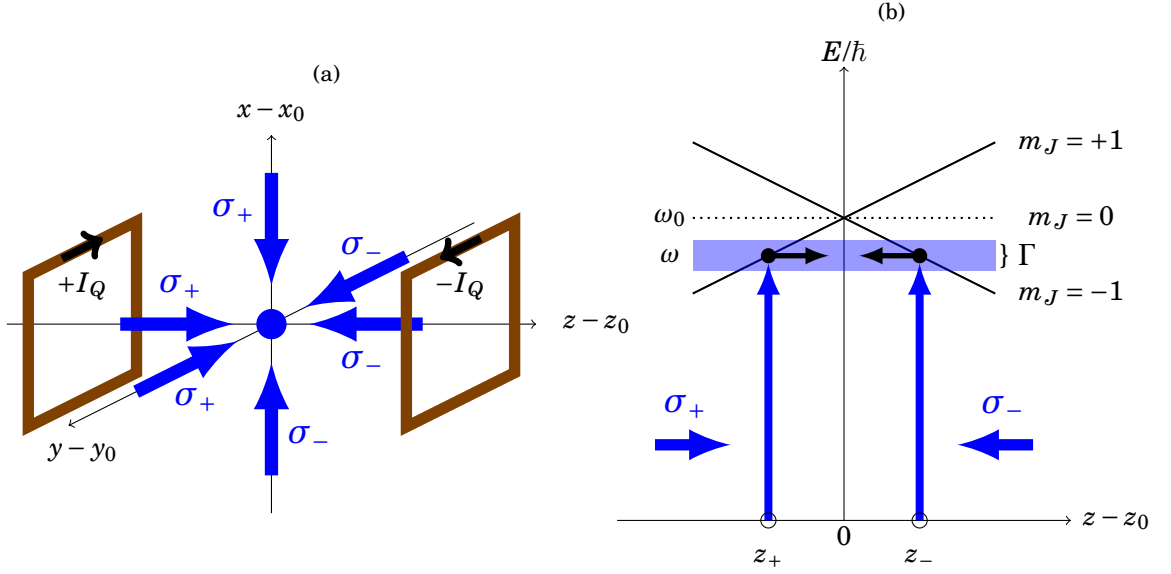


Figure 4.9: (a) Three-dimensional scheme of the MOT with three pairs of counter-propagating circular beams. The quadrupole coils are represented with opposite running currents generating the magnetic field linear dependency in the MOT region. (b) One dimensional scheme of a $|J_g = 0\rangle \rightarrow |J_e = 1\rangle$ MOT. A pair of beams with opposite circular polarizations addresses an atomic cloud exposed to the quadrupole magnetic field gradient. The excited Zeeman states energies are represented as a function of the spatial coordinate z .

with $s_{0\pm}$ the saturation parameters and $\Delta_{\pm} = \Delta_0 \mp \gamma_J B \mp k v_z$ the detunings for the corresponding polarizations. Both beam frequencies are set equal and red detuned compared to the bare atomic transition ($\Delta_0 < 0$). When $\Delta_{\pm} = 0$, the scattering force in equation 4.14 is maximum for the corresponding beam. As stated in equation 4.5, the magnetic field is linear in the central region of the coils. The resonance condition for the Zeeman part of the detuning is thus fulfilled at positions z_{\pm} defined as

$$(4.15) \quad z_{\pm} = \pm \frac{\Delta_0}{\gamma_J \partial_z B} + z_0,$$

where $z_0 = -B_{0z}/\partial_z B$ corresponds to an offset position due to non-zero bias fields. Atoms approaching these positions experience a higher scattering force from the beam pointing towards the central region than the one expelling them from the center, thus inducing restoring forces towards the magnetic field zero. Moreover, they coherently absorb photons along the z axis and scatter them in a random direction. Averaging over several absorption-emission cycles thus produces a mean velocity reduction $\langle \delta v \rangle = -\hbar k/m$, independent of the polarization. In the end, the MOT both traps and slows down the atoms, based on state selective laser absorption. In a paper published in 1989, Castin, Wallis & Dalibard made a clear distinction between two different MOT regimes, depending on the balance between the scattering and the recoil effects [170]. These regimes are described in the following paragraphs.

Transition	λ	$\Gamma/2\pi$	I_{sat}	$\hbar\Gamma/E_r$	T_D	T_r
Blue	460.862 nm	32 MHz	42 mW cm ⁻²	3×10^3	770 μ K	1.03 μ K
Red	689.449 nm	7.4 kHz	3 μ W cm ⁻²	1.6	180 nK	460 nK

Table 4.2: Relevant set of parameters for strontium cooling on the blue and red transitions.

4.3.1.1 Doppler cooling

In the first MOT regime, referred to as the Doppler regime, the natural energy width of the excited state $\hbar\Gamma$ is large compared to the recoil energy $E_r = \hbar^2 k^2 / 2m$. The competition between coherent cooling by the MOT lasers and the incoherent heating from photon scattering is well described by a semi-classical Fokker-Planck approach, physically corresponding to Brownian diffusion in momentum space [21]. For low-saturation beams with equal powers $s_{0+} = s_{0-} \ll 1$, a minimum for the final temperature is obtained for $\Delta_0 = -\Gamma/2$. This so-called Doppler temperature T_D is given by

$$(4.16) \quad k_B T_D = \frac{\hbar\Gamma}{2}.$$

In the low density regime, a simple argument consists in approximating the restoring force by an harmonic potential. Making use of the equipartition theorem, the typical size $\langle z^2 \rangle$ of the cloud is given by

$$(4.17) \quad \langle z^2 \rangle \simeq \frac{\Gamma}{4s_0 k \gamma_J \partial_z B}.$$

4.3.1.2 Narrow-line cooling

The second regime corresponds to $\hbar\Gamma \leq E_r$. In these conditions, the situation is fairly different from the Doppler case as only one scattering event can bring the laser beams out of resonance. The quantum nature of the light can then no longer be neglected, justifying the name quantum or narrow-line MOT regime. The minimum temperature is then no longer limited by the natural linewidth Γ , but rather by the recoil temperature T_r defined as

$$(4.18) \quad k_B T_r = \frac{\hbar^2 k^2}{m}.$$

The different parameters for the blue and red strontium transitions are presented in table 4.2. It shows that the blue MOT is operating in the Doppler regime, while the red MOT stands in the narrow-line regime.

4.3.2 Strontium fermionic MOT

For atomic species presenting an hyperfine structure, the MOT description is complicated by the fact that more atomic levels have to be taken into account. It is the case for the fermionic isotope

^{87}Sr , which has a nuclear spin $I = 9/2$. In addition to the hyperfine splitting between the different $F = I + J$ manifolds, the energy dependency on magnetic fields of the Zeeman states $|F, m_F\rangle$ within each manifold is modified through the Landé factor g_F . Considering a transition from a ground-state Zeeman level $|F_g, m_{F_g}\rangle$ to an excited $|F_e, m_{F_e}\rangle$, we can define an energy difference Δ_Z due to the Zeeman shift as follows

$$(4.19) \quad \hbar\Delta_Z = (m_{F_e}g_{F_e} - m_{F_g}g_{F_g})\mu_B B(z).$$

The hyperfine Landé factor calculation arise from the sum of the nuclear contribution governed by the factor g_I and the fine structure factor g_J , proportional to the electronic spin factor g_S [171]. It results in the following expressions

$$(4.20) \quad g_F = g_J \frac{F(F+1) + J(J+1) - I(I+1)}{2F(F+1)} - g_I \frac{F(F+1) - J(J+1) + I(I+1)}{2F(F+1)},$$

with

$$(4.21) \quad g_J = \frac{J(J+1) + L(L+1) - S(S+1)}{2J(J+1)} + g_S \frac{J(J+1) - L(L+1) + S(S+1)}{2J(J+1)}.$$

The spin factor is given by $g_S \simeq 2$. Generally, the nuclear contribution in equation 4.20 is neglected, as $g_I \ll g_S$. Indeed, the ratio of the two constants is equal to 658 according to [172].

The fundamental principle of the MOT is to induce light forces that bring back the atoms moving away from the center of the trap to this location. In the 1D case, described in the previous paragraph, this statement is fulfilled if σ_- (σ_+) resonances occur on the $z - z_0 > 0$ ($z - z_0 < 0$) region. These conditions can be expressed by fixing the sign of Δ_Z for the two different types of transitions in the appropriate region, reducing to

$$(4.22) \quad \frac{F_e - 1}{F_e} < \frac{g_{F_e}}{g_{F_g}} < \frac{F_g}{F_g - 1}.$$

A situation where the σ_+ and σ_- transitions occur on the same side of the z axis is made possible if equation 4.22 is not satisfied. This situation can induce drastic changes in the MOT operation. Indeed, one of the two transitions would bring the atoms back to the trap center, while the other one repels them and create MOT losses. For instance, considering our case of interest composed of a $|J_g = 0\rangle$ ground-state and a $|J_e = 1\rangle$ excited state, one immediately see from equation 4.20 that the electronic part of the Landé factor is reduced to 0. As the nuclear dependency to magnetic fields is extremely reduced compared to the electronic contribution, the ground-state manifold levels are basically insensitive to the MOT gradient, while the excited Zeeman states are shifted by an amount proportional to g_{F_e} , as shown in figure 4.10(a). Taking as an example an ^{87}Sr atom in the $z < 0$ region with a spin projection $m_{F_g} = 9/2$, it can absorb a σ_+ photon on the transition towards $m_{F_e} = 11/2$ that would decelerate it, but can also be resonantly driven by the σ_- transition towards $m_{F_e} = 7/2$ and be accelerated away from the magnetic field zero. This situation is

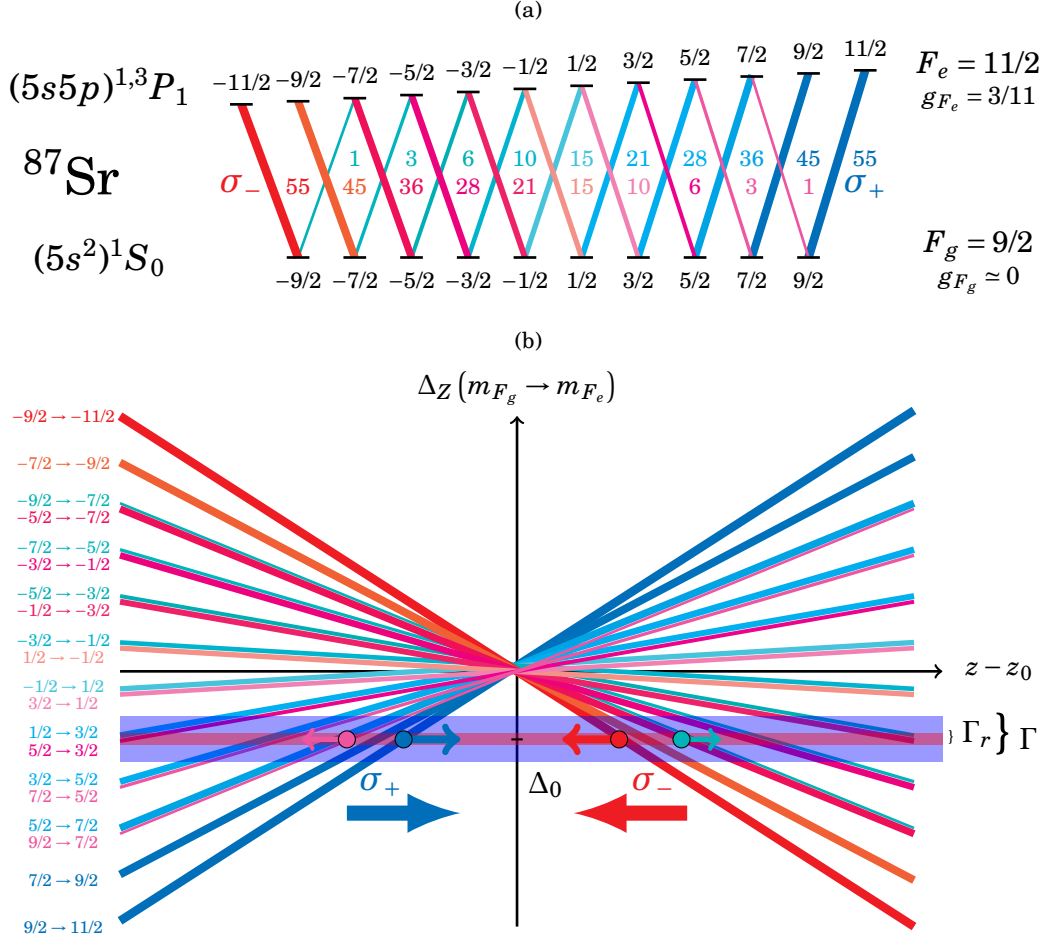


Figure 4.10: (a) Energy levels and relative transition strengths $c_{m_F}^2 \times 165$ for the dipole allowed and the intercombination transitions of ^{87}Sr . (b) As $g_{F_g} \ll g_{F_e}$, some σ_- (σ_+) are brought on resonance in the negative (positive) $z - z_0$ region, producing anti-trapping forces. This situation is represented for an atom in the stretched $m_{F_g} = 9/2$ ($-9/2$) ground state in the left (right) part of the graphic. The dipole allowed transition is represented as a broad blue line of width Γ , while the intercombination line corresponds to the smaller red line of width Γ_r .

exposed in figure 4.10(b). Fortunately, the Clebsch-Gordan coefficients favour the transitions to the stretched states which are trapping over the $|m_{F_e}| < |m_{F_g}|$ anti-trapping transitions, as can be seen in figure 4.10(a).

To summarize, we can emphasize two simple conditions for which the inequalities in equation 4.22 are not satisfied :

CONDITION 1 : $g_{F_g} \ll g_{F_e}$ ($J_g = 0$).

CONDITION 2 : $F_e > 2$.

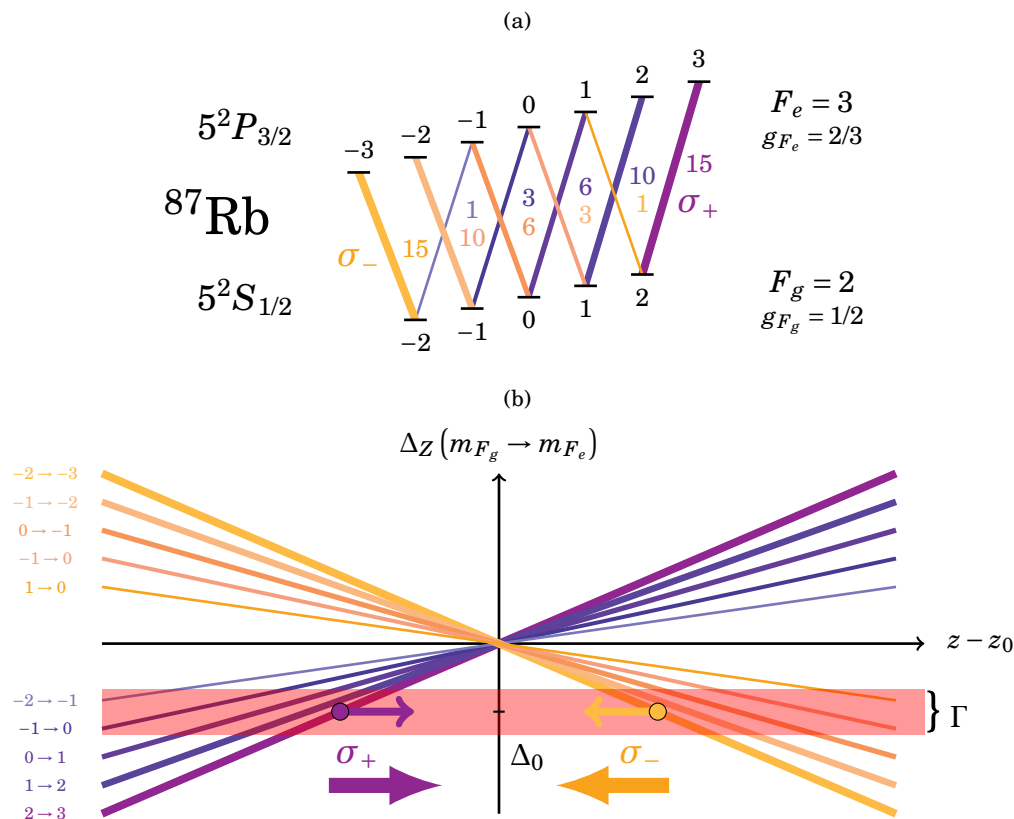


Figure 4.11: (a) Energy levels of ^{87}Rb for MOT operation on the D_2 line. The different Zeeman transitions are represented by coloured lines with the corresponding relative transition strengths $c_{m_F}^2 \times 30$ from equation 3.37. (b) Zeeman detunings for the $|5^2S_{1/2}, F_g = 2, m_{F_g}\rangle \rightarrow |5^2P_{3/2}, F_e = 3, m_{F_e}\rangle$ transitions along the z axis. The σ_+ and σ_- transitions can be separated in two distinct manifolds, all trapping the atoms toward the MOT center as shown for the stretched states.

For neutral alkalis, the first condition can not be verified due to the fact that the electronic spin projections S , and thus J , are only half-integers. To illustrate this purpose, we compare the ^{87}Rb MOT operation to the ^{87}Sr one in figures 4.10 and 4.11, respectively.

The MOT dynamics also play an important role in this anti-trapping process. Indeed, if the atoms are randomly distributed in the Zeeman ground states, the mean resulting force is still restoring the atoms to the trap center. This situation naturally appears for the dipole allowed ^{87}Sr MOT, where the natural linewidth is large compared to the recoil frequency shift and thus rapidly randomizes the sublevels populations. The effect is also increased by the vicinity of the $F_e = 7/2$ and $F_e = 9/2$ manifolds, which contributes to the population redistribution. In the red MOT case, the situation is different as each scattering event brings the atoms out of resonance. An ^{87}Sr atom absorbing a photon from the previously described anti-trapping transitions would

then be lost from the trap. The solution proposed by Mukaiyama *et al.* from the University of Tokyo is to add a “stirring” laser on the $| (5s^2)^1S_0, F_g = 9/2 \rangle \rightarrow | 5s5p^3P_1, F_e = 9/2 \rangle$ transition [173]. This state presents a 4.5 times lower magnetic field dependency than the $F_e = 11/2$ state, which induces resonances on a longer period and on an extended spatial region, thus redistributing the populations inside the Zeeman levels. As will be described in 4.5.1.1, another alternative to this problem is to use the recently developed *Saw-tooth WAve Adiabatic Passage* (SWAP) technique, which has been proven efficient to trap the fermionic strontium isotope without making use of a stirring laser [174].

4.4 Cooling on the dipole allowed blue transition at 461 nm

As described in section 4.3, the strontium blue MOT operates in a regime where scattering events dominates the cloud dynamics. In this section, the MOT characterization methods and results are detailed. Starting from the description of absorption imaging, used to determine the MOT population and temperature, we define the experimental procedure leading to a cold strontium sample using the 461 nm transition. As our apparatus combines Zeeman slowing and cooling in a single magnetic configuration, an optimization of the trap loading efficiency using the Zeeman slower beam is then presented. Finally, a full characterization of the blue MOT with respect to the different optical powers and detunings is given.

4.4.1 Absorption imaging

Cold atomic ensemble characterizations necessitate quantitative imaging processes. The common solutions are provided by either absorption or fluorescence imaging techniques. The later being more sensitive to calibration procedures, as no optical system can collect all the light coming out of the atomic sample and the detectors such as photodiodes do not have a perfect efficiency, absorption imaging provides a more direct determination of the atomic density. In the following paragraphs, we detail the calculations leading from the imaging beam intensity absorption to the atom number determination, as well as temperature measurement using the cloud expansion after a controlled expansion time.

4.4.1.1 Number of atoms calculation

The atomic detection is performed using absorption imaging on the blue transition at 461 nm. The basic principle of this technique is to take a picture of an imaging beam on resonance with the atomic cloud at frequency ω_0 after propagating through it and compare this image to the beam intensity without atoms. The intensity of the absorbed beam with atoms in the cell and the reference beam without atoms are noted I_w and I_{wo} , respectively. The shadow let by the atoms on the beam gives information on their number. In practice, a picture I_{dark} without any beam is also needed in order to compensate for stray light incoming on the CCD camera. The corrected

intensities are defined as $I_w^* = I_w - I_{dark}$ and $I_{wo}^* = I_{wo} - I_{dark}$. We consider a beam propagating along the b axis as pictured in figure 4.6. According to the Beer-Lambert law, the absorption can be written for a fine structure $|J_g = 0\rangle \rightarrow |J_e = 1\rangle$ transition and neglecting the Doppler effect as

$$(4.23) \quad \frac{dI}{I} = -n(h, v, b) \frac{\sigma_0}{1 + I(h, v, b)/I_{sat}} db,$$

with $\sigma_0 = 3\lambda^2/2\pi$ the atomic resonant cross section [175]. This equation allows to compute the column density of atoms n_c as

$$(4.24) \quad n_c(h, v) = \int_{-\infty}^{+\infty} n(h, v, b) db = \frac{1}{\sigma_0} \ln \left(\frac{I_{wo}^*(h, v)}{I_w^*(h, v)} \right) + \frac{I_{wo}^*(h, v) - I_w^*(h, v)}{\sigma_0 I_{sat}},$$

where we identify $I_{wo}^* = I(h, v, -\infty)$ and $I_w^* = I(h, v, +\infty)$.

As the CCD camera collects photons on pixels of effective area $A = (g \times p)^2$, where g is the magnification of the imaging system and p the actual pixel size, we have access to the corrected number of counts per pixel N_c^* . This quantity is proportional to the corrected intensity and can be expressed as

$$(4.25) \quad N_c^*(h, v) = G\eta \frac{TA\tau}{\hbar\omega_0} I^*(h, v),$$

where G corresponds to the CCD gain in counts per electron, η to the quantum efficiency of the chip in electrons per photon and the right part of the equation corresponds to the number of photons at the MOT position, taking into account the glass cell transmission T and the imaging pulse duration τ . Physically, the maximum of energy that a saturated atom can scatter corresponds to the saturation intensity multiplied by the cross-section such that

$$(4.26) \quad \sigma_0 I_{sat} = \frac{\Gamma}{2} \hbar\omega_0.$$

Integrating equation 4.24 over the pixel size along h and v , rewritten by means of equations 4.25 and 4.26, gives the number of atoms per pixel N expressed as

$$(4.27) \quad N(h, v) = \frac{A}{\sigma_0} \ln \left(\frac{N_{wo}^*(h, v)}{N_w^*(h, v)} \right) + \frac{2}{G\eta\Gamma T\tau} [N_{wo}^*(h, v) - N_w^*(h, v)].$$

In our system, the well depth capacity of 33×10^3 electrons converts into a maximum number of photons of 27×10^3 per pixel by the quantum efficiency $\eta = 0.8$ at 461 nm. The peak intensity at the camera position, even for short pulse durations of 5 μ s, can thus not exceed 2 mW cm⁻². In order not to saturate the camera, we use an imaging beam of power $P_{Im} = 800 \mu$ W and waist $w_0 = 7.3$ mm corresponding to approximately half the maximum intensity previously derived. The relatively large size of the beam is chosen to allow for direct imaging of the atomic transport from the MOT region to the ring cavity in the future version of the experiment. This configuration corresponds to a very low saturation parameter $s_0 = 0.02$. As the variance of the measured

number of atoms scales as $\sqrt{s_0}$ due to the *Photon Shot Noise* (PSN), and the number of photons scattered by the atoms as $s_0/(1 + s_0)$, an optimal signal-to-noise ratio is obtained around $s_0 = 1$ [176, 177]. Our current imaging setup is thus limited by the camera properties and the large saturation intensity of the blue transition. To tackle this problem, separated imaging systems could be implemented for the MOT and the transport to the cavity, with a reduced waist of the imaging beam in the MOT region in order to increase the saturation parameter while keeping the optical power constant.

4.4.1.2 Temperature determination by time-of-flight experiment

Widely used in the context of cold atoms [178], the time-of-flight technique allows to measure temperatures as cold as the one produced in MOT clouds, namely in the nK to mK range. The idea consists in releasing the atoms from the trap, and perform an absorption or fluorescence image after a given time t . Doing so, the initial momentum distribution of the cloud is mapped onto its spatial distribution. Indeed, neglecting interactions during the expansion, the momentum vector components p_i are linked to the spatial dimensions of the cloud through $p_i = mr_i/t$, with $i \in \{x, y, z\}$. The spatial distribution variance thus simply reflects the velocity variance as $\sigma_i^2(t) = \sigma_{v_i}^2(0)t^2$.

In the context of the MOT, the initial phase-space density distribution is ruled by the light forces on one side, and by the photon emission and reabsorption between atoms on the other side [179]. For a small reabsorption cross-section compared to the absorption one, which corresponds to a small number of atoms and thus low densities, the second effect can be neglected and both spatial and velocity distributions are found to be Gaussian. This type of MOTs are called thermal clouds as the atomic velocities follow a Maxwell-Boltzmann distribution with a variance $\sigma_{v_i}^2(0) = k_B T_i / m$. Assuming an initial spatial extension σ_{0i} along dimension i , such cloud expands as

$$(4.28) \quad \sigma_i^2(t) = \sigma_{0i}^2 + \frac{k_B T_i}{m} t^2.$$

A series of absorption images at different times of flight is given in figure 4.12(a), showing an example of typical cloud expansion. At these short times of flight, the influence of gravity is not visible. A summation over the images vertical axes is given in figure 4.12(b). With a Gaussian fit on this data, we extract the radius σ_h at different times, which corresponds to the CCD camera horizontal axis. The horizontal and vertical radii are reported in figure 4.12(c). Using equation 4.28, it gives a temperature $T_h = 14.7$ mK on the horizontal axis and $T_v = 11.8$ mK on the vertical one for this particular unoptimized blue MOT.

Comments on the Gaussian fit procedure : An important aspect in temperature determination lies in the fact that the MOT can be fitted with a two dimensional Gaussian function

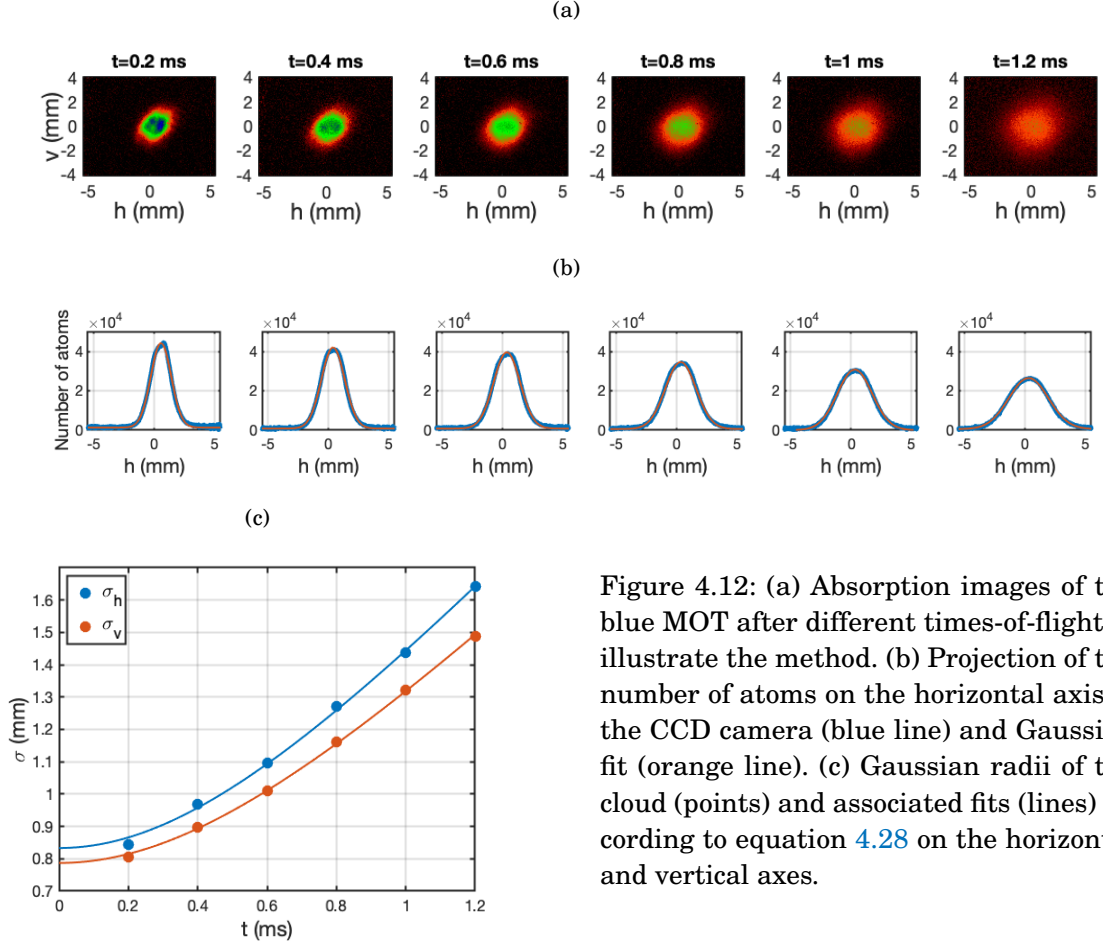


Figure 4.12: (a) Absorption images of the blue MOT after different times-of-flight to illustrate the method. (b) Projection of the number of atoms on the horizontal axis of the CCD camera (blue line) and Gaussian fit (orange line). (c) Gaussian radii of the cloud (points) and associated fits (lines) according to equation 4.28 on the horizontal and vertical axes.

presenting varying proper axes over the free fall. Labelling θ the angle between the smallest axis of the MOT and the horizontal direction of the camera h , these coordinates write down

$$(4.29) \quad \begin{pmatrix} h_\theta - h_{\theta 0} \\ v_\theta - v_{\theta 0} \end{pmatrix} = R(\theta) \begin{pmatrix} h - h_0 \\ v - v_0 \end{pmatrix},$$

with $R(\theta)$ the 2D rotation matrix. The number of atoms is thus expressed as

$$(4.30) \quad N(h_\theta, v_\theta) = N_0 e^{-\frac{(h_\theta - h_{\theta 0})^2}{2\sigma_{h\theta}^2} - \frac{(v_\theta - v_{\theta 0})^2}{2\sigma_{v\theta}^2}}.$$

Taking a two dimensional Gaussian fit to extract the temperature would then be sensitive to the MOT tilt θ . Instead, fitting the projections on the horizontal and vertical axes of the camera rules out this problem, as we always consider the same orientation. The link between the tilted radius $\sigma_{h\theta}$ ($\sigma_{v\theta}$) and the fixed one σ_h (σ_v) can be determined by integrating over the vertical (horizontal) axis as follows

$$(4.31) \quad N(h) = \int_{-\infty}^{+\infty} N(h_\theta, v_\theta) \frac{dv}{p} = N_{h0} e^{-\frac{(h-h_0)^2}{2\sigma_h^2}},$$

with p the pixel size, σ_h the horizontal radius defined as

$$(4.32) \quad \sigma_h = \sqrt{\cos^2 \theta \sigma_{h\theta}^2 + \sin^2 \theta \sigma_{v\theta}^2},$$

and N_{0h} the Gaussian amplitude which can also be expressed by means of the tilted parameters. A similar expression is obtained for σ_v by switching the roles of $\sigma_{h\theta}$ and $\sigma_{v\theta}$ in equation 4.32. The last possible issue is that, for nearly symmetric MOTs, the tilt can jump by $\pi/2$ between one picture and the following one, thus artificially exchanging σ_h and σ_v . Tracking this angle and correcting for the jumps allows to avoid this issue.

4.4.2 Experimental realization

In practice, running a MOT requires a proper set of laser beams, appropriate magnetic fields and a timing procedure in order to control the atomic internal states. In the following, we expose the blue MOT time sequence which controls the optical beam powers and detunings, as well as the magnetic field gradients. In a second part, the problem of power imbalance within the MOT beam pairs due to the glass cell transmission is explained. To deal with this phenomenon, we developed a spectroscopic technique including the red beams which allows to measure the MOT forces balance inside the blue cloud.

4.4.2.1 Blue MOT sequence

Using the optical configuration described in 4.1.1.2 and the time sequence generation hardware described in 4.1.2, we generate the physical signals presented in figure 4.13. At $t = 0$ s, the Zeeman slower, blue MOT and repumpers beams are switched on. At the same time, we run a current of 25 A inside the quadrupole coils in order to generate the magnetic profiles for atom slowing and trapping, creating a longitudinal gradient $\partial_z B = 32.7 \text{ G cm}^{-1}$ and a field amplitude $\Delta B = 300 \text{ G}$. During a loading time of 3 s, we let all the parameters constant to transfer strontium from the effusive atomic beam to the blue MOT. At the end of this loading phase, we switch off the Zeeman slower and implement a magnetic gradient ramp of 100 ms, rising up to 65 G cm^{-1} . At the same time, the blue MOT power is ramped down in order to compress the MOT. Finally, two imaging pulses delayed by 100 ms from one another are sent through the cold cloud after a variable time-of-flight. During this delay, the atoms theoretically fall on a distance $gt^2/2 = 5 \text{ cm}$, meaning that they have already reached the bottom of the glass cell when the second imaging pulse is applied.

4.4.2.2 MOT beams power imbalance

In this first step experiment towards strontium in a ring cavity, we decided to use a glass cell and vacuum viewports that were not coated with anti-reflecting layers at the wavelengths of interest. This choice implies that the transmission of these two optical elements is not perfect, as shown

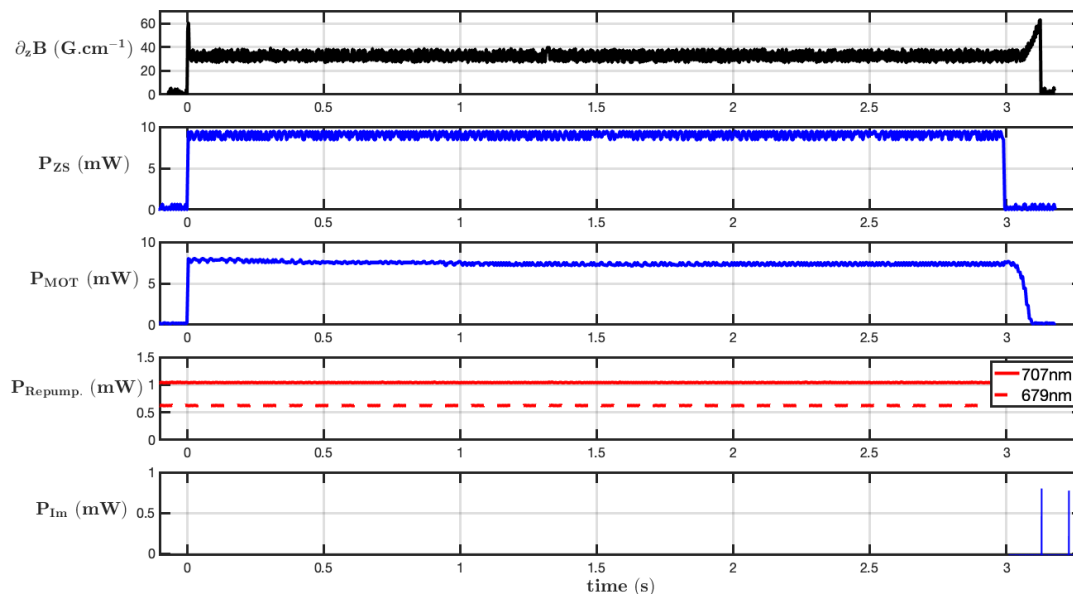


Figure 4.13: Time sequence for blue MOT operation with measured longitudinal magnetic field gradient and optical beams powers.

in figure 4.14. The data corresponds to transmission measurements of a blue beam through the glass cell and a viewport, for different angles of incidence. We find a good agreement with a simple model based on Fresnel's coefficients for p and s polarizations. For a beam propagating from a medium of refractive index n_i towards a medium with an index n_t , the reflection R_p and R_s in intensity for an angle of incidence θ_i follow the equations

$$(4.33a) \quad R_p(n_i, n_t, \theta_i) = \left| \frac{n_i \cos(\theta_t) - n_t \cos(\theta_i)}{n_i \cos(\theta_t) + n_t \cos(\theta_i)} \right|^2$$

$$(4.33b) \quad R_s(n_i, n_t, \theta_i) = \left| \frac{n_i \cos(\theta_i) - n_t \cos(\theta_t)}{n_i \cos(\theta_i) + n_t \cos(\theta_t)} \right|^2$$

where the angles are linked by $n_i \sin(\theta_i) = n_t \sin(\theta_t)$. The transmission of the cell and viewports are given by

$$(4.34) \quad T_{s,p}(\theta_i) = [1 - R_{s,p}(1, n, \theta_i)] \times [1 - R_{s,p}(n, 1, \theta_t)],$$

with $n = 1.5$ the refractive index of fused silica and θ_t the transmission angle from air to glass. At normal incidence, we experimentally find $T = 92\%$, independent of the polarization of the incident beam.

As we are using a retro-reflected scheme to operate both blue and red MOTs, the power of the reflected beam is decreased by a factor T^2 compared to the incident one. If the beams are

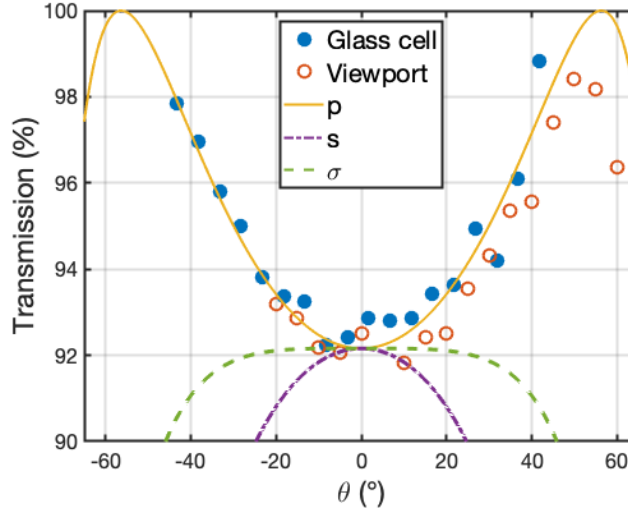


Figure 4.14: Glass cell (blue dots) and viewport (orange circles) transmissions as a function of the angle of incidence θ_i for a 461 nm horizontally polarized beam. The data are compared to a Fresnel coefficients model with a refractive index $n = 1.5$ for linear polarizations p (yellow solid line) and s (green point dotted line) as well as circular polarizations $\sigma = (s \pm ip)\sqrt{2}$ (purple point dotted line).

collimated, this imbalance induces scattering light forces that push the MOT away from the magnetic field zero. To understand this phenomenon, we make use of the one dimensional MOT force written in equation 4.14. An equilibrium is found at the position where $F_z = 0$, which can be expressed by

$$(4.35) \quad \frac{s_{0+}}{s_{0-}} = \frac{1 + \left(\frac{2\Delta_+}{\Gamma}\right)^2}{1 + \left(\frac{2\Delta_-}{\Gamma}\right)^2}.$$

For a constant beam waist, the cell and viewport transmissions induce that the saturation parameters of the beam propagating along $-\vec{u}_z$ and the retro-reflected one along $+\vec{u}_z$ are linked by $s_{0+} = T^2 s_{0-} \simeq 0.85 s_{0-}$. In this case, the MOT forms at a position where the detunings compensate for the intensity imbalance. If the induced displacement is larger than the typical size of the MOT, the average magnetic field over the cloud is non zero.

4.4.2.3 Spectroscopic method for power balance determination

In order to measure the MOT beams power balance, we determined an experimental spectroscopic technique including a red probe beam scanned over the intercombination line at 689 nm inside the blue MOT. Recording the blue MOT fluorescence at 689 nm gives rise to the spectra presented in figure 4.15. When the power difference between the blue MOT beams is not compensated, as represented in figure 4.15(a), we observe a fluorescence triplet corresponding to the different

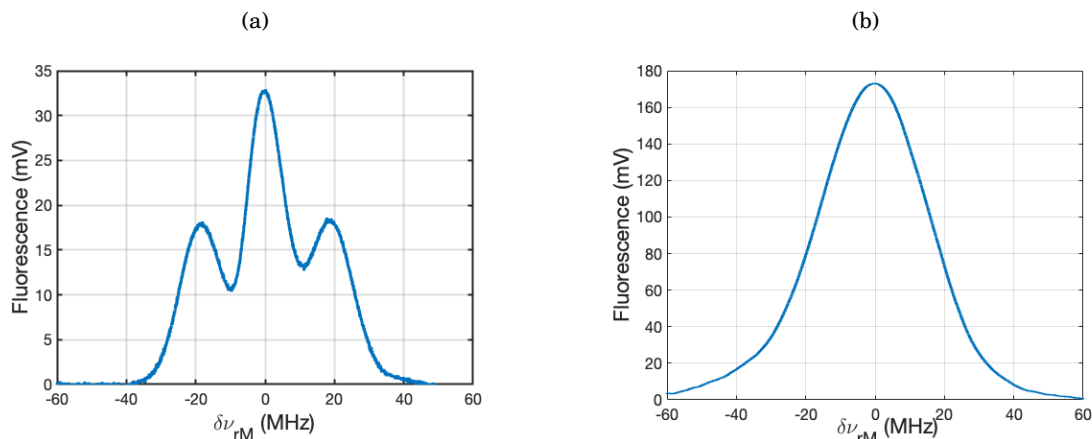


Figure 4.15: Fluorescence of the blue MOT at 689nm. (a) Blue MOT with intensity imbalance between the laser beams probed by a single 730 μ W probe on the red transition with a magnetic gradient $\partial_z B = 31 \text{ G cm}^{-1}$. (b) Blue MOT with balanced beams intensities probed by the six red MOT beams. The frequency axes are centred on the main peaks in each figure.

Zeeman transitions $|(5s^2)^1S_0\rangle \rightarrow |(5s5p)^3P_1, m_J\rangle$ of ^{88}Sr , with $m_J = 0$ for the central peak and $m_J = \pm 1$ for the side ones. The distance between the central and side peaks would correspond to a 3 mm displacement of the MOT on the z axis, larger than its typical radius of 1.5 mm. This displacement is far above the predicted value from the simple resonance condition in equation 4.35, and would need a more complex analysis including MOT repulsion forces to quantitatively describe the observed shifts.

The solution that we implement to compensate for the intensity imbalance is to focus the MOT beams such that the retro-reflected one has a smaller radius at the atomic position than the incident one. According to equation 4.35, the saturation parameters are equal for the two beams if their waists satisfy $w_{0+} = Tw_{0-}$. This condition can be reached experimentally by adjusting the positions of the fiber splitter output lenses such that the fluorescence on the red transition exhibits a singlet with minimum width. The result is presented in figure 4.15(b), where we observe the fluorescence at 689nm induced by the red MOT beams scanned in frequency inside the blue MOT.

4.4.3 Loading efficiency

In our peculiar setup geometry, the atomic loading and trapping from the effusive beam to the MOT are genuinely linked to each other. Indeed, the quadrupole magnetic field amplitude at the first coil position controls the Zeeman slowing procedure, while the gradient defines the MOT properties. The slowing procedure optimization has thus been realized in parallel with the MOT capture. The next paragraph describes this capture optimization by means of the Zeeman slowing

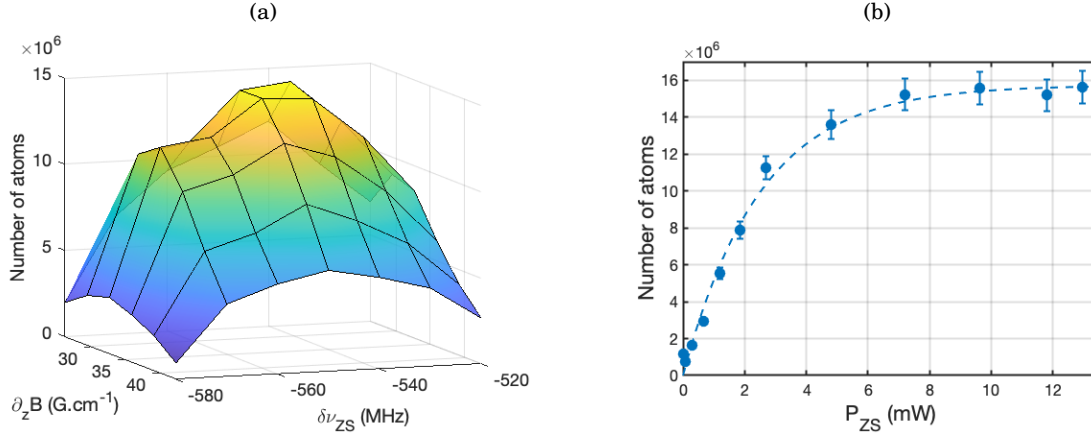


Figure 4.16: Number of atoms in the ^{88}Sr blue MOT as a function of (a) the magnetic field gradient $\partial_z B$ and the Zeeman slower beam detuning $\delta\nu_{ZS}$ and (b) the slower beam power before the glass cell. The dotted blue line is a guide to eye showing the saturation of the number of atoms. The oven is operated at 440°C .

parameters. In a second paragraph, we study the MOT loading and damping dynamics inside the vacuum chamber as a function of the oven temperature.

4.4.3.1 Slowing and capture optimization

The atoms leaving the effusive oven present a high average velocity $\bar{v} = 500\text{ms}^{-1}$. Adjusting the magnetic field gradient and Zeeman slower beam properties allows to adjust the mean velocity of the slowed particles from the atomic beam. An optimal value satisfying the propagation through the 5 cm separating the first quadrupole coil from the MOT region, as well as reducing the final atomic velocity can be found to maximize the MOT capture fraction. This optimization is shown in figure 4.16. The dataset in figure 4.16(a) shows the number of atoms in the blue MOT as a function of the longitudinal magnetic field gradient and the Zeeman slower detuning. The optical powers were set to $P_{ZS} = 12.0\text{mW}$ and $P_{MOT} = 11.1\text{mW}$ before the glass cell, with a detuning $\delta\nu_{MOT} = -32\text{MHz}$. The experimental data show a clear optimum for Zeeman slowing which corresponds to $\partial_z B = 32.5\text{Gcm}^{-1}$ and $\Delta\nu_{ZS} = -545\text{MHz}$. This value appears to be robust over experimental conditions variations, with a maximum of 1.5×10^6 trapped atoms in a range covering $\pm 2\text{Gcm}^{-1}$ and $\pm 2\text{MHz}$ around the maximum values.

The other adjustable parameter for the number of atoms optimization is the power of the Zeeman slower beam, represented in figure 4.16(b). The curve shows a plateau for powers higher than 8 mW and a linear decrease in atom number for smaller values. We thus operate the MOT with Zeeman slower powers typically equal to 10 mW or more, without changing the MOT characteristics.

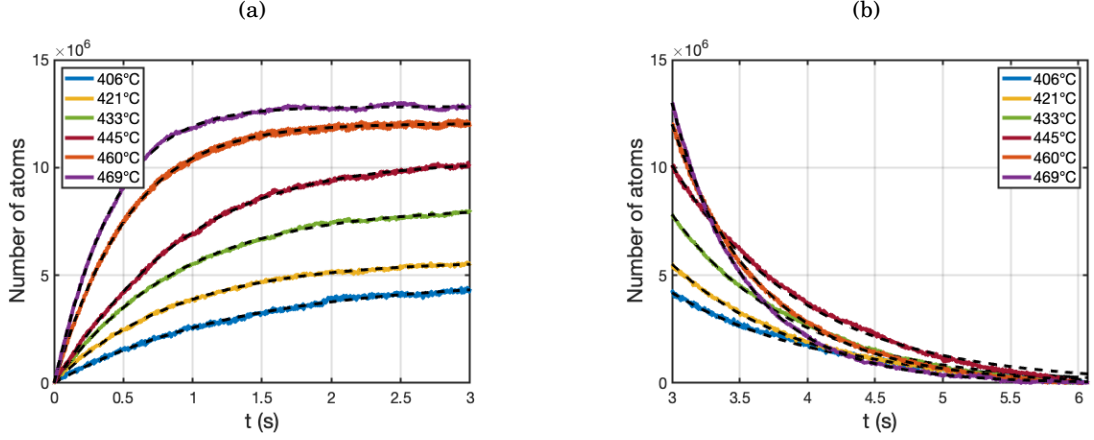


Figure 4.17: Fluorescence of the blue MOT when (a) loading the atoms by switching on the Zeeman slower beam and (b) switching it off for different oven temperatures. The data are represented by solid coloured lines while the black dotted lines correspond to fits according to equation 4.39.

4.4.3.2 MOT dynamics

The MOT dynamics is ruled by two competing effects. On one side, atoms are loaded into the trap by slowing a fraction of the effusive atomic beam and capturing it with the MOT beams. On the other side, collisions with the background gas, with strontium atoms from the effusive beam and from MOT particles themselves generate losses. At equilibrium, these mechanisms lead to a stationary atom number. The time evolution of the number of atoms N can be modelled by the following equation [24, 180]

$$(4.36) \quad \frac{dN}{dt} = R - \gamma N(t) - \beta N^2(t),$$

where R corresponds to the loading rate in atoms s^{-1} , γ to the one-body loss rate with the background gas in Hz and β to the strontium two-body collisions rate in Hz atom^{-1} . Generally, the lifetime $\tau = 1/\gamma$ is limited by the vacuum pressure inside the glass cell. The right-hand side of equation 4.36 being a polynomial of order 2 in N , we can rewrite it to find the number of atoms at time t starting from N_0 at t_0 as

$$(4.37) \quad \int_{N_0}^N \frac{dN}{\beta(N_+ - N_-)} \left(\frac{1}{N - N_-} - \frac{1}{N - N_+} \right) = \int_{t_0}^t dt,$$

with

$$(4.38) \quad N_{\pm} = -\frac{1}{2\beta} (\gamma \pm \sqrt{\Delta})$$

and $\Delta = \gamma^2 + 4R\beta$ the discriminant of the polynomial. The solution of this equation writes

$$(4.39) \quad N(t) = \frac{N_- - N_+ f(N_0) e^{-\sqrt{\Delta}(t-t_0)}}{1 - f(N_0) e^{-\sqrt{\Delta}(t-t_0)}}$$

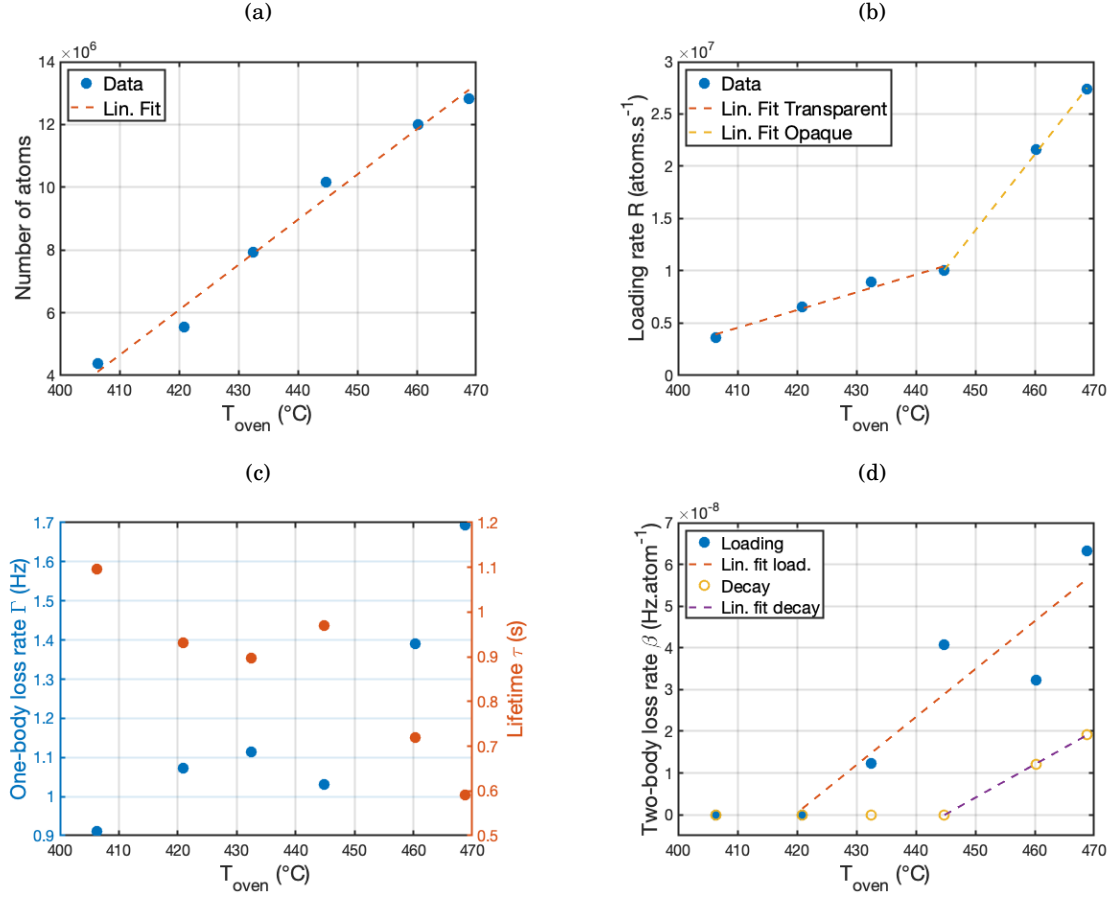


Figure 4.18: (a) Steady state number of atoms in the blue MOT as a function of the oven temperature (blue points) and adjustment by a linear function (orange dotted line). (b) Loading rate of the MOT from the fits in figure 4.17(a). Two linear functions (orange and yellow dotted lines) enlight the transparent and opaque regimes, respectively, delimited by the critical temperature $T_c = 450^{\circ}\text{C}$. (c) Loss rate and lifetime for the MOT decay from the fits in figure 4.17(b). (d) Two-body loss rate for both MOT loading (blue points) and damping (yellow points) with linear fits. The optical powers were set to $P_{\text{MOT}} = 11.3\text{mW}$ and $P_{\text{ZS}} = 12.0\text{mW}$, with respective detunings $\delta\nu_{\text{MOT}} = -28\text{MHz}$ and $\delta\nu_{\text{ZS}} = -545\text{MHz}$.

with $f(N_0) = (N_0 - N_-)/(N_0 - N_+)$. We experimentally verify this model by recording the fluorescence of the blue MOT at 461nm when switching on and off the Zeeman slower beam. When the laser is turned on at $t = 0\text{s}$, atoms are loaded into the MOT as shown in figure 4.17(a). After a time $t = 3\text{s}$, we turn it off and look at the atomic depletion due to collisions as can be seen in figure 4.17(b).

The different parameters from equation 4.39 for both MOT loading and damping are presented in figure 4.18. The atomic depletion corresponds to a loading rate $R = 0$ and an initial number of atoms $N_0 = N(t = 3\text{s})$ from the loading phase. The number of captured atoms with respect to the oven temperature is represented in figure 4.18(a). A linear fit gives a slope of $1.4 \times 10^5 \text{atom K}^{-1}$

in the studied temperature range. This linear dependency actually results from two competing effects. Indeed, for oven temperatures below the critical value $T_c = 450^\circ\text{C}$, the atomic loading rate is linearly increasing with a slope of $1.7 \times 10^5 \text{ atoms s}^{-1} \text{ K}^{-1}$. Above the critical temperature, the slope is getting steeper with a value of $7.3 \times 10^5 \text{ atoms s}^{-1} \text{ K}^{-1}$. This transition is also visible on the loss rate γ and the lifetime τ in figure 4.18(c). Moreover, the two-body loss rate in figure 4.18(d) is equal to 0 for the lowest temperatures, but starts to increase when the oven is heated up with a slope of $1.2 \times 10^{-9} \text{ Hz atom}^{-1} \text{ K}^{-1}$ for the loading phase and $8.0 \times 10^{-10} \text{ Hz atom}^{-1} \text{ K}^{-1}$ for the damping one. The two-body collisions thus remain negligible compared to one-body processes for a number of atoms in the 10^7 range. The critical temperature derived from this analysis corresponds to the passage from the transparent regime to the opaque mode in Knudsen's theory, derived in 3.1.2. In order to keep a typical MOT lifetime $\tau = 1 \text{ s}$ and yet have a sufficient number of atoms in the blue MOT, we operate the oven at the cross-over temperature T_c .

4.4.4 Blue MOT characterization

The MOT loading optimization allowed to determine the most efficient magnetic field gradient and Zeeman slower detunings, ending with $\partial_z B = 32.5 \text{ G cm}^{-1}$ and $\delta\nu_{ZS} = -545 \text{ MHz}$. In the following paragraphs, we describe the MOT number of atoms and temperature optimizations by means of the different laser beam frequencies and powers.

4.4.4.1 Blue MOT laser frequency

In Doppler cooling theory, the temperature of the MOT can reach a minimum given by the natural linewidth of the transition and the saturation parameter. At low intensities, it gives the limit written in equation 4.16. In the case of strontium, this theory completely fails in describing the MOT temperature [181] as extra-heating mechanisms due to laser intensity fluctuations are not included [182]. We thus have performed an experimental optimization presented in figure 4.19. The bosonic MOT properties were recorded with the imaging apparatus and the optimized parameters for Zeeman slowing described in the previous paragraph. The loading sequence was done with constant optical powers, detunings and magnetic field gradient, with an MOT beam power of $P_{MOT} = 10.5 \text{ mW}$ per axis before the glass cell.

The measured temperatures presented in figure 4.19(a) shows the discrepancy between the Doppler limit and the blue strontium MOT behaviour. With this constant loading procedure, we observe an increase in temperature for high absolute values of the MOT beams detuning, and a minimum of 10 mK at $\delta\nu_{MOT} = -15(5) \text{ MHz}$. The cloud size, presented in figure 4.19(b), follows the temperature behaviour to reach a minimum Gaussian radius of $600 \mu\text{m}$ at the same detuning. Concerning the number of atoms seen in figure 4.19(c), a clear maximum is observed at a higher absolute value $\delta\nu_{MOT} = -28(2) \text{ MHz}$.

Combining the MOT temperature, size and number of atoms allows to compute the phase space

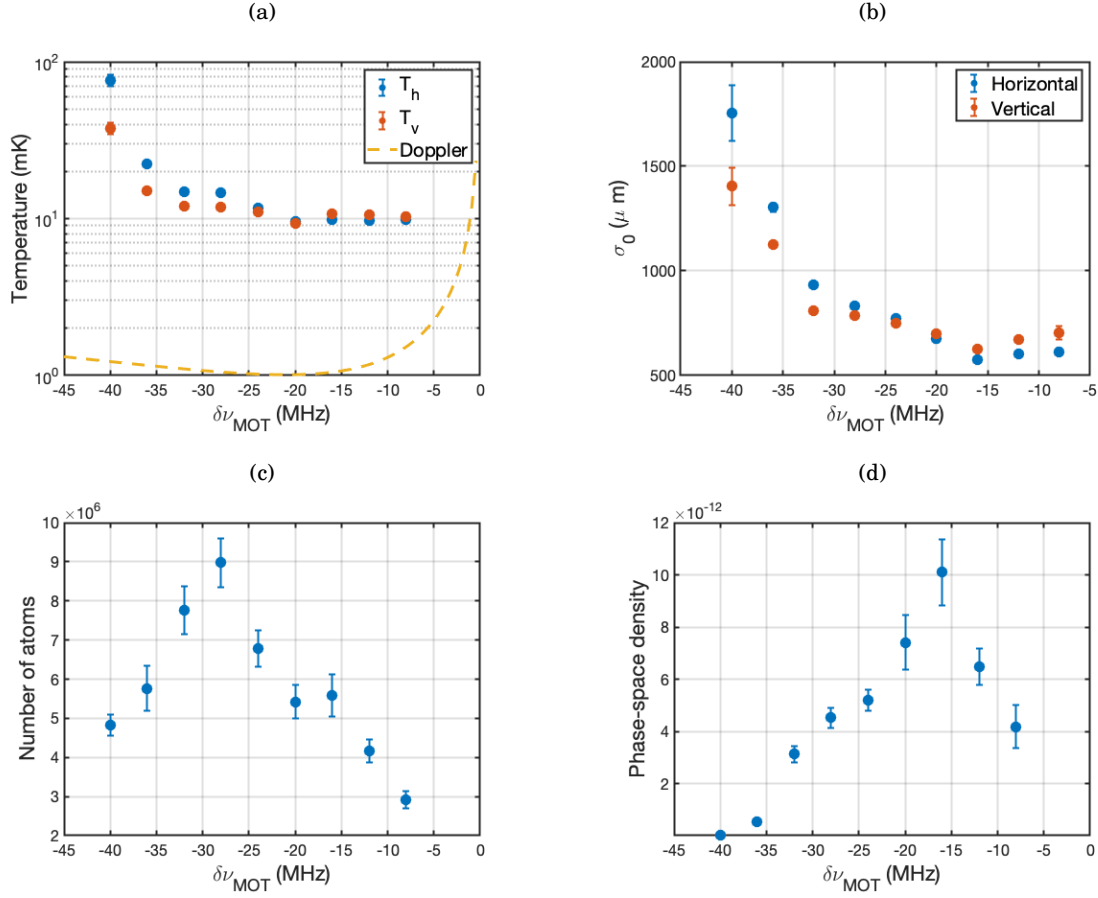


Figure 4.19: Bosonic blue MOT optimization as a function of the MOT beams detuning. (a) Temperature of the cloud in the horizontal h (blue points) and vertical v (orange points) directions of the CCD camera. The Doppler theory curve for $s_0 = 0.7$ (yellow dotted line) is drawn for comparison. (b) Gaussian radius of the MOT for both directions. (c) Number of trapped atoms. (d) Phase-space density derived from equation 4.40.

density ρ defined as

$$(4.40) \quad \rho = n\lambda_{dB}^3,$$

where $n = N/V$ is the number density for a MOT volume V and λ_{dB} the thermal de Broglie wavelength expressed as [183]

$$(4.41) \quad \lambda_{dB} = \sqrt{\frac{h^2}{2\pi mk_B T}}.$$

As we do not have access to the cloud size and temperature along the propagation axis of the imaging beam, we can approximate the MOT temperature and size by its arithmetic and geometric means over the camera axes, corresponding to $\bar{T} = (T_h + T_v)/2$ and $\bar{\sigma} = \sqrt{\sigma_h \sigma_v}$, respectively. The

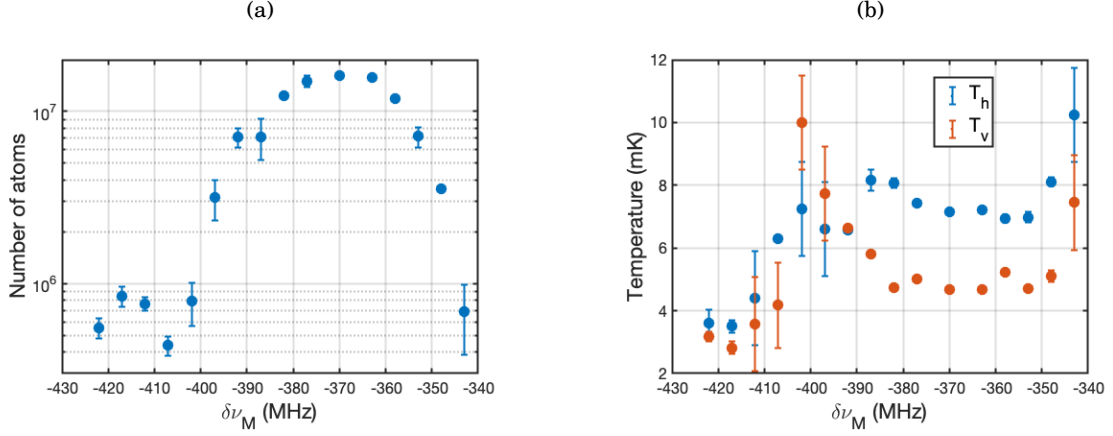


Figure 4.20: Blue MOT (a) number of atoms and (b) temperature as a function of the 461 nm master laser frequency referenced to the ^{88}Sr resonance. The double resonance feature demonstrates that trapping on the all the strontium isotopes is achieved, with a bosonic ensemble centred on $\delta\nu_M = -370\text{MHz}$ and a fermionic one at $\delta\nu_M = -415\text{MHz}$.

Gaussian volume of the MOT inferred by the absorption imaging fits is given by

$$(4.42) \quad V = (2\pi\bar{\sigma}^2)^{3/2}.$$

The phase-space density is presented in figure 4.19(d). It is maximum for a detuning $\Delta\omega_{MOT} = -\Gamma/2$, as predicted by the Doppler theory despite the quantitative disagreements between the theoretical and experimental temperatures. In order to maximize the number of atoms, we chose to operate the MOT with $\delta\nu_{MOT} = -28\text{MHz}$ in the following characterizations.

4.4.4.2 Isotopic populations

Even if the fermionic isotope ^{87}Sr has a richer level structure than the bosonic isotopes due to its nuclear spin $I = 9/2$, a MOT can be run in similar conditions as for ^{88}Sr by addressing the $|(5s^2)^1S_0, F_g = 9/2\rangle \rightarrow |(5s5p)^1P_1, F_e = 11/2\rangle$ transition. Switching from one isotope to the other thus resumes in red shifting all the blue beams frequencies compared to the ^{88}Sr resonance. Another key aspect is that the repumping levels also split into hyperfine manifolds, as described in 1.2.2.3. The repumping lasers thus need to be scanned over 5.42GHz in order to address the transitions from the five $|(5s5p)^3P_2, F = 5/2, \dots, 13/2\rangle$ manifolds towards the three $|(5s6p)^3S_1, F = 7/2, 9/2, 11/2\rangle$ manifolds at 707nm, as well as from the $|(5s5p)^3P_0, F = 9/2\rangle$ manifold towards the same excited states at 679nm. For technical reasons, we are only able to achieve this condition for the 707 nm laser scanned over 6.0GHz, while the 679nm suffers from mode hops for scan amplitudes larger than 1.7GHz.

To verify the fact that we can trap ^{87}Sr by shifting all the blue lasers frequencies, the number of atoms and the temperature of the blue MOT as a function of the blue laser master frequency

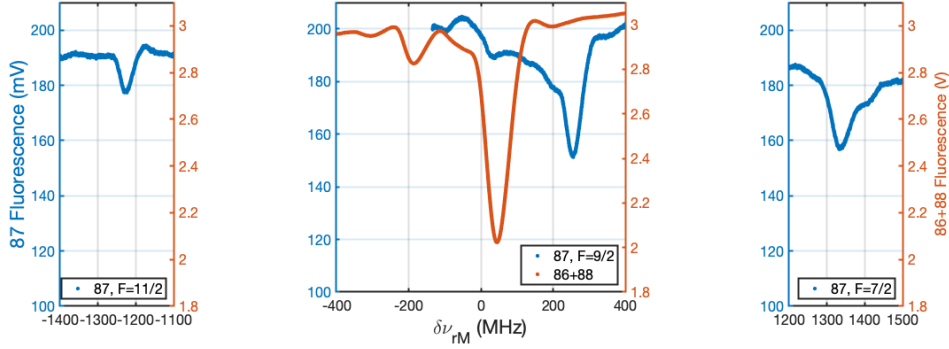


Figure 4.21: Fluorescence of the blue MOT at 461 nm depleted by the red MOT beams scanned over the 689 nm resonance. The blue curves corresponds to a fermionic blue MOT with resonances for the three different $|(5s5p)^3P_1, F_e\rangle$ manifolds, while the orange curve corresponds to an ^{88}Sr MOT with a fraction of ^{86}Sr atoms.

are presented in 4.20. This measurement was performed by changing the frequency f_D of the double passage AOM on the saturated absorption arm of the master laser, as represented in figure 2.4. The other AOM frequencies were kept constant such that the MOT, Zeeman slower and imaging detunings can be determined by $\delta\nu_{MOT} = \delta\nu_M + 342\text{MHz}$, $\delta\nu_{ZS} = \delta\nu_M - 175\text{MHz}$ and $\delta\nu_{Im} = \delta\nu_M + 380\text{MHz}$.

The number of atoms in figure 4.20(a) exhibits two clear peaks of 1.6×10^7 and 8.5×10^5 atoms. The frequency difference between the two maxima of -47MHz is close to the shift of the fermionic $|(5s^2)^1S_0, F_g = 9/2\rangle \rightarrow |(5s5p)^1P_1, F_e = 11/2\rangle$ transition compared to the $|(5s^2)^1S_0\rangle \rightarrow |(5s5p)^1P_1\rangle$ transition in ^{88}Sr , equal to -51.6MHz . This second peak thus indicates that the smaller peak corresponds to ^{87}Sr . The MOT temperature presented in figure 4.20(b) shows that the fermionic blue MOT is colder than the bosonic one by a factor of 2. This feature can be explained by the hyperfine structure of the ^{87}Sr states, allowing for Sisyphus cooling mechanisms [23].

Comparing the peak heights in figure 4.20(a) gives a ratio of 5.1%, while the natural abundance ratio between the ^{87}Sr and ^{88}Sr isotopes equals 8.3%. This reduced capture efficiency can be attributed to the repumping limitations on the 679 nm, but also to the fact that the bosonic MOT is actually containing a fraction of ^{86}Sr atoms. To confirm this hypothesis, we probe the blue MOT with the red beams scanned in frequency at 689 nm and observe the depletion on the fluorescence at 461 nm. The spectra for two different MOTs operating in the bosonic range at $\delta\nu_M = -370\text{MHz}$ and in the fermionic range at $\delta\nu_M = -417\text{MHz}$ are shown in figure 4.21. The presence of ^{84}Sr is also probable, but the small natural abundance of this isotope makes it harder to detect and we do not observe it with the implemented detection schemes.

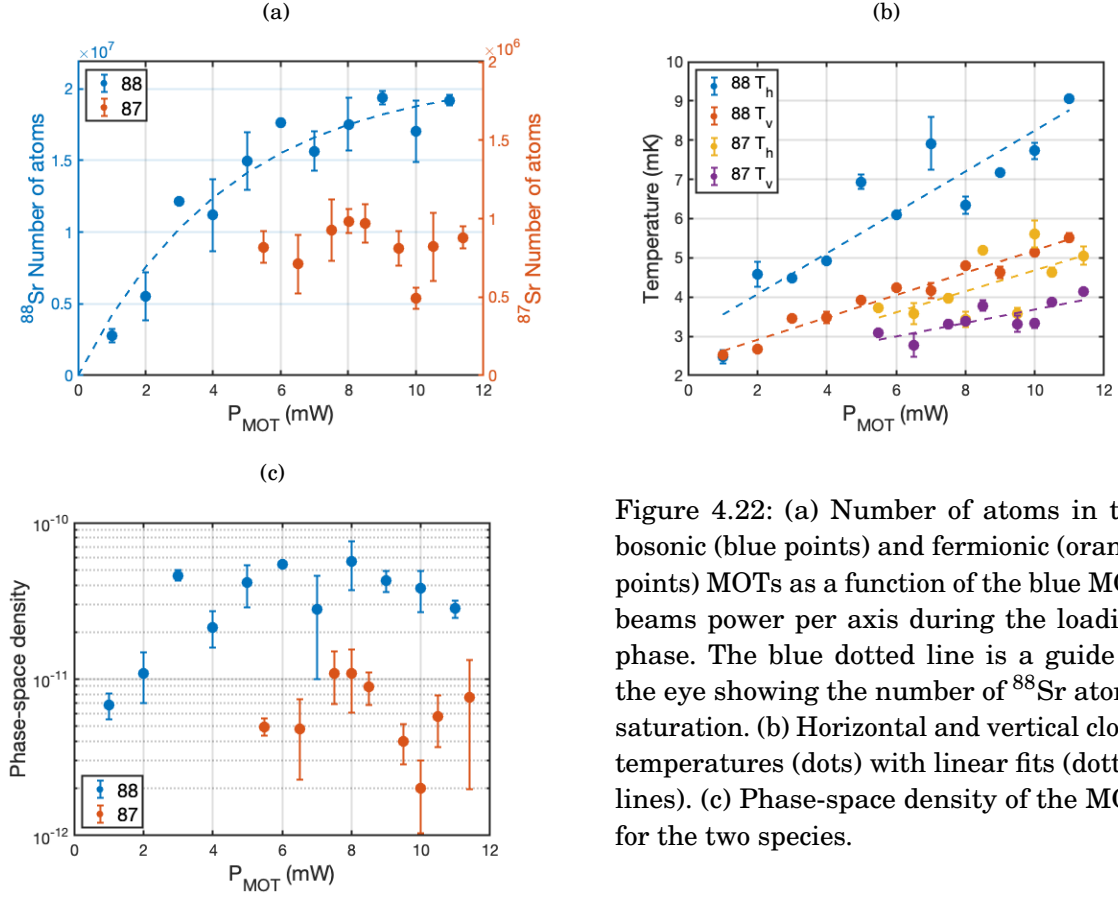


Figure 4.22: (a) Number of atoms in the bosonic (blue points) and fermionic (orange points) MOTs as a function of the blue MOT beams power per axis during the loading phase. The blue dotted line is a guide to the eye showing the number of ^{88}Sr atoms saturation. (b) Horizontal and vertical cloud temperatures (dots) with linear fits (dotted lines). (c) Phase-space density of the MOT for the two species.

4.4.4.3 Temperature reduction

The blue MOT temperature from the previous characterizations is equal to 10 mK, while commonly reported values stand in the 1–3 mK range [173, 184]. In order to further cool the blue MOT down, we implement a compression sequence as shown in figure 4.13. The first step of this temperature reduction consists in ramping down the power of the blue MOT beams. We characterize this process by applying a sequence with a power P_{MOT} during the loading phase ended by a linear RF amplitude ramp of 100 ms from the maximum power to a fraction of 20% of it. The results are given in figure 4.22.

The number of atoms in figure 4.22(a) shows a plateau for the boson when the optical power is above 8 mW. Also, the fermionic populations appears to be slightly peaked for this particular value. As the temperatures from figure 4.22(b) exhibit a linear behaviour with respect to P_{MOT} , the phase-space density in figure 4.22(c) presents a maximum at this power for both isotopes and we run the MOTs with this configuration. At the end of the ramp, the power is thus reduced to 200 μW . The horizontal and vertical temperature fits from figure 4.22(b) respectively give slopes of 0.52 and 0.29 mK mW $^{-1}$ for ^{88}Sr , while it is equal to 0.27 and 0.17 mK mW $^{-1}$ for ^{87}Sr . These results confirm the fact that the fermionic MOT is almost a factor of 2 colder than the bosonic

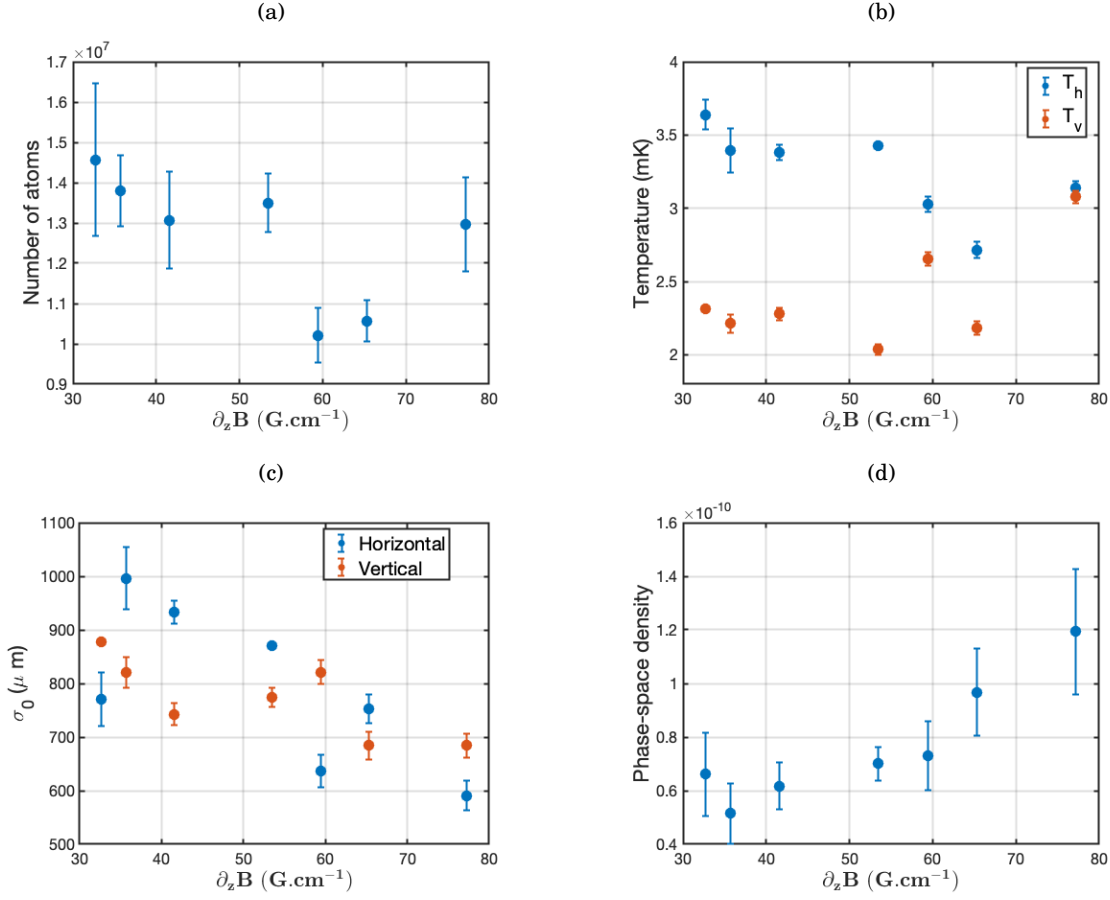


Figure 4.23: (a) Number of atoms, (b) temperature, (c) size and (d) phase-space density of the bosonic blue MOT as a function of the longitudinal magnetic field gradient final value for a 100ms long compression at the end of the sequence. The 3s loading phase is operated at $\partial_z B = 32.5 \text{ G.cm}^{-1}$.

one.

On the same time interval as the laser power ramp down, we implement a cloud compression by increasing the magnetic field gradient linearly, as shown in figure 4.13. The temperature and phase-space density resulting from a short compression at the end of a 3s loading sequence with $\partial_z B = 32.5 \text{ G.cm}^{-1}$ are shown in figure 4.23. The temperature, represented in figure 4.23(b), exhibits a minimum at $\partial_z B = 65 \text{ G.cm}^{-1}$, thus chosen to implement the optimized sequence. The phase-space density from figure 4.23(d) shows that the gradient ramp compresses the MOT, mostly by reducing its size more than the number of atoms as can be seen in figures 4.23(c) and 4.23(a), respectively. At the end of the temperature reduction procedure, we reach an average temperature $\bar{T} = 2.4 \text{ mK}$ for the ^{88}Sr blue MOT.

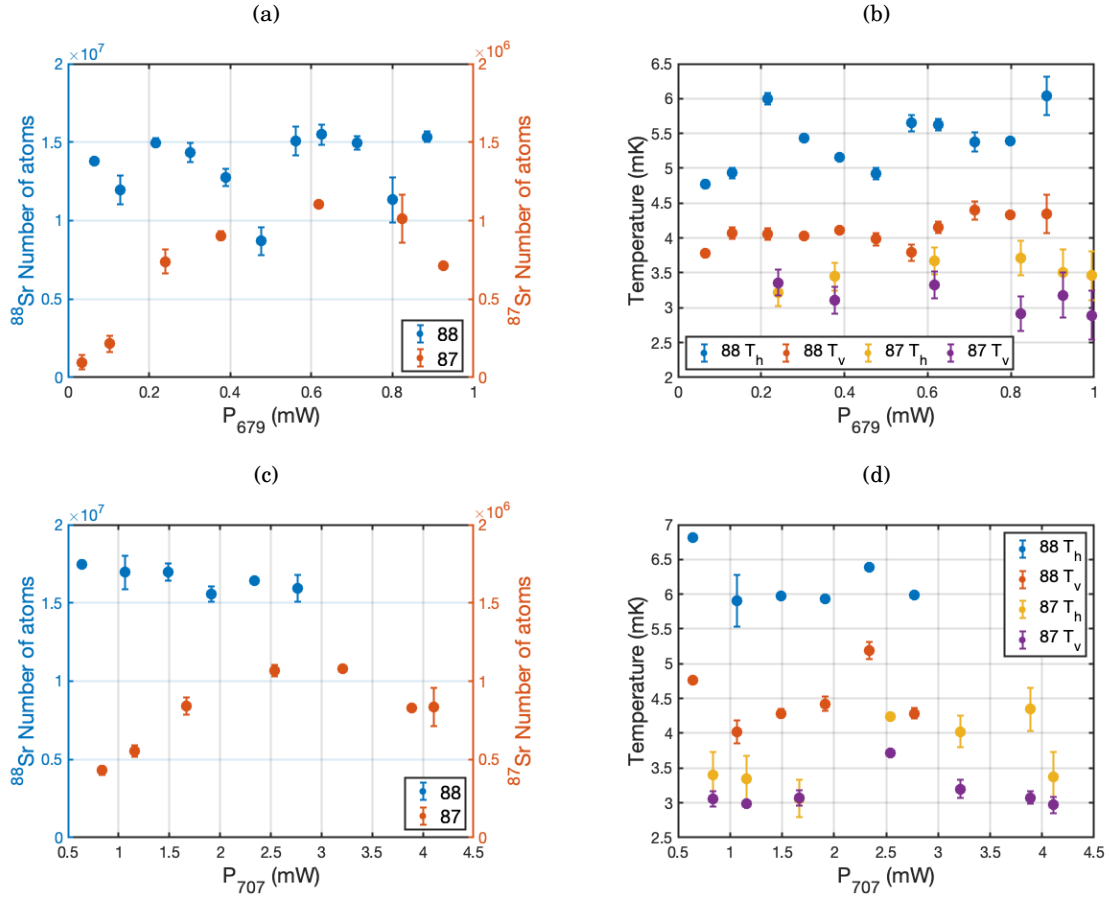


Figure 4.24: Number of atoms and temperature in the ^{88}Sr and ^{87}Sr blue MOTs as a function of the (a,b) 679nm and (c,d) 707nm repumpers lasers powers before the glass cell.

4.4.4.4 Repumping efficiency

In this last paragraph concerning the blue MOT characterization, we study the influence of the repumping lasers. When either the 679nm or 707nm beams are switched off, the MOT population is strongly reduced such that the number of atoms goes below the absorption imaging noise level. The dependencies of the ^{88}Sr and ^{87}Sr with the repumping beams on are presented in figure 4.24.

The number of atoms in the bosonic MOT presents a slight depletion near the 679nm laser power $P_{679} = 450\mu\text{W}$, as can be seen in figure 4.24(a). For the 707nm, no clear dependency upon the laser power is observed in figure 4.24(c). On the other side, the fermionic MOT is optimized for the values $P_{679} = 650\mu\text{W}$ and $P_{707} = 3.0\text{mW}$. Concerning the temperature, both isotopes do not seem to be particularly affected by these lasers powers, as presented in figures 4.24(b) and 4.24(d). In conclusion, both MOTs are optimized for these two powers, avoiding us from modifying the repumping power when switching from one isotope to the other.

Conclusion on the blue MOT

To conclude on the blue MOT characterization and optimization, we operate at the same laser powers for ^{88}Sr and ^{87}Sr but different frequencies. In the 3 s long loading phase, the Zeeman slower power is kept at $P_{ZS} = 10\text{mW}$, the repumping beams at $P_{679} = 650\mu\text{W}$ and $P_{707} = 3.0\text{mW}$, and the MOT power value verifies $P_{MOT} = 8.0\text{mW}$. The magnetic field gradient is also kept constant with a longitudinal amplitude $\partial_z B = 32.5\text{G cm}^{-1}$. In a final compression phase where the Zeeman slower beam is switched off, we linearly ramp the gradient up to $\partial_z B = 65\text{G cm}^{-1}$ and the RF amplitude of the AOM controlling the MOT beams power down, ending with $P_{MOT} = 200\mu\text{W}$. The difference between the two isotopes lies in the laser detunings, equals to $\delta\nu_{MOT} = -28\text{MHz}$ and $\delta\nu_{ZS} = -545\text{MHz}$ for the ^{88}Sr isotope, while all the blue laser frequencies for ^{87}Sr are detuned by -47MHz compared to the previous values. The repumpers are also scanned over wider ranges of 1.7 GHz for the 679 nm and 6.0 GHz for the 707 nm lasers.

With these parameters and the optimized time sequence from figure 4.13, we produce an ^{88}Sr blue MOT of typically 2×10^7 atoms at a temperature $T = 2.4\text{mK}$ and an ^{87}Sr cloud of 9×10^5 at half this temperature. We have also demonstrated that the bosonic MOT contains a fraction of ^{86}Sr isotopes. A picture of such bosonic blue MOT taken in the laboratory is presented in figure 4.25(a). An absorption image of the MOT in figure 4.25(b) shows a cloud with a Gaussian $e^{-1/2}$ radius of 1.5 mm, in agreement with the estimation from equation 4.17 which gives a size of $\sqrt{\langle z^2 \rangle} = 1.3\text{mm}$ for $s_0 = 0.5$ and $\partial_z B = 32.5\text{G cm}^{-1}$.

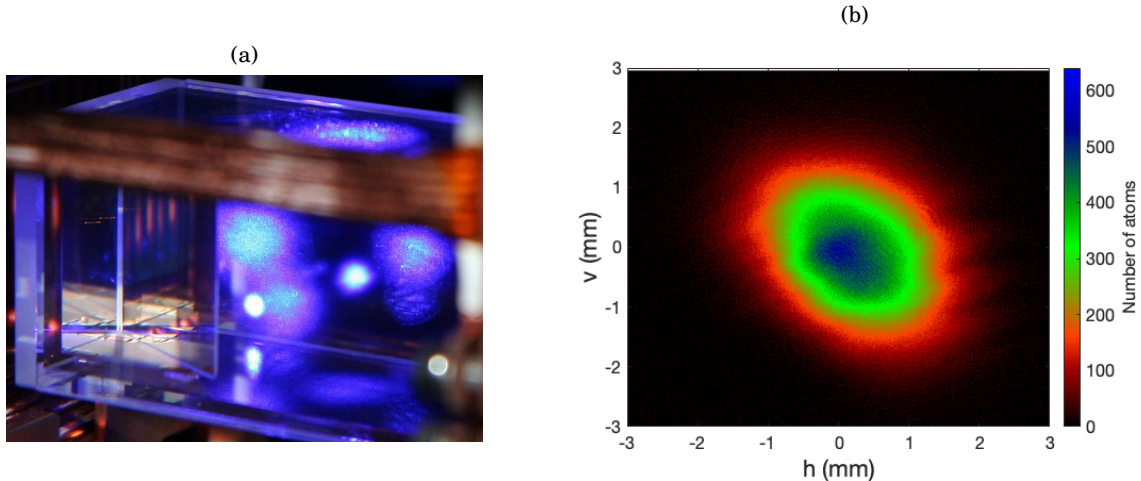


Figure 4.25: (a) Picture of a typical ^{88}Sr blue MOT inside the glass cell. The right-angled mirror prism is visible on the left part of the image. The MOT fluorescence corresponds to the highly saturated blue circle at the center, while the other ones correspond to MOT and Zeeman slower beams reflections onto the surfaces of the cell. (b) Absorption image of the blue MOT taken along the horizontal h and vertical v axes of the CCD camera.

4.5 Narrow-line cooling on the red intercombination line at 689 nm

Due to their two valence electrons structure, alkaline-earth elements present very interesting narrow transitions from singlet to triplet manifolds. Such so-called intercombination line operates between the strontium ground-state $|5s^2\ ^1S_0\rangle$ and the excited $|5s5p\ ^3P_1\rangle$ state at 689 nm. With a natural linewidth $\Gamma_r = 2\pi \times 7.4\text{ kHz}$, a MOT on this transition operates in the quantum regime, as described in section 4.3. It is theoretically limited to the recoil temperature, ending with a colder sample than in the Doppler regime. On the other hand, the dipole force induced by photons on such a transition is weaker than for a large transition, as it is proportional to Γ_r . This statement makes impossible a direct Zeeman slowing from the atomic beam on this transition with the available laser power. The common approach thus consists in slowing and trapping a large number of atoms using the dipole allowed transition at 461 nm, as described previously, to load a colder narrow-line MOT in a second stage. Similar schemes are applied for trapping and cooling of calcium [185], radium [186] and magnesium [187]. Interestingly, for barium [188] as well as for the lanthanides such as ytterbium [189] and dysprosium [190], the intercombination line is wide enough to directly operate a MOT after Zeeman slowing on the larger dipole allowed transitions.

4.5.1 Narrow-line cooling techniques

The main difference between Doppler and narrow-line cooling lies in the fact that the recoil effect from photon absorption cannot be neglected for the latter. Indeed, the recoil velocity induced by a single 689 nm photon $v_r = \hbar k/m = 6.6\text{ mm s}^{-1}$ induce a Doppler shift $\nu_r = \hbar k^2/m = 9.6\text{ kHz}$, larger than the natural linewidth $\Gamma_r/2\pi$. The quantum nature of light can then not be neglected in this regime, hence the name quantum regime.

At the end of the blue MOT stage, the Maxwell-Boltzmann standard-deviation of the Doppler shifts is given by $\sigma_v = \sqrt{k_B T/m\lambda^2} \simeq 1\text{ MHz}$ for a $T = 2\text{ mK}$ cloud. In order to load these atoms into the red MOT, one thus needs a broadening mechanism. Two ideas have been implemented to realize such broadening. First, the saturation intensity $I_{sat} = 3\text{ }\mu\text{W/cm}^2$ being very weak for the red transition, the line can easily be power broadened to a linewidth $\Gamma_r\sqrt{1+s_0}$. The second idea consists in broadening dynamically the red laser frequency. Until 2017, the traditional way of doing so was to modulate the MOT laser frequencies in a sinusoidal manner, for instance by modulating the voltage of a *Voltage Controlled Oscillator* (VCO). This method, developed by Katori *et al.* in 1998 [49], is referred to as the *Broad Band* (BB) phase. A variant of this scheme was developed by Norcia *et al.* at JILA [164]. Instead of modulating the phase in a sinusoidal manner, they generated upward linear frequency ramps in a saw-tooth way, hence naming the technique *Saw-tooth Wave Adiabatic Passage* (SWAP) [174]. Hereunder, we compare the two

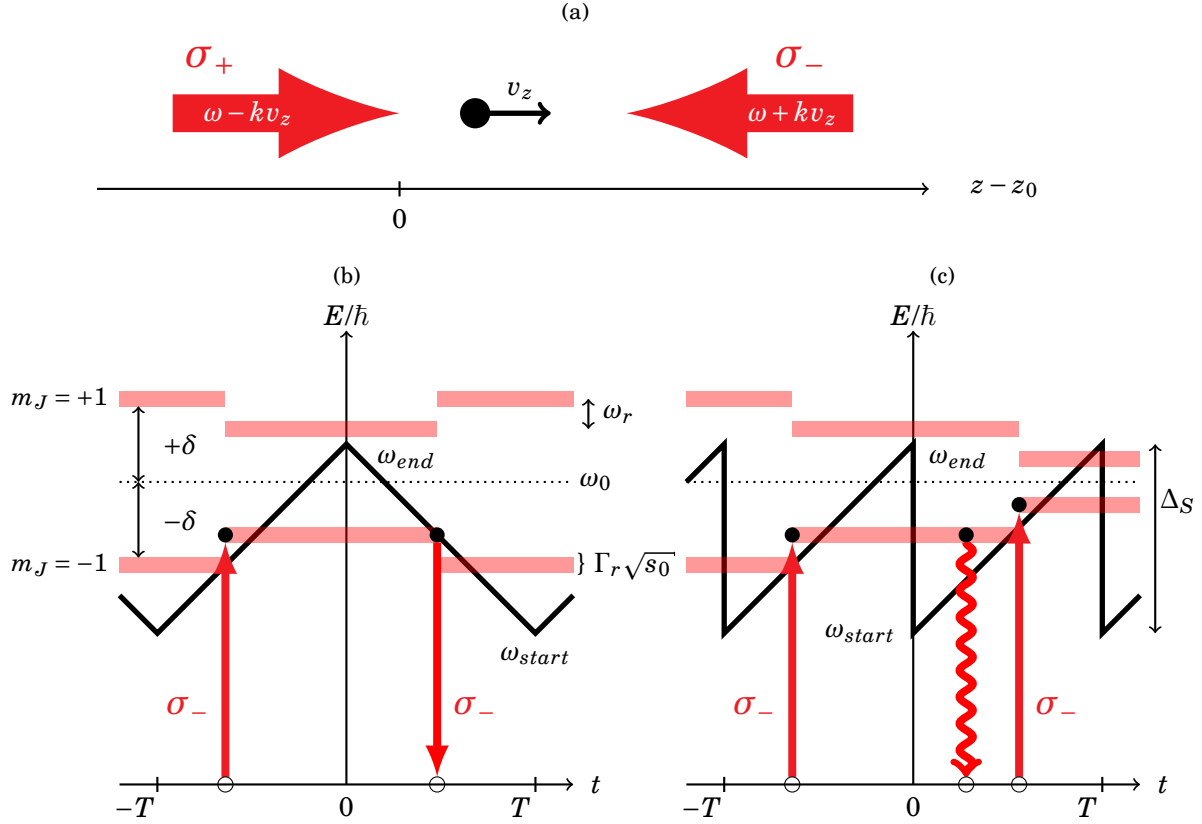


Figure 4.26: (a) One dimensional configuration for red MOT operation. Two counter-propagating beams with opposite circular polarizations are sent toward an atom with velocity \vec{v} . The Doppler shifted frequencies of the laser are indicated on the corresponding lasers. (b) BB phase scheme. The laser frequency is modulated symmetrically over time. The Doppler and Zeeman shifted energies of the excited state are represented as red lines, detuned by the recoil frequency ω_r at photonic absorption events. The stimulated emission events are presented as red arrows. (c) SWAP mechanism. The laser frequency is modulated in a saw-tooth manner, preventing stimulated emission in the beam absorbed during the upward ramp. The atoms thus have a higher probability to decay by stimulated emission, represented as a wavy arrow.

methods to motivate our choice of operating the first stage of the red MOT using SWAP.

4.5.1.1 SWAP mechanism

Broad Band technique : To understand the difference between the BB MOT operation and the novel SWAP technique, we briefly summarize the first technique. The idea behind frequency modulation is to generate a Dirac frequency comb in the Fourier domain, which acts as broaden laser spectrum. In BB modulation, the laser frequency is temporally modulated in a symmetrical manner, such as the triangular function of repetition period T and modulation amplitude $\Delta = \omega_{end} - \omega_{start}$ represented in figure 4.26(b). This type of temporal frequency modulation

traduces on the electrical field spectrum as a Dirac comb with peaks separated by $\delta\omega = \pi/T$, multiplied by an envelope with a width proportional to Δ . Increasing the modulation amplitude thus results in broadening the spectrum, with a price to pay being the reduction of the intensity per peak. This method can thus be compared to a MOT acting in the Doppler regime, where the large maximum force shell of spatial width $\Gamma/\gamma_J\partial_z B$ and radius $|\Delta_0|/\gamma_J\partial_z B$ is replaced by a sum of thinner shells distant from each other by an amount $\delta\omega/\gamma_J\partial_z B$.

SWAP advantages : The BB method described above has proven to efficiently cool strontium atoms from the blue MOT in a variety of experiments. Nevertheless, it can be improved by a simple modification. To understand the issue behind the BB mechanism, we consider an atom moving along the z axis with a given velocity v_z illuminated by two counter-propagating beams with opposite circular polarizations, as pictured in figure 4.26(a). The Doppler and Zeeman shifts experienced by the excited states $|(5s5p)^3P_1, m_J\rangle$ can be combined in a single parameter δ written as

$$(4.43) \quad \delta = kv_z + m_J\gamma_J\partial_z Bz.$$

Considering the case $\delta > 0$ and the laser frequency being ramped towards high frequencies, the counter-propagating beam σ_- gets on resonance with the lower energy $m_J = -1$ state before the co-propagating one with the higher energy state. An atom in the ground state is then transferred to the excited $m_J = -1$ state by absorbing a photon, which induces a Doppler shift of $-kv_r$. This situation is represented in figure 4.26(c), where the excited state energies of the considered atom and the laser frequency as a function of time are represented. Even if the authors originally envisioned stimulated emission from the co-propagating beam to bring back the atom to the ground state [164], this situation is prevented by the selection rules in a MOT. They finally showed that it remains in the excited state during the rising part of the ramp [174]. This conclusion has been corroborated by Snigirev *et al.* from the Munich Max Planck Institute in 2019, in a paper studying both numerically and experimentally the BB and SWAP mechanisms [109]. On the other hand, a stimulated emission process can occur in the BB case during the downward frequency ramp. As the atom emits a photon into the same beam than the absorbed one, the momentum exchange at the end of the cycle is strongly reduced and thus the cooling as well. Interestingly, the SWAP MOT works best in a regime that can neither fully be described by the Landau-Zener formalism for adiabatic transfer, which requires $T \ll \tau$, nor in the steady-state formalism for which $T \gg \tau$. We can thus only give an upper bound p_{LZ} for the adiabatic transition probability from the ground to an excited state, given by [191]

$$(4.44) \quad p_{LZ} = 1 - e^{-\frac{\pi}{2} \frac{\Omega^2}{\alpha}},$$

where $\alpha = \Delta_S/T$ corresponds to the sweep rate for a swap detuning amplitude Δ_S and the Ω to the Rabi frequency.

By suppressing the downward frequency ramp, the SWAP technique relies on spontaneous emission to achieve cooling. The probability for an atom promoted to one of the excited states to remain in that state thus follows an exponential decay with a lifetime given by the natural linewidth $\tau = 1/\Gamma$. Tuning the repetition period close to the excited state lifetime as $T \sim \tau$ allows to maximize the influence of spontaneous emission. Indeed, as soon as the atom is reset to the ground state, it gets excited by the next laser frequency sweep. The atom thus receives a momentum kick $\hbar k$ per sweep at maximum, opposed to its velocity. One can see from figure 4.26(c) that the process stops to be efficient at a detuning smaller than the Rabi frequency $|\delta| \leq \Omega$. In this regime, the competition between the two lasers for excited state promotion results in no momentum transfer on average.

Another main advantage of the SWAP technique is that it can efficiently trap fermionic ^{87}Sr atoms without the need for a stirring laser [174]. This major simplification, combined with the ease of implementation of SWAP using DDS systems, makes this technique a powerful tool for strontium red MOT implementations. This is the path we followed in our experiment, which experimental characterizations are presented in 4.5.3.

4.5.1.2 CW final phase

While the SWAP technique is an efficient tool for capturing strontium atoms from the blue MOT, its final temperature is limited to $k_B T_f = \hbar\Omega/2$ as in Doppler cooling [109]. To further cool the red MOT and achieve temperatures close to the recoil one, a *Continuous Wave* (CW) phase is necessary. In this second red MOT stage, the laser frequencies are set to a fixed detuning $\Delta_0 < 0$. The physics in this regime is different than for Doppler or SWAP operations, mainly because the light forces become very weak. Gravity is then no longer negligible as the maximum scattering force $F_{max} = \hbar k\Gamma/2$ is only 16-times larger than mg .

Usually, the dynamical transition from SWAP to CW is done by keeping in a first time the laser powers relatively high such that $s_0 \gg 1$. The induced force is thus comparable to the SWAP force. To achieve the smallest temperatures, the power has to be reduced until it reaches a level $s_0 \sim 1$. Under these conditions, the MOT density is expected to be concentrated at the bottom of the maximum force shell determined by the CW detuning. The experimental results concerning this phase will be presented in 4.5.4.

4.5.2 Red MOT time sequence

At the end of the blue MOT compression phase, the atoms are driven by the blue MOT lasers detuned by -28MHz with a longitudinal magnetic field gradient $\partial_z B = 60\text{Gcm}^{-1}$. During the SWAP and CW phases, the red beams detuning equals a few MHz for the former, and is even narrowed down to several kHz for the latter. In order to keep a capture region on the same

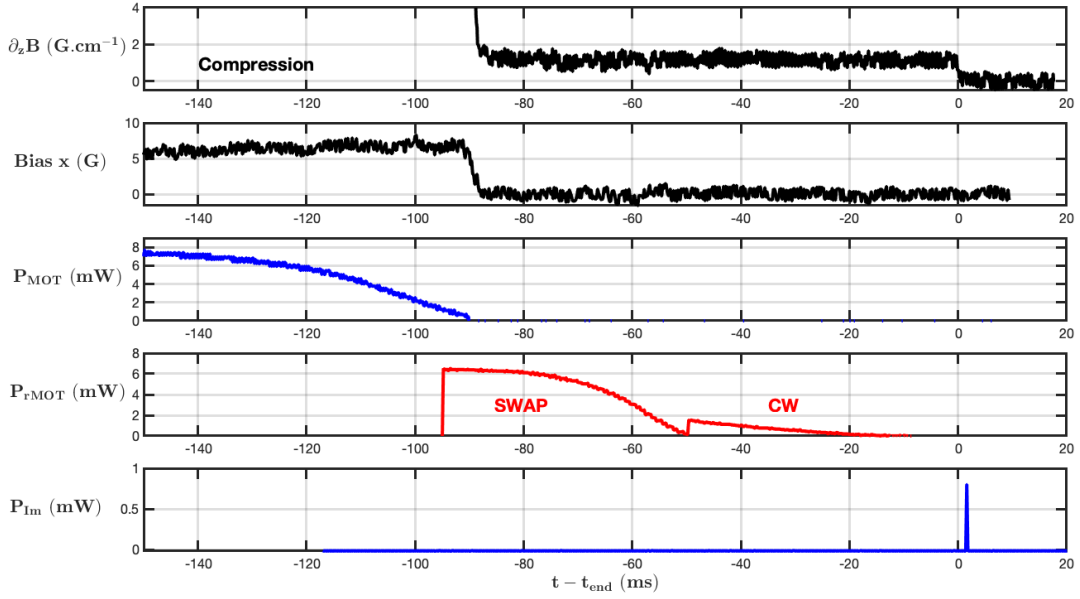


Figure 4.27: Time sequence for the red MOT operation. The time axis is referenced to the end of the sequence t_{end} . The blue MOT power switch off corresponds to 3.1 s after the beginning of the blue MOT loading from figure 4.13. The repumping beams are kept on with constant power during the whole sequence, while the y and z bias fields are null. Only the first imaging pulse is represented, the second one being delayed by 100 ms.

order of magnitude from the blue to the red MOT, the field gradient has to be reduced by the same amount. For this reason, we rapidly switch the gradient from the high blue MOT values to $\partial_z B = 1.3 \text{ G cm}^{-1}$ at the beginning of the SWAP sequence, as can be seen in figure 4.27. The transfer timing is limited by our SSR switch circuit, described in 4.1.1.1, which exponentially decays from one value to the other in a typical $1/e$ lifetime of $160 \mu\text{s}$. The magnetic bias fields are kept equal to 0 on the y and z axes, but the x axis is used during the compression phase to compensate for the fact that the MOT region is placed below the quadrupole coils axis. It thus has to be ramped up from 4.9 to 7.3 G at the same time as the quadrupole gradient in order to avoid any MOT displacement, and reset to 0 G during the red MOT. At the B-field switching time, it is important that the blue MOT lasers are completely switched off in order to avoid a fast and drastic rise of the forces that would make it implode. We thus impose a $200 \mu\text{s}$ delay between the blue beam extinction and the magnetic field drop off. On the other hand, we experimentally observe that switching on the red laser beams 5 ms before the drop off increases the recapture fraction from the dipole allowed to the narrow-line MOTs. Once the red MOT beams are switched on, we immediately start sweeping their frequency in a saw-tooth manner. The SWAP phase lasts 50 ms during which the 689 nm beam power is ramped down continuously by linearly ramping down the slave AOM RF power. At the end of the SWAP stage, we switch to the CW phase where

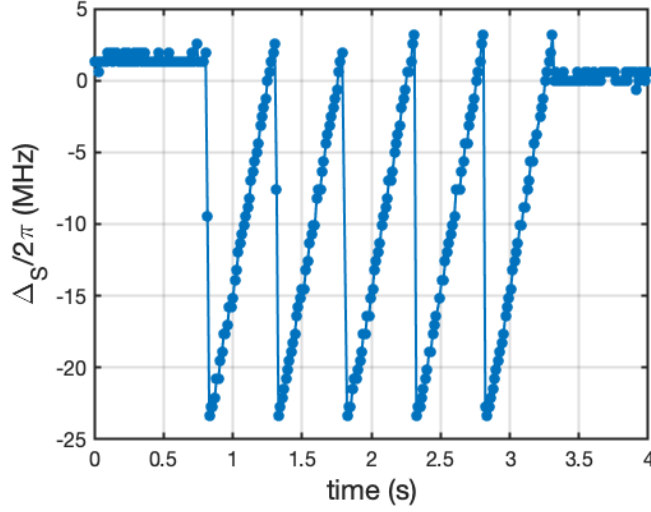


Figure 4.28: Sweep amplitude generated by the red master-slave architecture measured with a wavelength meter. The teeth repetition rate is intentionally slowed by 2 orders of magnitude compared to SWAP operation to stay below the instrument bandwidth.

the detuning is kept constant. The power of the beams is first increased to be then ramped down the same way as for the SWAP, in order to reduce the final CW MOT temperature. During the whole timing sequence, the repumping lasers are switched on with the powers specified in 4.4.4.4. The timings for the SWAP sequence are limited by the performances of our DDS box system. The minimum time step for any frequency or amplitude variation is limited to 8 ns, far below the lifetime of the $|5s5p\rangle^3P_1$ state $\tau = 21 \mu\text{s}$, thus not limiting the physics. On the other hand, delays on the order of τ occur when switching from a sweeping mode to a single frequency one. Fortunately, these delays remain small compared to the dynamics associated with atom falling and do not limit the recapture from SWAP to CW phases.

4.5.3 SWAP MOT characterization

The SWAP technique being a dynamical cooling process, it is very sensitive to the frequency amplitude and final value as well as precise timing. It has been demonstrated by Snigirev *et al.* [109] that the number of atoms captured by the SWAP MOT is not varying for $T \leq 2\tau$, but linearly decreases for higher repetition rates due to a reduced cooling rate which can not trap the fastest atoms. In all the experiments presented hereafter, we use a sweep time $T = 50 \mu\text{s} \approx 2\tau$. The characterization of the SWAP stage consists in an optimized blue MOT sequence followed by a varying number N_S of red frequency sweeps, ended by a time-of-flight free fall and absorption imaging of the cloud. The sweeps are generated by the DDS box driving the red master AOM. The red slave injection then follows this frequency teeth of amplitude Δ_S without jumping for values as high as $\Delta_S = 2\pi \times 25 \text{ MHz}$, as shown in figure 4.28.

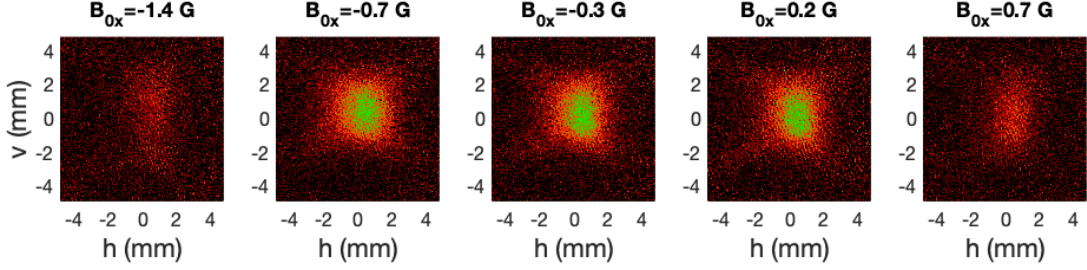


Figure 4.29: SWAP MOT pictures for different bias x field amplitudes with $N_S = 400$, $\Delta_S/2\pi = 3$ MHz and $\nu_{end} = 1.2$ MHz.

4.5.3.1 Alignment sensitivity and procedures

We demonstrated in 4.4.4.1 that the blue MOT has a typical diameter between 2 and 3 mm. The red beams being also relatively small, with a $1/e^2$ diameter of 4.8 mm, it would be easy to miss the cloud recapture if not adjusting carefully the bias fields and red MOT beams. To demonstrate the magnetic field sensitivity of the cloud, we show in figure 4.29 images of the SWAP MOT for different values of the bias x field after the gradient drop off. We observe a distortion of the cloud density for increasing absolute values of the B_{0x} , indicating induced light forces pushing the atoms towards the displaced field zero. We conclude that the bias fields need to be tuned with a precision of ± 0.5 G, corresponding to the *Half-Width at Half-Maximum* (HWHM) of the number of atoms versus B_{0x} .

To ensure that the red beams are correctly centred on the blue MOT cloud, we use a photodiode pointing towards the MOT region. The experimental alignment procedure follows the steps given hereafter.

STEP 1 : Periodically switch the magnetic field gradient on and off on a timescale on the order of 10^2 ms in order to make the blue MOT blink.

STEP 2 : Properly align the photodiode to maximize the fluorescence variations.

STEP 3 : Switch on the red MOT beams, scanned in frequency over the resonance.

STEP 4 : Maximize the 461 nm fluorescence depletion induced by the 689 nm beams axis per axis by modifying the corresponding red beam alignment.

Once this procedure is fulfilled, one can be sure that the red beams cross at the MOT position. At the current stage of the experiment, this optimization as to be done approximately every week, but this timescale could be enlarged by the active temperature stabilization of the optical tables. The last alignment procedure that had to be realized once and for all was the red beams focusing in order to compensate for power imbalance induced by the glass cell transmission. In contrast to the blue MOT, where we can use the fluorescence depletion produced by the red beams, an

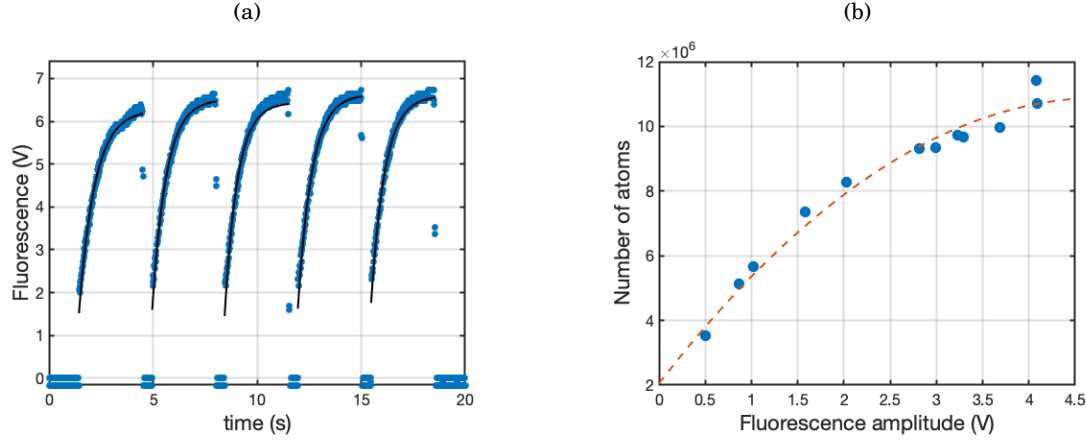


Figure 4.30: (a) Fluorescence signal of 5 blue MOTs in a raw. The data are presented as blue points while a fit according to equation 4.39 plus an offset is given as a black line. (b) Correlation between the fluorescence loading amplitudes and the number of atoms determined by absorption imaging. The blue points corresponds to the data and the orange dotted line to a quadratic fit.

equivalent procedure is extremely challenging for the red MOT. Indeed, this phase has to be produced dynamically and there are no narrower transitions to probe an eventual fluorescence triplet, apart from the clock transition which presents its own challenges for spectroscopy measurement. We thus only had a direct look at live absorption images of the SWAP MOT and tried to increase the number of trapped atoms while modifying the beams focusing, as well as ensuring a symmetrical density profile.

As we are interested in increasing the recapture from the blue to the red MOT, we also need a procedure for measuring the number of atoms in both phases during a given sequence. This can be done by using the same photodiode as mentioned above pointing at the blue MOT and recording its loading, while the number of atoms in the red phase is determined by absorption imaging. We average each MOT realization with fixed parameters over at least 5 cycles, and use the fluctuations in atom numbers to compute error bars. A sequence of 5 MOT loadings is presented in figure 4.30(a), with fits following equation 4.39 plus an offset due to blue MOT beams reflections on the glass cell. In order to correctly infer the number of atoms in the blue MOT from the fluorescence curves, we add a calibration procedure to each dataset where we record absorption images of the blue MOT and fluorescence loadings simultaneously and correlate the two, as shown in figure 4.30(b). The non-linearity between the fluorescence amplitude and the number of atoms reflects the MOT population dependency on the MOT beams power represented in figure 4.22(a). Indeed, the number of atoms saturates for $P_{MOT} \geq 8 \text{ mW}$, while the fluorescence signal is more linearly dependent to the beams power.

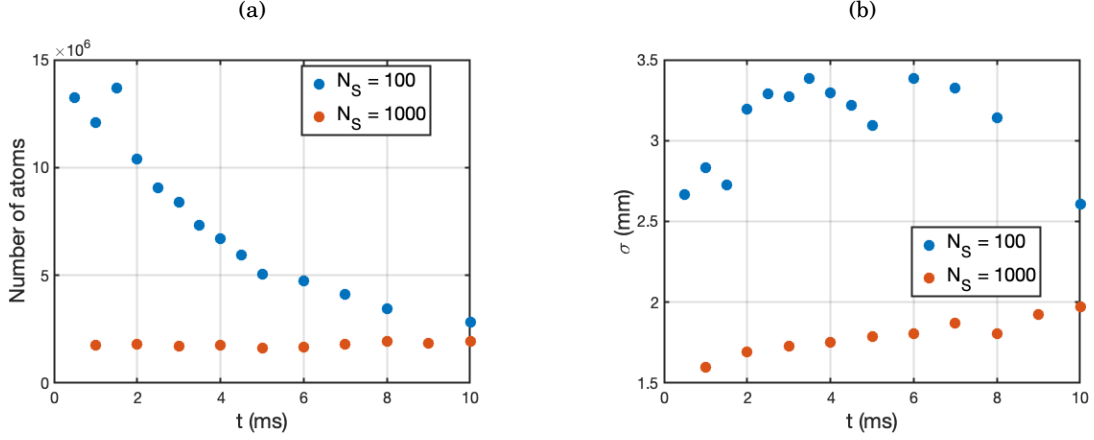


Figure 4.31: (a) Number of atoms and (b) Gaussian radius during a TOF experiment for a small number of sweeps $N_S = 100$ and a longer SWAP duration $N_S = 1000$.

4.5.3.2 Evolution of the density along the SWAP phase

In the time-of-flight (TOF) temperature measurement technique derived in paragraph 4.4.1.2, the atomic cloud spatial and velocity densities are assumed to be Gaussian. The extent of the cloud size as a function of the release time t then gives the temperature, as stated in equation 4.28. In our imaging system, the hottest measured clouds such as the blue MOT, where a temperature of 3 mK leads to a velocity distribution with a standard deviation of 0.55 ms^{-1} , get out of the imaging beam region for TOFs as short as 2 ms. This behaviour can be observed in figure 4.31(a), where the number of atoms in a hot SWAP MOT with a short number of sweeps $N_S = 100$ linearly drops down with t , while a colder SWAP MOT with $N_S = 1000$ is insensitive to the release time. A similar observation can be done with the cloud size, represented in figure 4.31(b), which saturates in the first case and linearly expands in the second case, as expected. Gravity is also a limitation for our imaging apparatus, as free falling atoms start to reach the bottom of the imaging region at $t = 20 \text{ ms}$.

In addition to the apparent atomic losses in the TOF experiment, the temperature determination is being complicated by the fact that the density profile is no longer Gaussian during the SWAP MOT. An illustration of this phenomenon is presented in figure 4.32(a), showing an absorption image of a cloud in the short SWAP times regime. The picture exhibits a crossed density profile, with an apparent Gaussian center. This assumption is confirmed by the projection of the number of atoms onto the camera horizontal axis in figure 4.32(b). My interpretation is that, during the recapture process from the blue to the SWAP MOT, the hottest fraction of atoms is not efficiently trapped by the red beams and is ejected from the cloud center. As the MOT force is maximum at the beams centres, the atoms leave the cloud along the minimum force axes. If one imagines the optical beams transverse intensities as squared profiles, these weak axes

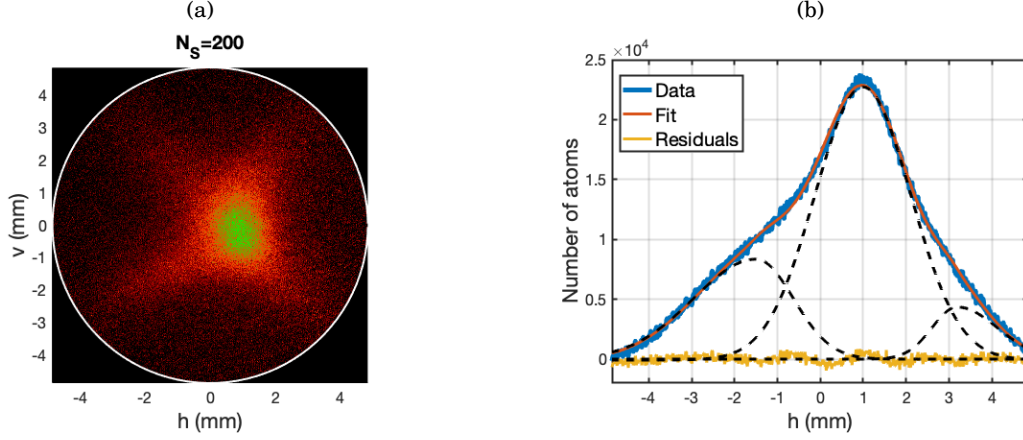


Figure 4.32: (a) Absorption image of a cloud after $N_S = 200$ sweeps and a TOF of 5.5 ms for a SWAP detuning amplitude $\Delta_S/2\pi = 8.0$ MHz and offset $v_{end} = 1.0$ MHz. The red beams are kept at the constant power $P_{rMOT} = 5.6$ mW per axis before the glass cell. The white circle corresponds to the fitting region which corresponds to 0.7 times the imaging beam $1/e^2$ diameter. (b) Histogram of the number of atoms on the horizontal axis of the camera. The data are presented in blue, while the orange curve represents a fit made of the sum of the three black dotted lines profiles according to equation 4.46. The central profile is gaussian while the wings are doubled-sided Gaussians from equation 4.45. The fit residuals are given by the yellow curve.

correspond to the diagonals of an imaginary cube created by the beams overlap region, explaining the cross profile observed in figure 4.32(a). Fitting the central part of the profile with a Gaussian leaves us with “wings” on the edges, with different amplitudes on the right and left probably due to remaining power imbalances. Inspired by coronal mass ejections models [192], I adjust the wings by double-sided Gaussian functions. These W functions are made of two half Gaussians sharing a common amplitude and central position, but distinct radii as follows

$$(4.45) \quad W_{f,s}(x - x_0) = e^{-\frac{(x-x_0)^2}{2\sigma^2}}, \text{ with } \sigma = \begin{cases} \sigma_f, & \text{if } x < x_0 \\ \sigma_s, & \text{if } x \geq x_0 \end{cases}.$$

The total number fitting function C in figure 4.32(b) is then a sum of a Gaussian with adjustable offset and two wings profiles with adjustable heights and sizes on both edges, according to the following equation

$$(4.46) \quad C(x) = N_l W_{fl,sl}(x - x_l) + N_0 e^{-\frac{(x-x_0)^2}{2\sigma_0^2}} + N_r W_{fr,sr}(x - x_r),$$

with l , 0 and r corresponding to the left wing, central gaussian and right wing, respectively.

As we apply longer and longer SWAP phases, the density profiles evolve towards a reduction of the number of atoms in the wings. This feature can be observed directly on the images taken for different N_S in figure 4.33(a). It is confirmed by figure 4.33(b), showing the fraction of atoms in the wings compared to the central Gaussian, expressed as $(N_l + N_r)/N_0$. The width of the

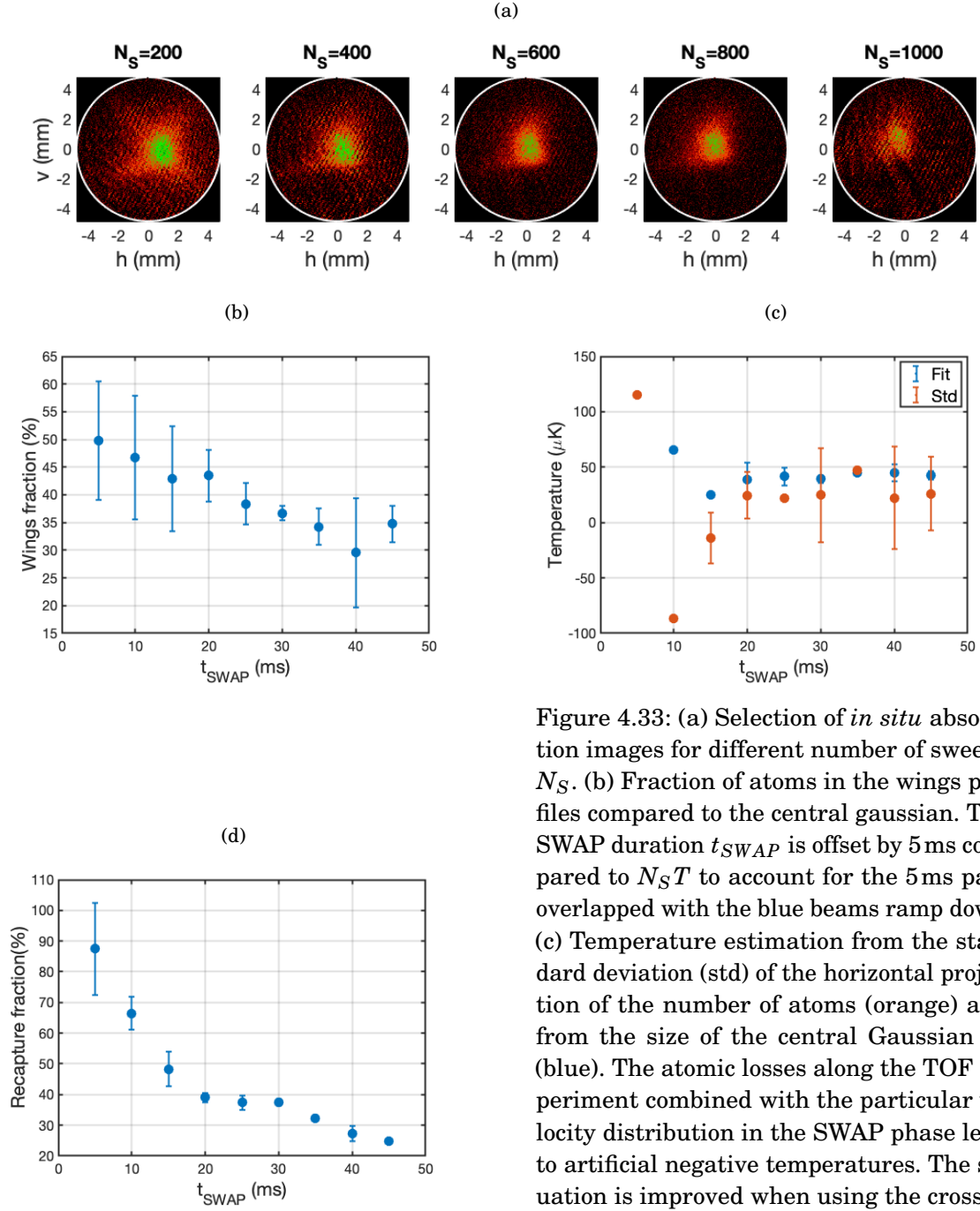


Figure 4.33: (a) Selection of *in situ* absorption images for different number of sweeps N_S . (b) Fraction of atoms in the wings profiles compared to the central gaussian. The SWAP duration t_{SWAP} is offset by 5 ms compared to $N_S T$ to account for the 5 ms part overlapped with the blue beams ramp down. (c) Temperature estimation from the standard deviation (std) of the horizontal projection of the number of atoms (orange) and from the size of the central Gaussian fit (blue). The atomic losses along the TOF experiment combined with the particular velocity distribution in the SWAP phase lead to artificial negative temperatures. The situation is improved when using the crossed profile fit function from equation 4.46. (d) Recapture fraction from the blue to the SWAP MOT, including all the atoms present on the absorption images.

error bars is directly linked to the atomic losses during the TOF and thus reduces at higher N_S . All the preceding effects combined lead to a complicated determination of the temperature,

even giving negative temperatures when considering the standard deviation of the number of atoms along the horizontal axis of the camera, as can be seen in figure 4.33(c). Taking into account only the central Gaussian width to determine the temperature improves the situation, but remains very sensitive to the fitting parameters and can not provide an accurate temperature determination. Nevertheless, the temperature estimation converges for long SWAP durations to a value $T_h = 40(10)\mu\text{K}$ for this set of parameters. The recapture evolution from blue to red as a function of the number of teeth is given in figure 4.33(d). After a first drop off within the first 20 ms starting from one half of the number of atoms in the blue MOT, the fraction stabilizes to about a third for these unoptimized parameters.

4.5.3.3 Frequency sweeps parameters

As detailed in 4.5.1.1, the sweep frequency amplitude Δ_S and its final value ν_{end} are key parameters in the SWAP dynamics. In this paragraph, we present a characterization by means of these two quantities, for a number of teeth $N_S = 600$ equivalent to a time $t_{SWAP} = 25\text{ms}$ with the blue beams off and the red beam power kept constant to $P_{rMOT} = 6.2\text{mW}$. The recapture fraction from the blue MOT is given in figure 4.34(a) for different Δ_S . We observe a maximum in the region ranging from $\Delta_S = 2\pi \times 6\text{MHz}$ to $\Delta_S = 2\pi \times 8\text{MHz}$, followed by a drop off for higher amplitudes. This recapture fraction reduction could be explained by the reduced intensity available per frequency tooth in the Fourier domain. Nonetheless, atoms are still trapped for amplitudes as high as 25 MHz, proving the robustness of the technique. The corresponding temperatures, pictured in figure 4.34(b), are estimated by taking the expansion of the central Gaussian from the crossed profile in equation 4.46. The results show that lower temperatures can be reached by increasing Δ_S .

In a second stage, we use the best detuning amplitude of 8 MHz to characterize the influence of the final frequency ν_{end} . In the recapture fraction from figure 4.34(c), one can see that the SWAP technique starts to be efficient when this frequency approaches 0. Moreover, the number of atoms is maximized for a significant part of the ramp lying above the atomic resonance, and only drops off when ν_{end} approaches the sweep amplitude Δ_S . This behaviour is explained by the fact that SWAP cooling relies on an imbalance between the probabilities of exciting an atom from the ground state to one of the $|(5s5p)^3P_1, m_J = \pm 1\rangle$ excited states. This process is robust to blue detuned laser frequencies, as an atom adiabatically promoted to the lowest lying energy state during the upward frequency ramp will remain in that state when the frequency crosses the highest excited state resonance [174]. We thus observe a recapture maximum from the blue MOT in figure 4.34(c) in a broad region centred around $2\pi\nu_{end} \simeq \Delta_S/2$. The temperatures in figure 4.34(d) follow the same considerations, with a minimal temperature range $\nu_{end} \in [1, 5]\text{MHz}$ corresponding to the maximum atomic recapture range.

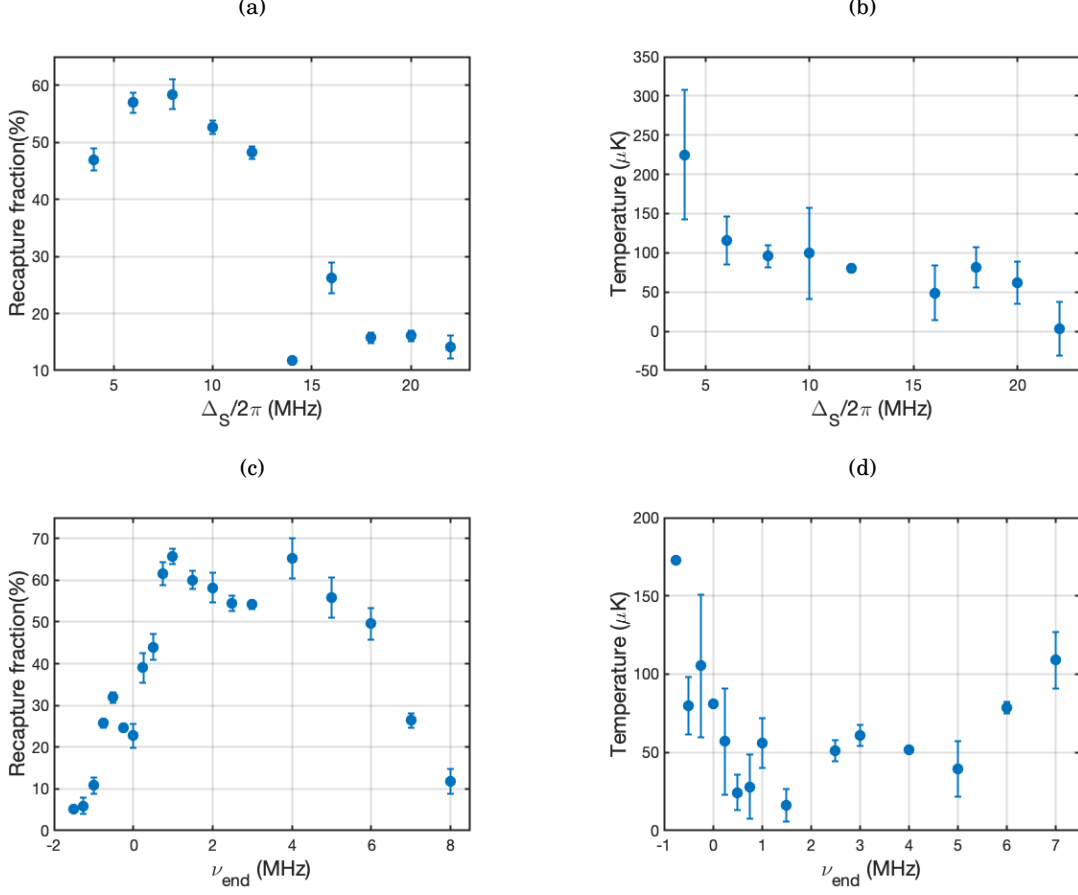


Figure 4.34: (a) Recapture fraction from the blue MOT and (b) temperature estimated with the central Gaussian for varying SWAP amplitude Δ_S with a fixed offset $\nu_{end} = 1.0$ MHz. (c) Recapture and (d) temperature as a function of the final frequency offset ν_{end} with a fixed amplitude $\Delta_S = 8.0$ MHz. Both dataset are taken at the fixed red beam power of 6.2 mW per axis and for a number of sweeps $N_S = 600$.

4.5.3.4 Red beams power

As is the case in Doppler theory, the red MOT beam powers during the SWAP phase influence both the recapture fraction and the temperature. It has been shown in the previous SWAP experiments that the number of trapped atoms increases linearly with the beam powers and reaches either a plateau or a maximum [109], while the temperature presents a minimum at smaller values [164]. To confirm these observations, we characterize the SWAP recapture and temperature in two steps. In the first experiment, we keep the laser power at a constant level and measure the number of atoms as shown in figure 4.35(a). We find a maximum recapture fraction from the blue MOT for a starting power $P_{rMOT} = 5.5$ mW, lower than the highest optical available powers of the red slave laser. In the second experiment, we linearly ramp down the red slave AOM RF power, and thus adiabatically ramp down the laser power from the maximum available

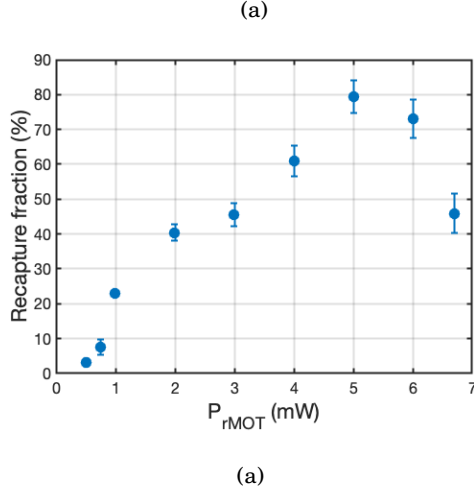
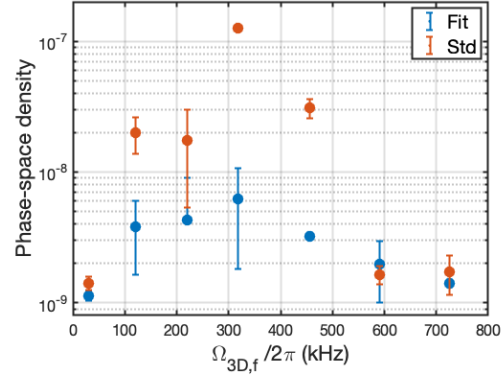
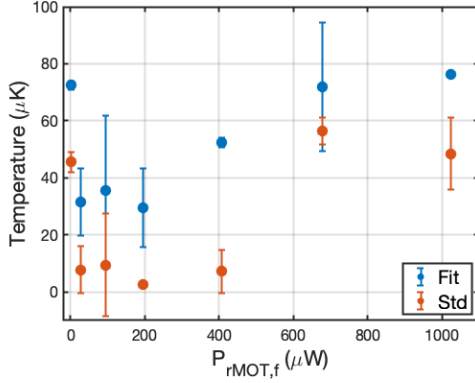


Figure 4.35: (a) Recapture fraction from blue to SWAP MOT for a constant power P_{rMOT} during a red phase of $N_S = 600$ teeth. The detuning amplitude is $\Delta_S = 2\pi \times 8.0\text{MHz}$ and the final value is $\nu_{end} = 1.1\text{MHz}$. (b) Temperature and (c) phase-space density of a $N_S = 900$ SWAP MOT with an initial power of 6.5mW ramped down to a final value $P_{rMOT,f}$. The detuning parameters are $\Delta_S = 2\pi \times 6.0\text{MHz}$ and $\nu_{end} = 1.2\text{MHz}$. The raw data estimation is presented in orange, while the blue points are inferred from the crossed fit profile.



value to a reduced one. The results are shown in figure 4.36(a). The corresponding phase-space density is presented in figure 4.36(b) as a function of the final three-dimensional Rabi frequency $\Omega_{3D,f}$. For one beam, the Rabi frequency can be expressed as $\Omega = \Gamma \sqrt{s_0/2}$. Summing over the six red MOT beams and accounting for the glass cell transmission T , this parameter is given by

$$(4.47) \quad \Omega_{3D} = \Gamma \sqrt{\frac{3}{2} s_0 T (1 + T^2)},$$

where $s_0 = I_0/I_{sat}$ is the saturation parameter computed with the incident intensity I_0 per beam before the glass cell. It appears from figures 4.36(a) and 4.36(b) that the fitting method developed in 4.5.3.2 tends to overestimate the temperature in this regime, but also smoothens divergences from the raw data. The results exhibit an optimum for the temperature and the phase-space density at a final power $P_{rMOT,f} = 200\mu\text{W}$. The estimated temperature at the end of this sequence lies below $30\mu\text{K}$, but a more precise study including longer time-of-flights would be necessary to give a precise value.

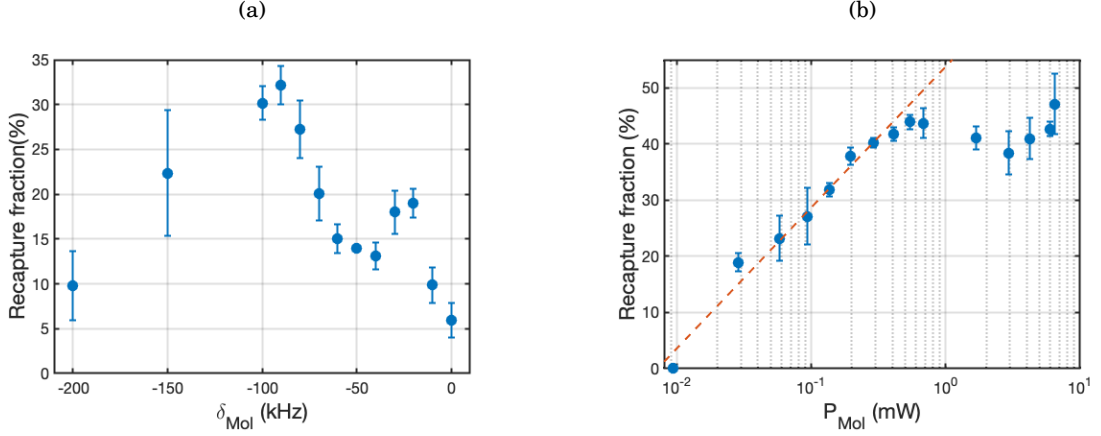


Figure 4.36: Recapture fraction from the blue MOT to a red optical molasses after an optimized SWAP phase as a function (a) of the 689nm laser detuning and (b) the laser power per beam in logarithmic scale. The data are represented as blue points and the orange dotted line is a fit on the lowest powers according to $\log\left(\frac{P_{CW}}{P_0}\right)^\alpha$ with $P_0 = 7\mu\text{W}$ and $\alpha = 0.1$. In the first dataset, the power is kept constant to $P_{CW} = 100\mu\text{W}$ while in the second one the detuning is fixed to $\delta_{CW} = -90\text{kHz}$.

4.5.4 CW operation

The final stage of the red MOT is a *Continuous Wave* (CW) phase where we keep the laser detuning constant during 50ms. Starting with the optimized SWAP phase described in the previous section, we present results on a CW MOT with a longitudinal magnetic gradient $\partial_z B = 1.3\text{Gcm}^{-1}$, as well as a molasses experiment where $\partial_z B = 0\text{Gcm}^{-1}$ in the continuous phase. In theory, optical molasses achieve colder temperatures than MOTs [193], making a potentially interesting tool to reduce the final red MOT temperature before the atomic transport to the ring cavity.

4.5.4.1 Red molasses

In this paragraph, we characterize a red optical molasses applied during 50ms with constant detuning δ_{Mol} and power P_{Mol} for the red MOT beams. As the temperatures get as low as a few μK in this phase, the realized studies do not provide a sufficient precision with our current imaging apparatus, and we only focus on the recapture fraction from the blue MOT presented in figure 4.36. The recapture as a function of the molasses detuning from figure 4.36(a) shows an optimum at $\delta_{Mol} = -90\text{kHz}$. For this particular value, we are able to recapture approximately one third of the atoms initially captured. This number can be improved by adjusting the laser power, as shown in figure 4.36(b). It appears that, for powers $P_{Mol} \leq 1\text{mW}$ on each MOT axis, the atomic recapture logarithmically drops down as demonstrated by the fit on the lowest powers. At higher laser powers, it saturates to 45(5)%, similarly to the SWAP MOT. The relatively high powers necessary to recapture all the atoms from the SWAP phase can be explained by the fact

that we switch from a broad frequency modulated MOT to a single frequency operation. Power broadening of the red transition in the molasses phase thus allows to recapture almost all the atoms from the SWAP MOT. As the temperature is known to decrease with laser intensities due to a reduction of the photonic diffusion, it is relevant to start the molasses phase with a power $P_{Mol} = 1 \text{ mW}$, lying above the final SWAP value, and ramp it down along the molasses operation.

4.5.4.2 CW MOT

At the end of the red MOT, a CW MOT operation has been studied with a magnetic gradient $\partial_z B = 1.3 \text{ G cm}^{-1}$ applied during 50 ms, at a constant optical power. In the laboratory frame $\{x, y, z\}$, the maximum of the MOT force for a detuning Δ_0 can be represented in three dimensions as an ellipsoid following the equation

$$(4.48) \quad \left(\frac{x - x_0}{r_x} \right)^2 + \left(\frac{y - y_0}{r_y} \right)^2 + \left(\frac{z - z_0}{r_z} \right)^2 = 1,$$

where $r_x = r_y = |\Delta_0|/(\gamma_J \partial_x B)$ and $r_z = |\Delta_0|/(\gamma_J \partial_z B)$ correspond to the elliptic radii, with $\gamma_J = 2.1 \text{ MHz G}^{-1}$ for a $J = 1$ transition. This equation can be parametrized as follows

$$(4.49) \quad \begin{cases} x - x_0 = r_x \cos \theta \cos \varphi \\ y - y_0 = r_y \cos \theta \sin \varphi \\ x - x_0 = r_z \sin \theta \end{cases}$$

with the reduced latitude $-\frac{\pi}{2} \leq \theta \leq \frac{\pi}{2}$ and the longitude $0 \leq \varphi \leq 2\pi$. Due to the angle α between our imaging system and the y axis shown in figure 4.6, the MOT shell projections onto the CCD camera follows

$$(4.50) \quad \begin{cases} v - v_0 = r_x \cos \theta \cos \varphi \\ h - h_0 = r_y \cos \theta \sin \varphi \sin \alpha + r_z \sin \theta \cos \alpha \end{cases}$$

where $\tan \theta = \frac{r_y \sin \varphi}{r_z \tan \alpha}$ is fixed by the condition $b = b_0$.

The absorption images taken for different detunings are shown in figure 4.37, with a closer look at $\delta_{CW} = -100 \text{ kHz}$ and its projections onto the horizontal and vertical axes of the CCD camera in figures 4.38(a) and 4.38(b), respectively. For these settings, the MOT shell from equation 4.50 presents radii $r_x = 730 \mu\text{m}$ and $r_z = 365 \mu\text{m}$, according to equation 4.48. The comparison between the cloud density and the MOT force shell reveals a large CW MOT compared to previously reported experiments [50, 101]. The main reason is that the intensity of the laser beam is kept as high as $2 \times 10^3 I_{sat}$ in order to recapture a maximum number of atoms from the SWAP MOT. Moreover, our experiment uses a quadrupole coil pair centred on a horizontal axis in the lab frame, while the usual implementations use vertically aligned coils. The atoms thus tend to accumulate at the bottom of a trap which is twice narrower in the z dimension than in its vertical coil pair counter-part. Nevertheless, we observe the previously reported gravitational sag

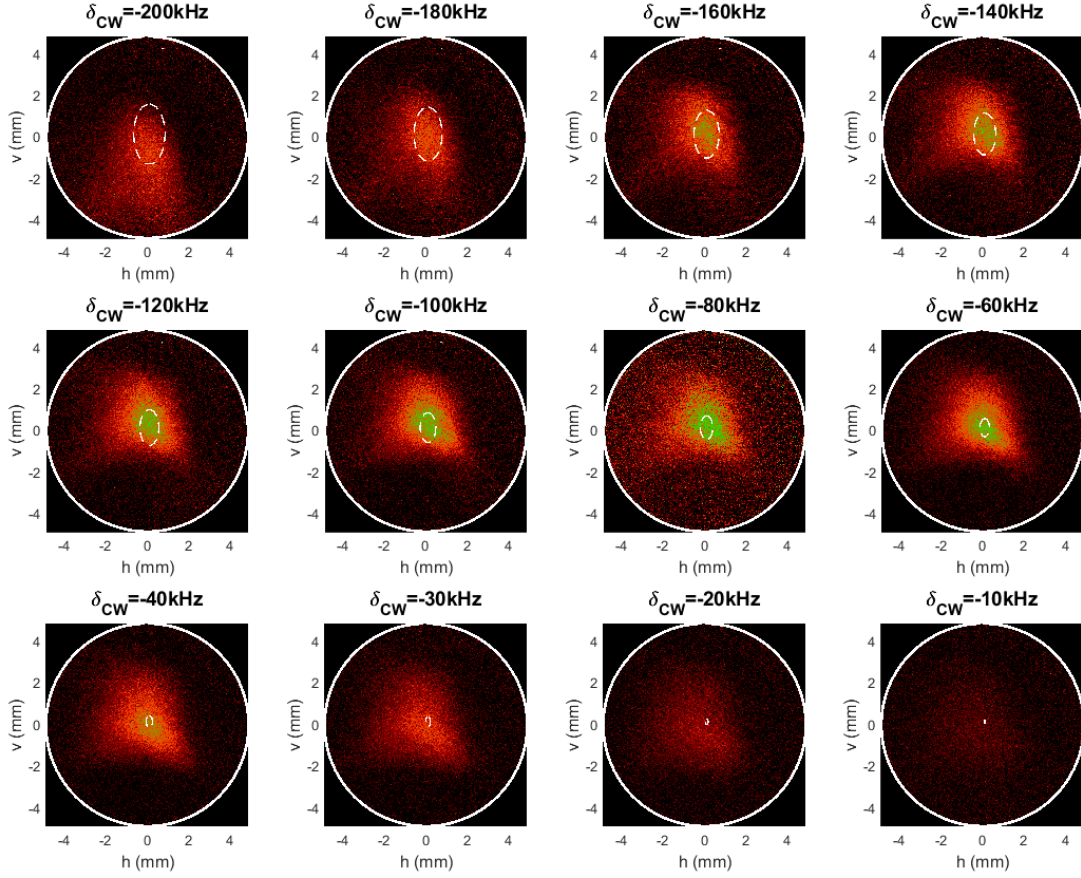


Figure 4.37: Absorption images of the CW MOT for different detunings. The maximum MOT force ellipsoids from equation 4.50 are represented as white dotted ellipses.

in figure 4.38(b) as the vertical atom number projection presents a steeper variation in the $v < 0$ region than in the $v > 0$ region.

The recapture fraction from the blue MOT for different CW detunings, presented in figure 4.38(c), presents a maximum of 65(5)% at $\delta_{CW} = -100\text{kHz}$. This value indicates that we capture all the atoms from the SWAP MOT, presenting a similar recapture fraction for optimized parameters. For smaller absolute values of the detuning, the trap ellipsoid becomes smaller and smaller and can not efficiently capture the remaining atoms. At the same time, it increases the cloud temperature as can be seen in figure 4.38(d). On the other side, for $\delta_{CW} < -100\text{kHz}$, atoms are leaking from the trap and fall as can be seen in figure 4.37. To conclude, the number of atoms is maximized at the transient value, ensuring at the same time a temperature below $20\mu\text{K}$. In order to further decrease the final temperature, we implement a power ramp down along the

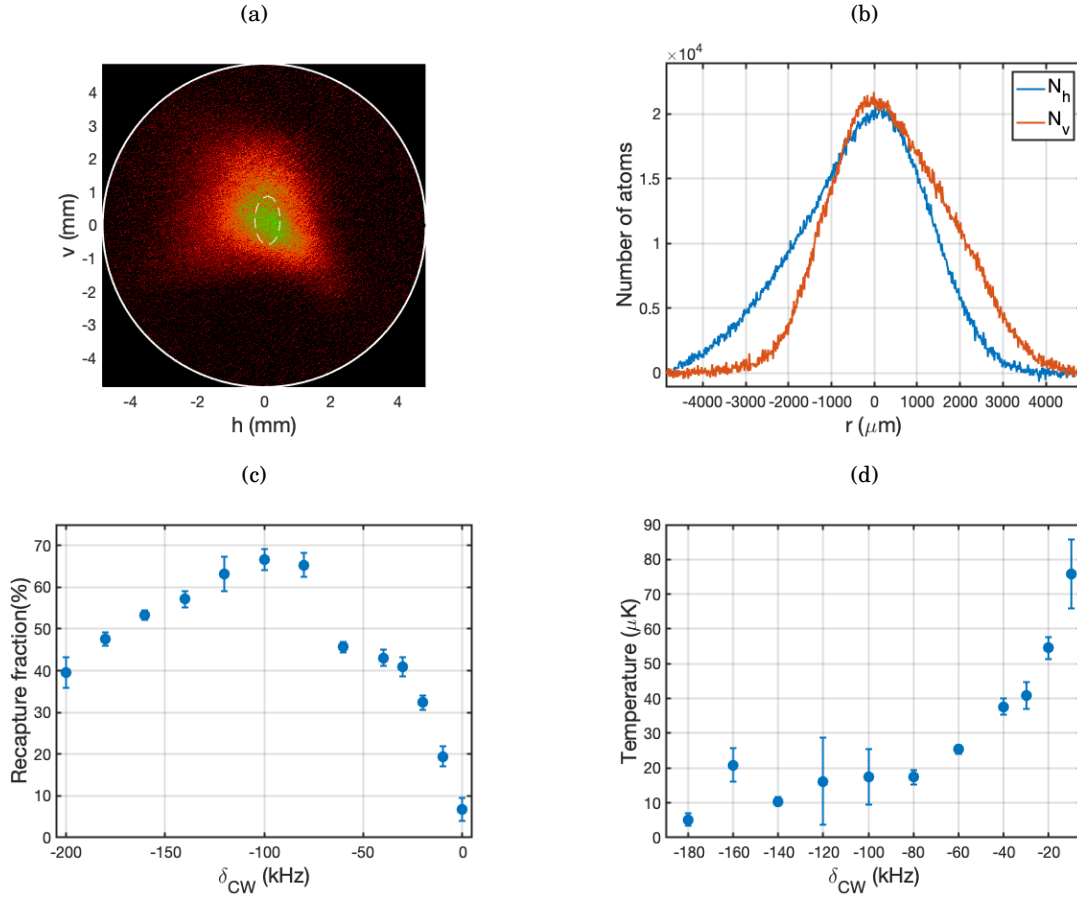


Figure 4.38: (a) Absorption image and (b) projection of the number of atoms on the two axes of the CCD camera $r \in \{h, v\}$ for $\delta_{CW} = -100$ kHz. (c) Recapture fraction from the blue to the CW MOT and (d) temperature inferred from the central Gaussian as a function of the detuning for a constant power $P_{CW} = 540 \mu\text{W}$.

50 ms CW phase by linearly ramping the red slave AOM RF power, as previously done during the SWAP phase. For a final power $P_{CW,f} = 1 \mu\text{W}$ we still trap 55(5)% of the atoms from the blue MOT at a temperature approaching the recoil limit, even if a precise temperature determination still needs to be realized.

Conclusion on the red MOT

At the end of the SWAP and CW MOT characterizations, we conclude that we are able to trap more than 50% of the atoms from the blue MOT, at a temperature approaching the μK . To realize this performance, we use a 45 ms long SWAP phase with 5 ms overlapped to the final blue MOT compression. Within this time interval, we implement saw-tooth frequency sweeps at a repetition rate $T = 50 \mu\text{s}$ with an amplitude $\Delta_S = 2\pi \times 8.0 \text{ MHz}$ and an offset $\nu_{\text{end}} = 2.0 \text{ MHz}$ compared to the $|(5s^2)^1S_0\rangle \rightarrow |(5s5p)^3P_1\rangle$ transition of ^{88}Sr . The red beams optical powers are ramped down from $P_{r\text{MOT}} = 5.5 \text{ mW}$ to $P_{r\text{MOT},f} = 200 \mu\text{W}$ on each retro-reflected MOT axis. In a second stage, we fix the detuning to $\delta_{\text{CW}} = -100 \text{ kHz}$ for a CW MOT operation. The laser power are once again ramped down from $P_{\text{CW}} = 500 \mu\text{W}$ to a final value $P_{\text{CW},f} = 1 \mu\text{W}$. During the whole red MOT sequence, the longitudinal magnetic field gradient is fixed to $\partial_z B = 1.3 \text{ G cm}^{-1}$. The cloud resulting from the total sequence is presented in figure 4.39(a), with its projections onto the CCD camera axes in figure 4.39(b). In order to increase the phase-space density before the transport from the MOT region to the ring cavity, a longer low power phase could be implemented at the end of the sequence, at the cost of loosing a fraction of the atoms. We also demonstrated that optical molasses at 689 nm can be implemented to further reduce the cloud temperature. This phase is optimized for a detuning $\delta_{\text{Mol}} = -90 \text{ kHz}$ and a power $P_{\text{Mol}} = 1 \text{ mW}$, which can be ramped down to decrease the temperature even further.

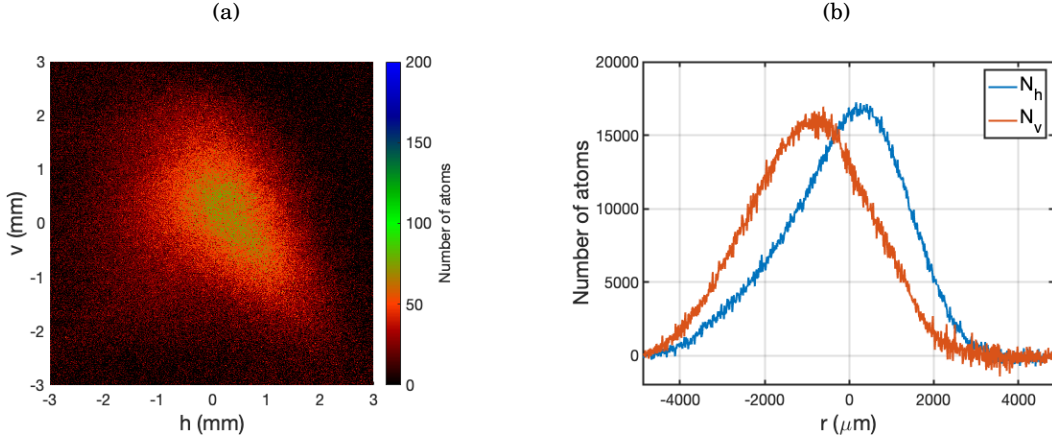


Figure 4.39: (a) Absorption image of the final CW MOT after optimization and (b) its projections onto the axes of the imaging camera $r \in \{h, v\}$.

CONCLUSION

During this project, we implemented a simple, compact and efficient apparatus for strontium trapping and cooling. In chapter 2, the laser system that I designed and built for operations on the blue, red, repumping and clock transitions has been presented. It results in laser lineshapes and stabilities narrower than the natural linewidths for all the transitions involved in MOT operations. Also, a versatile frequency generation setup allows to address the transitions of the most abundant bosonic ^{88}Sr and fermionic ^{87}Sr isotopes. A first determination of the clock laser linewidth, obtained with a stabilization on a high-finesse ultra-stable cavity, is equal to 200 Hz. This value gives an estimation of the expected Fourier limited resolution for future experiments on the clock transition, but can still be improved with higher bandwidth locking schemes. The day-to-day frequency drift of the Fabry-Pérot ultra-stable reference cavity has been measured to 5.94(3) kHz, which does not limit the red MOT operations but needs to be actively compensated with the 698 nm laser AOM in order to address the clock transition.

In chapter 3, the vacuum system designed and assembled by our team has been described. At the heart of this system, a low power consumption home-made oven allows to produce an effusive beam of strontium atoms with a total flow rate of $3.9(2) \times 10^{13} \text{ atoms s}^{-1}$ at 460°C, using only 13 W of electrical heating power. Its capillary design, characterized by a peaking factor of 3.9 at this temperature, combined with two cold apertures results in a collimated atomic beam of $3.0(2) \times 10^{10} \text{ atoms s}^{-1}$ in the MOT region located in the glass cell, 15 cm away from the oven. A characterization of the beam angular distribution has been performed by transverse absorption, with a theoretical description accounting for the finite probe laser beam diameter. We also measured a small atomic beam transverse velocity spreading of $7(2) \text{ m s}^{-1}$. With the presence of the differential pressure hole, we obtain a pressure of $1.3 \times 10^{-10} \text{ mbar}$ inside the glass cell.

This compact vacuum system is combined with a coil assembly that is used to achieve both Zeeman slowing and MOT capture on the blue transition simultaneously, simplifying the experimental apparatus compared to usual Zeeman slower setups as described in chapter 4. This hybrid slowing and cooling mechanism at 461 nm leads to the trapping of 2×10^7 atoms in 3 s at a temperature of 2 mK at the end of an optimized laser power and magnetic gradient time sequence. A second stage SWAP cooling on the red transition brings 80% of the atoms to a temperature of

approximately $20\,\mu\text{K}$ in 40 ms. Finally, a CW operation at constant detuning and reduced optical power lowers the temperature to the μK range, reaching the precision limitations of our current imaging setup. At the end of this sequence, a total fraction of 55% is held from the blue to the red MOT. Moreover, I proved that red optical molasses could be implemented to further reduce the temperature before transporting the atoms to the cavity.

PROSPECTIVES ON THE RING CAVITY

In the last months of my project, Torben Pöplau assembled a high-finesse micro ring cavity visible in figures 4.40(a) and 4.40(b), based on the design presented in his PhD thesis [61]. The cavity is made of an astigmatism compensated mirror dug onto the tip of a multi-mode optical fiber of diameter $210\mu\text{m}$ by CO_2 machining, and two planar mirrors consisting in $2.5 \times 2 \times 1\text{mm}$ fused silica wafers. The fiber is placed on a shearing piezo electric actuator allowing to adjust the cavity length around its nominal value of $500\mu\text{m}$. The near-concentric operation of the cavity leads to a beam waist of $3.5\mu\text{m}$. A first estimation of the cavity finesse gives $\mathcal{F} = 4 \times 10^4$, leading to a single atom cooperativity $C_1 = 80$ for future CQED schemes.

This cavity is assembled on a glass plate which will be glued onto the top inner surface of the glass cell. The atoms thus need to be transported from the MOT region to the cavity. For this purpose, we will use a green laser with an optical power of 5mW at 515nm ¹⁰ in a moving lattice configuration. The trapping potential will be produced by two counter-propagating beams detuned from each other by $\delta\omega$. The resulting trapping potential along the transport m axis writes

$$(4.51) \quad U(m, y, l) = \frac{w_0^2}{w^2(m)} e^{-\frac{2(l^2 + y^2)}{w^2(m)}} \cos\left(\frac{\delta\omega}{2}t - km\right)^2,$$

where the spatial coordinates are represented in figure 4.40(c), and U_0 is the trapping potential given by

$$(4.52) \quad U_0 = \frac{\hbar\Gamma}{2} \frac{\Gamma}{\Delta} \frac{I_0}{I_{\text{sat}}},$$

with $\Delta = \omega - \omega_0$ the detuning between the trapping light and the blue transition at 461nm , Γ the transition linewidth and I_0 the trapping beam intensity in each arm. This transport will occur on a distance of 1cm , at an angle of 50° compared to the vertical axis of the experiment, as pictured in figure 4.40(c). The longitudinal trapping potential is shown in figure 4.40(d). With a realistic optical power of 0.5W per beam and a trapping waist $w_0 = 40\mu\text{m}$ located inside the cavity, the obtained trap depth is large compared to the final red MOT temperature and should allow to efficiently transport a non negligible fraction of the atoms.

The experiment is thus ready to host the optical micro ring cavity in the glass cell and magically trap an ultra-cold strontium sample coupled to its light field at the clock frequency.

¹⁰Fiber laser ALS-GR-515-2-I-CC-SF from Azurlight Systems. See <https://azurlight-systems.com/>.

This promising platform will constitute an entirely new basis for many-body entanglement studies on an optical clock transition with two possibly interacting cavity modes. The available physical schemes will thus allow to bring a new contribution to the understanding and generation of multi-particles entangled states, as well as proposing quantum enhanced precision processes for quantum optical clocks.

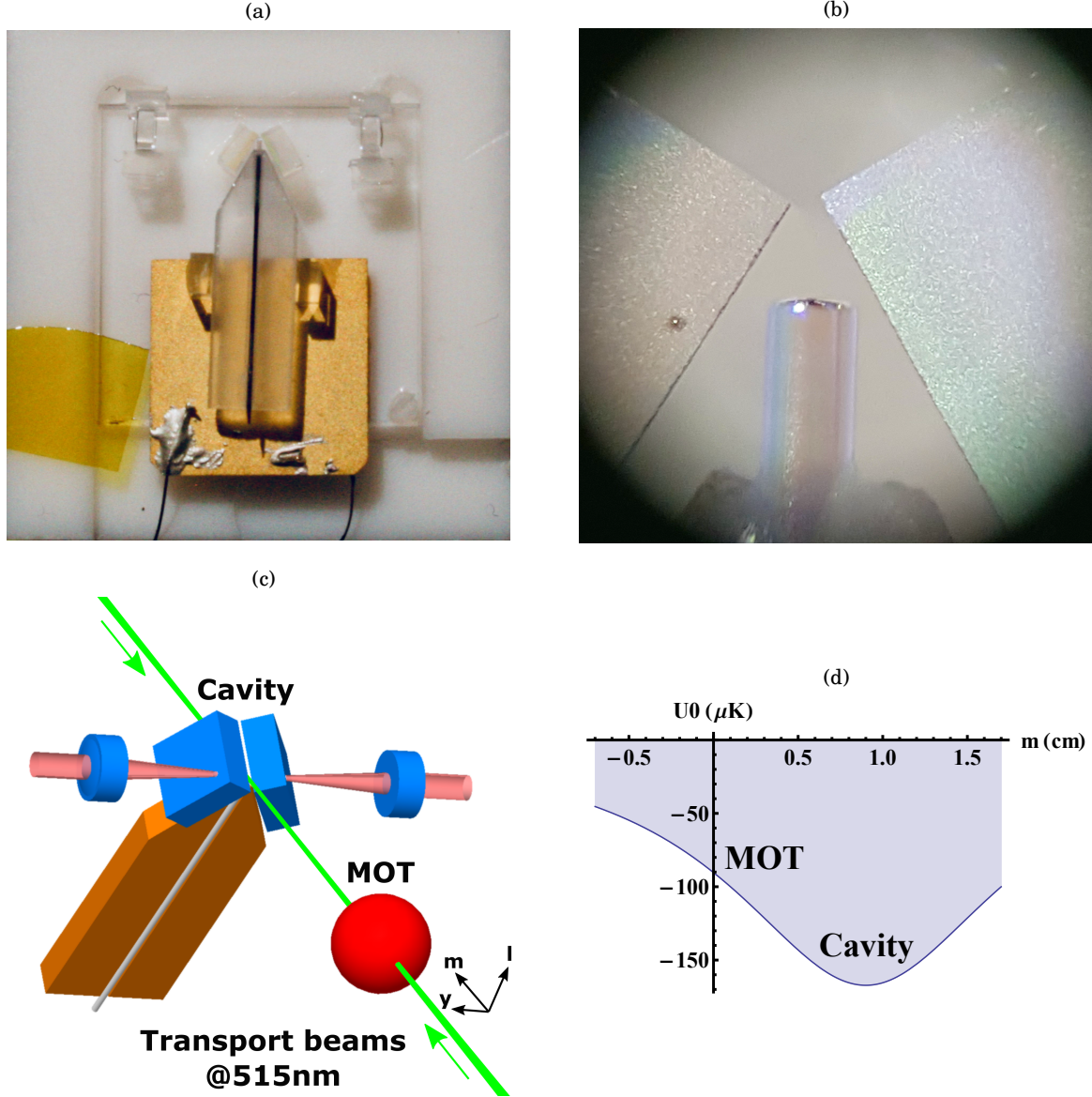


Figure 4.40: (a) Picture of the assembled high-finesse ring cavity. The fiber is held by a V-groove glued on a shearing piezoelectric actuator allowing to adjust the cavity length. The piezo, planar mirrors and coupling lenses are glued on a maintaining glass plate. (b) Picture of the cavity taken with a microscope objective. The cavity mode length is equal to $500\mu\text{m}$. (c) Scheme of the atomic transport from the red MOT to the ring cavity with two counter-propagating green laser beams at 515nm. (d) Trap depth potential along the transport axis m for a power $P_0 = 0.5\text{W}$ per beam and a waist $w_0 = 40\mu\text{m}$ located between the two planar mirrors of the cavity.



OPTICAL TABLES SCHEMES

The laser systems presented in sections 2.1 and 2.2 of chapter 2 are a simplified version of the complete optical setup that I developed. A more realistic scheme of the two optical tables containing the blue and repumping lasers on one side, and the red lasers on the other side are given in figures A.1 and A.2, respectively. The red laser system is placed on a breadboard located on the main experiment table, while the blue system is placed on another optical table located approximately 1 m away from the previous one.

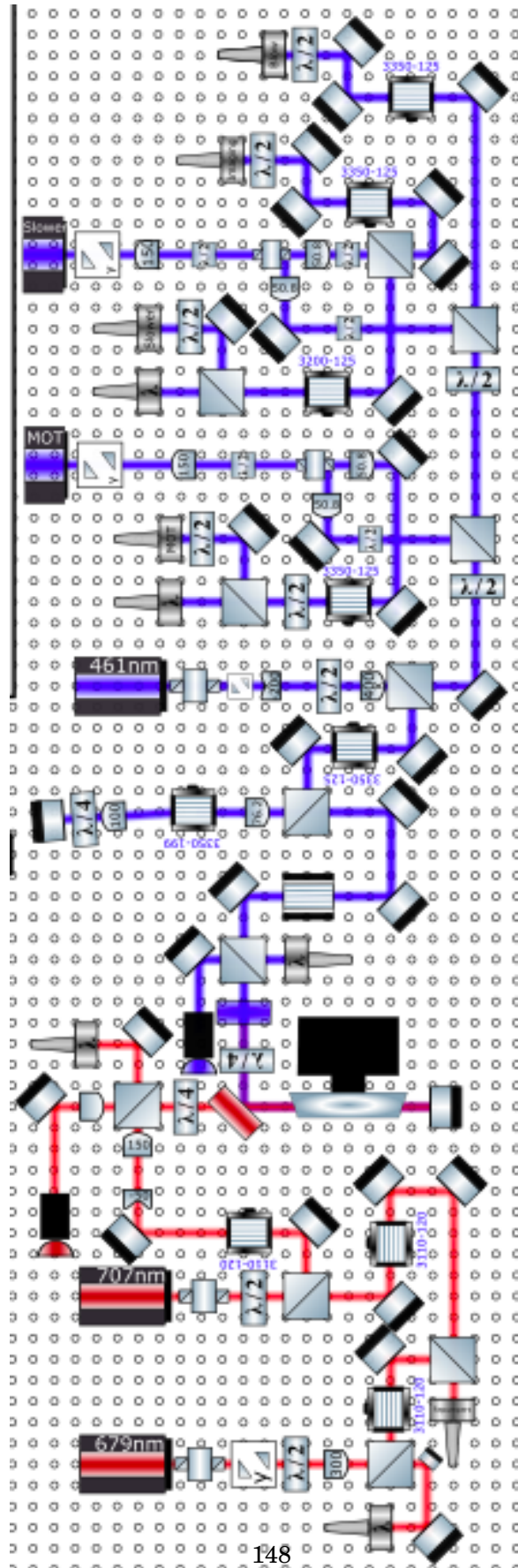


Figure A.1: On scale scheme of the optical table containing the lasers at 461nm, 679nm and 707nm.

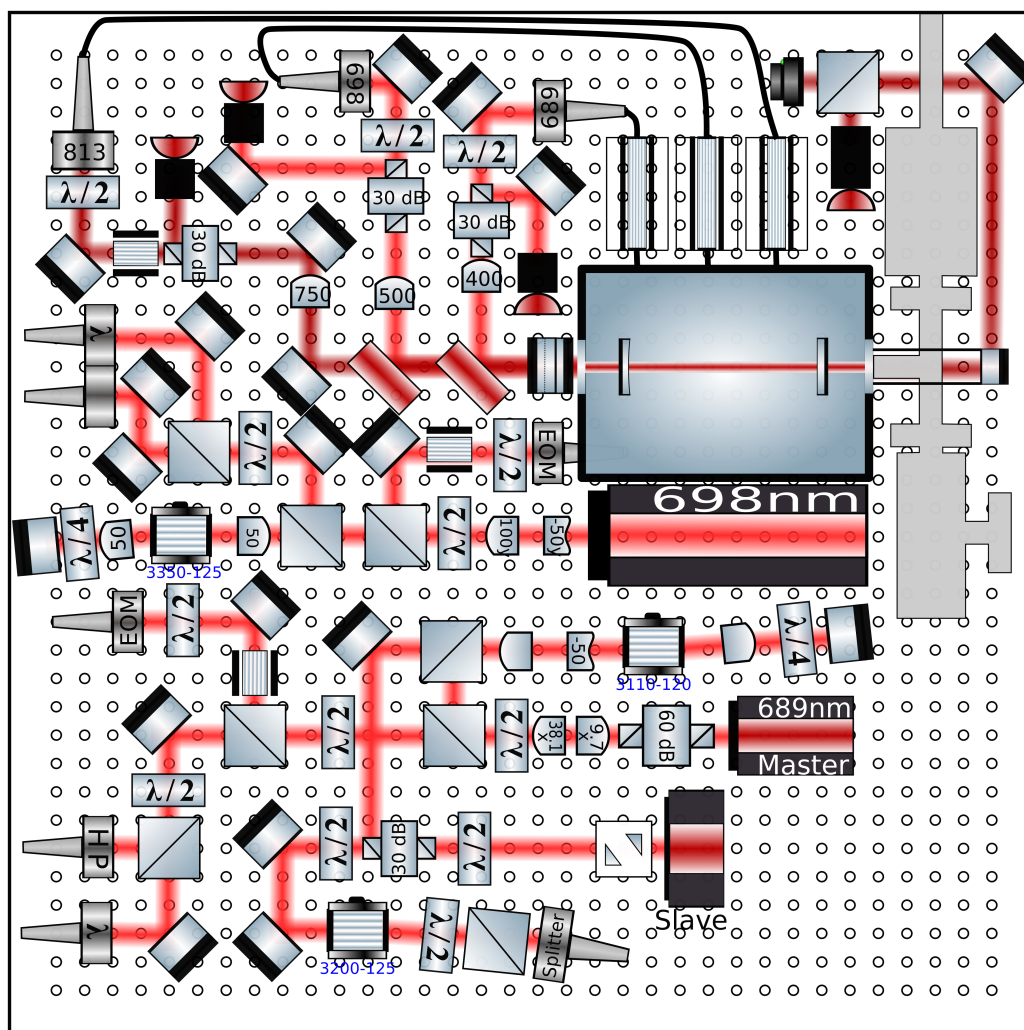


Figure A.2: On scale scheme of the optical breadboard containing the lasers at 689nm and 698nm, as well as the stabilization part of the 813nm laser.

LASER ASTIGMATISM COMPENSATION BASED ON ABCD MATRICES FORMALISM

Both light fields emitted by laser diodes and encountered in optical cavities can be decomposed on a basis of eigenmodes of the Maxwell's equations. In an homogeneous and isotropic medium of refractive index n , these expressions give rise to the Helmholtz equation written as

$$(B.1) \quad (\nabla^2 + k^2) \mathbf{E} = 0,$$

with $k = n\omega/c$ for a wave at frequency ω . A set of solutions of this equation in the paraxial approximation is given by the Hermite-Gauss *Transverse Electromagnetic Modes* (TEM _{mn}) [62]. The fundamental transverse mode TEM₀₀ is of particular interest in CQED experiments. Indeed, it is referred to as the Gaussian mode and is also solution of the free space propagation of laser beams. The explicit form of the Gaussian mode for a beam propagating along the z axis is given by

$$(B.2) \quad \mathbf{E}(x, y, z) = E_0 \sqrt{\frac{w_{0x}w_{0y}}{w_x(z)w_y(z)}} e^{-\frac{x^2}{w_x(z)^2} - \frac{y^2}{w_y(z)^2}} \cos \left[kz + \frac{kx^2}{2R_x(z)} + \frac{ky^2}{2R_y(z)} - \psi_x(z) - \psi_y(z) \right],$$

where w_{0i} represents the $1/e^2$ intensity radius, or beam waist, in dimension $i \in \{x, y\}$. The beam radii w_i , the wavefront radii of curvature R_i and the Gouy phases ψ_i depend on the position along the z axis, as represented in figure B.1. The beam radius expression is given by

$$(B.3) \quad w_i(z) = w_{0i} \sqrt{1 + \left(\frac{z - z_{0i}}{z_{Ri}} \right)^2},$$

where z_{0i} corresponds to the beam waist position and $z_{Ri} = n\pi w_{0i}^2/\lambda$ is called the Rayleigh range, corresponding to the distance from the waist for which the beam has expanded by a factor $\sqrt{2}$.

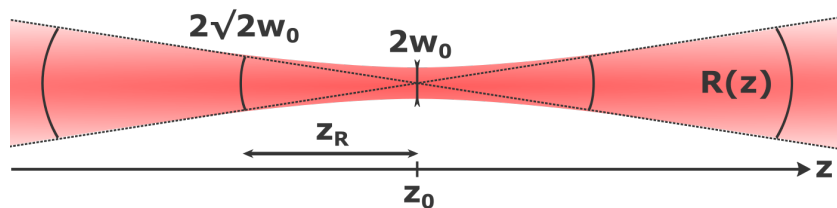


Figure B.1: Gaussian beam propagating along the z axis with a waist w_0 and a radius of curvature R .

The radius of curvature follows

$$(B.4) \quad R_i(z) = (z - z_{0i}) \left[1 + \left(\frac{z_{Ri}}{z - z_{0i}} \right)^2 \right],$$

and the Gouy phase is given by

$$(B.5) \quad \psi_i(z) = \arctan \left(\frac{z - z_{0i}}{z_{Ri}} \right).$$

In cavities, the Gaussian beam properties are determined by the radii of curvature of the mirrors, which shall match the wavefront radii of curvature of the light modes at the mirrors positions.

The Gaussian modes outcoming from laser diodes are generally astigmatic and elongated along one transversal axis. This is the case for the Moglabs ECDLs that we use to address the strontium transitions at 461nm, 689nm, 679nm and 707nm, as well as for the Toptica DLPro laser used for the clock transition at 698nm. In order to derive a formalism describing this astigmatism, one can combine the beam waist and radius of curvature along one of the transversal axes in a single expression known as the complex radius of curvature $q(z)$ given by

$$(B.6) \quad q(z) = (z - z_0) + iz_R.$$

The inverse of this relation writes

$$(B.7) \quad \frac{1}{q(z)} = \frac{1}{R(z)} - i \frac{w_0^2}{z_R w^2(z)}.$$

Equation B.7 thus serves useful in expressing all the Gaussian beam characteristics at a given position, knowing only the three parameters w_0 , z_0 and λ . Also, to infer the beam properties at a position z_2 from a measurement at position z_1 , the two complex radii of curvature are linked by

$$(B.8) \quad q(z_2) = \frac{Aq(z_1) + B}{Cq(z_1) + D},$$

which makes use of the ABCD matrices well known in geometrical optics. For instance, the free space matrix for a beam propagating over a distance d is given by

$$(B.9) \quad \begin{pmatrix} A & B \\ C & D \end{pmatrix} = \begin{pmatrix} 1 & d \\ 0 & 1 \end{pmatrix},$$

and the matrix of a lens of focal length f is expressed as

$$(B.10) \quad \begin{pmatrix} A & B \\ C & D \end{pmatrix} = \begin{pmatrix} 1 & 0 \\ -1/f & 1 \end{pmatrix}.$$

Using this formalism, I developed a Mathematica code used to compute the $1/e^2$ radii of the laser beams at the output of our ECDL lasers and compensate for the measured astigmatism with sets of cylindrical lenses and anamorphic prisms. To do so, a first step consisted in recording the beam profiles at different position using a CCD camera, performing a so-called *z-scan*. In a second step, the measured beam radii along the x and y axes were fitted by the $w(z)$ function in order to measure the beam waists positions and values. Finally, the software could be used to choose the right set of optics along these axes separately in order to focus the two waists at the same position on the optical table. A *z-scan* of the 689nm before any corrections is shown in figure B.2(a). A telescope on the x axis, pictured in figure B.2(b), allowed to correct the laser astigmatism to obtain the beam radii shown in figure B.2(c).

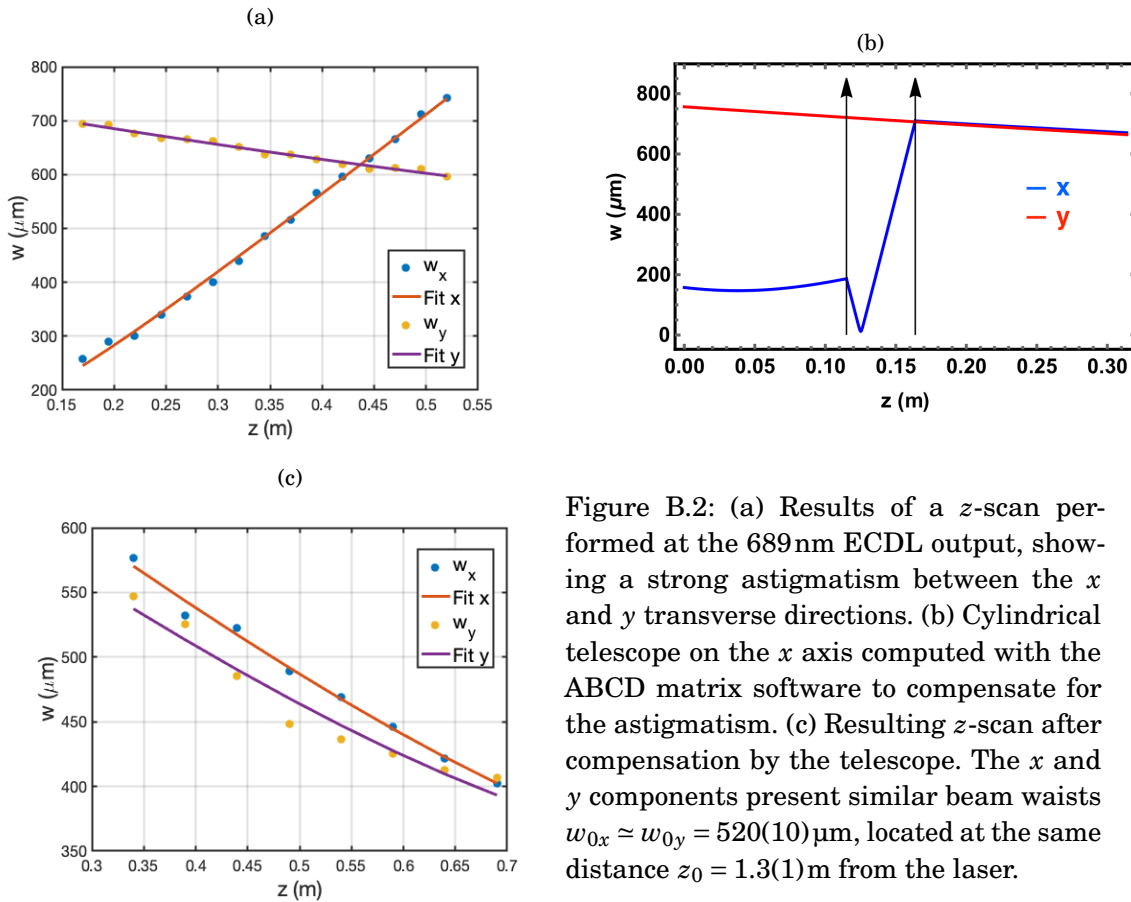


Figure B.2: (a) Results of a *z-scan* performed at the 689nm ECDL output, showing a strong astigmatism between the x and y transverse directions. (b) Cylindrical telescope on the x axis computed with the ABCD matrix software to compensate for the astigmatism. (c) Resulting *z-scan* after compensation by the telescope. The x and y components present similar beam waists $w_{0x} \simeq w_{0y} = 520(10)\mu\text{m}$, located at the same distance $z_0 = 1.3(1)\text{m}$ from the laser.

DDS BASED FREQUENCY GENERATION SETUP FOR AOMs

The frequency generation system used in our experiment to drive the AOMs is derived from the previous work of Francesco Ferri [194] on the SAROCEMA experiment. It relies on an AD9959 evaluation board from Analog Devices¹ combined with an Arduino Due². A python code generates a list of instructions controlling the four DDS output channels amplitudes, phases and frequencies. This list is loaded at the beginning of each experiment sequence through an ethernet link and stored in the Arduino memory. A *Serial Peripheral Interface* (SPI) communication transmits instructions from the arduino to the evaluation board. This exchange can either be instantaneous or triggered by an external time reference. At the current stage of the experiment, this reference is given by an independent computer responsible for the trigger generation via a C++ code. In a nearby future, we aim to implement a fully Python controlled platform following the spirit of the *labscript* suite developed by Starkey *et al.* [195]. This DDS system, shown in figure C.1(a), operates with an external clock frequency of 25 MHz which can internally be multiplied up to 500 MHz. The so-called Shannon criterion gives a theoretical limitation on the output frequencies to half this value. The channel output power at different frequencies presented in figure C.1(b) shows a strong attenuation above 200 MHz. We thus use passive frequency doublers for applications at higher frequencies. The minimum time interval between operations such as frequency steps in a sweep are limited to a rate of one fourth of the clock frequency, leading to 8.0 ns. In practice, another important limitation is the SPI communication delay linked to each instructions. These instruction-dependent delays lie in the 30 μ s range and can be anticipated, but still present a limitation in fast and complex sequences present in the red MOT operation or CQED schemes.

¹See <https://www.analog.com/>.

²See <https://www.arduino.cc/>.

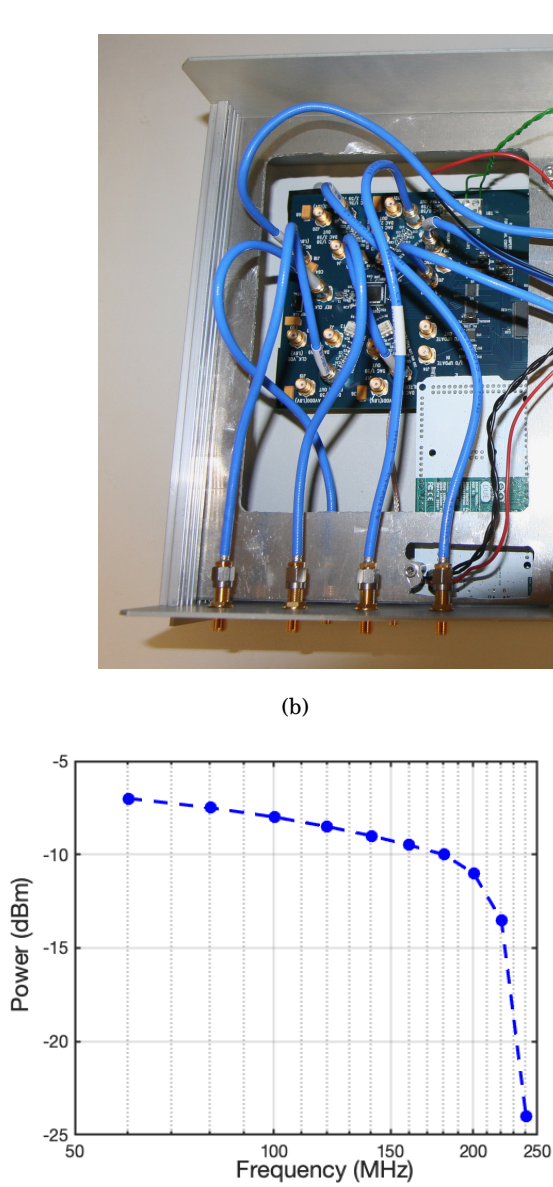


Figure C.1: (a) DDS box system including AD9959 evaluation board from Analog Devices, an Arduino Due with equipped ethernet shield and several power supplies. (b) Maximum output power of the DDS evaluation board per channel as a function of the frequency.

ABSORPTION ON THE $|(5s5p)^3P_2\rangle \rightarrow |(5s6s)^3S_1\rangle$ LINE AT 707 nm

Due to the need of scanning the repumping lasers for the fermionic MOT operation, we stabilize their frequencies with the numerical lock described in 2.1.2. For the 707 nm laser, a direct stabilization on the discharge strontium cell is also possible, as shown by Norcia *et al.* [125]. The absorption and error signals obtained in our experiment with a saturated absorption scheme similar to the 461 nm one are presented in figure D.1(a). Moreover, the theoretical absorption profile computed with the cross-sections derived in section 3.3.2, the isotope shifts in table 1.3 and the hyperfine shifts in table 1.2 for the ^{88}Sr and ^{87}Sr isotopes is shown in figure D.1(b). In the data, three absorption peaks are visible, with the side ones symmetrically located at $\pm 4\text{GHz}$ around the central feature. The theory only predicts the presence of the central peak, leaving the existence of the two extra peaks unknown. The relative amplitudes of the red and blue detuned peaks compared to the main one, equal to 70% and 45% respectively, rules out the possible effects concerning the hyperfine structure of the ^{87}Sr isotope. Moreover, even if the isotope shifts of ^{84}Sr and ^{86}Sr do not have been measured for this transition to my knowledge, and are thus not presented in figure D.1(b), their respective natural abundances of 0.56% and 9.86% can not generate such absorption peaks. Also, a Zeeman shift of the three components of the $|(5s6s)^3S_1\rangle$ state in ^{88}Sr would induce the presence of a magnetic field on the order of 0.1 T, which sounds unrealistic for such cell and is moreover not observed on the blue transition spectrum. These unpredicted peaks could thus come from other molecular species present in the cell, or strontium ions produced by the high electric fields in the hollow cathode.

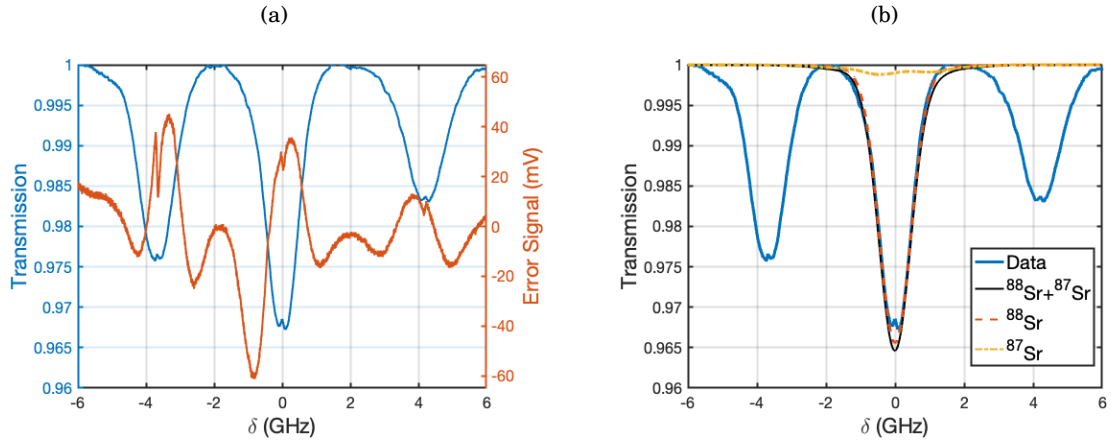


Figure D.1: (a) Saturated absorption signal (blue line) and error signal (orange line) of the 707 nm repumping laser. The frequency axis is referenced to the $|(5s5p)^3P_2\rangle \rightarrow |(5s6s)^3S_1\rangle$ transition of ^{88}Sr . (b) Theoretical absorption profile for ^{88}Sr and ^{87}Sr isotopes compared to the experimental spectrum in blue. The fermionic absorption line is a sum of all the transitions from the $|(5s5p)^3P_2, F_g \in [5/2, 7/2, 9/2, 11/2, 13/2]\rangle$ to the $|(5s6s)^3S_1, F_e \in [7/2, 9/2, 11/2]\rangle$ manifolds.



OPTICAL BLOCH EQUATIONS

In this appendix, we detail the theoretical electric field absorption profile of a two level atom with a ground state $|g\rangle$ and an excited state $|e\rangle$, separated by an energy $\hbar\omega_0$. This atom is placed in a laser field with amplitude \mathcal{E}_0 and frequency ω . We assume for simplicity that its relative phase is zero, without loss of generality. The Hamiltonian for the electric dipolar interaction in the *Rotating Wave Approximation* (RWA) can be written as

$$(E.1) \quad \hat{H} = \frac{\hbar\Delta}{2}\hat{\sigma}_z - \frac{\hbar\Omega}{2}(\hat{\sigma}_+ + \hat{\sigma}_-),$$

where σ_i corresponds to the Pauli matrix i , $\Delta = \omega - \omega_0$ is the atom-laser detuning and $\Omega = d\mathcal{E}_0/\hbar$ is the Rabi frequency for the transition with reduced dipole matrix element d . Equation E.1 is used to compute the time evolution of the density matrix operator $\hat{\rho}$ under spontaneous emission with the Lindblad master equation

$$(E.2) \quad \frac{d\hat{\rho}}{dt} = \frac{1}{i\hbar} [\hat{H}, \hat{\rho}] + \Gamma \left(\hat{\sigma}_- \hat{\rho} \hat{\sigma}_+ - \frac{1}{2} \hat{\sigma}_+ \hat{\sigma}_- \hat{\rho} - \frac{1}{2} \hat{\rho} \hat{\sigma}_+ \hat{\sigma}_- \right)$$

where Γ is the natural linewidth of the transition. The left part of equation E.2 describes the unitary evolution of the states populations, while the right part explicitates quantum jumps from the excited to the ground state. Assuming that the number of atoms is conserved through $\rho_{ee} + \rho_{gg} = 1$, and that the coherence writes $\rho_{eg} = \rho_{ge}^*$, equation E.2 leads to the *Optical Bloch Equations* (OBEs) expressed as

$$(E.3) \quad \begin{cases} \frac{d\rho_{ee}}{dt} = \Omega \Im \{ \rho_{eg} \} - \Gamma \rho_{ee} \\ \frac{d\rho_{eg}}{dt} = -i\Delta \rho_{eg} + i\frac{\Omega}{2} (1 - 2\rho_{ee}) - \gamma' \rho_{eg}. \end{cases}$$

The damping rate $\gamma' = \Gamma/2 + 1/T_2$ gives information on the longitudinal and transverse relaxation times. In the following equations, we will assume that the longitudinal relaxation is dominant,

leading to $\gamma' = \Gamma/2$. In the stationary regime, we can solve the OBEs and obtain the excited state population as well as the coherence between the ground and excited states

$$(E.4) \quad \begin{cases} \rho_{ee} = \frac{1}{2} \frac{s_0}{1+s_0+(\frac{2\Delta}{\Gamma})^2} \\ \rho_{eg} = \frac{\Omega}{2} \left(\frac{4\Delta}{\Gamma^2} + \frac{i}{\Gamma/2} \right) \frac{1}{1+s_0+(\frac{2\Delta}{\Gamma})^2}, \end{cases}$$

where $s_0 = 2(\Omega/\Gamma)^2 = I_0/I_{sat}$ is the saturation parameter. This equation shows that a two-level atom driven in an intense field, such that $s_0 \gg 1$, would only have a probability of one half to be found in the excited state.

The solution of the state populations in the stationary regime gives an information on the coherence between states $|g\rangle$ and $|e\rangle$. In classical physics, one can easily compute the absorption of a medium with complex refractive index n using the Beer-Lambert law. If we consider that the laser field is propagating through this medium along the z axis, the intensity of the field at position z depends on the initial intensity I_0 before the absorptive sample in the following way

$$(E.5) \quad \frac{I(z)}{I_0} = e^{-\int_{-\infty}^z \alpha(\Delta, \zeta) d\zeta},$$

where $\alpha = 2k\Im\{n\}$ is the polarizability of the atom. The complex refractive index can be expressed in terms of the susceptibility χ as $n = \sqrt{1+\chi}$. If the susceptibility of the medium for a given transition is small, we can approximate the refractive index as

$$(E.6) \quad n \underset{\chi \ll 1}{\simeq} 1 + \frac{1}{2}\Re\{\chi\} + i\frac{1}{2}\Im\{\chi\}.$$

We can thus rewrite the polarizability as $\alpha = k\Im\{\chi\}$. Finally, we relate the classical dipole operator to its quantum version via

$$(E.7) \quad D = \epsilon_0(1+\chi)E_0 = 2d\rho_{eg}\mathcal{N},$$

where \mathcal{N} is the number density. Combining equations E.4 and E.7, we obtain the polarizability for a two level ensemble of atoms written as

$$(E.8) \quad \alpha(\Delta, z) = \frac{1}{\hbar\epsilon_0} k d^2 \mathcal{N}(z) f_{\Gamma}(\Delta),$$

with a lineshape factor

$$(E.9) \quad f_{\Gamma}(\Delta) = \frac{2}{\Gamma(1+s_0)} \frac{1}{1 + \left(\frac{2\Delta}{\Gamma\sqrt{1+s_0}} \right)^2}.$$

We can notice that this Lorentzian atomic response is power broadened from the natural decay rate Γ by a factor $\sqrt{1+s_0}$ when the laser intensity is non negligible compared to the saturation intensity of the considered transition. Moreover, the absorption amplitude is decreased by a factor $1+s_0$ compared to the low saturation regime.

Doppler effect : An atom at velocity \vec{v} probed by a laser with a wave vector \vec{k} will present a frequency shifted absorption profile. This behavior, very well known as the Doppler effect, shifts the bare atomic detuning $\Delta_0 = \omega - \omega_0$ between the laser and the atomic frequency via the following expression

$$(E.10) \quad \Delta = \Delta_0 - \vec{k} \cdot \vec{v}.$$

For a laser beam propagating along z through an atomic ensemble with a normalized velocity distribution $p(v_z)$, the response function from equation E.9 has to be convoluted with this distribution in order to compute the polarizability. The new lineshape factor $s(\Delta_0)$ thus writes

$$(E.11) \quad s(\Delta_0) = \int f_{\Gamma}(\Delta_0 - kv_z) p(v_z) dv_z.$$

In the particular case of an atomic vapour, the velocity distribution along one axis is Gaussian with a standard deviation $u = \sqrt{2k_B T/m}$ for an ensemble of atoms of mass m at temperature T . The convolution with the Lorentzian line shape from equation E.9 results in a so-called Voigt profile. An explicit form of the imaginary part of the s function is given by

$$(E.12) \quad \Im\{s(y)\} = \sqrt{\pi} \Re \left\{ W\left(i \frac{a}{2} - y\right) \right\},$$

with $W(z) = i/\pi \int_{-\infty}^{+\infty} e^{-t^2}/(z-t) dt$ the complex error function or Faddeeva function [196], $y = \Delta_0/ku$ and $a = \Gamma\sqrt{1+s_0}/ku$.

BIBLIOGRAPHY

- [1] Dirac, P. A. M. *Principles of Quantum Mechanics(The First Edition)* (Press, The Clarendon, Oxford, 1930).
- [2] Einstein, A., Podolsky, B. & Rosen, N. Can Quantum-Mechanical Description of Physical Reality Be Considered Complete? *Phys. Rev.* **47**, 777–780 (1935). URL <https://link.aps.org/doi/10.1103/PhysRev.47.777>.
- [3] Schrödinger, E. Discussion of Probability Relations between Separated Systems. *Mathematical Proceedings of the Cambridge Philosophical Society* **31**, 555–563 (1935).
- [4] Bell, J. S. On the Einstein Podolsky Rosen paradox. *Physics Physique Fizika* **1**, 195–200 (1964). URL <https://link.aps.org/doi/10.1103/PhysicsPhysiqueFizika.1.195>.
- [5] Aspect, A., Grangier, P. & Roger, G. Experimental Realization of Einstein-Podolsky-Rosen-Bohm Gedankenexperiment: A New Violation of Bell’s Inequalities. *Phys. Rev. Lett.* **49**, 91–94 (1982). URL <https://link.aps.org/doi/10.1103/PhysRevLett.49.91>.
- [6] Gühne, O. & Tóth, G. Entanglement detection. *Physics Reports* **474**, 1–75 (2009). URL <http://dx.doi.org/10.1016/j.physrep.2009.02.004>. 0811.2803.
- [7] Shor, P. W. Polynomial-time algorithms for prime factorization and discrete logarithms on a quantum computer. *SIAM Journal on Computing* **26**, 1484–1509 (1997). 9508027.
- [8] Ladd, T. D. *et al.* Quantum computers. *Nature* **464**, 45–53 (2010). URL <https://doi.org/10.1038/nature08812>.
- [9] Feynman, R. P. Simulating physics with computers. *International Journal of Theoretical Physics* **21**, 467–488 (1982). URL <https://doi.org/10.1007/BF02650179>.
- [10] Gross, C. & Bloch, I. Quantum simulations with ultracold atoms in optical lattices. *Science* **357**, 995–1001 (2017). URL <https://science.sciencemag.org/content/357/6355/995>.
- [11] Wootters, W. K. & Zurek, W. H. A single quantum cannot be cloned. *Nature* **299**, 802–803 (1982). URL <https://doi.org/10.1038/299802a0>.

- [12] Bennett, C. H. & Brassard, G. Quantum cryptography: Public key distribution and coin tossing. In *Proceedings of IEEE International Conference on Computers, Systems, and Signal Processing*, 175 (India, 1984).
- [13] Ekert, A. K. Quantum cryptography based on Bell's theorem. *Phys. Rev. Lett.* **67**, 661–663 (1991). URL <https://link.aps.org/doi/10.1103/PhysRevLett.67.661>.
- [14] Brennen, G., Giacobino, E. & Simon, C. Focus on Quantum Memory. *New Journal of Physics* **17**, 14–17 (2015).
- [15] Ren, J. G. *et al.* Ground-to-satellite quantum teleportation. *Nature* **549**, 70–73 (2017). [1707.00934](https://doi.org/10.1038/549070a).
- [16] Wineland, D. J., Bollinger, J. J., Itano, W. M., Moore, F. L. & Heinzen, D. J. Spin squeezing and reduced quantum noise in spectroscopy. *Phys. Rev. A* **46**, R6797—R6800 (1992). URL <https://link.aps.org/doi/10.1103/PhysRevA.46.R6797>.
- [17] Heavner, T. P. *et al.* First accuracy evaluation of NIST-F2. *Metrologia* **51**, 174–182 (2014). URL <https://doi.org/10.1088/0026-1394/51/3/174>.
- [18] Kitching, J., Knappe, S. & Donley, E. A. Atomic sensors - A review. *IEEE Sensors Journal* **11**, 1749–1758 (2011).
- [19] Hänsch, T. W. & Schawlow, A. L. Cooling of gases by laser radiation. *Optics Communications* **13**, 68–69 (1975).
- [20] Wineland, D. J. & Dehmelt, H. Proposed $10^{14} \delta\nu/\nu$ laser fluorescence spectroscopy on Tl^+ mono-ion oscillator III (side band cooling). *Bull. Am. Phys. Soc* **20**, 637 (1975).
- [21] Dalibard, J. & Cohen-Tannoudji, C. Atomic motion in laser light: Connection between semiclassical and quantum descriptions. *Journal of Physics B: Atomic and Molecular Physics* **18**, 1661–1683 (1985).
- [22] Dalibard, J. & Cohen-Tannoudji, C. Dressed-atom approach to atomic motion in laser light: the dipole force revisited. *Journal of the Optical Society of America B* **2**, 1707 (1985).
- [23] Dalibard, J. & Cohen-Tannoudji, C. Laser cooling below the Doppler limit by polarization gradients: simple theoretical models. *Journal of the Optical Society of America B* **6**, 2023 (1989). URL <https://www.osapublishing.org/abstract.cfm?URI=josab-6-11-2023>.
- [24] Raab, E. L., Prentiss, M., Cable, A., Chu, S. & Pritchard, D. E. Trapping of Neutral Sodium Atoms with Radiation Pressure. *Phys. Rev. Lett.* **59**, 2631–2634 (1987). [arXiv: 1011.1669v3](https://arxiv.org/abs/1011.1669v3).

-
- [25] Anderson, M. H., Ensher, J. R., Matthews, M. R., Wieman, C. E. & Cornell, E. A. Observation of Bose-Einstein Condensation in a Dilute Atomic Vapor. *Science* **269**, 198–201 (1995). URL <https://science.sciencemag.org/content/269/5221/198>.
- [26] Davis, K. B. *et al.* Bose-Einstein Condensation in a Gas of Sodium Atoms. *Phys. Rev. Lett.* **75**, 3969–3973 (1995). URL <https://link.aps.org/doi/10.1103/PhysRevLett.75.3969>.
- [27] Petrich, W., Anderson, M. H., Ensher, J. R. & Cornell, E. A. Stable, Tightly Confining Magnetic Trap for Evaporative Cooling of Neutral Atoms. *Phys. Rev. Lett.* **74**, 3352–3355 (1995). URL <https://link.aps.org/doi/10.1103/PhysRevLett.74.3352>.
- [28] Chu, S., Bjorkholm, J. E., Ashkin, A. & Cable, A. Experimental Observation of Optically Trapped Atoms. *Phys. Rev. Lett.* **57**, 314–317 (1986). URL <https://link.aps.org/doi/10.1103/PhysRevLett.57.314>.
- [29] Estève, J., Gross, C., Weller, A., Giovanazzi, S. & Oberthaler, M. K. Squeezing and entanglement in a Bose-Einstein condensate. *Nature* **455**, 1216–1219 (2008). URL <https://doi.org/10.1038/nature07332>.
- [30] Riedel, M. F. *et al.* Atom-chip-based generation of entanglement for quantum metrology. *Nature* **464**, 1170–1173 (2010). URL <https://doi.org/10.1038/nature08988>.
- [31] Laudat, T. *et al.* Spontaneous spin squeezing in a rubidium BEC. *New Journal of Physics* **20**, 73018 (2018). URL <https://doi.org/10.1088/1367-2630/aac1fe>.
- [32] Monz, T. *et al.* Realization of the Quantum Toffoli Gate with Trapped Ions. *Phys. Rev. Lett.* **102**, 40501 (2009). URL <https://link.aps.org/doi/10.1103/PhysRevLett.102.040501>.
- [33] Sewell, R. J. *et al.* Magnetic Sensitivity Beyond the Projection Noise Limit by Spin Squeezing. *Phys. Rev. Lett.* **109**, 253605 (2012). URL <https://link.aps.org/doi/10.1103/PhysRevLett.109.253605>.
- [34] Kimble, H. J. Strong interactions of single atoms and photons in cavity QED. *Physica Scripta T* **76**, 127–137 (1998).
- [35] Schleier-Smith, M. H., Leroux, I. D. & Vuletić, V. States of an Ensemble of Two-Level Atoms with Reduced Quantum Uncertainty. *Phys. Rev. Lett.* **104**, 73604 (2010). URL <https://link.aps.org/doi/10.1103/PhysRevLett.104.073604>.
- [36] Davis, E. J., Bentsen, G., Homeier, L., Li, T. & Schleier-Smith, M. H. Photon-Mediated Spin-Exchange Dynamics of Spin-1 Atoms. *Phys. Rev. Lett.* **122**, 10405 (2019). URL <https://link.aps.org/doi/10.1103/PhysRevLett.122.010405>.

- [37] Chen, Z., Bohnet, J. G., Weiner, J. M., Cox, K. C. & Thompson, J. K. Cavity-aided nondemolition measurements for atom counting and spin squeezing. *Physical Review A - Atomic, Molecular, and Optical Physics* **89** (2014). [1211.0723](#).
- [38] Welte, S., Hacker, B., Daiss, S., Ritter, S. & Rempe, G. Cavity Carving of Atomic Bell States. *Phys. Rev. Lett.* **118**, 210503 (2017). URL <https://link.aps.org/doi/10.1103/PhysRevLett.118.210503>.
- [39] Léonard, J., Morales, A., Zupancic, P., Esslinger, T. & Donner, T. Supersolid formation in a quantum gas breaking a continuous translational symmetry. *Nature* **543**, 87–90 (2017). URL <https://doi.org/10.1038/nature21067>.
- [40] Kohler, J., Gerber, J. A., Dowd, E. & Stamper-Kurn, D. M. Negative-Mass Instability of the Spin and Motion of an Atomic Gas Driven by Optical Cavity Backaction. *Phys. Rev. Lett.* **120**, 13601 (2018). URL <https://link.aps.org/doi/10.1103/PhysRevLett.120.013601>.
- [41] Hunger, D. *et al.* A fiber Fabry-Perot cavity with high finesse. *New Journal of Physics* **12**, 65038 (2010). URL <http://stacks.iop.org/1367-2630/12/i=6/a=065038>.
- [42] Haas, F., Volz, J., Gehr, R., Reichel, J. & Estève, J. Entangled States of More Than 40 Atoms in an Optical Fiber Cavity. *Science* **344**, 180–183 (2014). URL <https://science.sciencemag.org/content/344/6180/180>.
- [43] Barontini, G., Hohmann, L., Haas, F., Estève, J. & Reichel, J. Deterministic generation of multiparticle entanglement by quantum Zeno dynamics. *Science* **349**, 1317–1321 (2015). [1601.07347](#).
- [44] Kitagawa, M. & Ueda, M. Squeezed spin states. *Phys. Rev. A* **47**, 5138–5143 (1993). URL <https://link.aps.org/doi/10.1103/PhysRevA.47.5138>.
- [45] Leroux, I. D., Schleier-Smith, M. H. & Vuletić, V. Implementation of Cavity Squeezing of a Collective Atomic Spin. *Phys. Rev. Lett.* **104**, 73602 (2010). URL <https://link.aps.org/doi/10.1103/PhysRevLett.104.073602>.
- [46] Bohnet, J. G. *et al.* Reduced spin measurement back-action for a phase sensitivity ten times beyond the standard quantum limit. *Nature Photonics* **8**, 731–736 (2014). URL <https://doi.org/10.1038/nphoton.2014.151>.
- [47] Bloom, B. J. *et al.* An optical lattice clock with accuracy and stability at the 10^{-18} level. *Nature* **506**, 71–75 (2014). [1309.1137](#).
- [48] McGrew, W. F. *et al.* Atomic clock performance enabling geodesy below the centimetre level. *Nature* **564**, 87–90 (2018). URL <https://doi.org/10.1038/s41586-018-0738-2>.

-
- [49] Katori, H., Ido, T., Isoya, Y. & Kuwata-Gonokami, M. Magneto-optical trapping and cooling of strontium atoms down to the photon recoil temperature. *Physical Review Letters* **82**, 1116–1119 (1999).
 - [50] Sorrentino, F., Ferrari, G., Poli, N., Drullinger, R. & Tino, G. M. Laser cooling and trapping of atomic strontium for ultracold atom physics, high-precision spectroscopy and quantum sensors. *Modern Physics Letters B* **20**, 1287–1320 (2006). URL <http://dx.doi.org/10.1142/S0217984906011682>. 0609133.
 - [51] Katori, H., Hashiguchi, K., Il'inova, E. Y. & Ovsiannikov, V. D. Magic Wavelength to Make Optical Lattice Clocks Insensitive to Atomic Motion. *Phys. Rev. Lett.* **103**, 153004 (2009). URL <https://link.aps.org/doi/10.1103/PhysRevLett.103.153004>.
 - [52] Norcia, M. A., Young, A. W. & Kaufman, A. M. Microscopic Control and Detection of Ultracold Strontium in Optical-Tweezer Arrays. *Physical Review X* **8**, 41054 (2018). URL <https://doi.org/10.1103/PhysRevX.8.041054>. 1810.06626.
 - [53] Cooper, A. *et al.* Alkaline earth atoms in optical tweezers. *Physical Review X* 1–16 (2018). URL <http://arxiv.org/abs/1810.06537>. 1810.06537.
 - [54] Norcia, M. A. *et al.* Seconds-scale coherence on an optical clock transition in a tweezer array. *Science* **366**, 93–97 (2019).
 - [55] Madjarov, I. S. *et al.* An atomic array optical clock with single-atom readout. *Physical Review X* 1–14 (2019). URL <http://arxiv.org/abs/1908.05619>. 1908.05619.
 - [56] Young, A. W. *et al.* Half-minute-scale atomic coherence and high relative stability in a tweezer clock. *Nature* **588**, 408–413 (2020). URL <https://doi.org/10.1038/s41586-020-3009-y>.
 - [57] Norcia, M. A. *et al.* Cavity-mediated collective spin-exchange interactions in a strontium superradiant laser. *Science* **361**, 259–262 (2018). 1711.03673.
 - [58] Braverman, B. *et al.* Near-Unitary Spin Squeezing in ^{171}Yb . *Phys. Rev. Lett.* **122**, 223203 (2019). URL <https://link.aps.org/doi/10.1103/PhysRevLett.122.223203>.
 - [59] Bataille, P. *et al.* Adiabatic spin-dependent momentum transfer in an $\text{SU}(N)$ degenerate Fermi gas. *Phys. Rev. A* **102**, 13317 (2020). URL <https://link.aps.org/doi/10.1103/PhysRevA.102.013317>.
 - [60] Wilson, J. T. *et al.* Trapped arrays of alkaline earth Rydberg atoms in optical tweezers. *arXiv* (2019). 1912.08754.
 - [61] Pöpplau, T. H. J. *Towards strong coupling of strontium to a miniature ring cavity*. Ph.D. thesis, Sorbonne University (2019).

- [62] Sébastien Garcia. *Interfaces fibrées entre atomes uniques et photons uniques*. Ph.D. thesis, École Normale Supérieure (2015). URL <https://hal.archives-ouvertes.fr/tel-01382230/document>.
- [63] Dicke, R. H. Coherence in spontaneous radiation processes (1954). 1407.7336.
- [64] Arecchi, F. T., Courtens, E., Gilmore, R. & Thomas, H. Atomic Coherent States in Quantum Optics. *Phys. Rev. A* **6**, 2211–2237 (1972). URL <https://link.aps.org/doi/10.1103/PhysRevA.6.2211>.
- [65] Stoop, H., Masiak, P. & Rzazewski, K. Atomic wave packet in a ring cavity. *Phys. Rev. A* **55**, 2254–2266 (1997). URL <https://link.aps.org/doi/10.1103/PhysRevA.55.2254>.
- [66] Schleier-smith, M. H. Cavity-Enabled Spin Squeezing for a Quantum-Enhanced Atomic Clock by. *Thesis* (2011).
- [67] Lee, J., Vrijsen, G., Teper, I., Hosten, O. & Kasevich, M. A. Many-atom-cavity QED system with homogeneous atom-cavity coupling. *Optics Letters* **39**, 4005 (2014). 1311.1805.
- [68] Kruse, D. *et al.* Cold atoms in a high-Q ring cavity. *Physical Review A - Atomic, Molecular, and Optical Physics* **67**, 518021–518024 (2003).
- [69] Purcell, E. M. Spontaneous emission probabilities at radio frequencies (1946).
- [70] Bonifacio, R. & Lugiato, L. A. Optical bistability and cooperative effects in resonance fluorescence. *Phys. Rev. A* **18**, 1129–1144 (1978). URL <https://link.aps.org/doi/10.1103/PhysRevA.18.1129>.
- [71] Bonifacio, R., De Salvo, L., Narducci, L. M. & D’Angelo, E. J. Exponential gain and self-bunching in a collective atomic recoil laser. *Phys. Rev. A* **50**, 1716–1724 (1994). URL <https://link.aps.org/doi/10.1103/PhysRevA.50.1716>.
- [72] Kruse, D., von Cube, C., Zimmermann, C. & Courteille, P. W. Observation of lasing mediated by collective atomic recoil. *Physical Review Letters* **91**, 1–4 (2003). 0305033.
- [73] Ling, H. Y., Pu, H., Baksmaty, L. & Bigelow, N. P. Theory of a collective atomic recoil laser. *Phys. Rev. A* **63**, 53810 (2001). URL <https://link.aps.org/doi/10.1103/PhysRevA.63.053810>.
- [74] Mivehvar, F., Ostermann, S., Piazza, F. & Ritsch, H. Driven-Dissipative Supersolid in a Ring Cavity. *Physical Review Letters* **120**, 1–7 (2018). 1801.00756.
- [75] Schuster, S. C., Wolf, P., Ostermann, S., Slama, S. & Zimmermann, C. Supersolid Properties of a Bose-Einstein Condensate in a Ring Resonator. *Phys. Rev. Lett.* **124**, 143602 (2020). URL <https://link.aps.org/doi/10.1103/PhysRevLett.124.143602>.

-
- [76] Tavis, M. & Cummings, F. W. Exact Solution for an N-Molecule-Radiation-Field Hamiltonian. *Physical Review* **170**, 379–384 (1968).
- [77] Jaynes, E. T. & Cummings, F. W. Comparison of quantum and semiclassical radiation theories with application to the beam maser. *Proceedings of the IEEE* **51**, 89–109 (1963).
- [78] Chen, Z., Bohnet, J. G., Sankar, S. R., Dai, J. & Thompson, J. K. Conditional spin squeezing of a large ensemble via the vacuum rabi splitting. *Physical Review Letters* **106**, 1–4 (2011). [1103.0335](#).
- [79] Lewis-Swan, R. J., Norcia, M. A., Cline, J. R., Thompson, J. K. & Rey, A. M. Robust Spin Squeezing via Photon-Mediated Interactions on an Optical Clock Transition. *Physical Review Letters* **121** (2018). [1804.06784](#).
- [80] Hosten, O., Engelsen, N. J., Krishnakumar, R. & Kasevich, M. A. Measurement noise 100 times lower than the quantum-projection limit using entangled atoms. *Nature* **529**, 505–508 (2016). URL <http://dx.doi.org/10.1038/nature16176>.
- [81] Schleier-Smith, M. H., Leroux, I. D. & Vuletić, V. Squeezing the collective spin of a dilute atomic ensemble by cavity feedback. *Physical Review A - Atomic, Molecular, and Optical Physics* **81** (2010).
- [82] Sørensen, A. S. & Mølmer, K. Entanglement and extreme spin squeezing. *Physical review letters* **86**, 4431–4434 (2001).
- [83] Ma, J., Wang, X., Sun, C. P. & Nori, F. Quantum spin squeezing. *arXiv* (2011). [arXiv:1011.2978v2](#).
- [84] Sun, L. H., Li, G. X., Gu, W. J. & Ficek, Z. Generating coherence and entanglement with a finite-size atomic ensemble in a ring cavity. *New Journal of Physics* **13** (2011). [1105.4948](#).
- [85] Li, G. X. & Ficek, Z. Creation of entangled states in a ring cavity. *AIP Conference Proceedings* **1363**, 283–286 (2011). [0907.4546](#).
- [86] Chen, W. *et al.* Carving Complex Many-Atom Entangled States by Single-Photon Detection. *Physical Review Letters* **115**, 1–5 (2015).
- [87] Greenberger, D. M., Horne, M. A., Shimony, A. & Zeilinger, A. Bell’s theorem without inequalities. *American Journal of Physics* **58**, 1131–1143 (1990). URL <https://doi.org/10.1119/1.16243>.
- [88] Wang, Y. K. & Hioe, F. T. Phase Transition in the Dicke Model of Superradiance. *Phys. Rev. A* **7**, 831–836 (1973). URL <https://link.aps.org/doi/10.1103/PhysRevA.7.831>.

- [89] Baumann, K., Guerlin, C., Brennecke, F. & Esslinger, T. Dicke quantum phase transition with a superfluid gas in an optical cavity. *Nature* **464**, 1301–1306 (2010). URL <https://doi.org/10.1038/nature09009>.
- [90] Norcia, M. A., Winchester, M. N., Cline, J. R. & Thompson, J. K. Superradiance on the millihertz linewidth strontium clock transition. *Science Advances* **2** (2016). [1603.05671](https://doi.org/10.1126/sciadv.1603056).
- [91] Noh, C. Emission of single photons in the weak coupling regime of the Jaynes Cummings model. *Scientific Reports* **10**, 1–8 (2020). URL <https://doi.org/10.1038/s41598-020-72945-0>.
- [92] Fujii, K., Higashida, K., Kato, R. & Wada, Y. Cavity QED and quantum computation in the weak coupling regime. *Journal of Optics B: Quantum and Semiclassical Optics* **6**, 502–509 (2004). URL <https://doi.org/10.1088/1464-4266/6/12/004>.
- [93] Ott, K. *Towards a squeezing-enhanced atomic clock on a chip*. Ph.D. thesis, Sorbonne University (2016). URL <https://tel.archives-ouvertes.fr/tel-01452767>.
- [94] Oelker, E. *et al.* Optical clock intercomparison with 6×10^{-19} precision in one hour. *arXiv* (2019). URL <http://arxiv.org/abs/1902.02741>. [1902.02741](https://arxiv.org/abs/1902.02741).
- [95] Hinkley, N. *et al.* An Atomic Clock with 10^{-18} Instability. *Science* **341**, 1215–1218 (2013). URL <http://science.sciencemag.org/content/341/6151/1215>.
- [96] Weyers, S., Lipphardt, B. & Schnatz, H. Reaching the quantum limit in a fountain clock using a microwave oscillator phase locked to an ultrastable laser. *Phys. Rev. A* **79**, 31803 (2009). URL <https://link.aps.org/doi/10.1103/PhysRevA.79.031803>.
- [97] Abgrall, M. *et al.* Atomic fountains and optical clocks at SYRTE: Status and perspectives (2015). [1507.04623](https://arxiv.org/abs/1507.04623).
- [98] Ye, S. *et al.* Production of very-high- n strontium Rydberg atoms. *Phys. Rev. A* **88**, 43430 (2013). URL <https://link.aps.org/doi/10.1103/PhysRevA.88.043430>.
- [99] Santra, R., Christ, K. V. & Greene, C. H. Properties of metastable alkaline-earth-metal atoms calculated using an accurate effective core potential. *Physical Review A - Atomic, Molecular, and Optical Physics* **69**, 1–13 (2004). [0312033](https://arxiv.org/abs/0312033).
- [100] Stellmer, S. Degenerate Quantum Gases of Strontium. *Annual Review of Cold Atoms and Molecules* 1–80 (2014). URL http://www.worldscientific.com/doi/abs/10.1142/9789814590174_0001.
- [101] Stellmer, S., Grimm, R. & Schreck, F. Production of quantum-degenerate strontium gases. *Physical Review A - Atomic, Molecular, and Optical Physics* (2013). [1212.2539](https://arxiv.org/abs/1212.2539).

-
- [102] Courtillot, I. *et al.* Accurate spectroscopy of Sr atoms. *European Physical Journal D* **33**, 161–171 (2005). [0410108](#).
- [103] Taichenachev, A. V. *et al.* Magnetic field-induced spectroscopy of forbidden optical transitions with application to lattice-based optical atomic clocks. *Physical Review Letters* **96**, 3–6 (2006).
- [104] Yasuda, M. & Katori, H. Lifetime Measurement of the 3P_2 Metastable State of Strontium Atoms. *Phys. Rev. Lett.* **92**, 153004 (2004). URL <https://link.aps.org/doi/10.1103/PhysRevLett.92.153004>.
- [105] Moriya, P. H. *et al.* Comparison between 403nm and 497nm repumping schemes for strontium magneto-optical traps. *Journal of Physics Communications* **2**, 1–11 (2018). [1806.09176](#).
- [106] Stellmer, S. & Schreck, F. Reservoir spectroscopy of 5s5p $3P_2$ - 5snd $3D_{1,2,3}$ transitions in strontium. *Physical Review A - Atomic, Molecular, and Optical Physics* **90**, 1–15 (2014). [1406.0409](#).
- [107] Bothwell, T. *et al.* JILA SrI optical lattice clock with uncertainty of 2.0×10^{-18} . *Metrologia* **56**, 65004 (2019). URL <https://doi.org/10.1088%2F1681-7575%2F564004>.
- [108] Madjarov, I. S. *et al.* High-fidelity entanglement and detection of alkaline-earth Rydberg atoms. *Nature Physics* **16**, 857–861 (2020). URL <https://doi.org/10.1038/s41567-020-0903-z>.
- [109] Snigirev, S., Park, A. J., Heinz, A., Bloch, I. & Blatt, S. Fast and dense magneto-optical traps for strontium. *Phys. Rev. A* **99**, 63421 (2019). URL <https://link.aps.org/doi/10.1103/PhysRevA.99.063421>.
- [110] Kluge, H. J. & Sauter, H. Levelcrossing experiments in the first excited 1P_1 states of the alkaline earths. *Zeitschrift für Physik A Hadrons and Nuclei* **270**, 295–309 (1974). URL <http://dx.doi.org/10.1007/BF01677766>.
- [111] Miyake, H., Pisenti, N. C., Elgee, P. K., Sitaram, A. & Campbell, G. K. Isotope-shift spectroscopy of the $^1S_0 \rightarrow ^3P_1$ and $^1S_0 \rightarrow ^3P_0$ transitions in strontium. *Phys. Rev. Research* **1**, 33113 (2019). URL <https://link.aps.org/doi/10.1103/PhysRevResearch.1.033113>.
- [112] Heider, S. M. & Brink, G. O. Hyperfine structure of ^{87}Sr in the 3P_2 metastable state. *Phys. Rev. A* **16**, 1371–1374 (1977). URL <https://link.aps.org/doi/10.1103/PhysRevA.16.1371>.
- [113] Yang, T. *et al.* A high flux source of cold strontium atoms. *European Physical Journal D* **69** (2015). [1505.04507](#).

- [114] Mitroy, J., Safronova, M. S. & Clark, C. W. Theory and applications of atomic and ionic polarizabilities. *Journal of Physics B: Atomic, Molecular and Optical Physics* **43** (2010). [1004.3567](#).
- [115] Katori, H., Ido, T. & Kuwata-Gonokami, M. Optimal Design of Dipole Potentials for Efficient Loading of Sr Atoms. *Journal of the Physical Society of Japan* **68**, 2479–2482 (1999). URL <https://doi.org/10.1143/JPSJ.68.2479>.
- [116] Safronova, M. S., Porsev, S. G., Safronova, U. I., Kozlov, M. G. & Clark, C. W. Blackbody-radiation shift in the Sr optical atomic clock. *Physical Review A - Atomic, Molecular, and Optical Physics* **87**, 1–9 (2013). [1210.7272](#).
- [117] Young, A. W. *et al.* A tweezer clock with half-minute atomic coherence at optical frequencies and high relative stability. *arXiv* (2020). [2004.06095](#).
- [118] Pedrozo-Peñafiel, E. *et al.* Entanglement on an optical atomic-clock transition. *Nature* **588**, 414–418 (2020). URL <https://doi.org/10.1038/s41586-020-3006-1>.
- [119] Nosske, I. *Cooling and trapping of strontium atoms for quantum simulation using Rydberg states*. Ph.D. thesis, University of Science and Technology of China (2018).
- [120] Mazzoni, T. *Atom interferometry with fermionic and bosonic isotopes of strontium for precision gravity measurements and test of the equivalence principle*. Ph.D. thesis, Università Degli Studi Di Firenze (2012).
- [121] Bilicki, S. *Strontium optical lattice clocks : clock comparisons for timescales and fundamental physics applications* Slawomir Bilicki To cite this version : HAL Id : tel-01691598. Ph.D. thesis, Sorbonne Université (2018).
- [122] Heinz, A. *Ultracold Strontium in State-Dependent Optical Lattices*. Ph.D. thesis, Fakultät für Physik Ludwig-Maximilians-Universität München (2020).
- [123] Poyntz-Wright, L. J. & Russell, P. S. J. Spontaneous relaxation processes in irradiated germanosilicate optical fibres. *Electronics Letters* **25**, 478–480 (1989).
- [124] Elliott, D. S., Roy, R. & Smith, S. J. Extracavity laser band-shape. *Physical Review A* **26**, 12–18 (1982).
- [125] Norcia, M. A. & Thompson, J. K. Simple laser stabilization to the strontium⁸⁸Sr transition at 707 nm. *Review of Scientific Instruments* **87** (2016). [1510.04329](#).
- [126] Martin, M. J. & Ye, J. High-precision laser stabilization via optical cavities. *Optical Coatings and Thermal Noise in Precision Measurement* **9781107003**, 237–258 (2012).

- [127] An, K., Yang, C., Dasari, R. R. & Feld, M. S. Cavity ring-down technique and its application to the measurement of ultraslow velocities. *Optics Letters* **20**, 1068 (1995).
- [128] Drever, R. W. P. *et al.* Laser phase and frequency stabilization using an optical resonator. *Applied Physics B* **31**, 97–105 (1983). URL <http://link.springer.com/article/10.1007/BF00702605>.
- [129] Maldonado, T. Electro-optic Devices. *The Optics Encyclopedia* 511–547 (2007).
- [130] Black, E. D. An introduction to Pound-Drever-Hall laser frequency stabilization. *American Journal of Physics* **69**, 79–87 (2001).
- [131] Di Domenico, G., Schilt, S. & Thomann, P. Simple approach to the relation between laser frequency noise and laser line shape. *Applied Optics* **49**, 4801–4807 (2010).
- [132] Stéphan, G. M., Tam, T. T., Blin, S., Besnard, P. & Têtu, M. Laser line shape and spectral density of frequency noise. *Physical Review A - Atomic, Molecular, and Optical Physics* **71**, 1–9 (2005).
- [133] Sterr, U. *et al.* Ultrastable lasers: new developments and applications. *Time and Frequency Metrology II* **7431**, 74310A (2009).
- [134] Huckans, J. *et al.* Note on the reflectance of mirrors exposed to a strontium beam. *arXiv* 2–6 (2018). URL <http://arxiv.org/abs/1802.08499>. 1802.08499.
- [135] Holtgrave, J. C. & Wolf, P. J. Pressure broadening and line shifting of atomic strontium $52S_{01} \text{ } 5s5p \text{ } ^1P_1$ and $5s5p \text{ } ^3P_{0,1,2,3} \text{ } 5s6s \text{ } ^1S_0$ absorption transitions induced by noble-gas collisions. *Physical Review A - Atomic, Molecular, and Optical Physics* **72**, 2–8 (2005).
- [136] Turnbull, J. C. Barium, strontium, and calcium as getters in electron tubes. *Journal of Vacuum Science and Technology* **14**, 636–639 (1977). URL <http://avs.scitation.org/doi/10.1116/1.569166>.
- [137] Schioppo, M. *et al.* A compact and efficient strontium oven for laser-cooling experiments. *Review of Scientific Instruments* **83**, 1–6 (2012). 1209.5639.
- [138] Bidel, Y. *Piégeage et refroidissement laser du strontium Etude de l'effet des interférences en diffusion multiple*. Ph.D. thesis, Université de Nice - Sophia Antipolis (2003).
- [139] Boyd, M. M. High Precision Spectroscopy of Strontium in an Optical Lattice: Towards a New Standard for Frequency and Time. *PhD thesis, U. of Colorado* 245 (2007).
- [140] Tarallo, M. *Development of a Strontium optical lattice clock*. Ph.D. thesis, Università degli Studi di Pisa (2009).

- [141] Blatt, S. *Ultracold Collisions and Fundamental Physics with Strontium*. Ph.D. thesis, University of Colorado (2005). URL https://jila.colorado.edu/yelabs/sites/default/files/uploads/theses_2011_SebastianBlatt.pdf.
- [142] Barker, D. S. *Degenerate Gases of Strontium for Studies of Quantum Magnetism*. Ph.D. thesis, University of Maryland (2016).
- [143] Hobson, R. An Optical Lattice Clock with Neutral Strontium. *Thesis* (2016).
- [144] Martin, P. J. *Development of a Strontium Magneto-Optical Trap for Probing Casimir-Polder Potentials*. Ph.D. thesis, University of Oregon (2017).
- [145] Finger, F. *A Transport Laser with Shape and Amplitude Control for Ultracold Strontium Atoms Ein Transportlaser mit Form-und Amplitudenkontrolle für ultrakalte Strontiumatome*. Ph.D. thesis, Fakultät für Physik der Technischen Universität München (2018).
- [146] Kock, B. O. Magneto-Optical Trapping of Strontium for use as a Mobile Frequency Reference. *Thèse* (2013).
- [147] Knudsen, M. & Partington, J. R. The Kinetic Theory of Gases. Some Modern Aspects. *The Journal of Physical Chemistry* **39**, 307 (1935). URL <https://doi.org/10.1021/j150362a021>.
- [148] Williams, M. L. CRC Handbook of Chemistry and Physics, 76th edition. *Occupational and Environmental Medicine* **53**, 504–504 (1996).
- [149] Beijerinck, H. C. & Verster, N. F. Velocity distribution and angular distribution of molecular beams from multichannel arrays. *Journal of Applied Physics* **46**, 2083–2091 (1975).
- [150] Livesey, R. G. Flow of Gases Through Tubes and Orifices. *Foundations of Vacuum Science and Technology* **25** (1998).
- [151] Narendra Babu, K. Thermal Contact Resistance: Experiments and Simulation Master’s thesis in Automotive Engineering. *Renewable and Sustainable Energy Reviews* **80**, 55 (2015). URL <http://publications.lib.chalmers.se/records/fulltext/223157/223157.pdf>.
- [152] Santeler, D. J. Gas-flow experiments in the transition region. *Journal of Vacuum Science and Technology A: Vacuum, Surfaces, and Films* **12**, 1744–1749 (1994). URL <http://avs.scitation.org/doi/10.1116/1.579048>.
- [153] Koichi, S. Characteristics of an Ammonia Beam Maser. *Journal of the Physical Society of Japan* **16**, 1728–1739 (1961). URL <https://doi.org/10.1143/JPSJ.16.1728>.

- [154] Rabi, I. I., Millman, S., Kusch, P. & Zacharias, J. R. The Molecular Beam Resonance Method for Measuring Nuclear Magnetic Moments. The Magnetic Moments of ${}^3\text{Li}^6$, ${}^3\text{Li}^7$ and ${}^9\text{F}^{19}$. *Phys. Rev.* **55**, 526–535 (1939). URL <https://link.aps.org/doi/10.1103/PhysRev.55.526>.
- [155] Giordmaine, J. A. & Wang, T. C. Molecular beam formation by long parallel tubes. *Journal of Applied Physics* **31**, 463–471 (1960).
- [156] Rowlinson, J. The Maxwell-Boltzmann distribution. *Molecular Physics* **103**, 2821–2828 (2005). URL <https://doi.org/10.1080/002068970500044749>.
- [157] Guéry-Odelin, D. & Lahaye, T. *Classical Mechanics Illustrated by Modern Physics: 42 Problems with Solutions* (Imperial College Press, 2010). URL <https://books.google.fr/books?id=wbNpG9Hh9qUC>.
- [158] Siddons, P., Adams, C. S., Ge, C. & Hughes, I. G. Absolute absorption on rubidium D lines: Comparison between theory and experiment. *Journal of Physics B: Atomic, Molecular and Optical Physics* **41** (2008). [0805.1139](#).
- [159] Einstein, A. Zur Quantentheorie der Strahlung. *Phys. Z.* **18**, 121–128 (1917).
- [160] Paul, W. Electromagnetic Traps for Charged. *Nobel Lecture* (1989).
- [161] Prodan, J. *et al.* Stopping atoms with laser light (1985).
- [162] McClelland, J. J. *et al.* Bright focused ion beam sources based on laser-cooled atoms. *Applied Physics Reviews* **3**, 1–63 (2016).
- [163] Dalibard, J. Une brève histoire des atomes froids (2014).
- [164] Norcia, M. A., Cline, J. R., Bartolotta, J. P., Holland, M. J. & Thompson, J. K. Narrow-line laser cooling by adiabatic transfer. *New Journal of Physics* **20** (2018). [1707.01944](#).
- [165] Bober, M., Zachorowski, J. & Gawlik, W. Designing Zeeman slower for strontium atoms - Towards optical atomic clock. *Optica Applicata* **40**, 547–555 (2010). [1006.1554](#).
- [166] Hill, I. R., Ovchinnikov, Y. B., Bridge, E. M., Curtis, E. A. & Gill, P. Zeeman slower for strontium based on permanent magnets. *Journal of Physics B: Atomic, Molecular and Optical Physics* **47** (2014). [1402.5271](#).
- [167] Herceg, D., Juhas, A. & Milutinov, M. A Design of a Four Square Coil System for a Biomagnetic Experiment. *Facta universitatis - series: Electronics and Energetics* **22** (2009).
- [168] Stanley, S. O. *et al.* The Loch Eil project: Sediment chemistry, sedimentation, and the chemistry of the overlying water in Loch Eil. *Journal of Experimental Marine Biology and Ecology* **55**, 299–313 (1981).

- [169] Ali, D. B. *et al.* Detailed study of a transverse field Zeeman slower. *Journal of Physics B: Atomic, Molecular and Optical Physics* **50**, 55008 (2017). URL <https://doi.org/10.1088/1361-6455/aa5a6a>.
- [170] Castin, Y., Wallis, H. & Dalibard, J. Limit of Doppler cooling. *J. Opt. Soc. Am. B* **6**, 2046–2057 (1989). URL <http://josab.osa.org/abstract.cfm?URI=josab-6-11-2046>.
- [171] Woodgate, G. K. *Elementary Atomic Structure* (Clarendon Press, 1980).
- [172] Karshenboim, S. G. & Ivanov, V. G. The g factor of the proton. *Physics Letters, Section B: Nuclear, Elementary Particle and High-Energy Physics* **566**, 27–34 (2003). [0306015v1](#).
- [173] Mukaiyama, T., Katori, H., Ido, T., Li, Y. & Kuwata-Gonokami, M. Recoil-Limited Laser Cooling of ^{87}Sr Atoms near the Fermi Temperature. *Physical Review Letters* **90**, 4 (2003).
- [174] Muniz, J. A., Norcia, M. A., Cline, J. R. K. & Thompson, J. K. A Robust Narrow-Line Magneto-Optical Trap using Adiabatic Transfer. *arXiv* **45**, 1–5 (2018). URL <http://arxiv.org/abs/1806.00838>. [1806.00838](#).
- [175] Reinaudi, G., Lahaye, T., Wang, Z. & Guéry-Odelin, D. Strong saturation absorption imaging of dense clouds of ultracold atoms. *Opt. Lett.* **32**, 3143–3145 (2007). URL <http://ol.osa.org/abstract.cfm?URI=ol-32-21-3143>.
- [176] Maussang, K. *États Comprimés Atomiques Sur Puce À Atomes*. Ph.D. thesis, Université Paris VI (2010).
- [177] Deutsch, C. *Trapped Atom Clock on a Chip Identical Spin Rotation Effects in an Ultracold Trapped Atomic Clock*. Ph.D. thesis, Université Pierre et Marie Curie (2011).
- [178] Lett, P. D. *et al.* Observation of atoms laser cooled below the doppler limit. *Physical Review Letters* **61**, 169–172 (1988).
- [179] Arnold, A. S. & Manson, P. J. Magneto-Optical Traps. *America* **17**, 497–506 (2000).
- [180] Prentiss, M. *et al.* Atomic-density-dependent losses in an optical trap. *Opt. Lett.* **13**, 452–454 (1988). URL <http://ol.osa.org/abstract.cfm?URI=ol-13-6-452>.
- [181] Xu, X., Loftus, T. H., Hall, J. L., Gallagher, A. & Ye, J. Cooling and trapping of atomic strontium. *Journal of the Optical Society of America B* **20**, 968 (2003). URL <https://www.osapublishing.org/abstract.cfm?URI=josab-20-5-968>.
- [182] Chanelière, T., Meunier, J.-L., Kaiser, R., Miniatura, C. & Wilkowski, D. Extra-heating mechanism in Doppler cooling experiments. *J. Opt. Soc. Am. B* **22**, 1819–1828 (2005). URL <http://josab.osa.org/abstract.cfm?URI=josab-22-9-1819>.

-
- [183] Townsend, C. G. *et al.* Phase-space density in the magneto-optical trap. *Physical Review A* **52**, 1423–1440 (1995).
- [184] Xu, X., Loftus, T. H., Hall, J. L., Gallagher, A. & Ye, J. Cooling and trapping of atomic strontium. *Journal of the Optical Society of America B* **20**, 968 (2003).
- [185] Dammalapati, U., Norris, I., Maguire, L., Borkowski, M. & Riis, E. A compact magneto-optical trap apparatus for calcium. *Measurement Science and Technology* **20** (2009).
- [186] Guest, J. R. *et al.* Laser trapping of Ra225 and Ra226 with repumping by room-temperature blackbody radiation. *Physical Review Letters* **98**, 98–101 (2007).
- [187] Sengstock, K. *et al.* Optical Ramsey spectroscopy on laser-trapped and thermal Mg atoms. *Appl. Phys. B* **59**, 99–115 (1994).
- [188] De, S., Dammalapati, U., Jungmann, K. & Willmann, L. Magneto-optical trapping of barium. *Physical Review A - Atomic, Molecular, and Optical Physics* **79**, 2–5 (2009). [0807.4100](#).
- [189] Kuwamoto, T., Honda, K., Takahashi, Y. & Yabuzaki, T. Magneto-optical trapping of Yb atoms using an intercombination transition. *Physical Review A - Atomic, Molecular, and Optical Physics* **60**, R745–R748 (1999).
- [190] Dreon, D. *et al.* Optical cooling and trapping of highly magnetic atoms: The benefits of a spontaneous spin polarization. *Journal of Physics B: Atomic, Molecular and Optical Physics* **50**, 1–12 (2017). URL <http://dx.doi.org/10.1088/1361-6455/aa5db5>. [1610.02284](#).
- [191] Zener, C. Non-adiabatic crossing of energy levels. *Proc. Roy. Soc. A* **33**, 696–702 (1932).
- [192] Kwon, R. Y. & Vourlidas, A. The density compression ratio of shock fronts associated with coronal mass ejections. *arXiv* (2018). [1801.04355](#).
- [193] Chang, R. *et al.* Three-dimensional laser cooling at the Doppler limit. *Phys. Rev. A* **90**, 63407 (2014). URL <https://link.aps.org/doi/10.1103/PhysRevA.90.063407>.
- [194] Ferri, F. *Strong coupling between a fiber-cavity mode and a commensurate atomic lattice. A new platform for many-body entanglement with single-particle control*. Ph.D. thesis, Paris Sciences et Lettres (2018).
- [195] Starkey, P. T. *et al.* A scripted control system for autonomous hardware-timed experiments. *Review of Scientific Instruments* **84** (2013). [1303.0080](#).
- [196] Abrarov, S. M. & Quine, B. M. Efficient algorithmic implementation of the Voigt/complex error function based on exponential series approximation. *Applied Mathematics and Computation* **218**, 1894–1902 (2011). URL <http://dx.doi.org/10.1016/j.amc.2011.06.072>.

